

Multiscale domain decomposition analysis of quasi-brittle materials



Oriol Lloberas-Valls

**Multiscale domain decomposition analysis
of quasi-brittle materials**

Multiscale domain decomposition analysis of quasi-brittle materials

Proefschrift

ter verkrijging van de graad van doctor
aan de Technische Universiteit Delft,
op gezag van de Rector Magnificus prof. ir. K.C.A.M. Luyben,
voorzitter van het College van Promoties,
in het openbaar te verdedigen op maandag 14 oktober 2013 om 10.00 uur
door Oriol LLOBERAS-VALLS
Enginyer Gedèleg, Universitat de Barcelona i
Universitat Politècnica de Catalunya
geboren te Terrassa, Spanje

Dit proefschrift is goedgekeurd door de promotoren:

Prof. dr. ir. L. J. Sluys

Prof. dr. ir. D. J. Rixen

Copromotor Dr. A. Simone

Samenstelling promotiecommissie:

Rector Magnificus

Voorzitter

Prof. dr. ir. L. J. Sluys

Technische Universiteit Delft, promotor

Prof. dr. ir. D. J. Rixen

Technische Universiteit Delft/Technische Universität München, Duitsland, promotor

Dr. A. Simone

Technische Universiteit Delft, copromotor

Prof. Dr.-Ir. C. Miehe

Universität Stuttgart, Duitsland

Prof. dr. ir. M. G. D. Geers

Technische Universiteit Eindhoven

Prof. dr. O. Allix

École Normale Supérieure de Cachan, Frankrijk

Prof. dr. ir. H. E. J. G. Schlangen

Technische Universiteit Delft

Prof. dr. ir. J. G. Rots

Technische Universiteit Delft, reservelid

Keywords: Multiscale analysis, domain decomposition methods, quasi-brittle materials, strain localization and softening

Cover: Jasmin Coleman's Concrete Cubes As Cube, July 2008. Picture © by Jasmin Coleman

Printed by Ipskamp drukkers

ISBN 978-94-6191-875-8

Copyright © 2013 by O. Lloberas-Valls

Acknowledgements

The research presented in this thesis was carried out at the Faculty of Civil Engineering and Geosciences at Delft University of Technology. Funding for this work was provided by the Flemish Institute for Science and Technology (SBO project IWT 03175).

A first word of thanks goes to my promotor Bert Sluys who gave me (two times) the opportunity to pursue a PhD position in the Structural Mechanics department. I'm indebted to him for the freedom, trust and support provided during all these years. Special thanks go to my second promotor Daniel Rixen for accepting to be involved in my work and providing crucial and positive feedback that definitely made this thesis possible. I thank my copromotor Angelo Simone for his supervision and active involvement in my research. His guidance and critical advice have greatly improved the quality of this manuscript.

I would like to express my gratitude to all past and present colleagues and collaborators at the department as well as all researchers involved in the SBO project. It has been a pleasure to work in such an international and stimulating working environment. In alphabetical order I thank A. Ahmed, J. Alfaiate, A. Alipour, R. Al-Khoury, H. Askes, R. Bellodi, G. Bol, K. van Breugel, J. Carmeliet, A. Caverzan, G. Degrande, K. De Proft, H. Derluyn, R. Esposito, J. Fan, S. François, A. García, G. Giardina, I. M. Gitman, S. Gupta, W. Haegeman, H. He, C. Iacono, A. Karamnejad, C. Karg, C. Kasbergen, M. Latifi, L. B. N. Le, S. Li, X. Liu, M. Malagu, P. R. Mandapalli, H. Masoumi, F. P. van der Meer, A. Meijer, S. Mertens, A. V. Metrikine, M. Musivand Arzanfudi, T. D. Nguyen, M. Nikbakht, K. B. Øelgaard, A. S. A. Ozbek, T. Pannachet, R. R. Pedersen, M. van der Perk, F. K. F. Radtke, J. G. Rots, M. Schevenels, H. E. J. G. Schlangen, Z. Shabir, X. Shan, M. G. Sierra, A. Sillem, E. Simons, A. Soto, M. Talebian, N. Ukrainczyk, J. Vantomme, I. Vegt, M. Villani, S. Weeratunge Kadawathagedara, J. Weerheijm, G. N. Wells and J. Zlopasa.

In particular I would like to thank Nguyen Vinh Phu, Frank Everdij, Martijn Stroeven and Peter Moonen for their fruitful involvement in my research.

My (long) stay in Delft has become now a special chapter in my life thanks to new people that I found during this adventure and old friends that shared part of this experience with short but intense visits from Barcelona. In alphabetical order I would like to thank Marta Auleda, Elisabeth Bakker, Anna Berenguer, Marta Bosch, Tine Brandau, Federica Butera, Ricard Canellas, Miguel Combarros, Nuria Cura, Yann Dufournet, Marta Faneca, Jordi Figueras, Hugo Fonteijn, Álvaro García, David Gonzalez, Linda Grimstrup, Jitske van der Laan, Giorgio Lasi, Martí Lloret, Peter Moonen, Laura Montero, Sandra Oudshoorn, Claudio Patriarca, Ronnie Pedersen, Simone Placidi, Michel Ponziani, Remon Pot, Ludo de Roo, María Luisa Ruiz, Toni Santiago, Anne Schenkkan, Albert Soto, Cristina Terribas, Paolo Tiso and Martijn van Vugt.

I specially enjoyed my last two years in Delft thanks to the swimming and water polo trainings. Therefore I'm grateful to all the members of the DSZ WAVE and specially to the water polo Heren 3 team.

A very special word of thanks goes to my family for their unconditional help and for supporting morally (and sometimes financially) all my steps in the academic world. There isn't a day that goes by that I don't miss my father Joaquim Lloberas Bosch who passed away during my PhD studies. From his example I will always try to learn the courage and attitude to deal with everyday life.

Finally, I can not find the words to thank Laura González for her love, trust and courage which have been crucial to shorten the distance that separated us (living in Barcelona and Delft) during all this time.

Oriol Lloberas-Valls
October 2013

To Laura

Contents

Acknowledgements	v
1 Recent developments in multiscale computational mechanics of failure	1
1.1 Overview of multiscale techniques	1
1.2 Scope of the analyses and applications	7
1.3 Comments on notation and modelling assumptions	8
2 The Finite element Tearing and Interconnecting method (FETI)	9
2.1 Formulation of the FETI method	10
2.2 Non-linear FETI framework	14
2.3 Notes on the FETI implementation adopted in this manuscript	15
3 Efficient domain decomposition techniques for quasi-brittle failure analysis	19
3.1 Framework enhancements for linear domains	20
3.2 Examples	27
3.3 Concluding remarks	41
4 Multiscale domain decomposition analysis of quasi-brittle material failure	45
4.1 Extensions for multiscale analysis	46
4.2 General multiscale framework for quasi-brittle heterogeneous materials	55
4.3 Examples	61
4.4 Concluding remarks	72
5 On micro-to-macro connections in domain decomposition multiscale analysis	75
5.1 General strong and weak micro-macro connections	76
5.2 Modified collocation techniques	82
5.3 Modified average compatibility techniques for heterogeneous interfaces	88
5.4 Mechanical characterization of the interscale links	91
5.5 Numerical examples	95
5.6 Concluding remarks	114
6 Multiscale analysis of failure in random granular heterogeneous materials	117
6.1 General procedure for the concurrent multiscale analysis of random heterogeneous materials	118
6.2 Numerical examples	121
6.3 Future opportunities: 3D analysis	136
6.4 Concluding remarks	136
7 Conclusions and recommendations	139
7.1 Summary of conclusions	140
7.2 Recommendations and future research	142

A Selected model for quasi-brittle failure	145
A.1 Gradient enhanced damage model and its FE implementation	145
A.2 Numerical aspects in a FETI framework	148
B A family of generalized inverses	151
C Iterative Solvers for the FETI interface problem	155
C.1 The Preconditioned Conjugate Gradient (PCG) method	155
C.2 Preconditioned Bi-Conjugate Gradient Stabilized (Bi-CGSTAB)	157
D Mechanically consistent preconditioners for the FETI interface problem	161
D.1 Extension to mechanically consistent preconditioners	162
D.2 Homogeneous problems (Multiplicity scaling)	163
D.3 Heterogeneous problems (Smoothing procedures)	163
E Assessment of the interface FETI solver for highly heterogeneous structures	167
E.1 Convergence study in a linear elastic heterogeneous material	167
E.2 The role of damage	171
E.3 General remarks	176
References	179
Summary	187
Samenvatting	189
Curriculum vitae	195

Chapter 1

Recent developments in multiscale computational mechanics of failure

Multiscale analysis of softening brittle materials has recently become a topic of main interest for the computational mechanics community. While many multiscale techniques for linear elastic and hardening solids are widely accepted [27, 76, 79], those that aim at resolving softening and strain localization phenomena at different scales are still under development. The main goal of a multiscale technique is to objectively capture the influence of the micro/meso-scale constituents and their interactions on the macroscale behaviour. Consequently, multiscale methods can be used to facilitate numerical analyses at a high level of detail and assist in the design of new materials.

Unfortunately, the analysis of failure phenomena at different scales cannot be accomplished with the use of standard homogenization schemes for non-linear heterogeneous materials [27]. In fact, the nucleation and propagation of cracks in a solid is an evolving phenomenon that transcends the scales. Moreover, the numerical treatment of strain localization and fracture has been a topic of great development in recent years due to the difficulty of achieving robust and regularized formulations. Multiscale methods for fracture analysis have to deal with these issues and often result in sophisticated schemes which are specifically tailored to a particular constitutive model.

1.1 Overview of multiscale techniques

In order to classify and motivate the main contribution of this work, a short overview of commonly used multiscale techniques is given in this section. Different types of multiscale techniques are introduced together with their capabilities and/or shortcomings when dealing with fracture processes. A classification is adopted in which the scale separation between upper (L) and lower (l) scales serves as the leading criterion (see Figure 1.1)¹. In this

¹The definition of upper and lower scales adopted in this classification refers to the length l of the material sample at the lower scale and the length L of the upper scale region over which

manner, two main groups may be distinguished: hierarchical and concurrent multiscale techniques. In the former, the upper and lower scales are completely separated ($L \gg l$) whilst in the latter they remain coupled ($L = l$). In addition, the structure of computation, as suggested by Belytschko and Song [7], is considered as a secondary criterion to make a subdivision of techniques. Consequently, one can distinguish between decoupled (or sequential), weak coupling, and strong coupling multiscale techniques. The following overview is based on this secondary criterion since it allows to distinguish more accurately between up-to-date established and emerging techniques.

1.1.1 Decoupled (or sequential) techniques

In these approaches, information is passed in one direction from the microscopic (or mesoscopic) to the macroscopic level. This information exchange is performed as a preprocessing step before the macroscopic analysis is initiated. Since the flow of information is performed only once, at the beginning of the analysis, these techniques extract a simplified microscopic constitutive behaviour which is, in most cases, linear elastic. Depending on the representation of both micro and macroscales, one can distinguish between continualization [77], and homogenization [79] procedures. In the former technique, the lower level is modelled as a discrete medium whilst in the latter both levels are described using the continuum theory.

Analytical homogenization techniques provide closed-form expressions of the effective properties obtained in a Representative Volume Element (RVE) [43] of the heterogeneous material. Conversely, in numerical homogenization techniques [110], the apparent properties are retrieved by using numerical procedures such as the Finite Element (FE) method [119]. For this reason, they are specially suitable to analyze RVEs with a more complex heterogeneous structure. In this approach, numerical homogenization techniques are used to compute elastic properties of the homogeneous bulk during the elastic regime.

Hierarchical decoupled multiscale techniques present some difficulties in synthesizing complex material behaviour such as fracture processes and, therefore, are mainly applicable to linear and non-linear constitutive models that do not show softening and strain localization.

the multiscale analysis is performed.

1.1 Overview of multiscale techniques

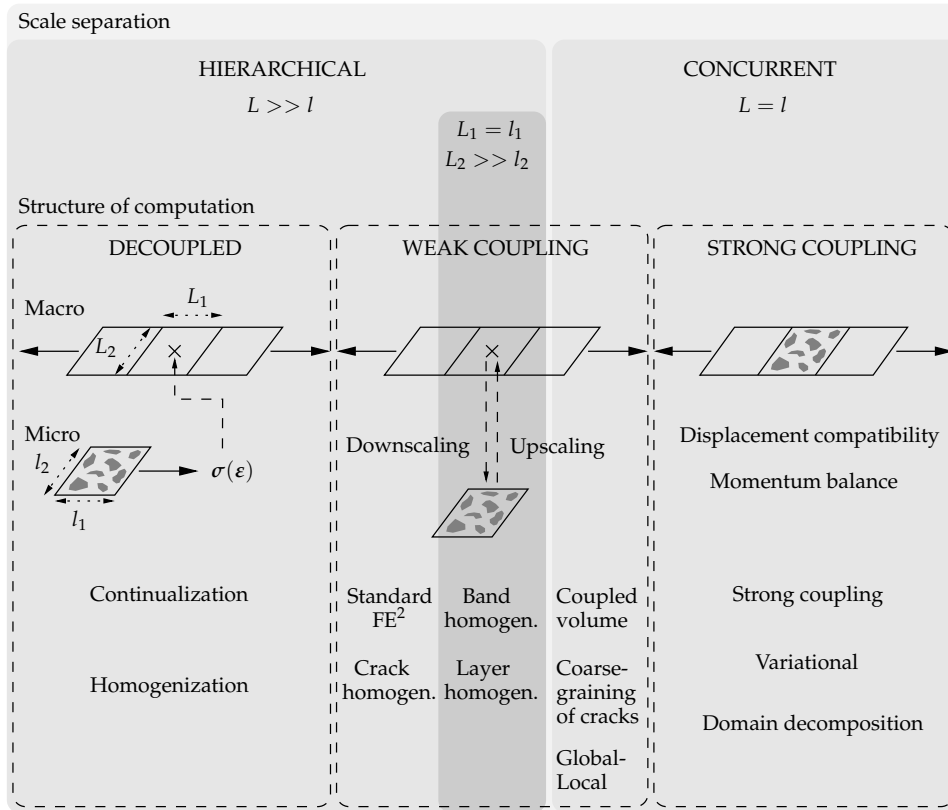


Figure 1.1 A two-fold classification of multiscale strategies based on the scale separation concept and structure of computation. Lengths L and l refer to macro and microscales, respectively.

1.1.2 Weak coupling techniques

In these multiscale techniques, the constitutive information driving the macroscopic FE analysis is the result of consecutive interactions between macroscale and microscale. Hence, the explicit macroscopic constitutive behaviour does not exist a priori but it is constructed by successive computations performed over the RVE of the microstructure. Two distinct stages, namely downscaling and upscaling, are typical of this kind of techniques (see Figure 1.1). The FE^2 approach proposed by Feyel et al. [28] is a typical weak coupling multiscale method which can tackle the non-linear behaviour of complex microstructures. Different types of boundary conditions [73] can be chosen for the downscaling and they highly influence the solution field at the boundary of the RVE. In the global-local approach proposed by Duarte and Kim [17], the downscaling is directly accomplished by imposing the global (macroscopic) field at the boundaries of the refined local (meso/micro) problem. In this approach, the upscaling consists of enriching the global shape functions with the local solution.

One of the main challenges of these multiscale schemes has been the analysis of strain localization and failure phenomena. In the first place, an RVE for the softening regime cannot be found using standard averaging techniques since the mechanical behaviour depends on the RVE size. This results in a mesoscopic or microscopic RVE size dependence when an FE^2 -like scheme is used [33]. On the other hand, the macroscopic discretization might suffer from mesh dependency and, at ultimate damage stages, the problem can become ill-posed if there is no regularization technique adopted thereby.

A strategy to account for the microscopic length scale is the use of gradient formulations [52, 59]. However, macroscopic localization beyond a quadratic nature of the displacements cannot be properly resolved [30]. A straightforward methodology to overcome macroscopic mesh size sensitivity in multiscale analysis of softening materials² is characterized by the direct coupling of the macroelements and RVE size ($L = l$) as adopted in the “coupled volume” [33] or “coarse-graining of cracks” [7] approaches. Other techniques are based on inserting a simplified representation of the failure mechanisms at the macrolevel. This can be accomplished with the use of embedded localization bands [68] or material layers [69] and the insertion of cracks [80, 112] or eigenstrains [117] at the macrolevel. The main drawback of all these techniques is that they all provide a simplified representation of

²Note that mesoscopic mesh size sensitivity may be still present if no regularization strategy is adopted at the mesoscopic level.

1.1 Overview of multiscale techniques

fracture at the macrolevel (i.e. crack, strain localization band, eigenstrain) which might not be able to fully capture the effects of more complex failure mechanisms (i.e. crack orientation, bridging and branching due to the micro/mesostructure).

The development of selective averaging techniques on the failure areas [81, 112] has been determinant for the use of an RVE to compute the cohesive and adhesive behaviour of macroscopic cracks [80, 82, 112]. Extensions of such schemes that also account for the inelastic processes taking place at the bulk material surrounding the crack are presented in [11, 83, 101, 109]. All these approaches can account for problems in which micro, and macroscopic, scales are separated ($l \ll L$) with a reasonable computational effort.

1.1.3 Strong coupling techniques

When a strong coupling technique is used, the lower and upper material level discretizations are resolved simultaneously. For this reason, global equilibrium and displacement compatibility need to be enforced across the whole structure resulting into a strong coupling between macro and meso/micro levels. The jump in scales is accomplished as a result of a zoom-in or local refinement since the relation $L = l$ is implicitly adopted in the construction of these methods.

When accounting for softening and strain localization phenomena, these techniques do not suffer from the shortcomings of the standard FE^2 schemes since the micro/mesoscopic cell size dependence vanishes due to the strong coupling between the different scales. Another advantage of these techniques is that failure processes can be accurately described, from crack nucleation to crack coalesce and propagation, and reliable results, comparable to those obtained with a direct numerical solution (DNS), can be obtained. On the other hand, a higher jump in scales requires a high increase in the computation resources.

Examples of strong coupling multiscale methods can be found in [49, 50, 71, 84, 88]. They are instances of the variational multiscale method introduced by Hughes et al. [48]. Essentially, they assume an additive decomposition of the displacement field into a macroscopic and a meso/microscopic counterpart; furthermore, the fine-scale regions that overlap the coarse-scale elements are glued with the use of Lagrange Multipliers. Obviously, all these formulations and domain decomposition methods share some common features. Nevertheless, most of the strong coupling multiscale methods are

based on sequential algorithms which might become computationally expensive when large systems need to be resolved. For this reason, the use of Multiscale methods based on domain decomposition techniques seem to be an adequate alternative. The multiscale application presented in this work falls in this group and shows some similarities with the contribution of Amini et al. [4] although it is specially tailored for non-linear analysis of brittle materials. Ladevèze et al. [60], Guidault et al. [36, 37] and Kerfriden et al. [54] have presented a related work where a more complex interface between domains is employed.

1.1.4 Qualitative comparison of different approaches

The classification shown in Figure 1.1 is specially useful to highlight the main features of each multiscale technique. In fact, the same classification is utilized in Figure 1.2 to provide a qualitative comparison between the different approaches based on six fundamental criteria: number of assumptions, generality, computational cost, scale jump and accuracy with respect to Direct Numerical Simulations (DNS). Roughly, one can observe that con-

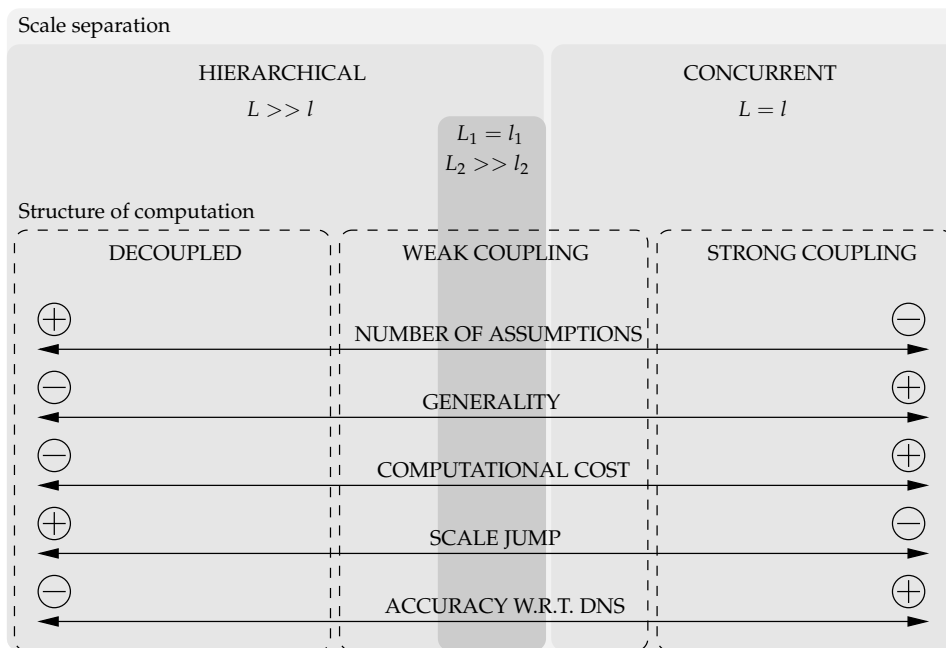


Figure 1.2 Qualitative comparison of multiscale strategies.

1.2 Scope of the analyses and applications

current approaches, i.e. $L = l$, involve higher computational costs due to the large fine scale area which is processed during the analysis. Considering that the computational resources are limited, the scale jump that can be accomplished with such techniques is moderate (one or two orders of magnitude) compared to hierarchical techniques which can cover scale jumps of more orders of magnitude.

Concurrent type approaches are mainly based on the zoom-in concept which reduces to the increase of resolution at areas of interest. The kernel of this methodology resides at the algebraic level and constitutes the constraint imposed to link material regions with different scale resolution. For such reason, these type of techniques are immediately applicable to a broad range of problems when compared to hierarchical techniques. In other words, concurrent type of techniques are considered more flexible or general since no specific assumptions related to the physics of the problem are needed a priori. Conversely, in hierarchical multiscale approaches, the multiscale strategy can be specifically tailored for one particular model and the number of assumptions adopted to derive the multiscale relations tends to be higher.

It is difficult to compare the solution of hierarchical multiscale techniques with DNS since, by definition, a full scale DNS with a high scale jump may not be possible with up-to-date commonly available computers. However, in academical analysis with a moderate scale jump, hierarchical techniques tend to provide less accurate results compared to concurrent multiscale techniques.

Key issues to consider before selecting an adequate multiscale technique consist in defining the scale jump of the analysis, the available computer power and the required accuracy.

1.2 Scope of the analyses and applications

The multiscale technique presented in this manuscript can be classified as a concurrent approach. However, it employs some procedures commonly used in hierarchical decoupled and weak coupling schemes. For this reason, the developed strategy is referred to as a hybrid multiscale framework. The approach relies on the strong coupling between scales and is based on domain decomposition techniques. Consequently, it is highly recommended for multiscale problems with a moderate scale jump between 10 to 10^2 length units between the upper and lower scale. The reason for this restriction is that we focus on failure analysis of quasi-brittle materials such as

concrete and, therefore, we seek a technique that can capture the interaction between mesoscopic scale components, e.g. aggregates, with the growth and propagation of fracture. However, the proposed multiscale technique may be applicable to a wider range of problems.

Multiscale analysis of failure in concrete-like materials is performed in which two main scales are distinguished, i.e. a macroscale, typically constituted of an homogeneous bulk, and a mesoscale, formed by material heterogeneity such as aggregates or reinforcement. Due to the academic character of the implementation utilized in this manuscript, the jump between scales is about one order of magnitude which is still low compared to optimized implementations in which parallel computations can be accounted for. However, the range of applications explored in this study allows a direct comparison with DNS. In this view, the main objective of the present study is to develop a robust multiscale algorithm which provides a solution close to DNS and reasonably independent of user defined parameters such as the FE discretization or domain decomposition type.

1.3 Comments on notation and modelling assumptions

Matrix or Voigt notation is employed throughout the present document. Array entities are distinguished from scalars using boldface characters. One-dimensional arrays are denoted by lowercase characters whilst two-dimensional arrays are denoted by uppercase characters. Tensor notation is only employed during the introduction of the governing and constitutive equations of the model utilized in the computations (cf. Appendix A). Index notation is only employed in equations (5.5), (5.6) and (5.10).

All simulations correspond to the solution of equilibrium problems under quasi-static analysis conditions. Small deformations are assumed in the description of the kinematics except from a few equations in Section 5.2 where large deformation kinematics are considered in order to provide a more general formulation. For clarity, all symbols and abbreviations are defined when they first appear in the text.

Chapter 2

The Finite element Tearing and Interconnecting method (FETI)

The computational analysis of structures with a high degree of resolution leads to the solution of large systems of equations. Consequently, strategies based on a divide-and-conquer approach such as model reduction and domain decomposition techniques [90] are well suited for these complex systems. Domain decomposition techniques [34, 90] can be seen as highly efficient parallel solvers in which the interface problem is solved iteratively. A reduced approximated basis is built for the interface degrees of freedom (DOFs). The first domain decomposition method was proposed by Schwarz in 1870 [102] and consisted in solving a partial differential equation on an overlapping union of two different domains. In the beginning, these methods were mostly mathematically oriented although the progressive interest in engineering problems gave rise to a family of non-overlapping domain decomposition methods formulated for discretization techniques such as the Finite Element (FE) method [119]. In this context, the Primal and Dual domain decomposition methods¹ appeared in [61] and [25], respectively. The reader is referred to [34] for an overview of non-overlapping domain decomposition techniques.

The basic formulation of the Finite Element Tearing and Interconnecting (FETI) method is introduced in this chapter. The FETI method, introduced by Farhat et al. [25], belongs to the family of Dual domain decomposition methods and constitutes the backbone of the present framework. For the sake of clarity, the formulation is presented for the case of a linear FE analysis. The extension to non-linear analysis is summarized at the end of this chapter.

¹Primal and Dual domain decomposition techniques differ in the adopted strategy to enforce compatibility between domains. In the Primal approach the boundary DOFs in each domain are unique and, therefore, their corresponding FE quantities are assembled at the same location in global arrays. In Dual methods the compatibility conditions are enforced with the use of Lagrange multipliers which can be seen as connecting forces.

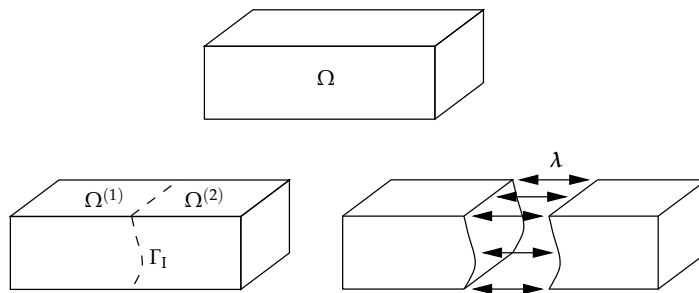


Figure 2.1 Decomposition of a body Ω in two domains. Lagrange multipliers λ are utilized at the interface.

2.1 Formulation of the FETI method

Consider the body Ω depicted in Figure 2.1 (top). The variational form of a general equilibrium problem can be discretized, in a linear context, using standard FE procedures. The resulting set of equations for Ω^s reads

$$\mathbf{K}\mathbf{u} = \mathbf{f}, \quad (2.1)$$

where the global stiffness matrix \mathbf{K} sets the relation between forces \mathbf{f} and displacements \mathbf{u} as

$$\mathbf{K} = \frac{\partial \mathbf{f}}{\partial \mathbf{u}} \quad (2.2)$$

and it is assumed in the remaining of this section that \mathbf{K} is symmetric and positive-definite.

The body Ω is divided in two domains, $N_s = 2$, as shown in Figure 2.1 (bottom). Continuity of the solution field between the two domains is enforced by the interface constraint

$$\mathbf{u}^{(1)} = \mathbf{u}^{(2)} \text{ at } \Gamma_I. \quad (2.3)$$

Discretization of the variational form of the equilibrium equations for each domain, together with the compatibility conditions in (2.3), gives rise to the system

$$\begin{bmatrix} \mathbf{K}^{(1)} & \mathbf{0} & \mathbf{B}^{(1)\top} \\ \mathbf{0} & \mathbf{K}^{(2)} & \mathbf{B}^{(2)\top} \\ \mathbf{B}^{(1)} & \mathbf{B}^{(2)} & \mathbf{0} \end{bmatrix} \begin{bmatrix} \mathbf{u}^{(1)} \\ \mathbf{u}^{(2)} \\ \lambda \end{bmatrix} = \begin{bmatrix} \mathbf{f}^{(1)} \\ \mathbf{f}^{(2)} \\ \mathbf{0} \end{bmatrix}. \quad (2.4)$$

2.1 Formulation of the FETI method

The matrices $\mathbf{B}^{(s)}$ contain the Boolean +1 or -1 at those positions that correspond to the interface of domain $\Omega^{(s)}$ and 0 elsewhere. The continuity condition shown in (2.3) can be rewritten accordingly as

$$\mathbf{B}^{(1)}\mathbf{u}^{(1)} + \mathbf{B}^{(2)}\mathbf{u}^{(2)} = \mathbf{0}. \quad (2.5)$$

The solution field is composed by the domain displacements $\mathbf{u}^{(s)}$ and the Lagrange multipliers λ , which are the forces that keep the domains together across the interface.

Without loss of generality, a local solution for domain $\Omega^{(s)}$ can be found as

$$\mathbf{u}^{(s)} = \mathbf{K}^{(s)+} \left(\mathbf{f}^{(s)} - \mathbf{B}^{(s)\text{T}}\lambda \right) - \mathbf{R}^{(s)}\boldsymbol{\alpha}^{(s)}. \quad (2.6)$$

Local singularities are handled by the generalized inverse $\mathbf{K}^{(s)+}$ [24, 25] (cf. Appendix B). Domains that are insufficiently constrained, i.e. statically indeterminate, exhibit rigid body modes (RBMs) $\mathbf{R}^{(s)}$ of amplitude $\boldsymbol{\alpha}^{(s)}$ spanning the null space of $\mathbf{K}^{(s)}$. These RBMs correspond to all displacement configurations that do not contribute to the deformation energy, thus satisfying $\mathbf{K}\mathbf{u}_{\text{rbm}} = \mathbf{0}$ at the corresponding domain $\Omega^{(s)}$. The generalized inverse $\mathbf{K}^{(s)+}$ coincides with the standard inverse $\mathbf{K}^{(s)-1}$ if $\mathbf{K}^{(s)}$ is non-singular.

The amplitudes $\boldsymbol{\alpha}^{(s)}$ of the RBMs are determined by imposing self-equilibrium between the prescribed external forces $\mathbf{f}^{(s)}$ and the tying forces $\mathbf{B}^{(s)\text{T}}\lambda$ between domains which results in the orthogonality condition:

$$\mathbf{R}^{(s)\text{T}} \left(\mathbf{f}^{(s)} - \mathbf{B}^{(s)\text{T}}\lambda \right) = \mathbf{0}. \quad (2.7)$$

The left hand side of (2.7) represents the mechanical work developed by the domain boundary forces in the rigid body modes. The tying forces λ and the amplitudes $\boldsymbol{\alpha}$ of the RBMs are found by solving the interface problem

$$\begin{bmatrix} \mathbf{F}_I & \mathbf{G}_I \\ \mathbf{G}_I^{\text{T}} & \mathbf{0} \end{bmatrix} \begin{bmatrix} \lambda \\ \boldsymbol{\alpha} \end{bmatrix} = \begin{bmatrix} \mathbf{d} \\ \mathbf{e} \end{bmatrix}, \quad (2.8)$$

which is obtained by substituting (2.6) in the compatibility condition (2.5) and taking into account the orthogonality condition (2.7) where

$$\mathbf{F}_I = \sum_{s=1}^{N_s} \mathbf{B}^{(s)}\mathbf{K}^{(s)+}\mathbf{B}^{(s)\text{T}}, \quad (2.9a)$$

$$\mathbf{d} = \sum_{s=1}^{N_s} \mathbf{B}^{(s)} \mathbf{K}^{(s)+} \mathbf{f}^{(s)}, \quad (2.9b)$$

$$\mathbf{G}_I = [\mathbf{B}^{(1)} \mathbf{R}^{(1)} \quad \dots \quad \mathbf{B}^{(N_s)} \mathbf{R}^{(N_s)}], \quad (2.9c)$$

$$\boldsymbol{\alpha} = [\boldsymbol{\alpha}^{(1)\top} \quad \dots \quad \boldsymbol{\alpha}^{(N_s)\top}]^\top, \quad \text{and} \quad (2.9d)$$

$$\mathbf{e} = [\mathbf{f}^{(1)\top} \mathbf{R}^{(1)} \quad \dots \quad \mathbf{f}^{(N_s)\top} \mathbf{R}^{(N_s)}]^\top. \quad (2.9e)$$

The operator \mathbf{F}_I represents the flexibility of the interface. When the RBMs are absent, the matrix \mathbf{F}_I sets the relation between the forces $\boldsymbol{\lambda}$ and the displacement gap \mathbf{d} at the interface created by the external forces. The operator \mathbf{G}_I is built considering the rigid body modes of each domain restricted onto the interface. The total number of domains is represented by N_s . The matrix product $\mathbf{B}^{(s)} \mathbf{R}^{(s)}$ considers only those configurations of the rigid body modes with components at the interface and neglects all inner degrees of freedom. The vector \mathbf{e} is the part of the applied force that is out of balance with respect to the rigid body modes.

The local problems shown in (2.6) are solved using a blend of direct solvers while the interface problem in (2.8) is processed using an iterative solver. To this end, the indefinite interface problem needs to be transformed into a semi-definite system of equations on $\boldsymbol{\lambda}$. This is done by eliminating the RBMs $\boldsymbol{\alpha}$ from (2.8), i.e. enforcing the constraint $\mathbf{G}_I^\top \boldsymbol{\lambda} = \mathbf{e}$, using the projection

$$\mathbf{P} = \mathbf{I} - \mathbf{Q} \mathbf{G}_I \left(\mathbf{G}_I^\top \mathbf{Q} \mathbf{G}_I \right)^{-1} \mathbf{G}_I^\top. \quad (2.10)$$

The full rank matrix \mathbf{Q} is often set equal to the identity matrix \mathbf{I} but can play the role of a preconditioner² for the coarse grid displacements as argued in [9, 26, 95] (cf. Appendix D). The Lagrange multipliers $\boldsymbol{\lambda}$ are decomposed according to

$$\boldsymbol{\lambda} = \boldsymbol{\lambda}_0 + \mathbf{P} \bar{\boldsymbol{\lambda}}, \quad (2.11)$$

with

$$\boldsymbol{\lambda}_0 = \mathbf{Q} \mathbf{G}_I \left(\mathbf{G}_I^\top \mathbf{Q} \mathbf{G}_I \right)^{-1} \mathbf{e}. \quad (2.12)$$

²A preconditioner $\tilde{\mathbf{K}}^{-1}$ is an approximation of the inverse \mathbf{K}^{-1} . The cost of computations involving $\tilde{\mathbf{K}}^{-1}$ in an iterative solver must be low. However, the preconditioner has a high impact on the convergence of the iterative solver in the sense that a well chosen preconditioner improves such a convergence.

2.1 Formulation of the FETI method

With the aid of the decomposition (2.11) and the projection operator \mathbf{P} , the interface problem defined in (2.8) is transformed into the alternative symmetric positive-semi-definite interface problem

$$\mathbf{P}^T \mathbf{F}_I \mathbf{P} \bar{\boldsymbol{\lambda}} = \mathbf{P}^T (\mathbf{d} - \mathbf{F}_I \boldsymbol{\lambda}_0) \quad \text{and} \quad (2.13a)$$

$$\boldsymbol{\alpha} = \left(\mathbf{G}_I^T \mathbf{Q} \mathbf{G}_I \right)^{-1} \mathbf{G}_I^T \mathbf{Q} (\mathbf{d} - \mathbf{F}_I \boldsymbol{\lambda}). \quad (2.13b)$$

The problem in (2.13a) is ready to be solved for the Lagrange multipliers $\boldsymbol{\lambda}$ applying a Preconditioned Conjugate Gradient (PCG) algorithm [5, 42] (cf. Appendix C). The amplitudes $\boldsymbol{\alpha}$ of the RBMs are found after solving (2.13a) as indicated in (2.13b). The displacement field at each domain $\mathbf{u}^{(s)}$ is recovered by evaluating (2.6) using the solution fields $\boldsymbol{\lambda}$ and $\boldsymbol{\alpha}$ from the alternative semi-definite interface problem (2.13).

In practice, an iterative solver is always adopted when using the FETI technique and, therefore, the system in (2.8) does not need to be explicitly assembled. Consequently, the FETI method can be regarded as a solver for a decomposed structure and usually consists of a blend of direct solvers for the independent local problems (2.6) and iterative solvers for the semi-definite interface problem (2.13). The design of the FETI algorithm allows to parallelize a considerable number of operations. Parallel performance is measured by means of the speed-up

$$S_p = t_1 / t_p \quad (2.14)$$

and the parallel efficiency

$$E_p = S_p / p, \quad (2.15)$$

where t_1 and t_p are the time required to perform the computation on one and p processors, respectively. Obviously, the parallel performance depends on the fraction f of tasks that must be carried out sequentially. In this view, Amdahl's law [3] states that the overall speed-up

$$S_p = \frac{1}{f + (1 - f) / p} \quad (2.16)$$

and, consequently, the ideal speed-up $S_p = p$ is achieved when all calculations are performed in a parallel fashion. Considering a large number of processors p and a given fraction of sequential work f , the maximum speed-up

$$S_{p,\max} = 1 / f. \quad (2.17)$$

It is, therefore, essential to design algorithms with a minimum fraction of sequential work in order to reach the optimum of parallel performance. A more realistic estimate of the speed-up for massive parallel calculations is provided by Gustafson's law [40] which states that

$$S_p = p(1 - f) + f \quad (2.18)$$

and it is assumed that the size of the problem increases with the number of processors. However, communication costs are not taken into account in (2.18) and, therefore, the speed-up is still too optimistic when compared to real analyses.

The FETI solvers represent a good compromise between communication costs and numerical scalability —the number of operations increases only weakly when the number of processors is increased. These properties confer to FETI, and to other similar domain decomposition methods, a good parallel efficiency [9].

2.2 Non-linear FETI framework

The mechanical behaviour of the materials considered in this study is non-linear. Hence, the system of equations that arises from the discretization of such a material model is non-linear as well and requires the use of an iterative procedure. At a generic load step, the updated solution and Lagrange multiplier fields at a Newton-Raphson (NR) iteration $i + 1$ are denoted by

$$\mathbf{u}_{i+1} = \mathbf{u}_i + \delta\mathbf{u}_{i+1}, \quad (2.19a)$$

$$\lambda_{i+1} = \lambda_i + \delta\lambda_{i+1}. \quad (2.19b)$$

The linearized system of equations for the non-linear FETI framework together with the compatibility conditions read

$$\mathbf{K}_i^{(s)} \delta\mathbf{u}_{i+1}^{(s)} + \mathbf{B}^{(s)\top} \delta\lambda_{i+1} = \mathbf{f}_{\text{ext}}^{(s)} - \mathbf{B}^{(s)\top} \lambda_i - \mathbf{f}_{\text{int},i}^{(s)}(\mathbf{u}_i^{(s)}), \quad (2.20a)$$

$$\sum_{s=1}^{N_s} \mathbf{B}^{(s)} \mathbf{u}_i^{(s)} + \sum_{s=1}^{N_s} \mathbf{B}^{(s)} \delta\mathbf{u}_{i+1}^{(s)} = \mathbf{0}. \quad (2.20b)$$

The arrays $\mathbf{K}_i^{(s)}$, $\mathbf{f}_{\text{ext}}^{(s)}$, $\mathbf{f}_{\text{int},i}^{(s)}$, $\delta\mathbf{u}^{(s)}$ and $\delta\lambda^{(s)}$ denote the domain tangent stiffness matrix, external and internal force vectors and the incremental vectors of the displacements and Lagrange multipliers, respectively. The NR scheme

2.3 Notes on the FETI implementation adopted in this manuscript

employed to solve the above system implies a quadratic convergence rate. If an energy norm is selected, the global system in (2.20) is converged when

$$\left\| \delta \mathbf{u}_i^T \mathbf{r}_i \right\| \leq \epsilon \left\| \delta \mathbf{u}_0^T \mathbf{r}_0 \right\|, \quad (2.21)$$

where the residual $\mathbf{r} = \mathbf{f}_{\text{ext}} - \mathbf{f}_{\text{int}}$ and ϵ denotes a sufficiently small tolerance, e.g. $\epsilon = 10^{-6}$. The global energy increment

$$\delta \mathbf{u}^T \mathbf{r} = \sum_{s=1}^{N_s} \delta \mathbf{u}^{(s)T} \mathbf{r}^{(s)}. \quad (2.22)$$

The algorithm of the non-linear FETI framework resembles the one of a standard non-linear FE method. However, loops over the different domains are needed to assemble the domain finite element quantities and the standard direct solver is replaced by the FETI solver. A solution process to the systems in (2.20) for a general non-linear model is summarized in Box 1.

The FETI method can be employed for the solution of large non-linear problems in which a Newton-like scheme is used to transform the governing equations into a sequence of linear systems. Provided that an iterative solver is chosen for processing the interface problem, the non-linear approach falls into the so-called Newton-Krylov-Schur (NKS) methods [13, 23]. Since the tangent stiffness matrix in (2.20a) changes for every NR-iteration (so called multiple left hand side case) one can reuse CG iterates of the interface problem for the previous NR-iteration in order to accelerate the convergence. Those techniques were originally proposed in [93, 100] and further developed in [35].

Other interesting techniques to tackle non-linearity with a DD method consist in solving a global linear interface problem and a set of independent nonlinear local problems at each global iteration [45, 86]. In other words, the domain decomposition method is used to split a global non-linear problem into a set of local non-linear problems.

2.3 Notes on the FETI implementation adopted in this manuscript

The next chapters focus on the modifications to the non-linear FETI framework for the efficient and multiscale analysis of quasi-brittle materials. The design of a full parallel implementation is out of the scope of this study. In fact, a direct solver is utilized for the solution of the interface problem in (2.8) which is explicitly assembled in all computations. Consequently, the

Box 1 Iterative scheme of the non-linear FETI framework

Initialize: $\mathbf{u}_0^{(s)}$, $\mathbf{K}_0^{(s)}$, $\mathbf{f}_{\text{ext},0}^{(s)}$, $\mathbf{f}_{\text{int},0}^{(s)}$ and λ_0 .

For each loading step Δt :

1. Add new force increment to external force vector $\mathbf{f}_{\text{ext},t+1}^{(s)} = \mathbf{f}_{\text{ext},t}^{(s)} + \Delta \mathbf{f}_{\text{ext},t+1}^{(s)}$ and compute interface connectivity $\mathbf{B}^{(s)}$.
2. Update tangent stiffness $\mathbf{K}_i^{(s)}$ using nodal data from last iteration i .
3. Set residual $\mathbf{r}_i^{(s)} = \mathbf{f}_{\text{ext},t+1}^{(s)} - \mathbf{B}^{(s)\top} \lambda_i - \mathbf{f}_{\text{int},i}^{(s)}$.
4. FETI solver:
 - Factorize stiffness matrix $\mathbf{K}_i^{(s)}$ and compute rigid body modes $\mathbf{R}^{(s)}$.
 - Assemble interface problem: $\mathbf{F}_{I,i}$, $\mathbf{G}_{I,i}$, \mathbf{d}_i and \mathbf{e}_i .
 - Solve for $\delta \lambda_{i+1}$ and $\delta \alpha_{i+1}$.
 - Compute total Lagrange multipliers $\lambda_{i+1} = \lambda_i + \delta \lambda_{i+1}$.
 - Compute iterative displacement increments

$$\delta \mathbf{u}_{i+1}^{(s)} = \mathbf{K}_i^{(s)+} \left(\mathbf{f}_{\text{ext},t+1}^{(s)} - \mathbf{B}^{(s)\top} \lambda_i - \mathbf{f}_{\text{int},i}^{(s)} \right) - \mathbf{R}^{(s)} \delta \alpha_{i+1}^{(s)}.$$
5. Update displacement increments $\Delta \mathbf{u}_{i+1}^{(s)} = \Delta \mathbf{u}_i^{(s)} + \delta \mathbf{u}_{i+1}^{(s)}$ and total displacements $\mathbf{u}_{i+1}^{(s)} = \mathbf{u}_i^{(s)} + \Delta \mathbf{u}_{i+1}^{(s)}$.
6. Compute strain increments $\Delta \boldsymbol{\varepsilon}_{i+1}^n \leftarrow \Delta \mathbf{u}_{i+1}^{(s)}$ for each integration point n in $\Omega^{(s)}$.
7. Compute stress increments $\Delta \boldsymbol{\sigma}_{i+1}^n \leftarrow \Delta \boldsymbol{\varepsilon}_{i+1}^n$ for each integration point n in $\Omega^{(s)}$.
8. Compute internal force increment $\Delta \mathbf{f}_{\text{int},i+1}^{(s)} \leftarrow \Delta \boldsymbol{\sigma}_{i+1}^n$ and update internal force vector $\mathbf{f}_{\text{int},i+1}^{(s)} = \mathbf{f}_{\text{int},i}^{(s)} + \Delta \mathbf{f}_{\text{int},i+1}^{(s)}$.
9. Assemble domain FE quantities $\mathbf{f}_{\text{ext},t+1}^{(s)}$ and $\mathbf{f}_{\text{int},i+1}^{(s)}$ into global quantities $\mathbf{f}_{\text{ext},t+1}$ and $\mathbf{f}_{\text{int},i+1}$.
10. Check for convergence:
 - If converged, go to 1.
 - Else, add new iteration i and go to 2.

All operations involving domain FE quantities (i.e. with superscript s) require a loop over all domains $\Omega^{(s)}$.

Quantities without a subscript t or i , i.e. $\mathbf{B}^{(s)}$ and $\mathbf{R}^{(s)}$, do not need to be re-computed at each step or iteration if the domain decomposition is not varied during the analysis.

2.3 Notes on the FETI implementation adopted in this manuscript

compatibility conditions between domains are expressed in a matrix form avoiding all possible redundant constraints. The resulting system would become singular if such redundancies were taken into account.

Adequate preconditioned iterative solvers for the FETI interface problem are introduced in Appendices C to E. All redundant constraints must be taken into account in these type of analyses in order to ensure the maximum efficiency of the iterative solver. However, Appendix E clearly shows that the performance of an iterative solver is challenged by the presence of material heterogeneities in the analysis.

It is pointed out that all extensions to the FETI method studied in this manuscript are compatible with a full parallel implementation.

Chapter 3

Efficient domain decomposition techniques for quasi-brittle failure analysis*

The study of cracking and failure phenomena is of utmost importance in the design of many engineering materials. Damage nucleation and growth can eventually cause the collapse of an existing structure. For this reason, the accurate modelling of these phenomena has been a topic of ongoing research in the last decades. It is therefore crucial to model those regions in the material that can potentially show failure and strain localization with great care. In this chapter, we develop strategies to concentrate the computational effort where it is needed most, i.e. in those regions that undergo inelastic processes. A domain decomposition method is employed to partition a discretized body into several domains and allow for a different treatment of linear and non-linear regions.

The capabilities of standard domain decomposition methods are extended in order to efficiently tackle the analysis of brittle and quasi-brittle materials. The approach brings the knowledge of the material and its behaviour into consideration allowing, in this way, a number of simplifications during the solution process. Rather than presenting a new method, the performance of well known techniques is improved for the analysis of failure phenomena with strain localization. Other similar approaches that aim at lowering the computational cost of the analysis of a complex system are related to model reduction techniques such as the Craig-Bampton reduction [12] (also referred as substructuring techniques). These techniques are designed to lower the burden of the problem to be solved by representing the behaviour of the model with a reduced number of well chosen modes. Recently, Yvonnet et al. [118] incorporated model reduction techniques in their multiscale analysis in order to reduce its complexity. Wiemer et al. [116] have simultaneously accounted for model reduction methods and recycling of spectral data. The reuse of spectral data in order to improve the efficiency of the solver has also been investigated by Risler et al. [94] and Guiraud

* This chapter is based on reference [64].

et al. [32]. Germain et al. [31] have parallelized the simulation of structure degradation with non-local damage models using Primal and Dual domain decomposition techniques. All these contributions have considered simplifications which are closely related to the mathematical nature of the solution approach and not to the nature of the constitutive model as it is proposed in this text.

The non-linear FETI framework introduced in Section 2.2 represents the starting point for the enhancements introduced in this chapter. The improvement, in terms of efficiency, allows the study of large structures or material samples at a high level of detail with a lower computational cost compared to standard analysis. Two illustrative examples are presented in Section 3.2 followed by final concluding remarks.

3.1 Framework enhancements for linear domains

This section contains the kernel of the enhancements that are performed in the FETI framework in order to efficiently tackle an analysis in which only part of a domain behaves in a non-linear fashion while the rest remains elastic. It is assumed that the nature of the non-linearities is related to the constitutive behaviour, and small deformations and rotations are considered.

A wide group of mechanical models describes the constitutive behaviour of solid materials by considering an initial linear elastic response followed by a non-linear behaviour after stress or strain thresholds are met. The non-linear branch can account for hardening (increase of stresses at increasing strains) and/or softening (decrease of stresses at increasing strains) behaviour. If no hysteretic effects are considered, the unloading-reloading branch is simply linear. In case of plasticity, the material unloads according to a linear elastic behaviour while in damage models the unloading branch coincides with a secant stiffness corresponding to the damaged material.

Elasto-plastic and continuum damage models consider, in general, a yield function or loading function that dictates the linear or non-linear character of the constitutive behaviour. After discretization and linearization of the governing equations, each solution increment is determined by solving a system of linear equations. The corresponding coefficient matrix might contain large parts that do not change from increment to increment. These parts are related to domains that behave in a linear fashion. The FETI method can be regarded as a valuable tool to treat those domains that undergo a linear behaviour differently. In other words, several computational stages can be

simplified.

3.1.1 Linear/non-linear domain indicators

In order to assign a linear or non-linear behaviour to a domain, the definition of reliable criteria is of utmost importance. These criteria are linked to the evolution of internal equivalent variables v involved in the yield surfaces or loading functions. Without loss of generality, one can identify the so-called strain- or stress-driven models in which a loading function $f(v)$ is formulated in terms of the stress or strain tensors, respectively. Continuum damage models normally adopt an initial strain or stress as v_0 while elastoplastic models consider a yield stress. It is therefore crucial to estimate the evolution of these internal variables at each domain in order to anticipate its linear or non-linear character.

In the general case, strains and stresses need to be computed in order to construct the equivalent quantities that control the constitutive behaviour. For this reason, standard assembly routines are called in order to compute the element shape functions \mathbf{N} and its derivatives \mathbf{B} . The strains are recovered, at the element level, as

$$\boldsymbol{\varepsilon} = \mathbf{B}\mathbf{u}, \quad (3.1)$$

where \mathbf{u} is the element vector of nodal displacements. The stresses at each element during the linear elastic or linear loading-unloading regime read

$$\boldsymbol{\sigma} = \mathbf{D}\boldsymbol{\varepsilon}. \quad (3.2)$$

The elastic constitutive tensor \mathbf{D} is set equal to the secant tensor for damage models or the initial elastic moduli in case of plasticity. The strain tensor $\boldsymbol{\varepsilon}$ represents the total strains (as computed in (3.1)) for a general damage model and the difference $\mathbf{B}\mathbf{u} - \boldsymbol{\varepsilon}^p$ between total and plastic strains for elastoplasticity. In our context, the derivatives in \mathbf{B} do not change during computation. In this scenario the equivalent strains and stresses can be computed with the available solution field data, the stored derivatives \mathbf{B} , and auxiliary quantities (secant moduli or total plastic strains), without the need to descend to the integration point level for linear domains. This is particularly convenient since, at the linear domains, we propose, among other things, to bypass the assembly routines as explained in the following section. For the case of an updated Lagrangian formulation the routines to compute the shape functions need to be entered but they are not considered as expensive

as those that account for the constitutive material behaviour. In particular cases, the internal variables that control non-linear processes are directly available as part of the solution field. The procedure explained above can then be simply bypassed. This is the case for the model adopted in this study which is detailed in Appendix A.

Once the equivalent measure of the internal variable is computed with the corresponding stresses or strains at a converged step for each nodal point n (v^n) in a domain $\Omega^{(s)}$, its representative maximum value per domain $v^{(s)}$ is computed as

$$v^{(s)} = \max_n (v^n), \quad \text{for nodes } n \text{ of } \Omega^{(s)}. \quad (3.3)$$

It is assumed that the non-linear character of the domain is controlled by the evolution of the maximum of the sampled internal variables. This assumption is particularly convenient for the modelling of strain localization phenomena since non-linearities are concentrated in regions that undergo the largest deformation. The predicted values (with subscript p) of the equivalent stress or strain at time $\tau + \delta t$ in domain $\Omega^{(s)}$ can be computed as

$$v_{p,\tau+\delta t}^{(s)} = v_{\tau}^{(s)} + \delta v_{\tau}^{(s)}, \quad (3.4)$$

where $v_{\tau}^{(s)}$ is the current value at time $t = \tau$, and the increment $\delta v_{\tau}^{(s)}$ can be approximated as

$$\delta v_{\tau}^{(s)} = \left. \frac{dv^{(s)}}{dt} \right|_{t=\tau} \delta t. \quad (3.5)$$

It is clear from the above expressions that the increment is added to the previous converged value in order to construct the prediction. The expression in (3.5) is general for any pseudo-time step subdivision. However, in this contribution, we assume a constant pseudo-time step δt , and, therefore, the derivative can be estimated using information at $t = \tau$, $t = \tau - \delta t$ and $t = \tau - 2\delta t$ as

$$\left. \frac{dv^{(s)}}{dt} \right|_{t=\tau} \approx \frac{\Delta v_{\tau,\tau-\delta t}^{(s)}}{\delta t} + \frac{\Delta v_{\tau,\tau-\delta t}^{(s)} - \Delta v_{\tau-\delta t,\tau-2\delta t}^{(s)}}{\delta t}. \quad (3.6)$$

The variations $\Delta v_{\tau_1,\tau_2}^{(s)}$ between time steps τ_1 and τ_2 can be defined as

$$\text{I: } \Delta v_{\tau,\tau-\delta t}^{(s)} = \left| \max_n (v_{\tau}^n) - \max_n (v_{\tau-\delta t}^n) \right|, \quad (3.7a)$$

3.1 Framework enhancements for linear domains

$$\text{II} : \Delta v_{\tau, \tau-\delta t}^{(s)} = \max_n (|v_{\tau}^n - v_{\tau-\delta t}^n|), \quad (3.7b)$$

$$\text{III} : \Delta v_{\tau, \tau-\delta t}^{(s)} = \max \left(\left| \max_n(v_{\tau}^n) - \min_n(v_{\tau-\delta t}^n) \right|, \left| \min_n(v_{\tau}^n) - \max_n(v_{\tau-\delta t}^n) \right| \right). \quad (3.7c)$$

The three heuristic definitions of the variation $\Delta v^{(s)}$ are aimed to provide a safe increment of $v^{(s)}$ which is of crucial importance to build a correct strain prediction. The first option, I, corresponds to a straightforward definition of $\Delta v^{(s)}$ based on the increments at those points n where the internal variable v^n is higher. The second definition II considers the highest increment of v^n among all sampled points. Finally the variation III is expected to be the most conservative estimate since the highest and lowest internal variables (at arbitrary sampled points) are involved in the computation of $\Delta v^{(s)}$. Note that, taking the definition I without the absolute value, the expression in (3.6) coincides with a backward differentiation method [46] (i.e. interpolating the evolution of $v^{(s)}$ with a second order polynomial) if the second term in (3.6) is premultiplied by 0.5.

The proposed $\Delta v^{(s)}$ are considered always positive in (3.7). This will lead to a safe increment for those cases in which the non-linear regime is reached when the internal value exceeds a positive threshold. In those cases where the threshold is negative (e.g. damage under compression), the increment defined by $-\Delta v^{(s)}$ should be also considered.

Our main interest is to accurately predict those regions in which there exists a transition from a linear to a non-linear regime. If this transition is underestimated, a correction procedure is explained at the end of this section. It is worth noting that other strategies can be adopted to estimate the occurrence of non-linearities at adjacent domains. The technique proposed in this contribution is compatible with other methods that can bring useful information regarding the evolution of non-linearities at the sample. The distance from the source of non-linearities (i.e. the crack tip [71] or damage front) to a particular domain or the evolution of the residual between computed and interpolated fields [2] are examples of alternative strategies. Once the indicator is constructed, it is possible to predict the linear character of the forthcoming steps using the domain loading function $f^{(s)}(v_p^{(s)})$ which is equivalent to the loading function $f(v)$ defined at each domain $\Omega^{(s)}$ (refer to Figure 3.1). Possible situations are: linear loading ($switch = 0$), non-linear loading ($switch = 1$) and linear unloading ($switch = -1$). These different

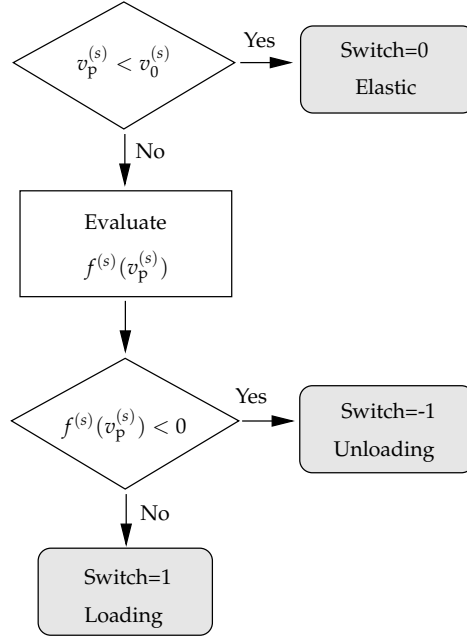


Figure 3.1 Switch criteria according to the domain internal variable $v^{(s)}$.

stages are exploited in the following by triggering a number of simplifications during the computations.

Despite the fact that the formulation of the predicted domain equivalent quantity is introduced for a generic internal variable model, this study focuses on softening and strain localization phenomena. Hardening behaviour can be tackled as well although the main difference with the present analyses would reside in the local character of the non-linearities.

3.1.2 Enhancements of assembly and factorization stages

In linear domains, the stiffness matrix $\mathbf{K}_i^{(s)}$ and internal force vector $\mathbf{f}_{\text{int},i}^{(s)} = \mathbf{f}_{\text{int},i-1}^{(s)} + \delta \mathbf{f}_{\text{int},i}^{(s)}$ in (2.20) do not need to be explicitly assembled at each global iteration i . It is possible to bypass the computation of these quantities by assuming $\mathbf{K}_i^{(s)} = \mathbf{K}_1^{(s)}$ and $\delta \mathbf{f}_{\text{int},i}^{(s)} = \mathbf{K}_1^{(s)} \delta \mathbf{u}_i^{(s)}$, where $\mathbf{K}_1^{(s)}$ is the stiffness matrix of the linear domain and $\delta \mathbf{u}_i^{(s)}$ is the displacement increment in $\Omega^{(s)}$. The linear stiffness $\mathbf{K}_1^{(s)}$ is equal to the elastic stiffness $\mathbf{K}_0^{(s)}$ when the initial domain

3.1 Framework enhancements for linear domains

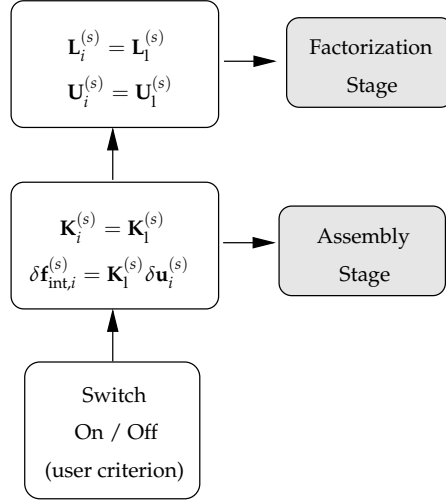


Figure 3.2 Assembly and factorization enhancements for a linear domain.

strain or stress threshold $v_0^{(s)}$ is not exceeded. If domain $\Omega^{(s)}$ experiences linear unloading, the linear stiffness $\mathbf{K}_1^{(s)}$ is equal to the secant stiffness $\mathbf{K}_s^{(s)}$ computed at the beginning of the unloading stage.

As indicated in Figure 3.2, the factorization of the linear stiffness into its upper and lower factors $\mathbf{K}_i^{(s)} = \mathbf{L}_i^{(s)} \mathbf{U}_i^{(s)}$ can be skipped as well. Note that the rigid body modes are only computed at the initial stage of the analysis and do not vary during the computations. Therefore, with the presented enhancement, non-necessary operations are bypassed at subdomains which are predicted to behave linearly.

It should be pointed out that many problems can be described by coupled set of equations that account for multiphysics processes. The discretized and linearized set of equations using the FE method give rise to a set of linear systems in which the solution field is heterogeneous with respect to its physical nature. It is then possible that a mechanically linear domain (i.e. a system for which the constitutive relation between stresses and strains is linear) might undergo non-linear phenomena of a different nature (e.g. temperature diffusion). In this scenario, the assembly enhancements described in Figure 3.2 only hold for the partitions with linear coefficients. Hence, the assembly of the remaining quantities needs to be performed anyway.

In the present study a Gradient-Enhanced Damage model (cf. Ap-

pendix A) is selected for the modelling of quasi-brittle failure. This model is formulated in terms of a coupled system of differential equations, namely the equilibrium equation and the modified Helmholtz equation. Consequently, the coefficients of the stiffness matrix and internal force vector that contain the non-local equivalent strain and its derivatives need to be re-assembled when non-linearities occur at an arbitrary domain. If the factorization enhancement is utilized and the stiffness factorization is reused, the true tangent is lost and a pseudo-tangent is employed to solve the global system of equations. It is shown in Section 3.2 that this procedure hardly affects the global convergence and, for this reason, the enhancement can be used with confidence.

3.1.3 Rewind strategy for domains with underestimated predicted internal variables

The assembly and factorization enhancements described above are meant to speed up the computations for linear domains. Nevertheless, underestimated values of predicted variables might fail to trigger domains that should enter the non-linear regime. The computed solution path can, in this situation, drift away from the expected solution (i.e. the solution obtained without the proposed framework enhancements). This situation can be encountered during the transition from elastic into non-linear regime or linear unloading into a loading regime. It is intended to overcome this situations by comparing the predicted, $v_p^{(s)}$, and current $v^{(s)}$, values at the end of each converged step. When the predicted values turn to underestimate the current ones in such a way that $v_p^{(s)}$ and $v^{(s)}$ fall into the linear and non-linear regimes, respectively, computations are rewound to the previous converged step and the assembly and factorization routines are entered for domain $\Omega^{(s)}$. The main difference between the proposed increments relies on the confidence of the predicted values and, therefore, there is also an impact on possible rewind episodes. Indeed, the three definitions shown in (3.7) are constructed such that the expected increments satisfy

$$\Delta v_I^{(s)} \leq \Delta v_{II}^{(s)} \leq \Delta v_{III}^{(s)}. \quad (3.8)$$

Consequently, the prediction using smaller values of $\Delta v^{(s)}$ is expected to underestimate the increments obtained with a reference solution and, therefore, the chances to encounter a rewind episode are higher.

3.2 Examples

It should be stressed that an heuristic approach is presented in this contribution without a mathematical proof. Its correct performance is shown in the presented numerical examples but further investigation should be performed in order to improve their efficiency and reliability for general cases.

3.2 Examples

3.2.1 Four-point bending test

The features of the proposed approach are firstly demonstrated with the aid of the simply supported concrete beam under four-point bending loading conditions shown in Figure 3.3. This test setup was proposed by Hordijk [47]. The beam has been numerically investigated by Pamin and de Borst [85] and Simone et al. [105] with a gradient-enhanced damage model (cf. Appendix A). Due to the symmetric geometry and the set of boundary conditions the resulting stress and strain fields are expected to be symmetric as well and, therefore, only half of the beam is considered. Model parameters, taken from [85, 105] are as follows: Young's modulus $E=40000$ MPa, Poisson's ratio $\nu=0.2$, exponential damage evolution law (A.6) with $\kappa_0=0.000075$, $\alpha=0.92$ and $\beta=300$, a modified Von Mises definition of the local equivalent strain (A.4) with $\gamma=10$, and gradient parameter $c=4$ mm². The test is performed under plane stress conditions and quadrilateral elements with bi-linear interpolation are adopted for both displacement and nonlocal equivalent strain fields. The notch of depth d is simulated as a zero-thickness notch by simply releasing the horizontal constraint from the corresponding vertical segment along the symmetry axis. All numerical simulations for this example are performed using a constant pseudo-time step division of 60 displacement steps unless otherwise specified.

The results of the simulation are compared to experimental data based on the work of Pamin and de Borst [85] where the vertical displacement u_y at point "m" in Figure 3.3 is measured against the applied load P . Different element sizes h are accounted for providing a solution which does not suffer from mesh dependency (left part of Figure 3.4). The element size h corresponds to the largest edge of the quadrilateral elements that appear in the finer domains (4 to 8) of the beam as shown in Figure 3.5. The resulting meshes for $h = 10, 5$ and 2.5 mm contain 364, 685 and 1360 elements, respectively. The material parameters adopted in these simulations allow to reasonably fit the numerical curves to the experimental ones as shown in Figure 3.4 (right).

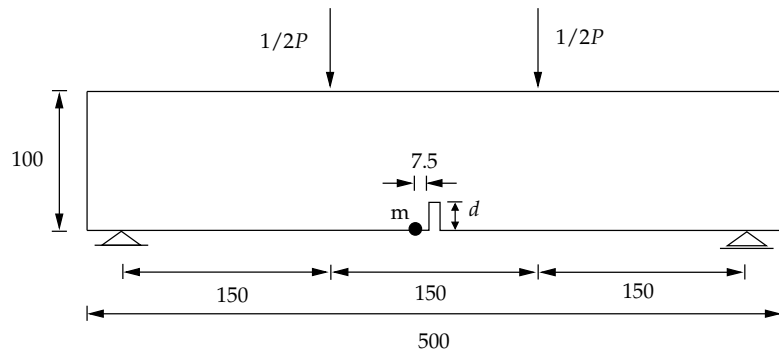


Figure 3.3 Geometry and boundary conditions (thickness = 50 mm; all dimensions in mm).

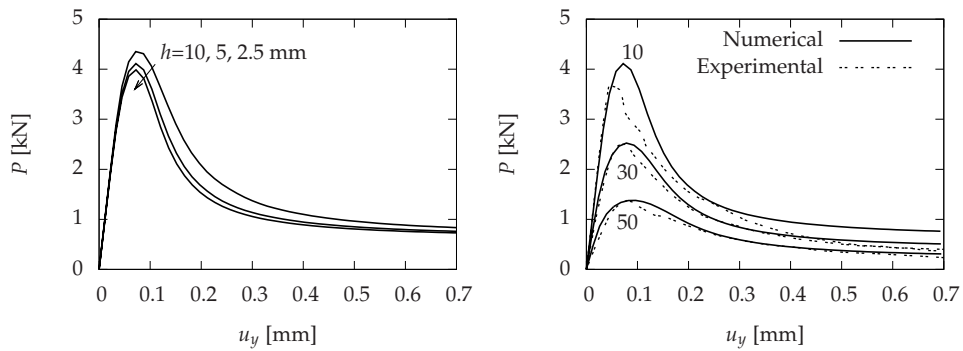


Figure 3.4 Load-deflection curves with different element sizes using a 10 mm deep notch (left) and different notch depths d for the $h = 5$ mm element size mesh (right).

3.2 Examples

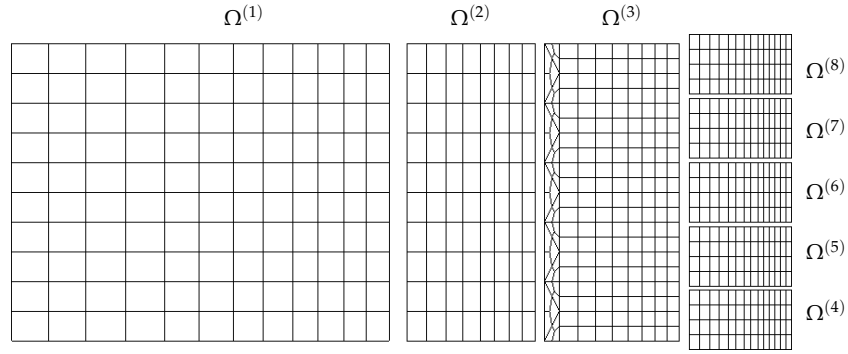


Figure 3.5 Decomposition of the concrete bar (left part) in 8 domains using the medium mesh ($h=5$ mm).

The beam, taking into account symmetry, is decomposed in eight domains as shown in Figure 3.5. The goal of this study is to verify the correct activation of each of the four domains (numbers 4 to 8) covering the area in which damage grows. The damage evolution in domains 4 to 8 is depicted in Figure 3.6. Nucleation of damage occurs at the notch and rapidly propagates along the symmetry axis towards the top of the beam. The relation between damage and strains set by the softening damage evolution law is observed in Figure 3.7 where the spatial distribution of nonlocal equivalent strain and damage is plotted for three different pseudo-time steps. The spatial distribution of the damage field obtained with the proposed framework is identical to that provided by a direct numerical simulation (DNS) and is therefore not reported. It should be stressed that the DNS consists in solving the problem by means of a monolithic approach, thus considering a standard FE implementation on the full mesh. Nevertheless, it is obvious that the DNS solution fully coincides with a standard FETI approach solution. For this reason, the performance of the presented enhanced framework is compared in the sequel to the one of the standard (or full) domain decomposition approach.

The transition from an elastic or linear unloading regime into a non-linear loading regime is controlled by monitoring and predicting the evolution of internal variables. For the case of the Gradient-Enhanced Damage model, the nonlocal equivalent strain $\tilde{\epsilon}_{nl}$ is taken as the state equivalent internal variable v as mentioned in Section 3.1.1. The loading function $f^{(s)}(v^{(s)})$ for each domain is equivalent to the one shown in (A.2) evaluated with $\kappa^{(s)}$ which is, in turn, computed using the highest strain $\tilde{\epsilon}_{nl}^n$ measured at all dis-

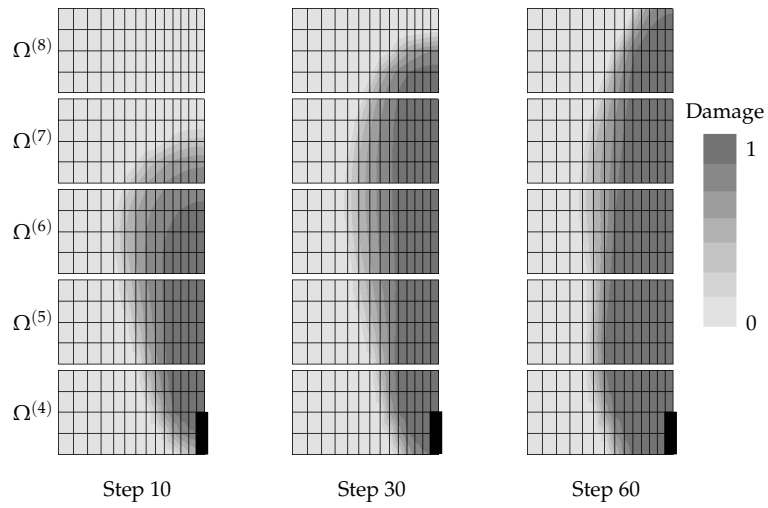


Figure 3.6 Damage evolution at domains $\Omega^{(4)}$ to $\Omega^{(8)}$ for the $h = 5$ mm mesh. The black thick line represents the 10 mm deep notch.

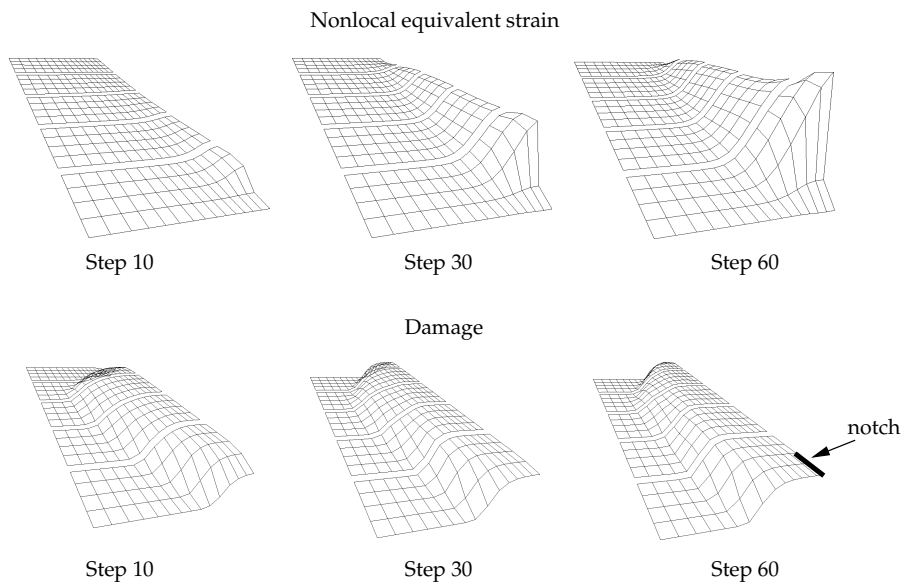


Figure 3.7 Nonlocal equivalent strain and damage evolution at domains 4 to 8 ($h = 5$ mm and $d = 10$ mm).

3.2 Examples

crete points n of domain $\Omega^{(s)}$. The loading function $f^{(s)}$ for each domain follows the Kuhn-Tucker loading-unloading conditions (A.3). In order to simplify the analysis without losing generality, the behaviour of the predictor is assessed in the following by observing the transition from elastic to non-linear regime. Results are presented for domains 4 to 8 which capture all damage processes in the specimen. In Figure 3.8, a comparison is made between the current $\varepsilon_{nl}^{(s)}$ and predicted $\varepsilon_{nl,p}^{(s)}$ strain at each domain using a constant pseudo-time step discretization of 60 and 240 steps. The predicted strain based on strain increment II, as described in Section 3, is considered in the examples except in those cases where the choice of $\Delta\tilde{\varepsilon}_{nl}^{(s)}$ is explicitly mentioned.

It is observed that the predicted strains of the first domain that enters into the non-linear regime will always be underestimated but they will provide a safe guess (i.e. they will correctly detect the initiation of non-linearities even if they turn to be smaller than the current strains at that step). From then on, the strain increments in the elastic domains that surround the crack will be characterized by the linear response of these domains influenced by strain and stress gradients caused by damage growth at its immediate vicinity. Hence, future strain increments are likely to be higher than the past ones for a given pseudo-time step increment.

In our case, there is a safe strain prediction in all domains except for domain 5 (when using 60 steps) in which the predicted strains at step 4 fall slightly under the non-linear threshold $\kappa_0^{(s)}$. In this scenario, it is risky to continue without activating these domains since the solution can eventually drift away from the true solution path or damage propagation is delayed. Computations are therefore rewound to the last converged step (step 2) and domain 5 is activated so all assembly routines will be entered when computing the corresponding solution increment for step 3. As observed in Figure 3.9 (left), a smaller step subdivision gives rise to a better predicted strain. Despite the fact that a finer step subdivision is more expensive from a computational standpoint, it provides a better strain prediction and a reduced number of rewind events. The choice of strain increment $\Delta\tilde{\varepsilon}_{nl}^{(s)}$ gives rise to different predicted values (right part of Figure 3.9). Note that predictors I and II provide an identical result for this case. This indicates that the maximum of the strain increments at the particular domain is found at the same sample point where the highest strains are registered. The prediction using the strain increment III provides higher strain values and, in this case, a rewind event is not encountered during the loading regime as

opposed to the other predictors. The evolution of the current strain, taking into account the possible rewind events, is identical for all three cases and equal to the reference solution (i.e. without considering linear enhancements). The load-deflection curves for the standard and enhanced models are in agreement and the relative error between them does not exceed 0.25% as shown in Figure 3.10. The proposed enhancement in the computation of linear domains does not significantly affect the number of iterations in the Newton-Raphson solution procedure (refer to left part of Figure 3.11). The first-order work $\|E\|$, computed as $\|\mathbf{f}_{\text{int}}^T \delta \mathbf{u}\|$, is shown in Figure 3.11 (right) for each iteration in step A.

Quantification of the assembly and factorization enhancements

The framework enhancements are quantified by representing the evolution of the active mesh. The active mesh ratio is defined as the ratio of elements in those domains where the assembly and factorization routines are accessed with respect to the total number of elements. In our particular implementation it is not advisable to measure CPU times explicitly since the code is based on an interpreter and it is compiled during execution. Nevertheless, the active mesh evolution might give an objective measure of the effort required to solve the problem.

The evolution of the active mesh for the four-point bending test using a decomposition of 8 domains is shown in Figure 3.12 for different pseudo-time steps. The activation sequence for the different domains is shown for stages A to C. At the beginning, all domains need to be loaded, stage A, in order to initialize the FE arrays. Immediately after the first steps, all domain switches are set to elastic. The first domain is activated at stage B, when damage is initiated at the notch, while the highest amount of active mesh is reached at stage C where domain 8 is still not active and domains 2 and 3 are about to unload linearly. Due to the monotonic loading, a plateau is reached at stage D where domains 4 to 8 are loading, domains 2 and 3 unload linearly and domain 1 remains elastic. There is indeed a small dependence on the step size. Smaller step sizes optimize the amount of active mesh that is triggered.

The number of domains in which the structure is decomposed plays also an important role. Results are reported in Figure 3.13 where it is shown that a larger number of domains corresponds to a smaller active mesh ratio. However, the number of degrees of freedom involved in the interface problem grows with the number of decomposed domains. Hence, it is con-

3.2 Examples

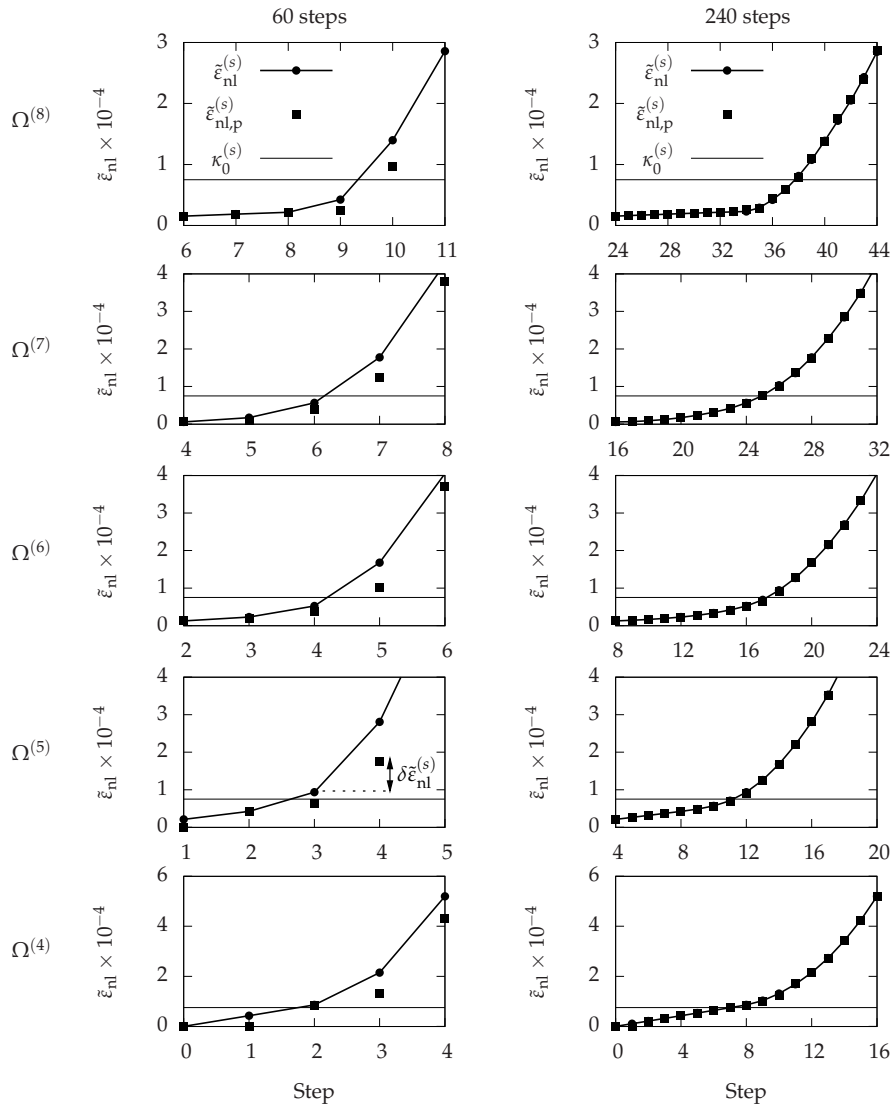


Figure 3.8 Current and predicted strain evolution for 60 and 240 steps. Step t on the left column corresponds to step $4 \times t$ on the right column. The construction of the predicted nonlocal equivalent strain is indicated in the case of domain $\Omega^{(5)}$ where $\delta \xi_{nl}^{(s)}$ is the increment of the nonlocal equivalent strain.

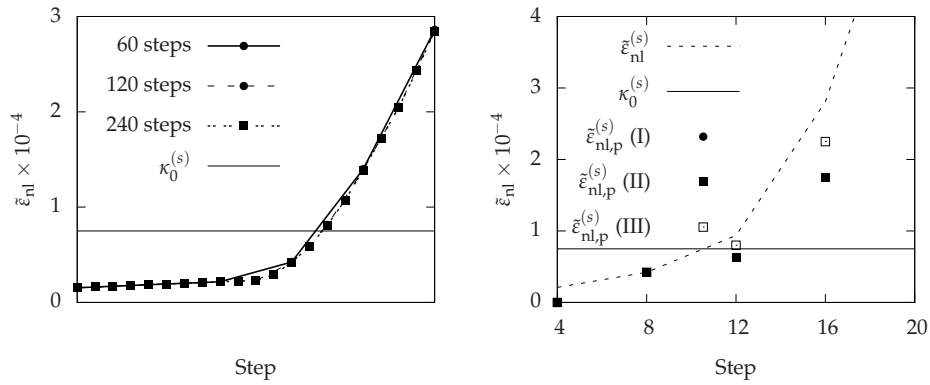


Figure 3.9 Current strain evolutions for different step sizes at domain $\Omega^{(5)}$ (left) and predicted strains at domain $\Omega^{(5)}$ according to the different variations $\Delta\tilde{\epsilon}_{nl}^{(s)}$.

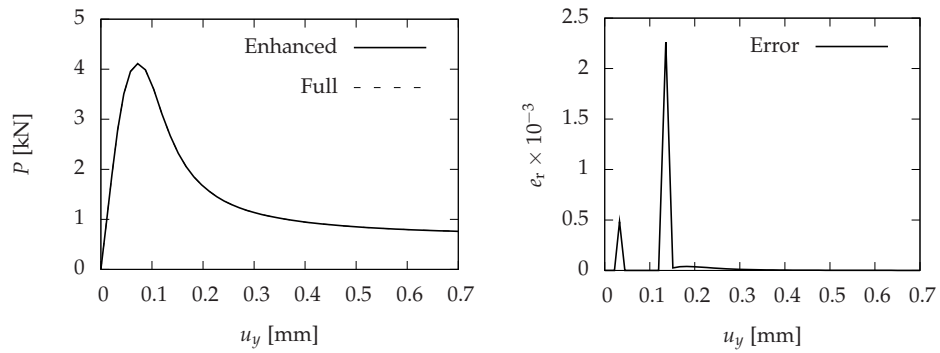


Figure 3.10 Load-deflection curves (left) and relative error (right) of the full and enhanced analysis.

3.2 Examples

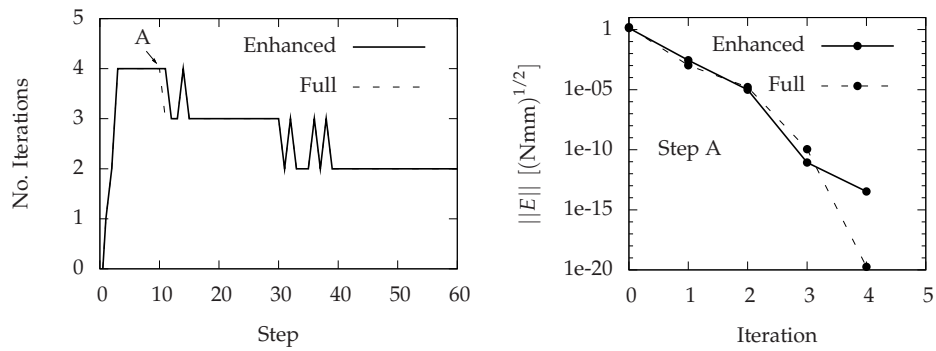


Figure 3.11 Number of iterations (left) and convergence rate at step A (right). All iteration counters refer to Newton-Raphson iterations.

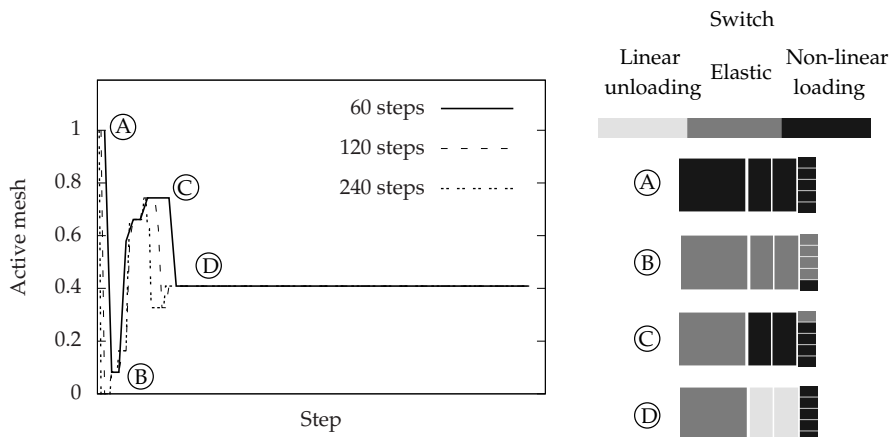


Figure 3.12 Active mesh evolution for a decomposition in 8 domains.

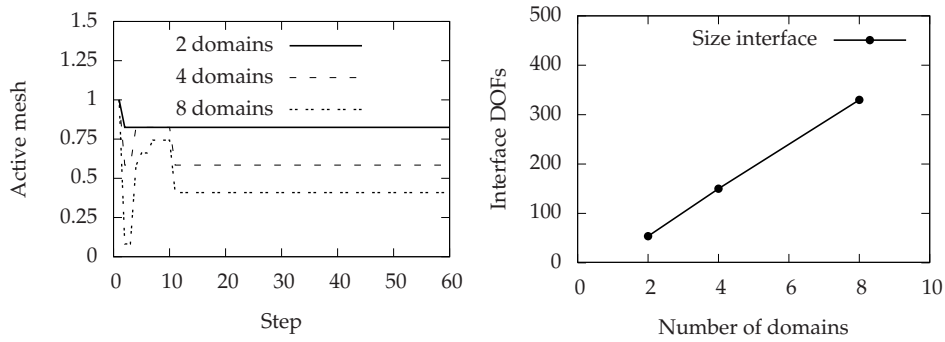


Figure 3.13 Active mesh evolution (left) and size of the interface problem (right).

venient to perform decompositions such that the number of degrees of freedom is balanced in each domain. Situations with a low number of degrees of freedom per domain should be avoided since the enhancement would not be efficient.

3.2.2 Tensile test on a concrete specimen

We present an illustrative example of strain localization in a concrete sample under tensile loading. The mesoscopic structure is generated by means of a discrete particle simulation software [39]. Once the distribution of the particles is obtained, the mesh is generated considering a three-phase material description with aggregates, matrix and an interfacial transition zone (ITZ) between the aggregates and the matrix as shown in Figure 3.14.

The ITZ is considered as a weak porous region of the material where damage is expected to nucleate and propagate through the matrix until complete failure of the specimen. The thickness of the ITZ is normally considered to be of the order of the cement particles (1-100 μm). In this study, such thickness is set to 500 μm in order to reduce the number of elements of the resulting mesh. This assumption is acceptable since the focus is on an academic analysis which is not validated against experimental results. Nevertheless, the failure mechanisms mimic the ones we expect in a real case. Plane strain conditions are adopted for the two-dimensional analysis. This assumption is definitely artificial since the heterogeneities have a finite dimension in the out of plane direction. However, plane stress conditions would not improve the quality of the analysis compared to a true three-dimensional set up in which the damage percolation paths would be more realistic.

3.2 Examples

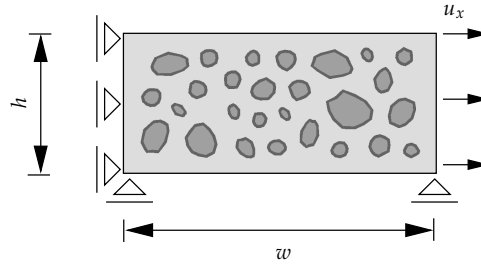


Figure 3.14 Tensile test for the concrete specimen: geometry, boundary conditions, and mesoscopic structure.

In the first part of this example the effect of the selected decomposition on the solver efficiency is studied. To this end, the concrete sample depicted in Figure 3.14, with details of the geometry and material parameters listed in Tables 3.1 and 3.2, is decomposed according to two distinct criteria as illustrated in Figure 3.15. First, a decomposition using graph partitioning algorithms (i.e. using standard software like Metis [53]) is performed in which any of the three phases can be present at each domain. The second criteria assigns each of the aggregates and ITZ phases to a separate domain. The rest of the matrix is decomposed using a standard graph partitioning criteria. This decomposition type is referred to as “mixed decomposition” since it combines different criteria when performing the partitions. The idea behind this kind of decomposition is to prove that knowledge of the nature of the components can significantly improve the solver efficiency. In our problem, aggregates can be assumed to behave elastically throughout the computations and a significant computational effort can be skipped. This beneficial property may also be exploited in other composite materials where the mechanical nature of the components is well known a priori.

We could not consider the same number of domains in the two decompositions as shown in Figure 3.15. The problem that we encountered with a decomposition based on a standard graph partitioner is related to the presence of domains with a high aspect shape ratio. This is a consequence of using unstructured meshes with variable element size. In this scenario, the domain matrices present poor conditioning and the analysis can not be performed. In these cases, the proposed mixed decomposition can be also seen as a strategy to prevent high aspect shape ratios of the decomposed domains.

Upon increasing load, damage starts at the weak ITZ between aggregates

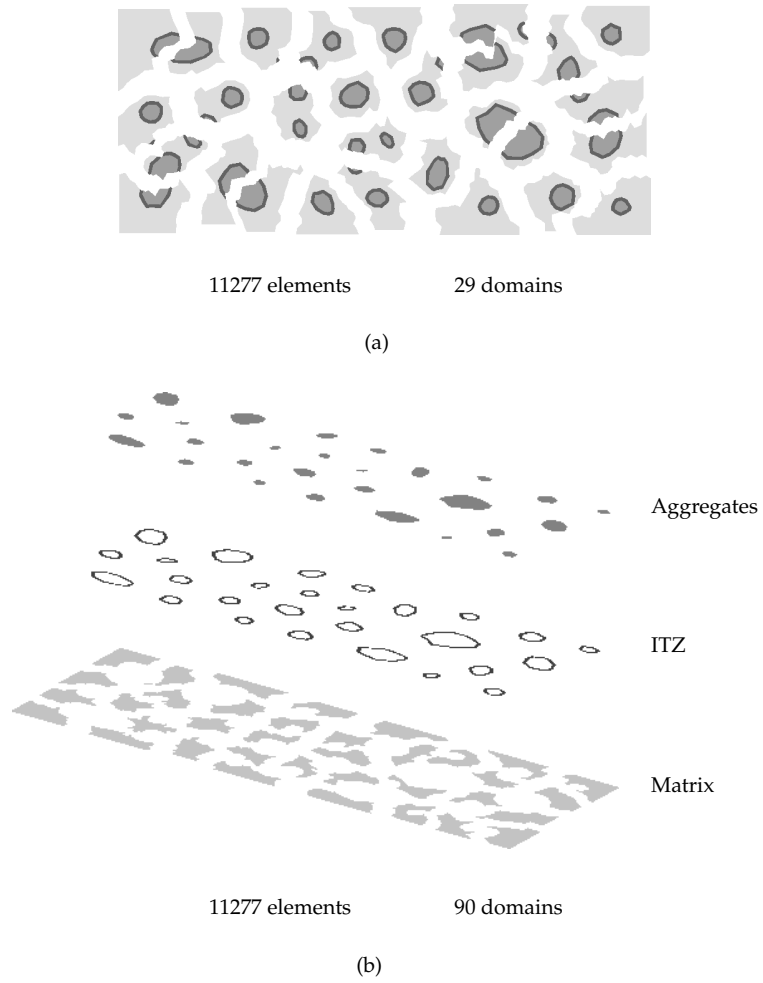


Figure 3.15 Standard (a) and mixed decomposition (b) of the concrete sample.

3.2 Examples

w [mm]	h [mm]	\varnothing particle [mm]	u_x [mm]
66.67	30	2 – 12	0.03

Table 3.1 Test data.

Material parameters			Aggregates	Matrix	ITZ
E	Young's modulus	[GPa]	35.0	30.0	20.0
ν	Poisson's ratio	[-]	0.2	0.2	0.2
$\tilde{\epsilon}_{nl}$	Equiv. strain (non-loc.)	[-]	Mazars	Mazars	Mazars
κ_o	Dam. init.	[-]	Dummy	0.124×10^{-4}	0.1×10^{-4}
c	Gradient param.	[mm ²]	0.75	0.75	0.75
$\omega(\kappa)$	Dam. evol. law	[-]	Exponential	Exponential	Exponential
α	Resid. stress param.	[-]	0.999	0.999	0.999
β	Soft. rate param.	[-]	500	500	500
Two-dimensional analysis type				Plane strain	

Table 3.2 Material data.

and matrix. At late loading stages strains localize in a narrow band where the main non-linearities take place while the rest of the sample tends to unload as shown in the top part of Figure 3.18. The mechanical response for both decompositions is obviously identical since the partitioning type does not affect the final result and, therefore, is not reported. However, there are differences regarding the efficiency of the computations as observed in Figure 3.16. It can be observed that the mixed decomposition yields a more efficient analysis. For this decomposition, all elastic domains (i.e. the domains representing the aggregates) significantly contribute to the computational cost only at the initial step. From then on, this part of the mesh is treated in a simplified way by the solver. Close to failure, the active mesh ratio reaches a plateau which is related to the size of the decomposed domains and the area where the non-linearities take place. If the number of domains used in the standard decomposition increases, the resulting efficiency would approach that of the mixed decomposition. However, for an identical number of decomposed domains, the standard decomposition will never be more efficient than the mixed decomposition since the linear areas containing the aggregates are not considered separately.

In the second part of the example, the influence of sample size on computation efficiency is studied. Two samples are considered that correspond

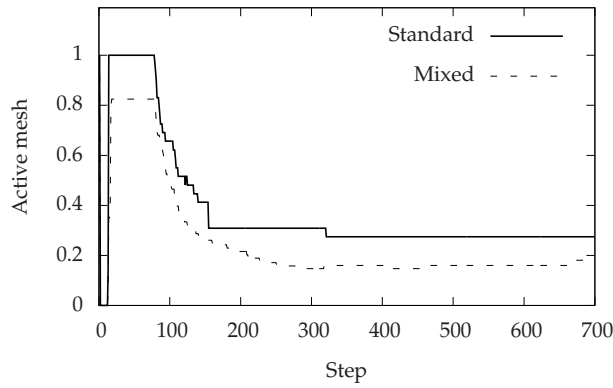


Figure 3.16 Active mesh evolution for the standard and mixed decompositions.

to the same material (i.e. the mesoscopic structure is characterized by aggregates with similar size and density). The samples are decomposed following a mixed decomposition. The mesh is decomposed in a number of domains such that the local matrices are of similar size for both samples (Figure 3.17). Geometry and material properties for the small sample are listed in Tables 3.1 and 3.2. The geometry and applied displacement for the large sample are taken as $1.5 \times w$, $1.5 \times h$ and $1.5 \times u_x$, keeping the same material properties as the small sample.

Strain localization at late loading stages is observed in Figure 3.18 for both samples. The mechanical response of the samples show the well-known size effect since the average fracture energy is clearly higher for the smaller sample (Figure 3.19). At high damage levels, the ratio of damaging areas to the total specimen area is higher for the smaller sample. This is depicted in Figure 3.18 for a situation close to failure. The computational effort will be relatively lower for larger samples as observed in the active mesh plot (left part of Figure 3.20).

As argued in Section 3.1.1, the behaviour of predictor III is always more conservative. Figure 3.20 (right) shows that a larger amount of domains are fully processed. The active mesh profiles obtained using predictors I and II are very similar. This indicates that in our analyses the sampled points with largest strains and largest strain increments are in most cases the same. A few rewind episodes were registered when using predictor I. In general the linear enhancements during the unloading regime are triggered after a few consecutive unloading episodes are registered. This increases the robust-

3.3 Concluding remarks

ness of the method in situations where the convergence is more difficult, e.g., around the limit point or snap-through.

An increase in the number of domains can be observed for a few analyses in Figure 3.20 during late loading stages. This is due to spurious damage growth caused by the nonlocal computation of the equivalent strain [29, 105]. The load deflection curves provided with the three strain indicators are equivalent and equal to the one obtained with a full analysis.

3.3 Concluding remarks

The presented enhanced FETI technique is proven to be efficient for the modelling of brittle materials. The kernel of the enhancements relies on bypassing a number of standard FE computations at domains that remain linear during the analysis. Both the assembly and factorization stages are skipped at linear elastic domains and the obtained solution does not differ from a full analysis. A key issue is the definition of the strategy to anticipate the linear/non-linear character of the continuing non-linear computations in order to trigger the above mentioned enhancements. This strategy is introduced in a general sense for elasto-plastic and continuum damage models and tailored in this work to a Gradient-Enhanced Damage model.

The efficiency of our approach is quantified by monitoring the amount of elements that fully enter the assembly and factorization routines (active mesh). Materials that present highly localized failure modes show the least amount of active mesh during the computations and, for this reason, the efficiency of the solution process is improved and the time needed to obtain a solution is proportionally lower compared to a full analysis. The effect of the decomposition type, sample size, number of subdomains, and strain prediction criteria is studied in the examples. A decomposition into a high number of subdomains naturally minimizes the active mesh, although the progressive growth of the interface problem has to be taken into account as well.

The methodology presented in this chapter has been applied using a direct solver for the interface problem, making the present work similar to an intelligent multi-frontal approach. The approach is, however, naturally suited for parallel computing. In that case, the interface problem should be solved iteratively, like in standard Schur complement methods, in order to minimize communication costs. When iterative solvers are applied for the

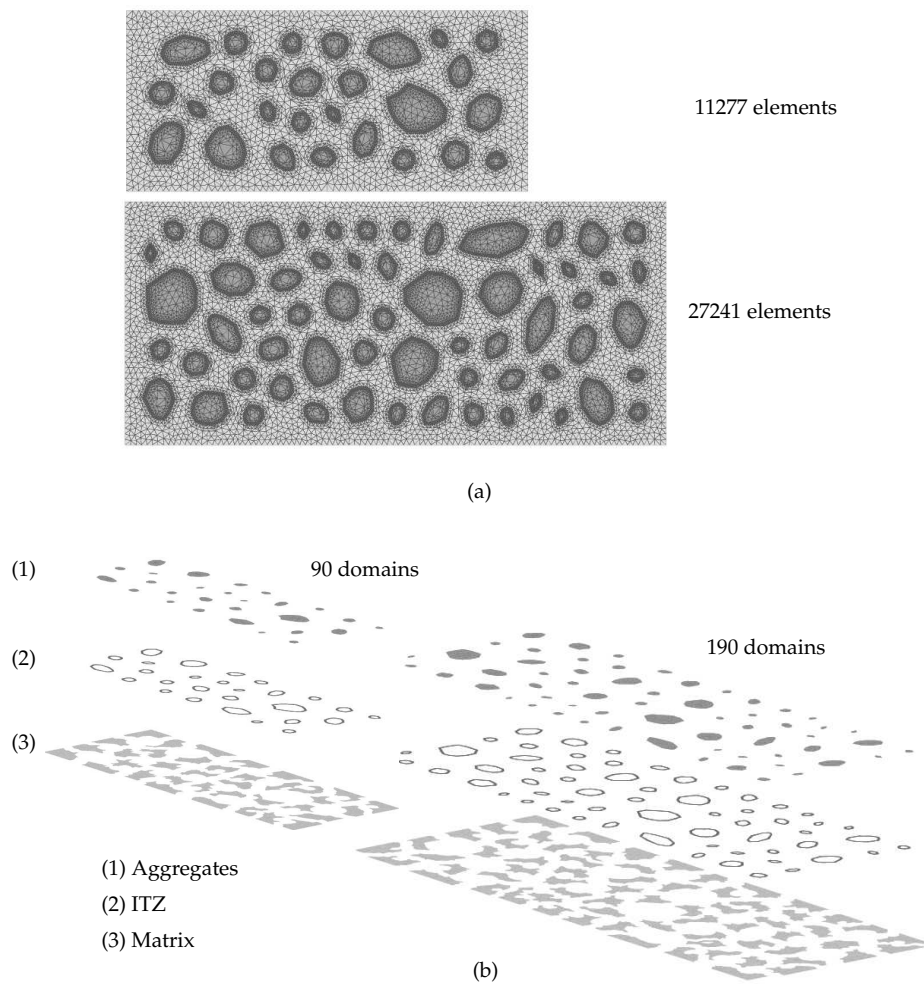


Figure 3.17 FE meshes (a) and mixed decompositions of the concrete samples (b).

3.3 Concluding remarks

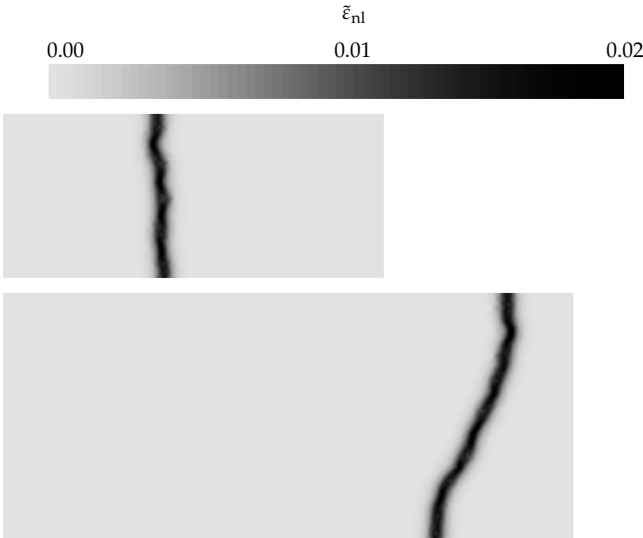


Figure 3.18 Nonlocal equivalent strain contours at ultimate loading stages for the small (top) and large (bottom) samples.

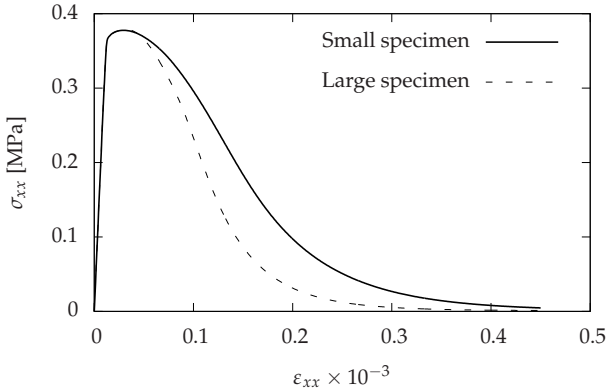


Figure 3.19 Average stress-strain curves for the small and large samples.

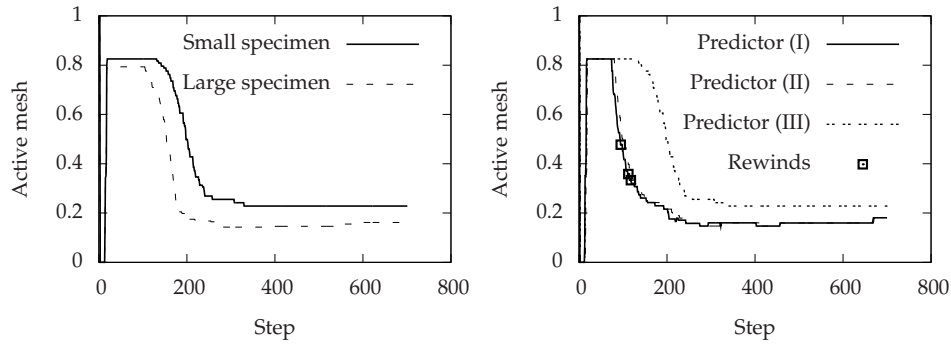


Figure 3.20 Active mesh curves for both specimens using predictor III (left) and active mesh curves for all predictors at the small sample (right).

interface problem, efficient preconditioners and coarse grids need to be used (cf. Appendices C to E). In addition, techniques to recycle previously computed directions of descent should also be applied (see for instance [94]).

Implementing the methodology in a parallel computing environment also raises another challenge: since some domains will be factorized only once whereas others (those entering the non-linear regime) need to be factorized several times anew, the work load of the processors will be unbalanced if each processor handles one domain. Hence techniques such as automatic load-balancing and multi-threading should be considered to handle this issue. This is however outside the scope of this work.

Chapter 4

Multiscale domain decomposition analysis of quasi-brittle material failure*

The non-linear FETI framework is extended in this chapter in order to tackle multiscale analysis of failure phenomena. The enhancements introduced in Chapter 3 are also taken into account in the multiscale framework. Consequently, the present hybrid multiscale framework is suitable for the analysis of non-linear heterogeneous materials and specifically designed for the study of brittle and quasi-brittle materials in which softening and strain localization phenomena occur.

The specimen under analysis is split into a number of non-overlapping domains which are processed using the FETI method. This, together with an adaptive refinement of the domains, allows to selectively process the material in a multiscale fashion. The macroscopic and mesoscopic material scales are processed concurrently with the use of non-conforming interfaces between different resolution domains. A “zoom-in” strategy is employed at those domains that enter a non-linear regime via the use of a hierarchical technique. During this process, the coarse-scale domain is substituted by its corresponding fine-scale domain considering an equivalent deformation path. Since the procedures that facilitate the multiscale analysis operate at the algebraic level, the framework is general and does not depend upon the chosen constitutive model. However, linear/non-linear indicators used to trigger a zoom-in event need to be tailored to the constitutive relation. The main features explored in this chapter are the efficiency of the framework and the quality of the description of failure phenomena when compared to the one provided by a full scale analysis. The goal is to develop a strategy which is convenient for multiscale analysis with a moderate jump in scales and when the subscale heterogeneities play an important role during the nucleation and propagation of failure processes.

* This chapter is based on reference [65].

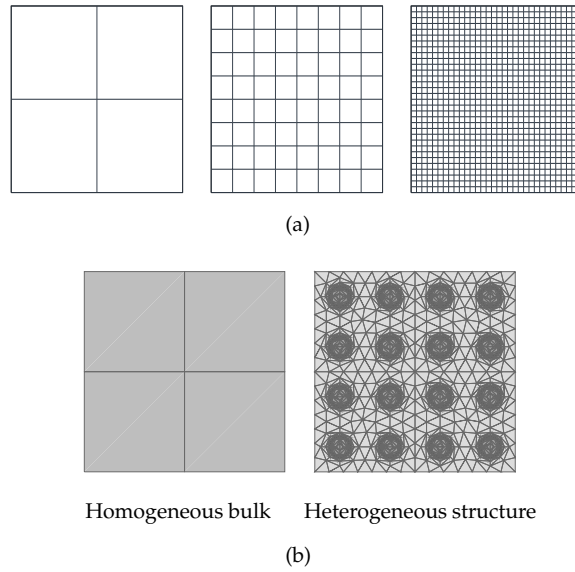


Figure 4.1 Multiple resolutions (a) and scale transition (b) of a discretized material.

4.1 Extensions for multiscale analysis

Several extensions to the classical FETI [25] method are introduced in this section in order to account for the multiscale analysis of structures. The extensions allow different scales or material resolutions to coexist in the sample under consideration. The present multiscale analysis is limited to the case of two different scales. Both are referred to as coarse and fine-scale or low and high resolution. Nevertheless, the multiscale extension can also be employed for problems in which more than two scales or resolutions coexist in the specimen as shown in Figure 4.1(a). The main ingredients of the multiscale extension include: (i) a procedure to glue different domain resolutions at the interface, (ii) a zoom-in strategy to proceed with a higher resolution analysis in a particular domain, and (iii) a set of global iterations in order to enforce displacement compatibility and satisfy equilibrium in the whole sample.

4.1.1 Connecting different resolutions

During multiscale analysis it is expected that different domain resolutions coexist. A strategy is therefore needed in order to glue the incompatible meshes corresponding to different resolution domains. To this end, a set of constraints, which needs to be satisfied upon convergence of the Newton-Raphson scheme, is described in the following.

Displacement compatibility is enforced at the interface Γ_I between fine, Ω^f , and coarse, Ω^c , domains by means of

$$\mathbf{u}^f(\mathbf{x}) = \mathbf{u}^c(\mathbf{x}), \quad \forall \mathbf{x} \in \Gamma_I, \quad (4.1)$$

where $\mathbf{u}^f(\mathbf{x})$ and $\mathbf{u}^c(\mathbf{x})$ refer to the fine and coarse displacements of a point \mathbf{x} at the interface. The most common strategies to connect non-matching meshes, leading to non-conforming interfaces, are simple collocation [95] and mortar methods [8]. The weak version of the previous continuity relation (4.1) can be expressed as

$$\int_{\Gamma_I} w(\mathbf{x}) \left(\mathbf{u}^f(\mathbf{x}) - \mathbf{u}^c(\mathbf{x}) \right) d\Gamma_I = \mathbf{0}. \quad (4.2)$$

Simple collocation is accounted for in this study by setting the weight function w equal to the Dirac function δ on all nodes of Ω^f that belong to interface Γ_I . In other words, the fine-scale displacements \mathbf{u}^f can be interpolated using the shape functions \mathbf{H}^c of the coarse elements restricted onto the interface and the displacements \mathbf{u}^c at the coarse nodes as

$$\mathbf{u}^f = \mathbf{H}^c \mathbf{u}^c \quad \text{at } \Gamma_I. \quad (4.3)$$

The fine resolution mesh is obtained by successive refinement of the coarse one. In this procedure, the coarse mesh nodes located at the interface are kept in the refined resolution mesh. In this manner, the coarse mesh nodes at the interface have a corresponding node at the refined domain. Nodes that are matching at the interface will be called “independent” in what follows. In order to restrain the DOFs of a non-conforming interface, linear multi-point constraints (LMPCs) are applied at the nodes of the fine mesh which do not have a corresponding node at the adjacent coarse domain (dependent nodes). These LMPCs are referred to as interscale LMPCs in the rest of this manuscript. The collocation of the dependent nodes onto the interface is illustrated in Figure 4.2. Clearly, the group of independent nodes belonging to the refined domain suffices in order to set the interscale LMPCs.

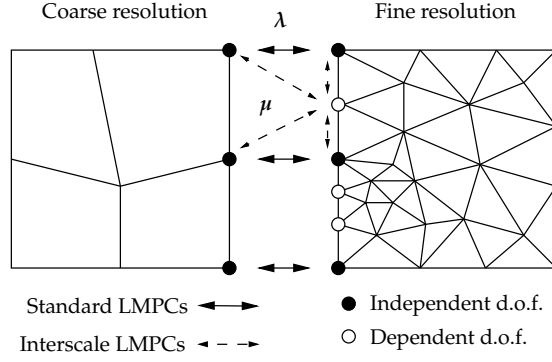


Figure 4.2 Linear multipoint constraints (LMPCs) at non-conforming adjacent domains.

However, the addition of redundant relations using adjacent independent nodes would improve the quality of the preconditioners in case an iterative solver is selected for the interface problem [97]. In this study a direct solver is employed for the solution of the interface problem and, therefore, the redundant relations are not considered.

The set of interscale LMPCs is cast in a matrix form and reads, for the case of two domains, as

$$\mathbf{C}\mathbf{u} = \begin{bmatrix} \mathbf{C}^{(1)} & \mathbf{C}^{(2)} \end{bmatrix} \begin{bmatrix} \mathbf{u}^{(1)} \\ \mathbf{u}^{(2)} \end{bmatrix} = \mathbf{0}, \quad (4.4)$$

where $\mathbf{u}^{(s)}$ is the solution field related to domain $\Omega^{(s)}$. The matrix $\mathbf{C}^{(s)}$, which contains the multipoint constraints, sets the link between dependent and independent DOFs at domain $\Omega^{(s)}$. The links are formed considering the shape functions of the coarse domain restricted onto the interface as explained in (4.3). The set of interscale LMPCs can be implemented in the FETI method by simply adding extra equations via the use of Lagrange multipliers. These extra equations are included by defining the modified Boolean matrices $\bar{\mathbf{B}}^{(s)}$ which are built by row-wise concatenation of the original Boolean matrices containing standard LMPCs $\mathbf{B}^{(s)}$ and the constraint matrices $\mathbf{C}^{(s)}$ as

$$\begin{bmatrix} \bar{\mathbf{B}}^{(1)} & \bar{\mathbf{B}}^{(2)} \end{bmatrix} = \begin{bmatrix} \mathbf{B}^{(1)} & \mathbf{B}^{(2)} \\ \mathbf{C}^{(1)} & \mathbf{C}^{(2)} \end{bmatrix}. \quad (4.5)$$

The extended field of Lagrange multipliers $\boldsymbol{\Lambda}$ contains the forces that glue the adjacent domains, λ , and those arising from the multipoint constraints,

μ :

$$\Lambda = \begin{bmatrix} \lambda \\ \mu \end{bmatrix}. \quad (4.6)$$

The continuity condition (2.5), written in terms of the modified Boolean matrices $\bar{\mathbf{B}}^{(s)}$, reads

$$\bar{\mathbf{B}}^{(1)} \mathbf{u}^{(1)} + \bar{\mathbf{B}}^{(2)} \mathbf{u}^{(2)} = \mathbf{0}, \quad (4.7)$$

and the system in (2.4) can be rewritten in the equivalent form

$$\begin{bmatrix} \mathbf{K}^{(1)} & \mathbf{0} & \bar{\mathbf{B}}^{(1)\top} \\ \mathbf{0} & \mathbf{K}^{(2)} & \bar{\mathbf{B}}^{(2)\top} \\ \bar{\mathbf{B}}^{(1)} & \bar{\mathbf{B}}^{(2)} & \mathbf{0} \end{bmatrix} \begin{bmatrix} \mathbf{u}^{(1)} \\ \mathbf{u}^{(2)} \\ \Lambda \end{bmatrix} = \begin{bmatrix} \mathbf{f}^{(1)} \\ \mathbf{f}^{(2)} \\ \mathbf{0} \end{bmatrix}. \quad (4.8)$$

It is important to realize that the domain stiffness matrices $\mathbf{K}^{(s)}$ remain unaltered and the modified Boolean matrices $\bar{\mathbf{B}}^{(s)}$ partially lose their original Boolean character because of the addition of the interscale LMPCs. It is indicated by Rixen [97] that an appropriate preconditioner for the interface problem can be constructed using the modified Boolean matrices $\bar{\mathbf{B}}^{(s)}$ instead of the original ones. The incorporation of extra rows in the $\bar{\mathbf{B}}^{(s)}$ matrices representing the interscale LMPCs is no longer needed at conforming interfaces. During a multiscale analysis, it is expected that the number of high resolution domains will vary. Hence, the interface problem needs to be re-computed every time a domain resolution is changed.

Stability of the augmented system in (4.8) is guaranteed in the sense of the Ladyzhenskaya-Babuška-Brezzi (LBB) condition for the case of a strong interscale link (collocation) between coarse and refined meshes [107]. The LBB condition is satisfied for linear and higher order elements assuming that the fine domains are obtained by h -refinement of the coarse ones [107]. To the author's knowledge a formal proof of the LBB stability in the case of non-conforming interfaces gluing FE of different order still needs to be provided. For very fine meshes the LBB condition is still fulfilled as shown in [107]. This condition does not directly depend on the number of constraints in $\bar{\mathbf{B}}$, however an increasing number of interscale relations in $\bar{\mathbf{B}}$ is linked to an increasing ratio between the size of the domain and the size of the FE used in the discretization. In case redundant constraints are defined in $\bar{\mathbf{B}}$ (such as sometimes found in the presence of corners), the solution for Λ is not unique, but still a unique solution for $\mathbf{u}^{(s)}$ is found. Furthermore, it can be

shown that in case the entire system is floating, i.e. has global rigid body modes, a solution exists if the applied forces are self-equilibrated (see [96]).

A related work to the proposed multiscale framework in which both collocation and mortar methods are studied for the incompatible interface is provided by Amini et al. [4]. A different version of the FETI method is used in their work where a primal assembly is considered for the independent nodes and a dual assembly is used for the rest of the nodes at the interface.

4.1.2 Zoom-in update procedure

When specific criteria are satisfied, the low resolution domains need to be upgraded to their corresponding high resolution representation. This is accomplished by using the so called zoom-in strategy which consists of solving a boundary value problem (BVP) on the undeformed fine domain in order to reach the latest deformed configuration of the coarse domain at the boundary. Consequently, the initial (null) displacement field $\mathbf{u}_0^{\text{f}(s)}(\mathbf{x})$ of the fine resolution domain $\Omega^{\text{f}(s)}$ needs to be updated following a deformation-driven process imposed at the boundary $\Gamma^{(s)}$ which satisfies

$$\mathbf{u}^{\text{f}(s)}(\mathbf{x}) = \mathbf{u}^{\text{c}(s)}(\mathbf{x}), \quad \forall \mathbf{x} \in \Gamma^{(s)}. \quad (4.9)$$

Clearly, the values of the coarse displacement field $\mathbf{u}^{\text{c}(s)}$ restricted at the boundary $\Gamma^{(s)}$ are utilized to constrain the fine resolution domain rendering a statically determined problem. The BVP emerging from (4.9) is enforced with the addition of a set of constraints which involve boundary unknowns within the same domain. At the end of a zoom-in event (refer to Figure 4.3), a residual force $\mathbf{r}^{(s)}$ appears as a consequence of the imbalance between the pre-existing external forces at the old interface configuration and internal forces developed after equilibrium of the new BVP. The external and internal force fields restricted onto the boundary of $\Omega^{(s)}$ correspond to different interface configurations. For this reason the residual $\mathbf{r}^{(s)}$ needs to be computed following the procedure described in Section 4.1.3. The zoom-in has some similarities with the BVP imposed at unit cells in order to extract a constitutive relation for the macroscale of the so called FE² methods [27, 58] and strong coupling multiscale techniques [67]. For clarity, the update process is solved before non-linearities are expected. In small deformation quasi-static analyses, the zoom-in update procedure can be accomplished in one single step. However, in case local weak non-linearities develop during the zoom-in, it is advised to use more than one loading step in order to avoid compromising the convergence of the Newton-Raphson solution procedure.

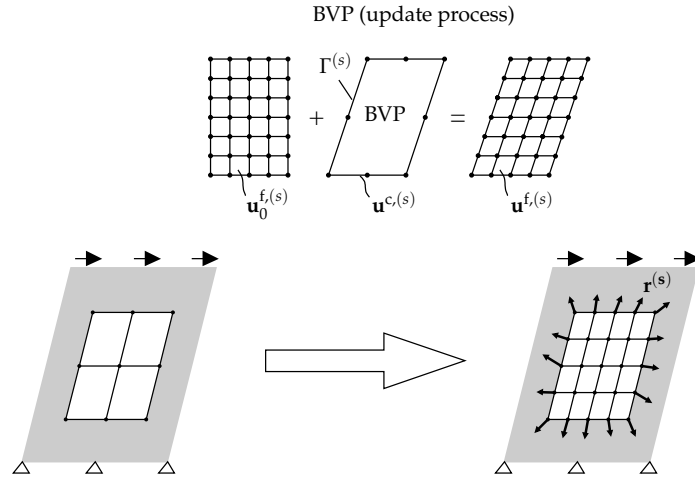


Figure 4.3 Zoom-in update procedure: the residual $\mathbf{r}^{(s)}$ represents the difference between external and internal forces at domain $\Omega^{(s)}$.

The solution of the fine-scale BVP is detached from the normal flow of the FETI method. Nevertheless, the subscale problem is only accounted for during a zoom-in event and, from then on, the different scales are processed concurrently until the end of the analysis. For convenience, an incremental formulation is adopted in the following for the FETI equations. All previous relations in this section hold for a non-linear setting by simply substituting the total solution field and external force vector by the corresponding solution increment and residual forces. A detailed formulation of the non-linear FETI framework is provided in Chapter 2.

4.1.3 Global relaxation process

After the zoom-in update procedure, displacement compatibility is satisfied at the interface since the fine-scale displacement field is interpolated using the previous coarse-scale field. However, this does not guarantee that global equilibrium is satisfied as well. For this reason, it is necessary to perform a set of global iterations, without changing the load level, in order to satisfy global equilibrium. These iterations constitute the global relaxation process.

Considering a structure decomposed in two domains, the relaxation process consists in a set of iterations needed to re-equilibrate the system, that is

to reach the following conditions:

$$\mathbf{K}^{(1)} \delta \mathbf{u}^{(1)} + \bar{\mathbf{B}}^{(1)\top} \delta \boldsymbol{\Lambda} = \mathbf{f}_{\text{ext}}^{(1)} - \bar{\mathbf{B}}^{(1)\top} \boldsymbol{\Lambda} - \mathbf{f}_{\text{int}}^{(1)}, \quad (4.10a)$$

$$\mathbf{K}^{(2)} \delta \mathbf{u}^{(2)} + \bar{\mathbf{B}}^{(2)\top} \delta \boldsymbol{\Lambda} = \mathbf{f}_{\text{ext}}^{(2)} - \bar{\mathbf{B}}^{(2)\top} \boldsymbol{\Lambda} - \mathbf{f}_{\text{int}}^{(2)}, \quad (4.10b)$$

$$\bar{\mathbf{B}}^{(1)} \delta \mathbf{u}^{(1)} + \bar{\mathbf{B}}^{(2)} \delta \mathbf{u}^{(2)} + \bar{\mathbf{B}}^{(1)} \mathbf{u}^{(1)} + \bar{\mathbf{B}}^{(2)} \mathbf{u}^{(2)} = \mathbf{0}, \quad (4.10c)$$

where $\mathbf{f}_{\text{ext}}^{(s)}$ and $\mathbf{f}_{\text{int}}^{(s)}$ stand for the external and internal force vectors, respectively. Note that the term $\bar{\mathbf{B}}^{(s)\top} \boldsymbol{\Lambda}$ contains the accumulated interface forces. This term can be interpreted as an external force vector acting at the interface of $\Omega^{(s)}$. The interface forces $\bar{\mathbf{B}}^{(s)\top} \boldsymbol{\Lambda}$ are related to a particular interface configuration. Hence, after updating a domain to its fine scale representation, the existing interface forces need to be migrated to the new interface configuration. For the sake of completeness, the migration of interface data is sketched in Figure 4.4 for a structure decomposed in two domains which experience zoom-in. Configuration I represents an initial situation where two coarse domains are glued with a set of Lagrange Multipliers λ_I which enforce the standard LMPCs. Since interscale LMPCs are not needed, the extended field of Lagrange Multipliers $\boldsymbol{\Lambda}_I$ reads

$$\boldsymbol{\Lambda}_I = \lambda_I. \quad (4.11)$$

After zoom-in at domain (2) a set of interscale LMPCs needs to be considered in order to properly link coarse and fine scale domains. The new stiffness $\mathbf{K}_{\text{II}}^{(2)}$ and internal force $\mathbf{f}_{\text{int,II}}^{(2)}$ for domain (2) are obtained after the resolution of the BVP. The external force vector $\mathbf{f}_{\text{ext,II}}^{(2)}$ is computed based on the global boundary conditions applied at the new refined domain. Conversely, the new extended field of Lagrange Multipliers $\boldsymbol{\Lambda}_{\text{II}}$ is calculated using the previous interface forces $\boldsymbol{\Lambda}_I$ as

$$\boldsymbol{\Lambda}_{\text{II}} = \mathbf{R}_{\lambda,\text{II}} \lambda_I. \quad (4.12)$$

The matrix $\mathbf{R}_{\lambda,\text{II}}$ is used to export the accumulated interface forces from configuration (I) to configuration (II). Note that, in this case, the interscale forces μ_{II} are set to zero.

When zoom-in is performed at domain (1) a similar process is observed. The new FE quantities, namely the stiffness $\mathbf{K}_{\text{III}}^{(2)}$ and internal force $\mathbf{f}_{\text{int,III}}^{(2)}$ are obtained after equilibrium of the prescribed BVP at domain (1). The external

4.1 Extensions for multiscale analysis

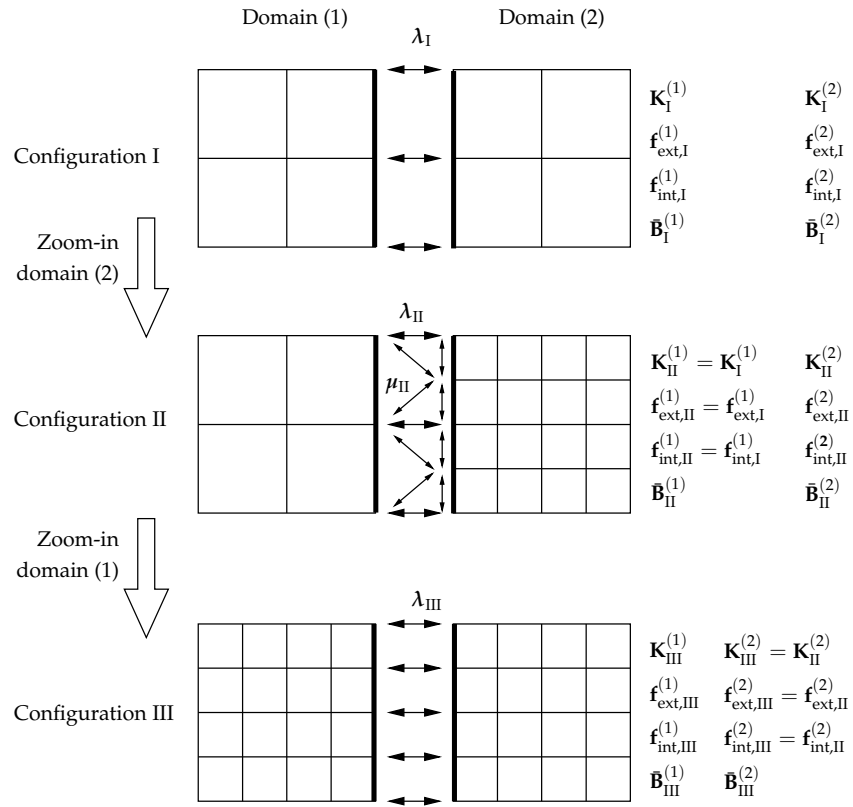


Figure 4.4 Possible resolution configurations at neighboring domains.

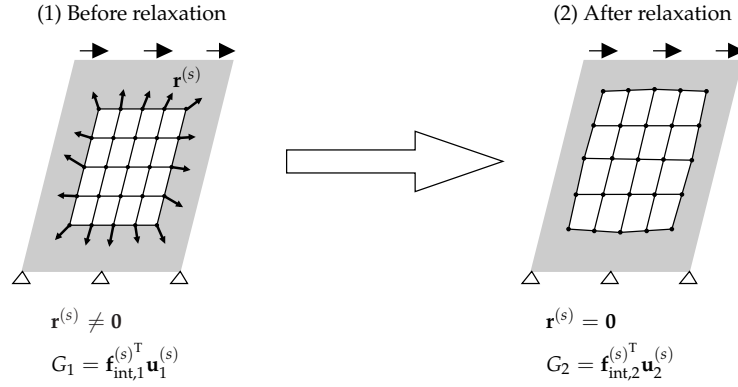


Figure 4.5 Global relaxation process.

load is applied to the new mesh through $\mathbf{f}_{\text{ext,III}}^{(1)}$ and the interface forces $\mathbf{\Lambda}_{\text{III}}$ read

$$\mathbf{\Lambda}_{\text{III}} = \mathbf{R}_{\lambda,\text{III}} \lambda_{\text{II}} + \mathbf{R}_{\mu,\text{III}} \mu_{\text{II}}. \quad (4.13)$$

Note that both standard λ_{II} and interscale μ_{II} forces are migrated to the new interface through $\mathbf{R}_{\lambda,\text{III}}$ and $\mathbf{R}_{\mu,\text{III}}$, respectively. The interface forces on the nodes, present before and after the refinement, are kept unchanged whereas the forces related to the additional nodes are computed as the sum of the interscale forces μ on a node before refinement. If redundancies are accounted for in the interscale relations, the matrices $\mathbf{R}_{\lambda,\square}$ and $\mathbf{R}_{\mu,\square}$ need to contain the entries that correspond to the redundant equations. Therefore, the strategy developed to migrate interface forces does not depend on the redundant character of the adopted interscale relations.

The residual force vector

$$\mathbf{r}^{(s)} = \mathbf{f}_{\text{ext}}^{(s)} - \bar{\mathbf{B}}^{(s)\text{T}} \mathbf{\Lambda} - \mathbf{f}_{\text{int}}^{(s)} \quad (4.14)$$

appears as a consequence of the difference between coarse and fine domain resolutions and their interaction with the global strain and stress fields. These residual forces are canceled at the updated interfaces after the relaxation process as indicated in Figure 4.5.

The deformation energy is computed considering the internal forces \mathbf{f}_{int} and total displacements \mathbf{u} at each domain as $G^{(s)} = \mathbf{f}_{\text{int}}^{(s)\text{T}} \mathbf{u}^{(s)}$. This quantity is computed before and after the relaxation by monitoring the energy

imbalance

$$\Delta G_{12}^{(s)} = \left| \mathbf{f}_{\text{int},1}^{(s)\text{T}} \mathbf{u}_1^{(s)} - \mathbf{f}_{\text{int},2}^{(s)\text{T}} \mathbf{u}_2^{(s)} \right|. \quad (4.15)$$

The energy at each stage k of the zoom-in procedure is computed as $G_k^{(s)} = \mathbf{f}_{\text{int},k}^{(s)\text{T}} \mathbf{u}_k^{(s)}$. Consequently, the relative energy imbalance is $G_{r_{12}}^{(s)} = G_{12}^{(s)} |G_1^{(s)}|^{-1}$. Low values of $G_{12}^{(s)}$ indicate that the deformation energies of the coarse and fine domains do not differ significantly. Monitoring the relative energy imbalance is particularly interesting for heterogeneous materials since one can draw conclusions about the quality of the effective properties assigned to the coarse homogeneous domain. This issue is discussed in more detail in the examples reported in Section 4.3.

Remark 4.1.1. It should be stressed that both zoom-in and relaxation processes could be merged in one single stage. Considering that only linear phenomena take place during the zoom-in of domain $\Omega^{(s)}$, it is possible to satisfy (4.10) by simply setting $\mathbf{f}_{\text{int}}^{(s)} = \mathbf{0}$. However, we propose two distinct stages in order to facilitate the detection of weak non-linearity during the zoom-in. Moreover, the relative energy imbalance $G_{r_{12}}^{(s)}$ can be monitored during the relaxation process and turns out to be a good indicator of the quality of the analysis.

4.2 General multiscale framework for quasi-brittle heterogeneous materials

The multiscale extensions to the FETI method allow the solver to deal with different domain resolutions in an adaptive manner. In the study of heterogeneous materials, a homogeneous bulk is considered with elastic effective properties for the coarse domains. These effective properties are retrieved from the analysis of the heterogeneous material. The criterion adopted to trigger the zoom-in events is related to the linear/non-linear character of the constitutive behavior at each domain (cf. Chapter 3). When non-linearities are expected in a certain domain, a zoom-in event takes place and the analysis is continued. The flowchart of the multiscale FETI method is shown in Figure 4.6 and reveals that, although a significant part of the analysis of the decomposed structure is performed in a concurrent manner, a hierarchical approach is employed for both zoom-in events and the RVE analysis. Since

a BVP needs to be solved during the zoom-in update procedure, the framework presents some similarities with other weak coupling methods. Next, the methodologies used in this contribution to retrieve the elastic effective properties and the criteria to trigger the zoom-in events are described. The latter is referred to as “Linear/non-linear switch” in the multiscale flowchart depicted in Figure 4.6.

4.2.1 RVE concept and effective properties

In this section we restrict ourselves to the study of static analyses of heterogeneous linear elastic solids. In this context, it has been proved by several authors [79] that an RVE can be found for a heterogeneous material sample. Assuming that the scales separation principle holds [58], the RVE provides an estimation of the effective material properties of a mechanically equivalent homogeneous media.

The agreement of the multiscale analysis compared to the DNS may depend on the accuracy of the chosen effective properties. In the sequel, a few analytical and numerical approaches to derive the effective elastic moduli are briefly introduced. The influence of the method in the results of the multiscale analysis will be demonstrated in Section 4.3.2.

Any elastic effective moduli obtained through a homogenization technique falls within the so-called Voigt [113] and Reuss [92] analytical bounds. Considering the constitutive tensor of a material phase \mathbf{D}_i and their corresponding volume fraction v_i , the effective moduli \mathbf{D}^{eff} computed with the Voigt, i.e. constant strain, assumption reads

$$\mathbf{D}^{\text{eff}} = \sum_{i=1}^{N_{\text{phase}}} v_i \mathbf{D}_i, \quad (4.16)$$

where N_{phase} stands for the total number of phases present in the heterogeneous sample. Considering the Reuss, i.e. constant stress, assumption, the effective moduli can be expressed as

$$\mathbf{D}^{\text{eff}} = \left[\sum_{i=1}^{N_{\text{phase}}} v_i \mathbf{D}_i^{-1} \right]^{-1}, \quad (4.17)$$

4.2 General multiscale framework for quasi-brittle heterogeneous materials

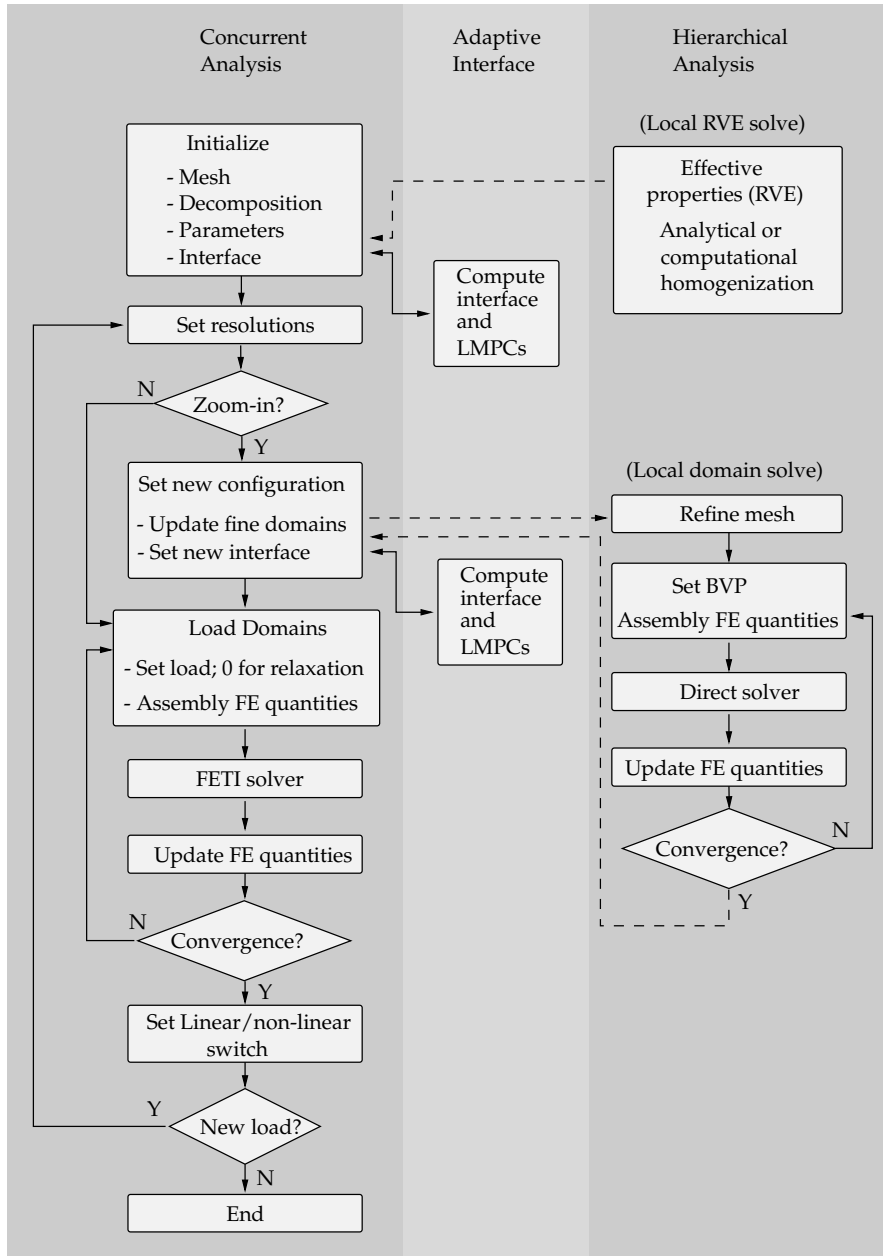


Figure 4.6 Flowchart of the proposed multiscale FETI method.

where the volume fractions v_i satisfy the relation

$$\sum_{i=1}^{N_{\text{phase}}} v_i = 1. \quad (4.18)$$

The Mori-Tanaka scheme [75] is a widely used analytical homogenization scheme for regularly shaped inclusions accounting for a weak interaction between them. The combined effective moduli of a multi-phase heterogeneous material consisting of N_{phase} inclusion phases v_i surrounded by a matrix material v_0 can be computed as [15]

$$\mathbf{D}^{\text{eff}} = \mathbf{D}_0 \left[\mathbf{I} + \left(\sum_{i=1}^{N_{\text{phase}}} v_i \mathbf{L}_i \right) \left(\mathbf{I} + \sum_{i=1}^{N_{\text{phase}}} v_i (\mathbf{S}_i - \mathbf{I}) \mathbf{L}_i \right)^{-1} \right]^{-1}. \quad (4.19)$$

The localization tensor

$$\mathbf{L}_i = - [(\mathbf{D}_i - \mathbf{D}_0) \mathbf{S}_i + \mathbf{D}_0]^{-1} (\mathbf{D}_i - \mathbf{D}_0), \quad (4.20)$$

where \mathbf{S}_i stands for the Eshelby tensor [20] of a spherical inclusion, and \mathbf{D}_0 corresponds to the elastic moduli of the matrix phase.

The computation of effective properties for more complex heterogeneous materials requires the use of numerical techniques. Several approaches are formulated based on the selected boundary conditions used to load the RVE. These conditions satisfy the Hill-Mandel or macro-homogeneity condition [43] which constitutes a weak coupling between the separated scales. For the case of fully prescribed displacements and periodic boundary conditions, the effective moduli

$$\mathbf{D}^{\text{eff}} = \frac{1}{V} \mathbb{D} \mathbf{K}^* \mathbb{D}^T, \quad (4.21)$$

where \mathbf{K}^* represents the condensed stiffness matrix of the internal nodes a of the RVE volume V to the boundary nodal points b . As indicated by Miehe and Koch [73], the operator \mathbb{D} is obtained by taking into account the nature of the prescribed boundary conditions at the RVE. For the case of fully prescribed displacements, the relation between the strain tensor $\boldsymbol{\varepsilon}$, displacement vector \mathbf{u} and position vector \mathbf{x} considered for the derivation of the effective elastic moduli reads

$$\mathbf{u}_b = \boldsymbol{\varepsilon} \mathbf{x}_b. \quad (4.22)$$

In the case of periodic boundary conditions, the kinematic condition reads

$$\llbracket \mathbf{u}_b \rrbracket = \boldsymbol{\varepsilon} \llbracket \mathbf{x}_b \rrbracket. \quad (4.23)$$

Note that the jump notation $\llbracket \square_b \rrbracket := \square_b^+ - \square_b^-$ denotes a difference between quantities at opposite faces of the RVE.

Considering fully prescribed tractions, the effective moduli

$$\mathbf{D}^{\text{eff}} = \left[\mathbf{S} (\mathbf{K}^*)^{-1} \mathbf{S}^T \right]^{-1}, \quad (4.24)$$

where the operator \mathbf{S} is obtained considering constant tractions at the boundary,

$$\mathbf{t}_b = \boldsymbol{\sigma} \mathbf{n}_b, \quad (4.25)$$

recast according to a deformation driven approach as discussed by Miehe and Koch [73]. The computation of the effective linear and non-linear constitutive relations derived from RVE analysis is treated in detail in [58, 73, 76].

4.2.2 Criteria to trigger zoom-in events

A key issue of the present multiscale framework is the assumption that a coarse description of the structure with homogenized effective properties suffices during the linear elastic analysis. This hypothesis is in agreement with other multiscale techniques based on analytical [79] or computational homogenization [58, 73, 76, 110] and the RVE concept for the elastic behavior of heterogeneous materials [41, 43]. Consequently, the adopted criteria for the zoom-in events are linked to the prediction of non-linearities in the corresponding domain of interest as explained in Chapter 3. The predictor II in 3.7 is adopted for all analyses.

It should be noted that a error estimation procedure should be employed to complement the criteria to trigger the zoom-in event. This would overcome situations in which the coarse scale discretization do not suffice to provide an accurate solution. This improvement has not been implemented in the present framework.

When non-linearities are predicted at a certain domain, the resolution is upgraded using the zoom-in procedure described in the Section 4.1.2. If an upgraded domain experiences unloading, the high resolution is kept but certain enhancements can be performed at the solver level in order to speed up the computations as argued in Chapter 3. These enhancements rely on

bypassing the assembly and factorization stages. In this scenario, both the domain stiffness $\mathbf{K}_i^{(s)}$ and its lower $\mathbf{L}_i^{(s)}$ and upper $\mathbf{U}_i^{(s)}$ triangular components do not need to be recomputed at each Newton-Raphson iteration i since they remain constant and equal to the stored linear quantities $\mathbf{K}_1^{(s)}$, $\mathbf{L}_1^{(s)}$ and $\mathbf{U}_1^{(s)}$. The internal force vector can be computed as $\mathbf{f}_{\text{int},i}^{(s)} = \mathbf{f}_{\text{int},i-1}^{(s)} + \delta\mathbf{f}_{\text{int},i}^{(s)}$. Hence the increment $\delta\mathbf{f}_{\text{int},i}^{(s)}$ is simply obtained as $\mathbf{K}_1^{(s)}\delta\mathbf{u}_i^{(s)}$. The solver enhancement is particularly useful for the study of brittle materials provided that strain localization occurs and the non-linearities are concentrated in a narrow zone of the specimen. The work load of the solution process is quantified by monitoring the evolution of the active mesh which is defined as the relative amount of finite elements in which the assembly and factorization stages need to be performed completely. The active mesh is given as the ratio between the elements corresponding to the non-linear domains and the total number of elements considered at the current stage of the analysis.

In the present approach, it is assumed that the high resolution domains are not needed during the initial elastic regime. Hence, those domains that experience linear behavior are normally described by means of their coarse-scale (or low resolution) representation and the linear enhancements are activated. Obviously, the initial step represents an exception since all FE quantities need to be initialized and therefore the linear enhancements need to be skipped. When non-linearities are predicted at a particular domain, its corresponding high resolution is employed and the assembly and factorization enhancements are switched off. During the linear loading/unloading regime, the assembly and factorization enhancements become active in order to reduce the computational cost of the solution but the high resolution mesh is kept. One could decide to re-coarsen the mesh of the corresponding domain but, if a new non-linear episode is encountered after reloading, the correct distribution of non-linear history variables can not be easily recovered.

It should be stressed that these enhancements can only be accounted for when the domain FE discretization does not change. Hence, the use of adaptive h -refinement in order to obtain a smooth transition between coarse and fine domains is not compatible with such enhancements.

4.3 Examples

4.3.1 Homogeneous L-shaped specimen

The performance of the multiscale FETI method is investigated in the analysis of a homogeneous L-shaped specimen which is loaded under plane strain conditions. This example clearly shows how displacement continuity is satisfied all over the interfaces during damage growth and propagation. It is also interesting to test the objectivity of the method with respect to the number of partitioned domains.

Geometry and boundary conditions are indicated in Figure 4.7(a). The specimen is divided into a number of domains which, using mesh refinement, can be replaced by corresponding high resolution domains shown in Figure 4.7(b) when necessary. The gradient-enhanced damage model (cf. Appendix A) is adopted for both coarse and fine-scale domains although the coarse discretization will only undergo linear elastic behavior. The parameters adopted for the analysis are listed in Table 4.1.

Damage is expected to be initiated at the re-entrant corner of the specimen and propagate across different domains until the opposite bottom left edge is reached leading to complete failure. Damage evolution is shown in the top part of Figure 4.8. It is observed that high domain resolutions are activated right before damage nucleation. Full compatibility of the solution field is satisfied across the interfaces. For visualization purposes, the domains are drawn separately from each other.

The evolution of the linear/non-linear character of the domains is shown in the sequence at the bottom of Figure 4.8. In the initial step, all domains need to be loaded and, therefore, the assembly and factorization routines are entered completely. In the following elastic steps, the assembly and factorization enhancements become active. When non-linearities are predicted in a certain domain, the spatial resolution is improved, and the assembly and factorization enhancements described in Section 4.2.2 are disabled (i.e. the mesh is fully processed). It is observed that certain areas experience unloading at later loading stages. In these cases, the high resolution is kept but the assembly and factorization enhancements remain active. The computation cost is linked to the size of the non-linear loading region (in red) and the interface. The procedure is domain-decomposition independent as demonstrated by the results reported in Figures 4.9 and 4.10 related to three different decompositions (12, 21 and 75 domains). The same damage pattern is obtained in all cases (refer to the top part of Figure 4.9) and the main

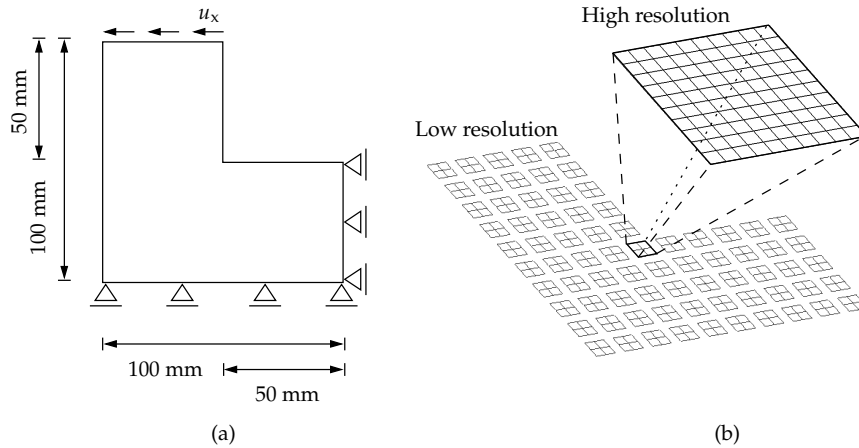


Figure 4.7 Boundary conditions (a) and different resolution domains (b) for the L-shaped specimen.

difference resides in the efficiency of the computations. As shown at the bottom of Figure 4.9, the total refined area decreases with an increasing number of domains.

The load deflection curves of the three multiscale analyses are compared to that obtained with a DNS. A good agreement is found in terms of the global response as shown in Figure 4.10. The zoom-in events are responsible for the small jumps registered in the equilibrium path. These jumps are related to the different flexibilities of the coarse and fine resolution domains. A decomposition into a larger number of domains leads naturally to a slightly stiffer response since a smaller fine-scale area (with higher flexibility) is involved in the analysis. The overall efficiency of the multiscale analysis can be quantified by following the evolution of the active mesh. In other words, the total number of elements which are fully processed by the assembly and factorization routines is monitored. This quantity is compared to the total number of elements used to discretize the sample as shown in the left part of Figure 4.11. A larger number of domains leads naturally to the lowest active mesh ratio and, for this reason, to the most efficient analysis. On the other hand, the number of DOFs present at the interface increases when the structure is subdivided into a larger number of domains (see right part of Figure 4.11). This effect diminishes, to a certain extent, the efficiency achieved with a low active mesh ratio.

4.3 Examples

Test data			
E	Young's modulus	[N/mm ²]	35.0×10^3
ν	Poisson's ratio	[-]	0.2
$\tilde{\varepsilon}_{nl}$	Non-local equivalent strain	[-]	Mazars
κ_0	Damage initiation threshold	[-]	5.0×10^{-4}
c	Gradient parameter	[mm ²]	0.5
$\omega(\kappa)$	Damage evolution law	[-]	Exponential
α	Residual stress parameter	[-]	0.999
β	Softening rate parameter	[-]	50
u_x	Displacement	[mm]	1.0
Two-dimensional analysis type			Plane strain

Table 4.1 Test data.

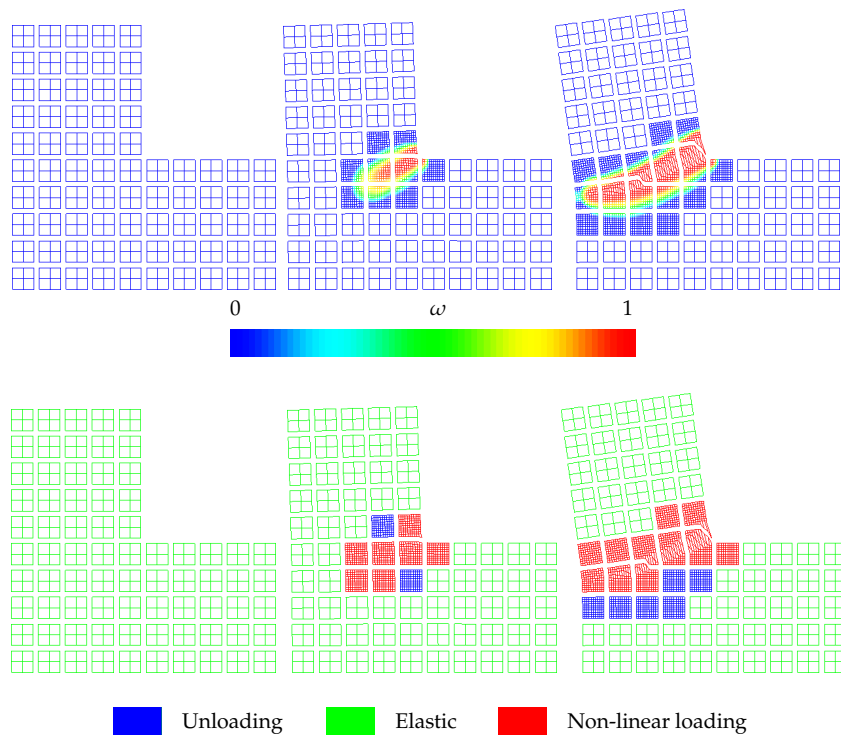


Figure 4.8 Evolution of damage growth (top) and loading domains (bottom). $10\times$ displacement magnification.

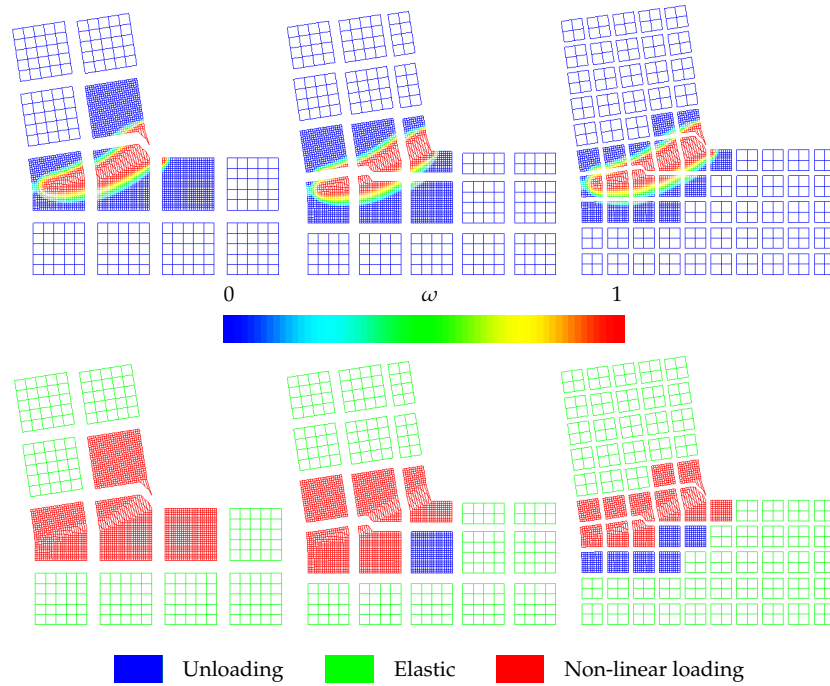


Figure 4.9 Final damage contours and loading regimes for 12, 21 and 75 domains. $10\times$ displacement magnification.

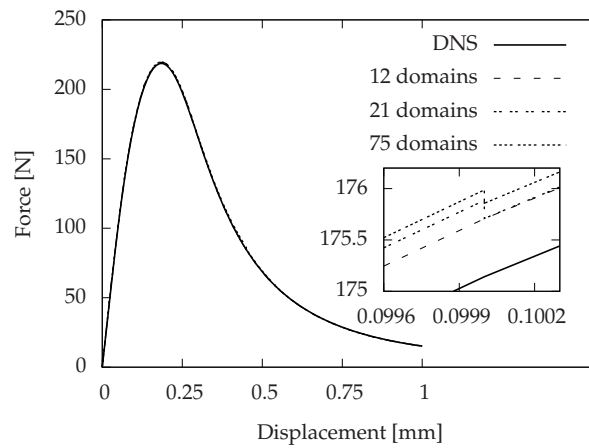


Figure 4.10 Load-deflection curves for different domain decompositions. The inset shows the close-up of a zoom-in event.

4.3 Examples

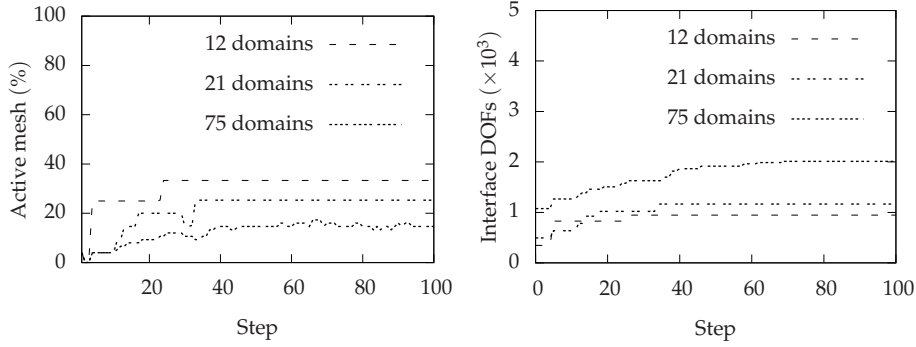


Figure 4.11 Evolution of active mesh (left) and interface DOFs (right).

4.3.2 Reinforced L-shaped specimen

In this example the multiscale framework is tested for a heterogeneous material. We study the influence of different effective properties retrieved from RVE computations using analytical and computational homogenization techniques. An L-shaped concrete specimen is considered with a regular distribution of steel fibers (oriented perpendicular to the cross section of the specimen). The boundary conditions applied to the coarse discretization of the specimen and the RVE associated to each of the integration points of the coarse finite elements are shown in Figure 4.12. Plane strain conditions are assumed and the material parameters are listed in Table 4.2. The coarse-scale mesh is defined by a homogeneous bulk discretized by Q4 bilinear elements. The specimen is decomposed into 27 domains and, after mesh refinement using T3 linear elements, the underlying heterogeneous structure is represented by steel fibers surrounded by an interfacial transition zone (ITZ) and a matrix as shown in Figure 4.13. The ITZ phase is used to model fiber debonding. Effective elastic properties derived from the RVE in Figure 4.12 are used during the computations with the coarse-scale discretization. Due to the regular distribution of fibers, the RVE is simply defined by one single fiber surrounded by the ITZ and a matrix. In order to provide accurate results, the size of the RVE should not exceed the tributary area of its corresponding Gauss integration point at the coarse-scale: $A_{\text{RVE}} \leq A_{\text{ip}}$. Here, it is assumed that $A_{\text{RVE}} = A_{\text{ip}}$, with A_{RVE} the area associated to the RVE and A_{ip} related to the Gauss point of the coarse element. The heterogeneous material described in the RVE is naturally taken into account in the refined domains—the fine mesh includes all the heterogeneities of the

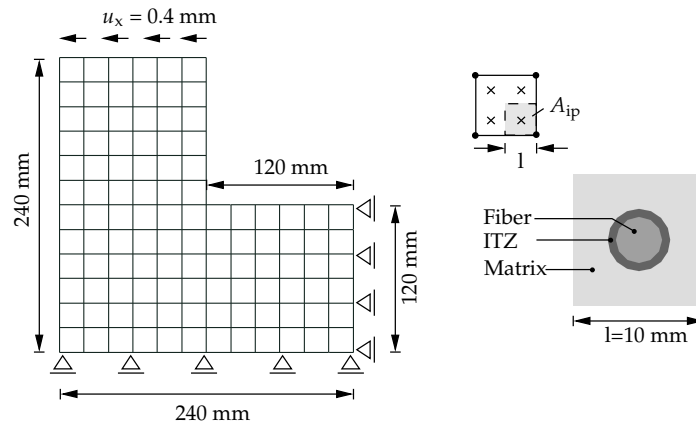


Figure 4.12 Boundary conditions (left) and selected RVE for effective properties (right). The area of the RVE should not exceed the one of the macroscopic integration point A_{ip} .

Material parameters	Fibers	ITZ	Matrix	Coarse bulk
E	20.0×10^4	20.0×10^3	40.0×10^3	Effective
ν	0.2	0.2	0.2	Effective
$\tilde{\epsilon}_{nl}$	Mazars	Mazars	Mazars	Mazars
κ_0	Dummy	5.0×10^{-5}	8.5×10^{-5}	5.0×10^{-5}
c	1.5	1.5	1.5	1.5
$\omega(\kappa)$	Exponential	Exponential	Exponential	[-]
α	0.999	0.999	0.999	[-]
β	400	400	400	[-]
Two-dimensional analysis type			Plane strain	

Table 4.2 Material parameters.

4.3 Examples

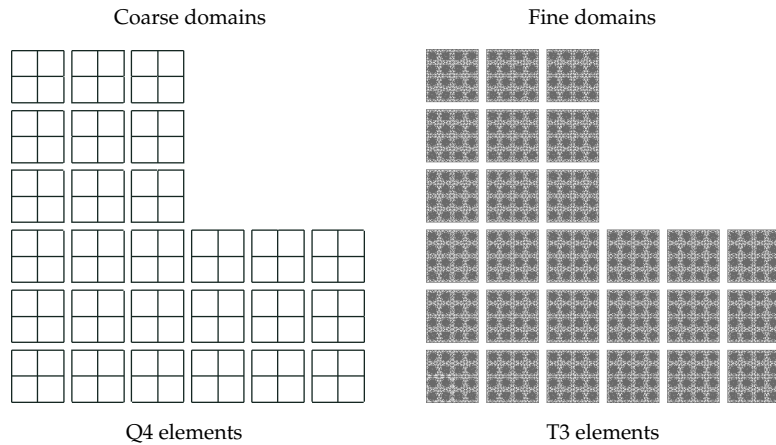


Figure 4.13 Coarse (left) and fine (right) discretizations.

lower scale.

High resolution domains are activated when damage growth and propagation is predicted in coarse domains. Non-linear phenomena initiates near the re-entrant corner of the specimen at the ITZ between the fibers and the matrix as shown in Figure 4.14. Damage propagates through the matrix of the new refined domains resulting in a final curved crack (top part of Figure 4.15). Due to strain localization, some refined domains experience unloading. In this case, the computational cost can be reduced by activating the assembly and factorization enhancements (refer to bottom part of Figure 4.15).

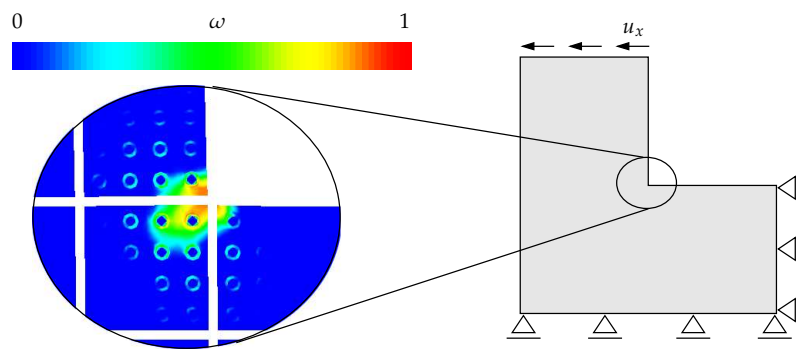


Figure 4.14 Close-up of damage initiation.

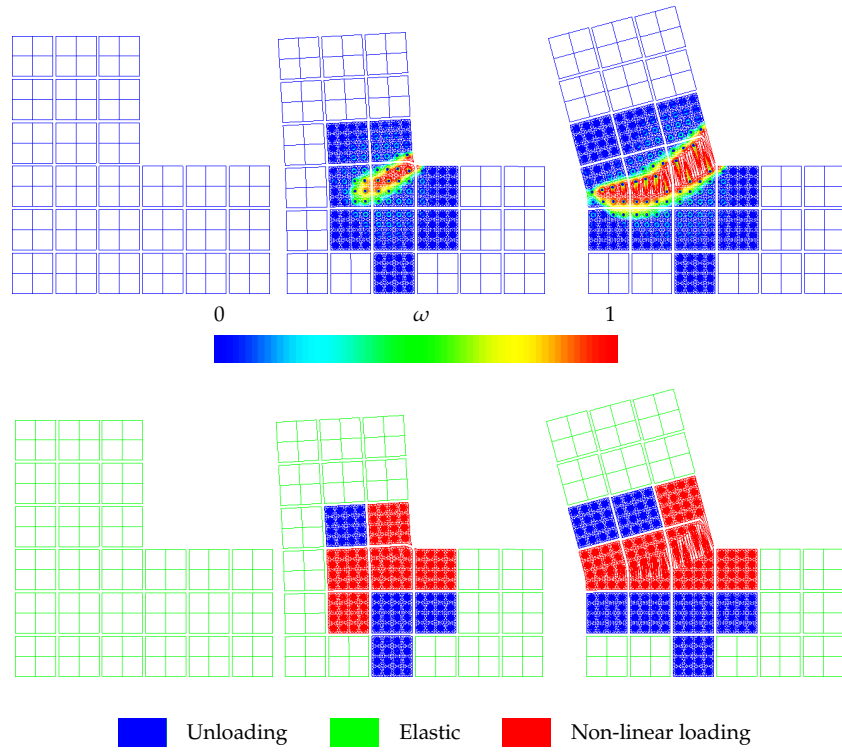


Figure 4.15 Evolution of damage growth (top) and loading domains (bottom). 100× displacement magnification.

4.3 Examples

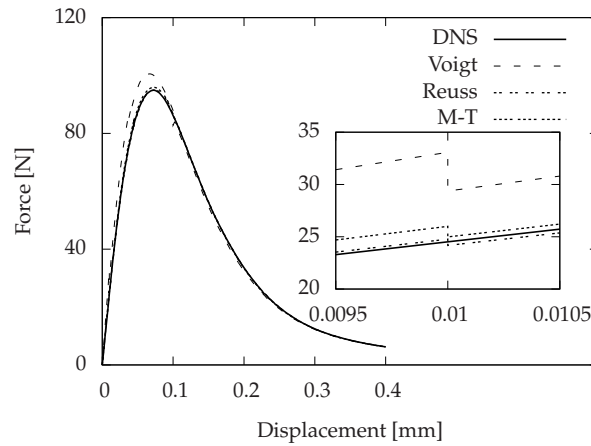


Figure 4.16 Load-deflection curves for the DNS and multiscale analysis based on analytical homogenization. The inset shows the close-up of the load-deflection curve around a zoom-in event.

Multiscale analyses are performed considering different methodologies to estimate the effective elastic properties. Analytical approaches (Voigt, Reuss and Mori-Tanaka) and numerical techniques based on different assumptions for the boundary conditions (see Section 4.2.1) are considered. The load deflection curves of the structure depicted in Figure 4.16 are obtained considering effective properties based on analytical Voigt and Reuss bounds and a Mori-Tanaka two-step scheme. The curves show that the Voigt assumption clearly overestimates the elastic modulus whilst Reuss and Mori-Tanaka assumptions provide a response which is closer to the one of the fine-scale analysis (DNS). This is due to the fact that the Voigt assumption always overestimates the modulus when considering stiff inclusions. The energy mismatch after a zoom in episode is translated into a jump at the load deflection curves. These jumps are higher when the effective properties are not accurate (e.g. in case of the Voigt assumption).

The results obtained using computational homogenization show less spreading between the resulting load-displacement curves (Figure 4.17). It is observed that the three approximations result in a stiffer response than the DNS. This result can be explained by arguing that the coarse discretization is, in this case, slightly too coarse to reproduce the elastic response accurately and, therefore, the homogenized bulk is artificially stiffened. Otherwise one would expect the effective properties based on prescribed tractions

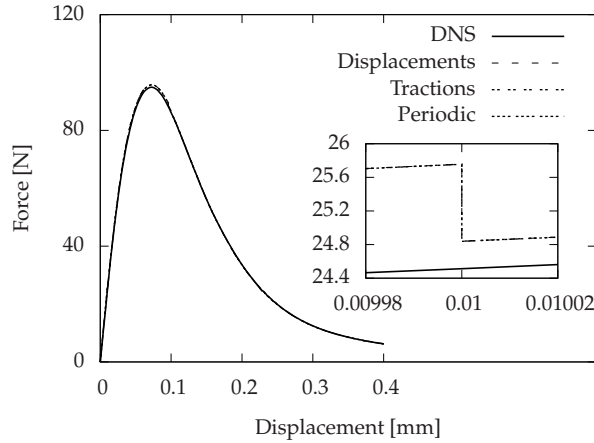


Figure 4.17 Load-deflection curves for the DNS and multiscale analysis based on computational homogenization. The inset shows the close-up of the load-deflection curve around a zoom-in event.

to slightly underestimate the stiffness observed at the DNS. In this case, error estimators should be used in order to ensure that the mesh is not too coarse during the computations and complement the switch criteria for the high resolution domains. It should be also pointed out that the size of the lower scale heterogeneity considered in this problem is about one order of magnitude smaller than the size of the complete specimen. Consequently, the principle of scale separation needed to guarantee the adequacy of the homogenization procedure is not fully satisfied.

The jumps along the load-deflection curve after zoom-in events are translated in an energy imbalance (refer to Section 4.1.3). In Figure 4.18, the values of $G_{r_{12}}$ are plotted for each zoom-in event. If more than one zoom-in is performed at a particular step, the maximum of all relative energies is considered. High values of the relative energy $G_{r_{12}}$ are observed at the first zoom-in event. This indicates that the mesh used during the elastic analysis is slightly too coarse and produces an artificial stiffening that is detected after the first zoom-in event. In this case it is advised to refine the coarse mesh around the re-entrant corner of the L-shaped specimen. However a smaller element size at the coarse mesh cannot fulfill the requirement $A_{RVE} \leq A_{ip}$ for this example. Consequently, the multiscale analysis can also be performed considering the refined mesh for the three domains located at the re-entrant corner of the sample. Results shown in Figure 4.19 indicate that the relative energy

4.3 Examples

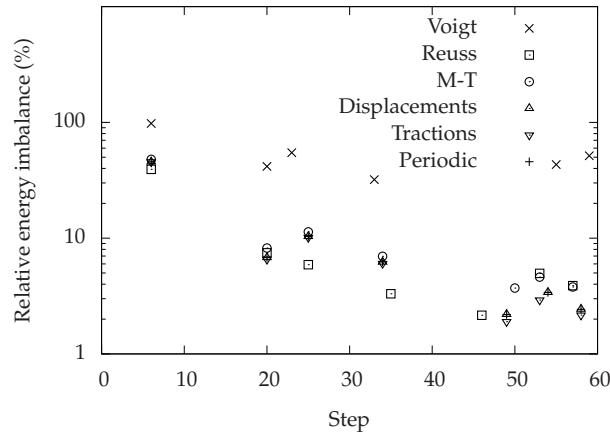


Figure 4.18 Evolution of relative energy imbalance after the zoom-in events.

jumps are in agreement with those presented in Figure 4.18 after the first zoom-in event. These results highlight that the high jumps values observed in Figure 4.18 are related to the coarse-scale mesh. Results show that a more accurate estimation of the effective properties naturally leads to smaller relative energy imbalance after the zoom-in events. It can be observed that the relative energy imbalance after the zoom-in events is higher for the Voigt assumption of effective properties. The use of computational homogenization together with the Reuss assumption brings, in this case, the lowest values of the energy jumps. Moreover, the deviation between results is hardly visible for the three different choices of computational homogenization schemes.

As shown in Figure 4.20, around 20% of the total mesh is fully processed during the multiscale analysis. The computational cost is related to the ratio between nonlinear and linear areas and is, therefore, linked to each particular problem and decomposition. If damage is localized in a small specimen region, the computational cost will be relatively low. The evolution of the number of DOFs at the interface grows according to the newly refined domains considered during the calculation and, unless it is decided to re-coarsen the mesh, will not decrease afterwards. The ratio between the number of interface DOFs of the multiscale analysis and the one of the corresponding high resolution analysis using domain decomposition is depicted in Figure 4.20 (active interface). The size of the active interface is below 60% in the analysis but depends on the studied problem. If the failure zone concentrates in a small portion of the material, both active mesh and active

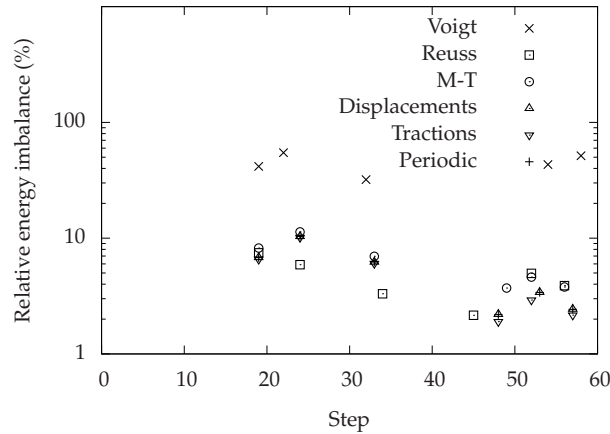


Figure 4.19 Evolution of relative energy imbalance after the zoom-in events. An initial refined mesh is considered for the three domains placed at the re-entrant corner.

interface remain low compared to a high resolution domain decomposition analysis.

4.4 Concluding remarks

The presented multiscale framework is essentially based on a FETI method with extensions to enable adaptive zoom-in at particular domains of interest. It can be seen as an extension of the work introduced in Chapter 3 to the multiscale analysis of heterogeneous materials.

The framework proves to be capable of accounting for damage nucleation and propagation across computational domains satisfying displacement compatibility at domain interfaces. This is possible since the zoom-in starts right before damage nucleation. Other weak coupling strategies (see Section 1.1.2) only account for a higher resolution when localization has appeared. The damage growth and path of the multiscale analyses are in agreement with the corresponding direct numerical simulation results, are independent of the number of the decomposed domains, and it is expected that they are not influenced by the shape of the decomposed domains. The agreement between the results of a direct numerical simulation and a multiscale analysis of a heterogeneous structure depends on the adequacy of the effective properties chosen during the linear elastic regime.

The presented multiscale framework allows to selectively focus the com-

4.4 Concluding remarks

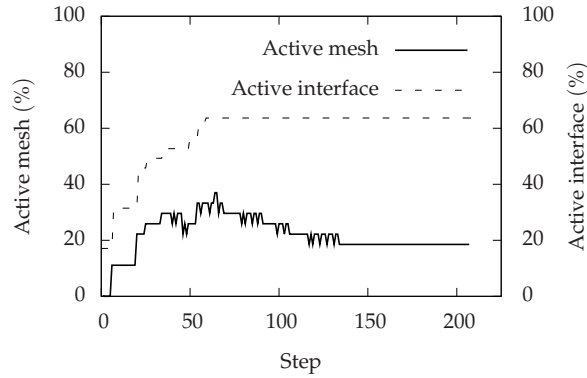


Figure 4.20 Evolution of active mesh ratio and size of the interface problem.

putational effort where needed since only non-linear domains are processed entirely. Given that no fundamental changes are performed to the FETI method, the framework can be easily parallelized for the study of large 2D and 3D structures.

As mentioned earlier, the interface problem of the FETI iterations were handled by direct solvers. The adaptive nature of the multiscale framework will pose challenges when implemented in a parallel computing environment. Considering that each processor handles a single domain, the work load becomes clearly unbalanced if different resolutions are simultaneously active. In such cases, automatic load-balancing and multi-threading need to be accounted for.

Chapter 5

On micro-to-macro connections in domain decomposition multiscale analysis*

The strategy to enforce interscale relations constitutes a key issue in the formulation of any multiscale analysis. Assumptions made on the interaction between micro- and macroscopic stress and strain fields determine the nature of such interscale relations and have a high impact on the overall behaviour. Early examples of interscale relations in multiscale approaches are found in classical homogenization theories [79]. In this context, constant strain and stress assumptions at the microscale, together with Hill's energy condition [43], lead to the well known Voigt [113] and Reuss [92] bounds [79, 120]. These hierarchical multiscale techniques are well suited to derive closed-form expressions of effective elastic properties.

The study of more complex microstructures with non-linear behaviour has stimulated the development of computational homogenization techniques [28, 58, 76]. Discretization methods such as the finite element method (FEM) are used therein in order to capture the constitutive behaviour of a representative volume element (RVE). Adopting different assumptions, inherited from classical homogenization techniques, three main types of boundary conditions can be imposed on the microstructural RVE. These are known as fully prescribed displacements, fully prescribed tractions, and periodic boundary conditions [73]. The first two techniques are based on the uniform strain and stress assumptions, respectively, and define the upper and lower bound of the effective constitutive behaviour; the latter enforces a displacement constraint which is suited for periodic media. The construction of these constraints is compatible with the development of microscopic fluctuations of the solution field at the sample boundaries. For this reason, they are adequate for material RVEs with heterogeneous boundaries and for the development of strain or stress localization effects. Many hierarchical multiscale techniques employed in the study of non-linear heterogeneous materials adopt these kind of constraints [28, 58, 76]. In particular, they are

* This chapter is based on reference [66].

specially attractive for the study of softening materials showing localized failure phenomena [33, 68, 69, 80]. The recently developed Minimal Kinematic Boundary Conditions [51, 72] exhibit similar capabilities and can be applied to a wider range of materials which are not necessarily periodic.

In those cases where the separation of scales principle does not hold, the use of concurrent multiscale techniques [48, 49, 60] is preferred. In these methodologies, the coarse and fine scale regions are processed simultaneously and are glued together through interscale relations or micro-to-macro connections. As observed in classical homogenization and computational homogenization, the adopted micro-to-macro relations influence the concurrent multiscale analysis as well [51, 73]. However, their role in an adaptive multiscale analysis of brittle materials has not been sufficiently investigated. Micro-to-macro connections in concurrent multiscale analysis are determined by the methodology employed to connect two incompatible meshes (see Figure 5.1). The simplest choice corresponds to the well established collocation method [10, 91]. Conversely, mortar methods [6, 8] belong to a family of techniques that “weakens” interface compatibility. To the author’s knowledge, the first parallelism between concurrent and hierarchical multiscale approaches, regarding the use of strong and weak constraints, was described by Amini et al. [4]. In their contribution, collocation and mortar methods are compared to the strain and stress approaches of the Hill-Mandel theory [43].

Other methodologies for the connection of incompatible meshes hinge on the use of interface elements [55], special strategies based on overlapping domains [16, 38] and shape function clustering [18]—these methodologies are not investigated in this study.

In the present chapter, several interscale relations of strong and weak type are assessed in the DD adaptive multiscale technique introduced in [65] and Chapter 4.

5.1 General strong and weak micro-macro connections

The main goal of the micro-macro connection strategy is to provide continuity of the solution field along the segment Γ_1^{cf} of the interface Γ_1 (Figures 5.1 and 5.2) such that

$$\mathbf{u}^f(\mathbf{x}) = \mathbf{u}^c(\mathbf{x}) \quad \forall \mathbf{x} \in \Gamma_1^{\text{cf}}. \quad (5.1)$$

Note that, for convenience, a total displacement formulation is followed in this section (as well as in Sections 5.2 and 5.3) although an incremental so-

5.1 General strong and weak micro-macro connections

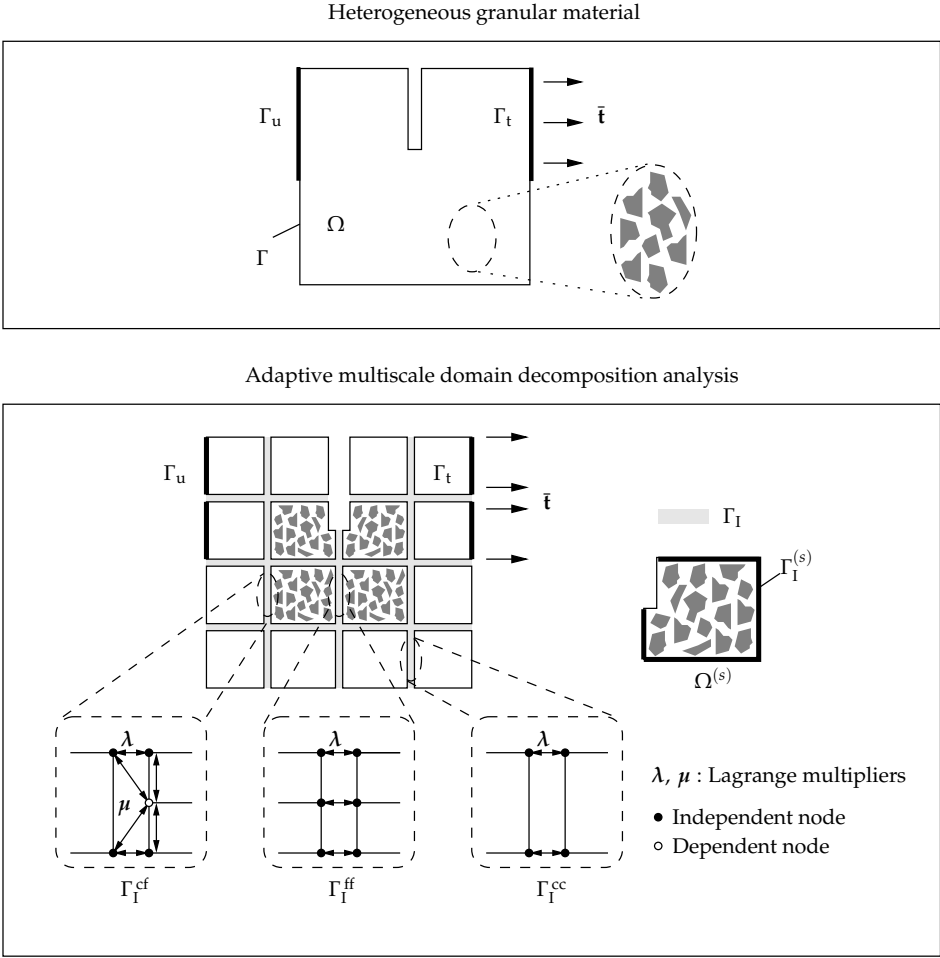


Figure 5.1 Strong and weak micro-macro connections.

lution field should be considered in a non-linear setting.

Several methods exist to connect incompatible interfaces. A general weak form of the interface compatibility can be written as

$$\int_{\Gamma_1^{\text{cf}}} w(\mathbf{x})(\mathbf{u}^f(\mathbf{x}) - \mathbf{u}^c(\mathbf{x})) \, d\Gamma_1^{\text{cf}} = \mathbf{0}, \quad (5.2)$$

where $w(\mathbf{x})$ represents a weighting function which gives rise to different types of connection.

5.1.1 Strong compatibility by collocation

A straightforward way to satisfy the weak condition in (5.2) is to set the weighting function $w(\mathbf{x})$ as Dirac functions δ on all nodes belonging to the fine mesh side of the interface. This connection type is referred to as collocation and can be expressed point-wise for the interface nodes corresponding to the fine mesh as

$$\mathbf{u}_{\text{ind},i}^f = \mathbf{u}_{\text{ind},i'}^c, \quad i = 1, 2, \quad (5.3a)$$

$$\mathbf{u}_{\text{dep},i}^f = \mathbf{u}^c(\mathbf{x}_i), \quad i = 1, nf. \quad (5.3b)$$

The subscript ind refers to the independent nodes, namely nodes that have a corresponding node along the boundary of the adjacent domain. The nf nodes at the interface Γ_1^{cf} , related to the fine resolution and without a corresponding node at the adjacent coarse domain, are considered as dependent and are indicated by the dep subscript (see top part of Figure 5.2). In the present implementation no redundancies are considered when enforcing the interscale constraints, and all dependent DOFs \mathbf{u}^f of the fine domain are linked to independent DOFs within the same domain. In this manner, the constraints for the dependent nodes at the interface can be recast in a matrix form as (cf. (4.4))

$$\mathbf{C}_{nf \times n} \mathbf{u}^f = \mathbf{0}. \quad (5.4)$$

For convenience we use the same notation for \mathbf{C} as in (4.4). Assuming no redundancies in the set of LMPCs, Eq. (4.4) is still valid if the rows concerning the redundant constraints are nullified. The matrix \mathbf{C} for the fine domain is built considering the shape functions of the coarse domain restricted onto the interface and contains a number of rows equivalent to the number of dependent DOFs that belong to the fine mesh nf . The number of

5.1 General strong and weak micro-macro connections

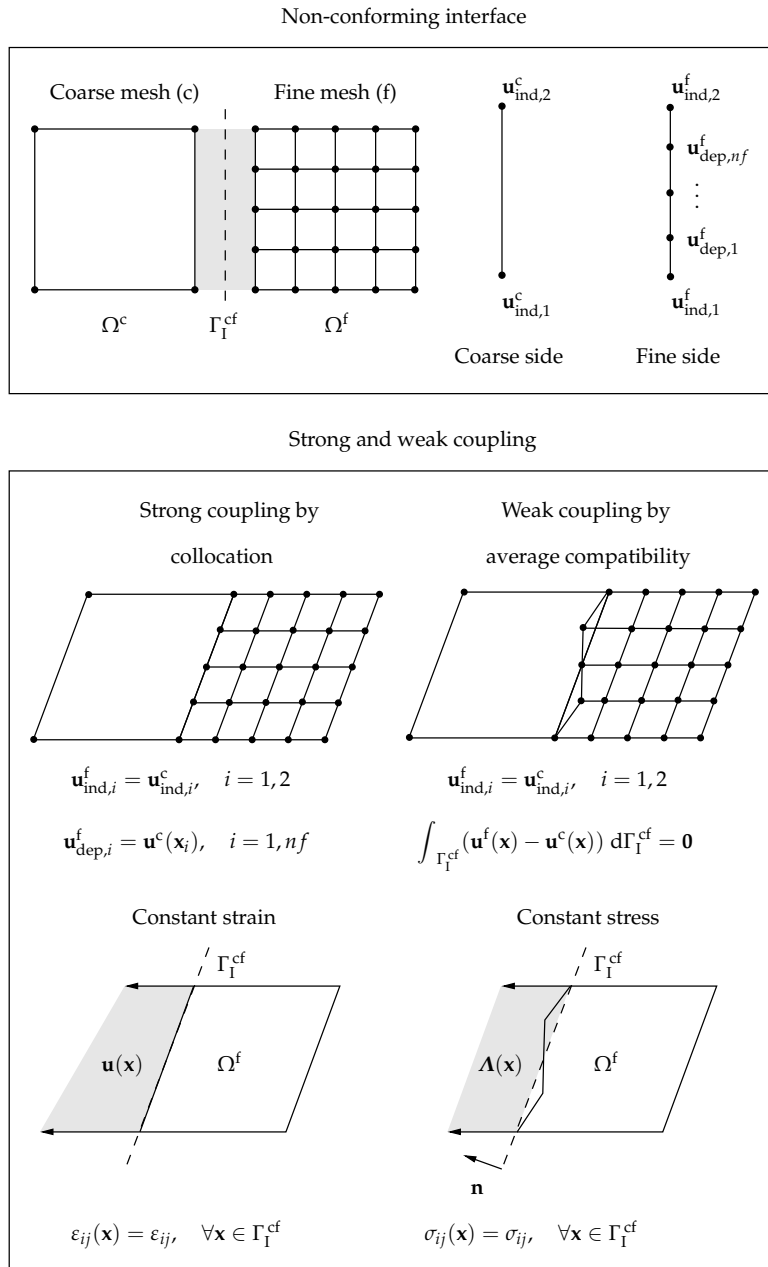


Figure 5.2 Strong and weak micro-macro connections.

columns of \mathbf{C} is equal to the total number of DOFs of the fine domain n as indicated in (5.4). The domain constraint matrix $\mathbf{C}^{(s)}$ is incorporated into the domain Boolean matrix $\mathbf{B}^{(s)}$ in order to form the extended Boolean matrix $\bar{\mathbf{B}}^{(s)}$ (cf. (4.5)).

The distribution of strains at the interface reads

$$\varepsilon_{ij}(\mathbf{x}) = \frac{1}{2} \left[\frac{\partial u_i(\mathbf{x})}{\partial x_j} + \frac{\partial u_j(\mathbf{x})}{\partial x_i} \right] \quad \forall \mathbf{x} \in \Gamma_I^{\text{cf}}. \quad (5.5)$$

If linear triangular elements or bilinear quadrilateral elements are chosen, the displacement field becomes uniform along the interface Γ_I^{cf} (Figure 5.2 bottom). The corresponding strain tensor components become constant due to the linear nature of the displacement field and (5.5) can be re-written as

$$\varepsilon_{ij}(\mathbf{x}) = \varepsilon_{ij} \quad \forall \mathbf{x} \in \Gamma_I^{\text{cf}}. \quad (5.6)$$

Clearly, this approach is equivalent to the constant strain assumption developed in classical homogenization theory.

5.1.2 Average compatibility constraints

The family of methods obtained for a variety of continuous weight functions $w(\mathbf{x})$ is referred to as mortar methods [8]. In the sequel the weight function is set to a constant which is an adequate choice for the case of linear shape functions as argued in [4]. The weak interscale constraint adopted in this study consists in satisfying exact compatibility at independent nodes and average compatibility at the dependent nodes. This interscale constraint is referred to as average compatibility. The constraints between independent and dependent nodes for the case of an average compatibility interface can be expressed as

$$\mathbf{u}_{\text{ind},i}^{\text{f}} = \mathbf{u}_{\text{ind},i'}^{\text{c}} \quad i = 1, 2, \quad (5.7a)$$

$$\int_{\Gamma_I^{\text{cf}}} (\mathbf{u}^{\text{f}}(\mathbf{x}) - \mathbf{u}^{\text{c}}(\mathbf{x})) \, d\Gamma_I^{\text{cf}} = \mathbf{0}. \quad (5.7b)$$

The set of constraints for all dependent fine nodes at the interface can also be written in a matrix form as

$$\mathbf{C}_{n\Gamma_I^{\text{cf}} \times n} \mathbf{u}^{\text{f}} = \mathbf{0}. \quad (5.8)$$

Note that the number of rows of \mathbf{C} is now equal to the number of coarse-fine interfaces $n\Gamma_I^{\text{cf}}$. This is an important issue to bear in mind since the average

compatibility involves a lower number of LMPCs and this translates into a computationally cheaper interface problem.

The weak form of the interface compatibility at Γ_I^{cf} reads

$$\int_{\Gamma_I^{\text{cf}}} \Lambda(\mathbf{x})(\mathbf{u}^f(\mathbf{x}) - \mathbf{u}^c(\mathbf{x})) \, d\Gamma_I^{\text{cf}} = \mathbf{0}, \quad (5.9)$$

where $\Lambda(\mathbf{x})$ represents the distributed tying forces at the interface. In this view, the average compatibility in (5.7b) can be recovered by setting a constant distribution of Lagrange multipliers $\Lambda(\mathbf{x})$ at Γ_I^{cf} . Consequently, the equilibrium equation at the interface can be expressed as

$$\Lambda_i = \sigma_{ij}(\mathbf{x})n_j = \sigma_{ij}n_j \quad \forall \mathbf{x} \in \Gamma_I^{\text{cf}}. \quad (5.10)$$

Considering that both the Lagrange multiplier components Λ_i and the normal vector components n_j are constant along the interface Γ_I^{cf} , the components of the Cauchy stress tensor σ_{ij} on the face of the interface become constant as well. For this reason, one can draw a parallelism between the adopted average compatibility constraint and the constant stress assumption in classical homogenization (see Figure 5.2 bottom).

The set of LMPCs involved in (5.7) can be interpreted from a micro-macro point of view as argued by Amini et al. [4]. To this end, the displacement field of the fine mesh restricted to the interface is decomposed into a macroscopic $\mathbf{u}^{\text{f,M}}(\mathbf{x})$ and a microscopic part $\mathbf{u}^{\text{f,m}}(\mathbf{x})$ as

$$\mathbf{u}^f(\mathbf{x}) = \mathbf{u}^{\text{f,M}}(\mathbf{x}) + \mathbf{u}^{\text{f,m}}(\mathbf{x}) \quad \forall \mathbf{x} \in \Gamma_I^{\text{cf}}. \quad (5.11)$$

Expressing the macroscopic part of $\mathbf{u}^f(\mathbf{x})$ as the interpolation of the coarse field at the fine mesh nodes of the interface one obtains

$$\mathbf{u}^{\text{f,M}}(\mathbf{x}) = \mathbf{u}^c(\mathbf{x}) \quad \forall \mathbf{x} \in \Gamma_I^{\text{cf}}. \quad (5.12)$$

The combination of (5.3) and (5.12) together with the micro-macro split in (5.11) yields to

$$\mathbf{u}^{\text{f,m}}(\mathbf{x}) = \mathbf{0} \quad \forall \mathbf{x} \in \Gamma_I^{\text{cf}}. \quad (5.13)$$

Consequently, the use of collocation at the interface is equivalent to set the microscopic fluctuation field to zero. In the case of average compatibility, the microscopic fluctuation field at the interface reads

$$\int_{\Gamma_I^{\text{cf}}} \mathbf{u}^{\text{f,m}}(\mathbf{x}) \, d\Gamma_I^{\text{cf}} = \mathbf{0} \quad \forall \mathbf{x} \in \Gamma_I^{\text{cf}}, \quad (5.14)$$

which is equivalent to state that the microscopic field is in average canceled at the interface but can be locally different from zero.

5.2 Modified collocation techniques

The formulation of standard collocation techniques [10, 91] is here revised in order to introduce the concept of partial collocation techniques which is proposed as a new micro-macro connection in concurrent multiscale analysis. Partial collocation techniques arise from an orthogonal decomposition of the full (or standard) collocation constraint introduced in Section 5.1.1 through (5.3).

Let us consider the interface Γ_I^{cf} between a coarse and fine mesh as depicted in Figure 5.2 (top). Full collocation of the dependent (dep) nodes is defined as

$$\mathbf{u}_{\text{dep},i}^{\text{f,col}} \stackrel{\text{def}}{=} \mathbf{u}^c(\mathbf{x}_i) = \sum_{j=1}^2 \mathbf{H}_{\text{ind},j}^c(\mathbf{x}_i) \mathbf{u}_{\text{ind},j}^c, \quad i = 1, nf. \quad (5.15)$$

The shape functions of the coarse mesh independent (ind) nodes $\mathbf{H}_{\text{ind},j}^c$ are used to interpolate the value of the fine mesh displacement $\mathbf{u}_{\text{dep},i}^{\text{f,col}}$. These shape functions are expressed using the initial position \mathbf{x}_0 of the independent nodes. The final position \mathbf{x} in the deformed configuration reads

$$\mathbf{x} = \mathbf{x}_0 + \mathbf{u}. \quad (5.16)$$

Note that the above expression relates to a large deformation setting. For the case of small deformations, which is adopted in our numerical examples, (5.16) reads

$$\mathbf{x} \approx \mathbf{x}_0. \quad (5.17)$$

Defining the deviation from the collocation constraint as

$$\left[\mathbf{u}_{\text{dep},i}^{\text{f}} \right]^{\text{col}} \stackrel{\text{def}}{=} \mathbf{u}_{\text{dep},i}^{\text{f,col}} - \mathbf{u}_{\text{dep},i}^{\text{f}}, \quad i = 1, nf, \quad (5.18)$$

full collocation is satisfied when

$$\left[\mathbf{u}_{\text{dep},i}^{\text{f}} \right]^{\text{col}} = \mathbf{0}, \quad i = 1, nf. \quad (5.19)$$

Figure 5.3 illustrates the definition of $\left[\mathbf{u}_{\text{dep},i}^{\text{f}} \right]^{\text{col}}$. Note that (5.19) requires the addition of a constraint equation for each dependent DOF.

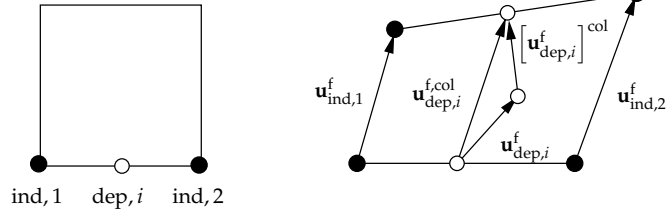


Figure 5.3 Deviation from the collocation constraint $[\mathbf{u}_{\text{dep},i}^f]^{\text{col}}$.

Partial collocation arises from the decomposition of the deviation from the collocation constraint $[\mathbf{u}_{\text{dep},i}^f]^{\text{col}}$ into the components normal and tangential to the deformed boundary of the coarse mesh. In a two-dimensional setting and using linear or bilinear elements for the coarse mesh, the tangential, \mathbf{s} , and normal, \mathbf{n} , directions are defined as

$$\mathbf{s} = \mathbf{x}_{\text{ind},2} - \mathbf{x}_{\text{ind},1}, \quad \text{and} \quad \mathbf{n} = \begin{bmatrix} -s_y \\ s_x \end{bmatrix}. \quad (5.20)$$

Consequently, the unit tangential and normal vectors read

$$\hat{\mathbf{s}} = \frac{\mathbf{s}}{\|\mathbf{s}\|}, \quad \text{and} \quad \hat{\mathbf{n}} = \frac{\mathbf{n}}{\|\mathbf{n}\|}. \quad (5.21)$$

Note that higher order Lagrangian elements can also be considered. However, the enforcement of these constraints turns to be mathematically more involved due to the expression of the corresponding tangential and normal vectors.

As shown in Figure 5.4, the deviation from the collocation constraint can be decomposed into its orthogonal components as

$$[\mathbf{u}_{\text{dep},i}^f]^{\text{col}} = \left([\mathbf{u}_{\text{dep},i}^f]^{\text{col}} \cdot \hat{\mathbf{n}} \right) \hat{\mathbf{n}} + \left([\mathbf{u}_{\text{dep},i}^f]^{\text{col}} \cdot \hat{\mathbf{s}} \right) \hat{\mathbf{s}}, \quad (5.22)$$

$i = 1, nf.$

5.2.1 Normal collocation

Normal collocation is defined as a partial collocation technique in which the normal component of the deviation is nullified. The corresponding con-

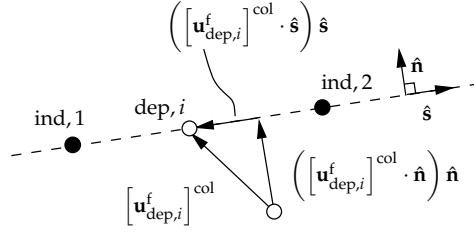


Figure 5.4 Orthogonal decomposition of the deviation from the collocation constraint $[\mathbf{u}_{\text{dep},i}^f]^{\text{col}}$.

straint equation can be therefore written as

$$[\mathbf{u}_{\text{dep},i}^f]^{\text{col}} \cdot \mathbf{n} = 0, \quad i = 1, nf. \quad (5.23)$$

Physically, this is equivalent to state that the coarse and fine interfaces are conforming in terms of the resulting deformed geometry. However, the dependent nodes are now free to slide along the tangential direction $\hat{\mathbf{s}}$ of the deformed coarse mesh. This extra freedom permits the development of solution field gradients at the interface that cannot be captured by the coarse mesh shape functions. In this way, the interface stiffness is not overestimated as it typically occurs when using a full collocation technique on a highly heterogeneous interface (with heterogeneities placed along the interface). In other words, the constant strain distribution in the tangential direction along the heterogeneous interface is avoided when normal collocation is employed and high stresses do not develop at the stiffer interface regions.

5.2.2 Tangential collocation

Tangential collocation is equivalently defined as a partial collocation technique in which the tangential component of the deviation is nullified. Its corresponding constraint equation can be written as

$$[\mathbf{u}_{\text{dep},i}^f]^{\text{col}} \cdot \mathbf{s} = 0, \quad i = 1, nf. \quad (5.24)$$

Geometrically, this condition enforces a dependent node to move along the direction $\hat{\mathbf{n}}$ normal to the deformed coarse segment and passing through $\mathbf{u}_{\text{dep},i}^{\text{f,col}}$. Since this constraint is difficult to justify from a physical point of view, it is only introduced for completeness and will not be further considered.

5.2 Modified collocation techniques

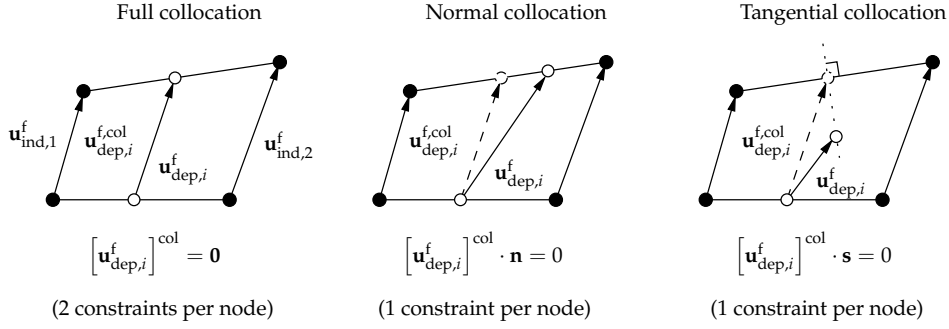


Figure 5.5 Two-dimensional full, normal and tangential collocation techniques.

Figure 5.5 illustrates the difference between full, normal and tangential collocation techniques. Note that the enforcement of partial collocation techniques, as shown in (5.23) and (5.24), requires the addition of only one constraint equation per dependent node.

The formulation of partial collocation techniques is valid for large and small deformation settings provided that the right choice of \mathbf{x} is adopted in the construction of the normal and tangential vectors (refer to Eqs. (5.16) and (5.17)).

Partial collocation techniques can easily be generalized to a three-dimensional plane surface by considering one normal, \mathbf{n} , and two tangential, \mathbf{s}_1 and \mathbf{s}_2 , surface vectors.

5.2.3 Implementational aspects

The matrix containing all constraints related to the deviation from a full collocation condition is denoted by $[\mathbf{C}]$ as in (5.15). The matrix form for a full collocation constraint reads

$$[\mathbf{C}] \mathbf{u} = \mathbf{0}. \quad (5.25)$$

Considering an incremental formulation at pseudo-time step t and iteration k the total displacement $\mathbf{u}^{t,k+1}$ can be found as

$$\mathbf{u}^{t,k+1} = \mathbf{u}^{t,k} + \delta \mathbf{u}^{t,k+1}. \quad (5.26)$$

Hence, the expression in (5.25) reads for the case of an incremental formulation

$$[\mathbf{C}] \delta \mathbf{u}^{t,k+1} = -[\mathbf{C}] \mathbf{u}^{t,k}. \quad (5.27)$$

In a standard implementation using Lagrange Multipliers, the right hand side of (5.27) is assembled in the global system of equations while the matrix $[\mathbf{C}]$ is assembled in the augmented global stiffness. Note that the coefficients of $[\mathbf{C}]$ do not change within the iterations k since they are a function of the initial node locations \mathbf{x}_0 .

The collection of normal vectors \mathbf{n} related to the dependent nodes is denoted with \mathbf{N} . The linearized form of normal collocation reads as

$$\mathbf{N}^{t,k^T} [\mathbf{C}] \delta \mathbf{u}^{t,k+1} = -\mathbf{N}^{t,k^T} [\mathbf{C}] \mathbf{u}^{t,k}. \quad (5.28)$$

In a large deformation setting, the normal directions are defined using the current positions and thus depend on the displacement \mathbf{u} . However, if the displacement of the independent nodes is known a priori, $\mathbf{N}^{t,k}$ does not depend on the iteration and one can write

$$\mathbf{N}^{t^T} [\mathbf{C}] \delta \mathbf{u}^{t,k+1} = -\mathbf{N}^{t^T} [\mathbf{C}] \mathbf{u}^{t,k}. \quad (5.29)$$

In a general situation where the displacement of the independent nodes is not known, (5.28) implies that the factor \mathbf{N}^{t,k^T} of the constraint matrix $\mathbf{N}^{t,k^T} [\mathbf{C}]$ needs to be recomputed at every iteration.

Noteworthy, upon convergence at iteration $k + 1$,

$$\left\| \mathbf{u}^{t,k+1} - \mathbf{u}^{t,k} \right\| \leq \epsilon, \quad (5.30)$$

epsilon being a sufficiently small tolerance. Hence, the constraint (5.28) is equivalent to (5.29) at convergence —this is in agreement with the work of Narayanaswamy [78].

In the present multiscale FETI framework the total displacement and Lagrange multiplier fields read

$$\mathbf{u}^{t,k+1} = \mathbf{u}^{t,k} + \delta \mathbf{u}^{t,k+1}, \quad (5.31a)$$

$$\mathbf{\Lambda}^{t,k+1} = \mathbf{\Lambda}^{t,k} + \delta \mathbf{\Lambda}^{t,k+1}, \quad (5.31b)$$

with the field of Lagrange multipliers

$$\mathbf{\Lambda}^{t,k} = \begin{bmatrix} \boldsymbol{\lambda}^{t,k} \\ \boldsymbol{\mu}^{t,k} \end{bmatrix} \quad (5.32)$$

containing quantities related to independent and dependent nodes. The modified matrices $\bar{\mathbf{B}}^{(s)}$ are defined by row-wise concatenation of the constraint matrices $\mathbf{C}^{(s)}$ and the original signed Boolean matrices $\mathbf{B}^{(s)}$ as shown

5.2 Modified collocation techniques

in (4.5). The resulting linearized domain equations of the multiscale FETI framework read

$$\mathbf{K}^{(s)t,k} \delta \mathbf{u}^{(s)t,k+1} + \bar{\mathbf{B}}^{(s)\top} \delta \boldsymbol{\Lambda}^{t,k+1} = \mathbf{f}_{\text{ext}}^{(s)t} - \bar{\mathbf{B}}^{(s)\top} \boldsymbol{\Lambda}^{t,k} - \mathbf{f}_{\text{int}}^{(s)t,k}(\mathbf{u}^{(s)t,k}), \quad (5.33a)$$

$$\sum_{s=1}^{N_s} \bar{\mathbf{B}}^{(s)} \delta \mathbf{u}^{(s)t,k+1} = - \sum_{s=1}^{N_s} \bar{\mathbf{B}}^{(s)} \mathbf{u}^{(s)t,k}. \quad (5.33b)$$

If normal collocation is chosen to form the LMPCs, the constraint matrices $\mathbf{C}^{(s)}$ for load step t and iteration k read

$$\mathbf{C}^{(s)t,k} = \left(\mathbf{N}^{t,k} \right)^\top [\mathbf{C}]^{(s)}. \quad (5.34)$$

Hence, the modified matrices $\bar{\mathbf{B}}^{(s)}$ depend on step t and iteration k as

$$\left[\bar{\mathbf{B}}^{(1)t,k} \quad \dots \quad \bar{\mathbf{B}}^{(N_s)t,k} \right] = \begin{bmatrix} \mathbf{B}^{(1)} & \dots & \mathbf{B}^{(N_s)} \\ \mathbf{C}^{(1)t,k} & \dots & \mathbf{C}^{(N_s)t,k} \end{bmatrix}. \quad (5.35)$$

The global linearized equations considering normal collocation become

$$\mathbf{K}^{(s)t,k} \delta \mathbf{u}^{(s)t,k+1} + \left(\bar{\mathbf{B}}^{(s)t,k} \right)^\top \delta \boldsymbol{\Lambda}^{t,k+1} = \mathbf{f}_{\text{ext}}^{(s)t} - \left(\bar{\mathbf{B}}^{(s)t,k} \right)^\top \boldsymbol{\Lambda}^{t,k} - \mathbf{f}_{\text{int}}^{(s)t,k}, \quad (5.36a)$$

$$\sum_{s=1}^{N_s} \bar{\mathbf{B}}^{(s)t,k} \delta \mathbf{u}^{(s)t,k+1} = - \sum_{s=1}^{N_s} \bar{\mathbf{B}}^{(s)t,k} \mathbf{u}^{(s)t,k}. \quad (5.36b)$$

Note that the Jacobian in (5.36) does not correspond to the true Jacobian since the change of the normals is not accounted for in the tangent matrix—the true Jacobian can only be obtained by using $\bar{\mathbf{B}}^{(s)t,k+1}$ in (5.36) but this quantity is not known at iteration k . The use of normal collocation in such a framework involves re-computing the modified matrices $\bar{\mathbf{B}}^{(s)t,k}$ at each iteration k and the cost of the analysis increases. However, only the factor \mathbf{N}^{t,k^\top} needs to be re-assembled and the constraint matrices $\mathbf{C}^{(s)t,k}$ are computed with a matrix product. Assuming a small deformation setting, the matrix \mathbf{N}^{t,k^\top} is approximated to \mathbf{N}_0^\top and contains constant coefficients since it is computed using the initial position vector \mathbf{x}_0 . In this case, the modified matrices $\bar{\mathbf{B}}^{(s)}$ do not need to be recomputed at each iteration k .

5.3 Modified average compatibility techniques for heterogeneous interfaces

In this section a modified average compatibility condition is presented. The new constraint type differs from the one presented in Section 5.1.2 in the sense that the coarse and fine displacement fields at the interface are weighted using a scalar field based on the stiffness of the material on both sides of the interface. The weighting function can be interpreted as the Lagrange multiplier representing the stress field along the interface. Such stress field will be higher at locations where stiffer material is found. The choice of weighting functions according to interface stiffness will thus enforce a compatibility closer to the exact one. This type of average compatibility can be adequate in situations involving highly heterogeneous interfaces since the distribution of tying forces therein is not constant.

The weak compatibility with stiffness weighting reads

$$\mathbf{u}_{\text{ind},i}^f = \mathbf{u}_{\text{ind},i}^c, \quad i = 1, 2, \quad (5.37a)$$

$$\int_{\Gamma_1^{\text{cf}}} (k_j^f(\mathbf{x})u_j^f(\mathbf{x}) - k_j^c u_j^c(\mathbf{x})) \, d\Gamma_1^{\text{cf}} = 0, \quad j = 1, N_{\text{DOF}}, \quad (5.37b)$$

where N_{DOF} is the number of DOFs per node and $k_j^f(\mathbf{x})$ represents a piecewise continuous function along Γ_1^{cf} which is taken as the diagonal stiffness coefficient K_{ll} of the fine resolution domain—the index l corresponds to node i (located at \mathbf{x}) and DOF j . Conversely, k_j^c is taken as a constant stiffness coefficient which corresponds to the average value $k_j^f(\mathbf{x})$ along the fine side of the interface. Let us observe that this approach can be seen as defining higher interface forces in stiff regions, and thereby enforcing in those regions a stronger compatibility. In order to be consistent, one needs to guarantee that the interscale condition (5.37b) allows for exact compatibility. Assuming full compatibility along Γ_1^{cf} and a constant distribution of the solution field, the coarse and fine displacements read

$$\mathbf{u}^f(\mathbf{x}) = \mathbf{u}^c(\mathbf{x}) = \mathbf{u}. \quad (5.38)$$

Substituting (5.38) in (5.37b), the homogenized interface stiffness for the DOF j is found as

$$k_j^c = \int_{\Gamma_1^{\text{cf}}} k_j^f(\mathbf{x}) \, d\Gamma_1^{\text{cf}} / \int_{\Gamma_1^{\text{cf}}} d\Gamma_1^{\text{cf}}, \quad (5.39)$$

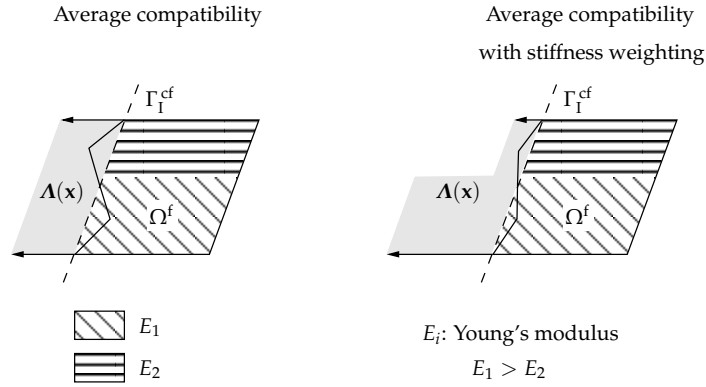


Figure 5.6 Standard and stiffness weighted average compatibility.

which is equivalent to apply classical homogenization theory to the heterogeneous interface segment Γ_I^{cf} . The expression in (5.39) guarantees that the choice of $k_j^f(\mathbf{x})$ and k_j^c correspond to a weak form of the strong compatibility. Note that the force field tying two incompatible meshes increases at stiff interface segments (Figure 5.6).

The use of stiffness weighting at the interface between two domains has been already introduced by Rixen and Farhat [98]. In their approach, stiffness weighting was introduced in order to improve the quality of the preconditioners used to construct the interface problem of heterogeneous nature. Conversely, in the present study a different version of the stiffness weighting is considered in order to provide a better set of tying forces at a heterogeneous non-conforming interface. Somewhat similar approaches have been presented in [56, 57] where the material modulus is used in the weighting. The use of stiffness coefficients in the scaling is perturbed by the FE discretization but it is capable of weighting heterogeneous solution fields independently of its nature. This is particularly convenient for the weighting of solution fields arising from the coupling of different governing equations or in the case where the weighting is subjected to the evolution of internal variables.

Numerical integration of the weak constraints along the segment Γ_I^{cf} is performed by associating a weight \tilde{w}_i to each node i . Such weights \tilde{w} are related to the metric of the element interface (an example is given in Figure 5.7). The integral expression in (5.7b) for the coarse and fine interface

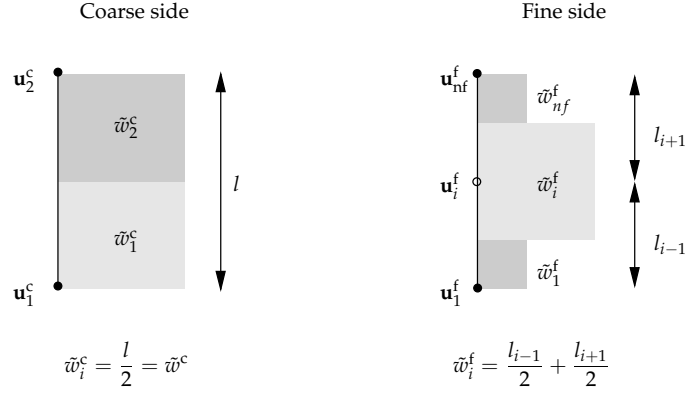


Figure 5.7 Numerical integration.

segments is computed numerically as

$$\int_{\Gamma_1^{\text{cf}}} (\mathbf{u}^f(\mathbf{x}) - \mathbf{u}^c(\mathbf{x})) \, d\Gamma_1^{\text{cf}} = \sum_{i=1}^{nf} \tilde{w}_i^f \mathbf{u}_{i,j}^f - \sum_{i=1}^2 \tilde{w}^c \mathbf{u}_{i,j}^c, \quad (5.40)$$

$j = 1, N_{\text{DOF}},$

where $\mathbf{u}_{i,j}$ refers to the displacement \mathbf{u} at node i and DOF j . For the case of average compatibility with stiffness weighting, the integral expression in (5.37b) reads

$$\begin{aligned} & \int_{\Gamma_1^{\text{cf}}} (k^f(\mathbf{x}) \mathbf{u}^f(\mathbf{x}) - k^c \mathbf{u}^c(\mathbf{x})) \, d\Gamma_1^{\text{cf}} \\ &= \sum_{i=1}^{nf} \tilde{w}_i^f k_{i,j}^f \mathbf{u}_{i,j}^f - \sum_{i=1}^2 \tilde{w}^c k_j^c \mathbf{u}_{i,j}^c, \quad j = 1, N_{\text{DOF}}, \end{aligned} \quad (5.41)$$

where it is assumed that $k_{i,j}^f = K_{ll}$, l being the position at the stiffness matrix of the fine resolution domain corresponding to node i and DOF j . The value of k_j^c is determined as

$$k_j^c = \frac{\sum_{i=1}^{nf} \tilde{w}_i^f k_{i,j}^f}{\sum_{i=1}^{nf} \tilde{w}_i^f}. \quad (5.42)$$

5.4 Mechanical characterization of the interscale links

In order to assess the performance of different interscale constraints the tension test sketched in Figure 5.8 (top) is conducted on a linear elastic heterogeneous solid. The structure is decomposed in two domains with different spatial resolutions and material distributions (Figure 5.8 (middle and bottom)). Domain $\Omega^{(1)}$ constitutes a homogeneous bulk while domain $\Omega^{(2)}$ is formed by two layers of soft and stiff material, respectively. The ratio between stiff and soft material Young's modulus

$$\kappa = \frac{E_{\text{stiff}}}{E_{\text{soft}}}, \quad \kappa \geq 1. \quad (5.43)$$

The behaviour of the interscale constraints is studied for a homogeneous interface ($\kappa = 1$) and for a highly heterogeneous interface ($\kappa = 10^5$). Effective elastic properties for the coarse bulk are given using the constant strain Voigt's assumption

$$\mathbf{D}^{\text{eff}} = \sum_{i=1}^{N_{\text{phase}}} v_i \mathbf{D}_i, \quad (5.44)$$

where \mathbf{D} , v and N_{phase} denote the elastic tensor, the volume fraction of the phase and the total number of phases, respectively.

The uniaxial strength of the sample

$$K_1 = \frac{f_1}{u_1}, \quad (5.45)$$

f_1 and u_1 being the resultant horizontal reaction and the applied displacement at the right boundary, respectively. The resulting uniaxial strength is compared to a reference value K_1^{ref} obtained by considering the heterogeneous material distribution and FE discretization assigned to $\Omega^{(2)}$ throughout the whole sample. In this view, the relative error in the uniaxial strength

$$e_K = \frac{K_1 - K_1^{\text{ref}}}{K_1^{\text{ref}}}. \quad (5.46)$$

Table 5.1 shows the uniaxial strength error e_K for the homogeneous and heterogeneous analyses with different interscale constraints.

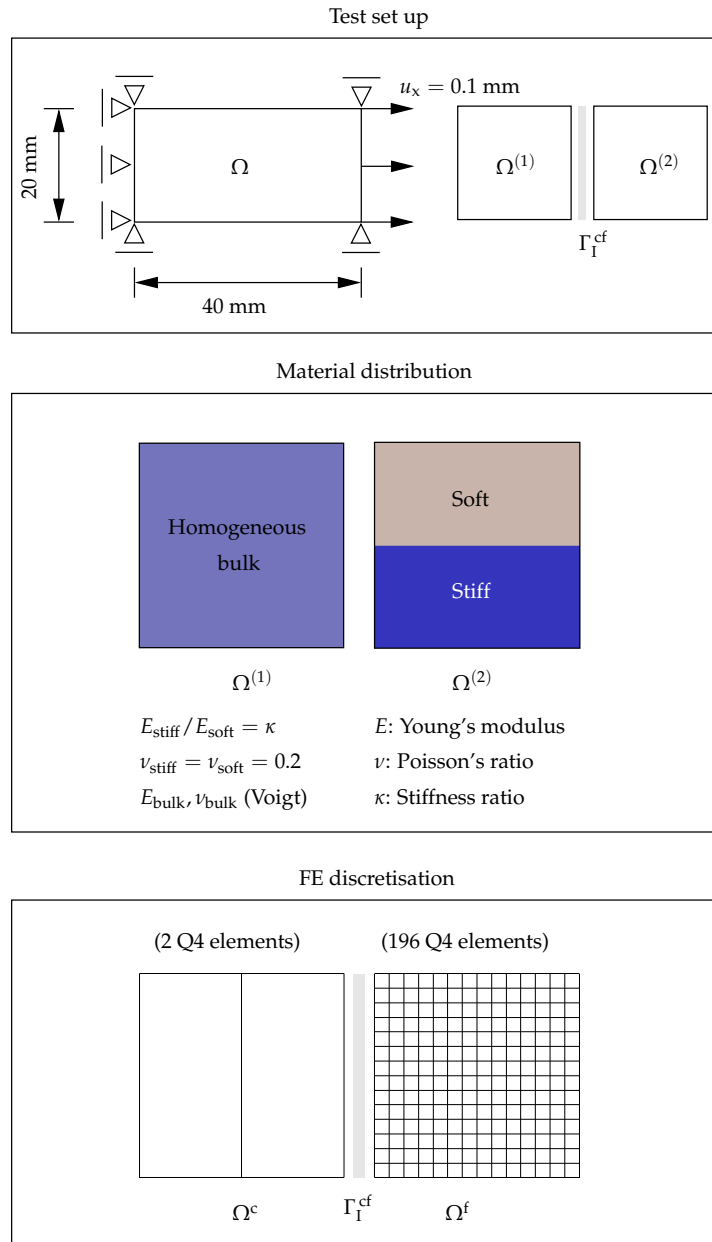


Figure 5.8 Boundary conditions and domain decomposition (top). Material distribution (middle). FE discretization (bottom).

5.4 Mechanical characterization of the interscale links

Analysis	Full coll.	Normal coll.	Av. comp.	Stiff. weight.
$\kappa = 1$	0.4021	0.4020	0.4019	0.4019
$\kappa = 10^5$	-11.5896	-12.5126	-76.2915	0.8171

Table 5.1 Uniaxial strength error e_K (%) for different interscale constraints.

In general, strong compatibility techniques provide a stiffer link than average compatibility techniques. Moreover, full collocation constraints behave slightly stiffer than normal collocation constraints for all homogeneous tests ($\kappa = 1$). In the heterogeneous tests ($\kappa = 10^5$), full collocation behaves stiffer than normal collocation but both provide a uniaxial strain which is around 10% lower than the reference value. As shown in Figure 5.9, the strong interscale constraints induce a higher deformation at the upper (soft) layer which softens the overall response. The same effect is magnified for the case of average compatibility conditions where the soft layer undergoes excessive deformation while the stiff layer is only deformed around the lower left corner where the material is glued to the coarse bulk. The results obtained with the stiffness weighting constraints are remarkably improved. The stiffness-based weight is able to transfer a higher interface force to the stiff material and, therefore, induce a uniform deformation along the horizontal axis.

The force distributions at the heterogeneous interface Γ_1^{cf} are depicted in Figure 5.9. A stiffness ratio $\kappa = 10^1$ is selected here in order to be able to visualize properly the difference in magnitude between forces acting at dependent and independent nodes. It can be observed that the force distributions given by full and normal collocation differ in the sense that only the horizontal component (normal to Γ_1^{cf}) is present for the normal collocation constraint. However, the differences are not very noticeable since the horizontal force is dominating in this example. It is worth noting that a uniform force distribution is acting at all dependent nodes when using the average compatibility technique. The interface force field given by the stiffness weighting is clearly higher in magnitude at the interface regions constituted by a stiffer material.

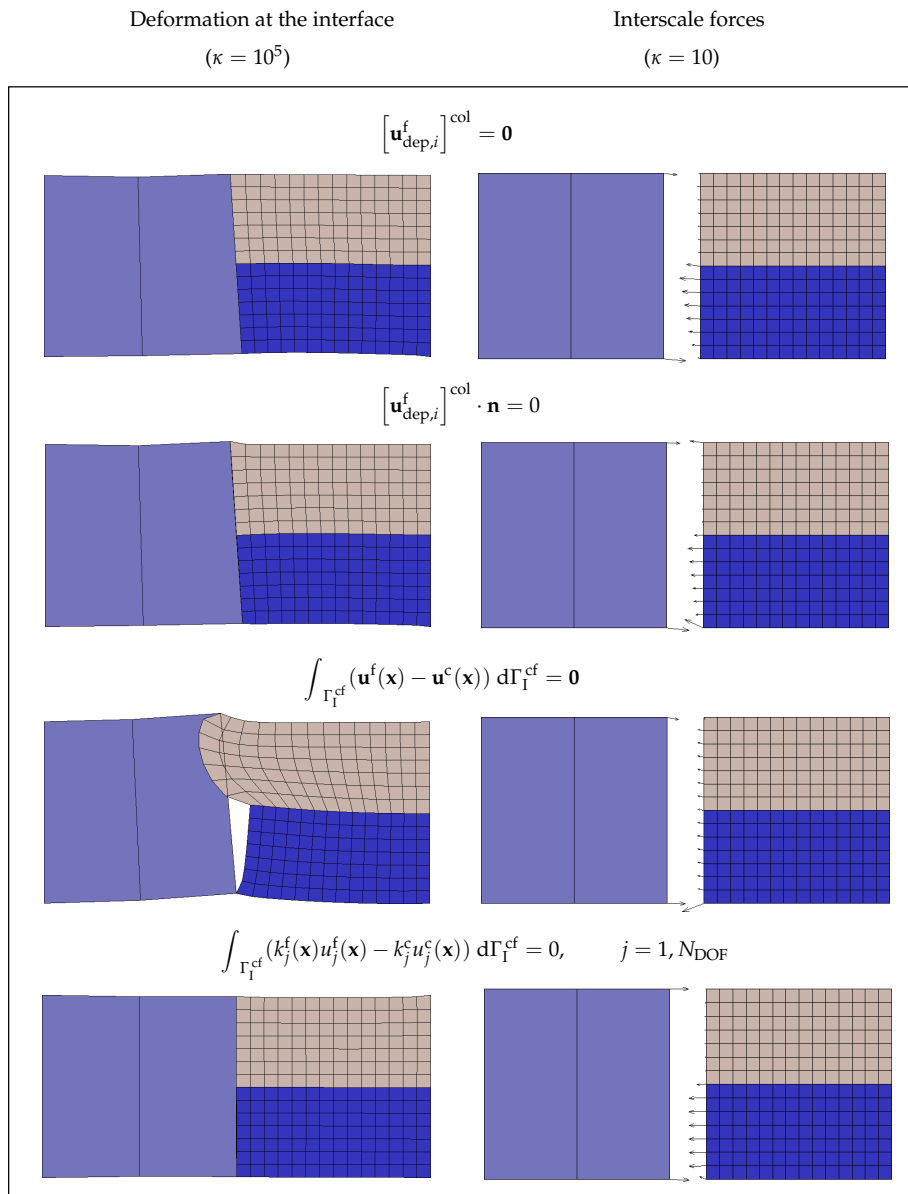


Figure 5.9 Left: Deformation configurations for the heterogeneous interface ($\kappa = 10^5$) using different interscale constraints. 25 \times displacement magnification. Right: Force distributions at the heterogeneous interface Γ_1^{cf} ($\kappa = 10$) using different interscale constraints.

5.5 Numerical examples

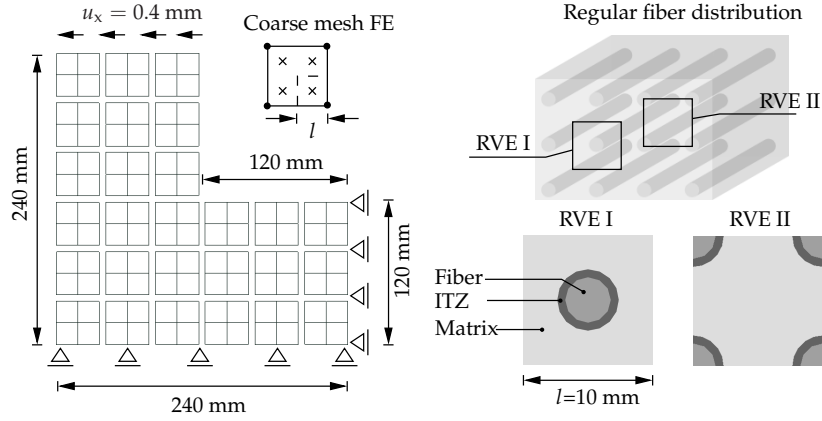


Figure 5.10 L-shaped concrete specimen: boundary conditions (left) and selected RVE for effective properties (right)

5.5 Numerical examples

In this section a series of multiscale analyses are performed on the L-shaped concrete specimen shown in Figure 5.10. The specimen is meshed using a coarse discretization and partitioned into 27 regular domains. Effective properties are retrieved by means of computations over an RVE of the underlying mesostructure. The relation $A_{RVE} = A_{ip}^c$, which is a particular case of the relation $A_{RVE} \leq A_{ip}$, is used in order to limit the cost of the multiscale analysis.

Crack nucleation and propagation is simulated by means of a gradient-enhanced damage model [87] (cf. Appendix A). In order to reproduce tensile failure, the equivalent strain definition proposed by Mazars and Pijaudier-Cabot [70] is adopted. The evolution of damage ω is expressed in terms of the monotonically increasing deformation history parameter κ . In the present analyses, an exponential damage evolution law [87] is adopted — this damage law is function of the model parameters α and β representing the residual stress level at high strains and the softening rate parameter, respectively. As discussed in [64, 65], the non-local equivalent strain $\tilde{\epsilon}_{nl}$ is adopted as the internal variable. Its representative value for each domain is denoted by $\tilde{\epsilon}_{nl}^{(s)}$. The activation of a zoom-in in a domain $\Omega^{(s)}$ is dictated by the presence of non-linearity which is anticipated by evaluating the domain loading function. This function is analogous to the standard loading function of the damage model in terms of the domain equivalent strain $\tilde{\epsilon}_{nl}^{(s)}$ and

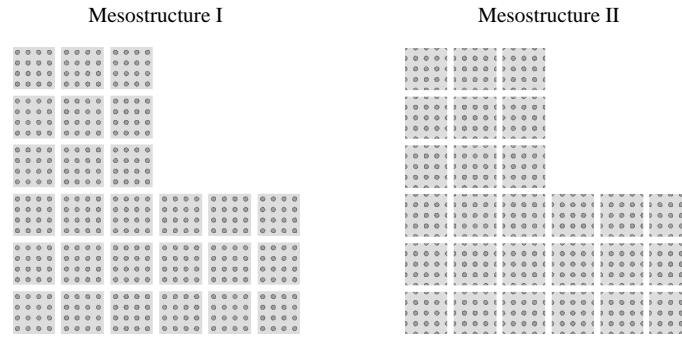


Figure 5.11 Fine scale decomposition according to mesostructures I and II.

history parameter $\kappa^{(s)}$.

The non-local equivalent strain $\tilde{\epsilon}_{nl}$ is treated as an extra DOF in the gradient-enhanced damage model. For this reason, its continuity at domain interfaces is automatically enforced in a domain decomposition framework.

In the next analyses a concrete specimen with regularly distributed heterogeneities is studied. Two RVE arrangements are considered as illustrated in Figure 5.10 (right). They are connected to the mesostructures depicted in Figure 5.11. Mesostructure I is designed such that it contains all heterogeneities inside the RVE and the corresponding fine scale domains. However, in mesostructure II the heterogeneities are partly included in the RVE and in the corresponding fine domains –this leads to a heterogeneous interface between different domains.

The following results are reported in order to investigate the influence of the mesostructure on the multiscale analysis, the influence of the micro-to-macro connection on the different mesostructures, and the effect of the position of dependent and independent nodes at the heterogeneous interface. The analyses are performed considering a concrete matrix containing a number of stiff inclusions such as steel reinforcement. A brittle interface transition zone (ITZ) between the reinforcement and the matrix is introduced in order to model debonding of the fibers (Figure 5.10). Damage growth at the steel fibers is prevented by using an artificially large damage initiation strain threshold κ_0 since the gradient-enhanced damage is adopted for all material phases. The selected material data are listed in Table 5.2.

5.5 Numerical examples

Material parameters		Fibers	ITZ	Matrix	Coarse bulk
E	[N/mm ²]	20.0×10^4	20.0×10^3	40.0×10^3	Effective
ν	[–]	0.2	0.2	0.2	Effective
$\tilde{\epsilon}_{nl}$	[–]	Mazars	Mazars	Mazars	Mazars
κ_0	[–]	Dummy	5.0×10^{-5}	8.5×10^{-5}	5.0×10^{-5}
c	[mm ²]	1.5	1.5	1.5	1.5
$\omega(\kappa)$	[–]	Exponential	Exponential	Exponential	[–]
α	[–]	0.999	0.999	0.999	[–]
β	[–]	400	400	400	[–]
Two-dimensional analysis type				Plane strain	

Table 5.2 Material parameters.

5.5.1 Influence of the mesostructure on the multiscale analysis

Collocation is adopted in this example as the micro-to-macro connection method for both the zoom-in events and the link between coarse and fine scale domains. Displacement compatibility is, therefore, encountered during the whole deformation process and the damage field representing the fracture processes shows continuity at the interface between domains. The amount of refined domains varies according to the damage evolution. Different domain mesostructures give rise to different strain increments which influence the prediction of non-linearities at neighboring domains. Therefore, the amount of fine domains (and their spatial distribution) for both mesostructures at ultimate damage stages is similar but not equal (Figure 5.12). The choice of the effective elastic properties for the bulk influences the mechanical response of the multiscale analysis as seen in Figures 5.13 and 5.14. Note that the light gray area corresponds to the region representing the spread between the different multiscale analyses. Analytical effective properties typically provide a less accurate guess than the one resulting from computational homogenization procedures. This difference is more evident for mesostructure II (see close-up in Figure 5.14). This is because the boundary conditions adopted in the computational homogenization scheme are sensitive to the nature of the boundary. The homogenized mechanical behaviour of an RVE with heterogeneous boundary is expected to be more sensitive to the mechanical properties of the heterogeneities. The jumps observed in the load-displacement curves (Figures 5.13 and 5.14) are translated into a series of energy imbalances $\Delta G_{12}^{(s)}$ (4.15) which are considered in or-

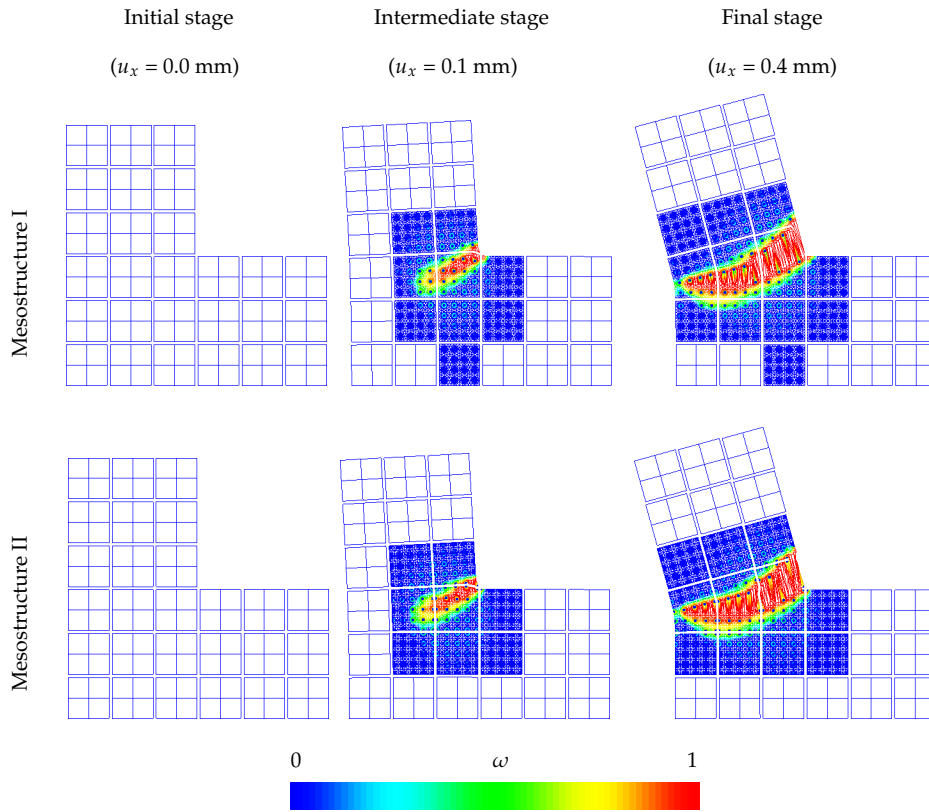


Figure 5.12 Evolution of damage growth. $10\times$ displacement magnification.

5.5 Numerical examples

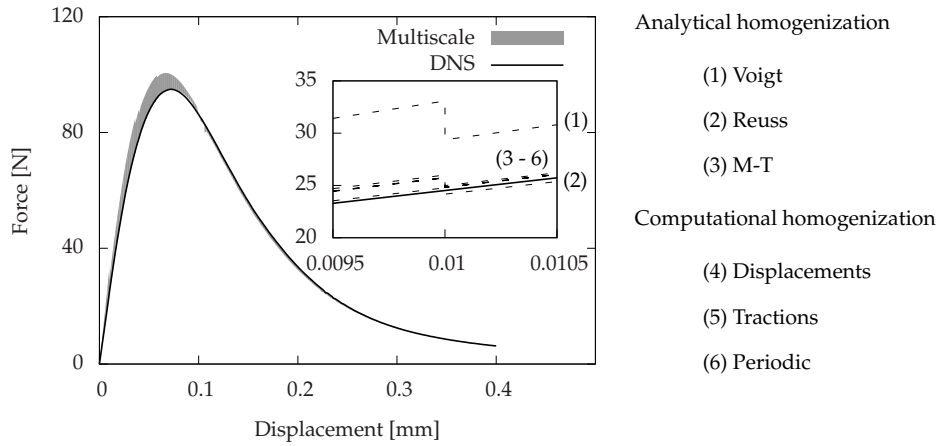


Figure 5.13 Load-displacement curves for the direct numerical simulation (DNS) and multiscale analysis based on mesostructure I. The inset shows the close-up of the load-displacement curve around a zoom-in event. Depending on the homogenization assumption for the bulk, different curves are obtained. The coarse-fine compatibility constraints are enforced by collocation.

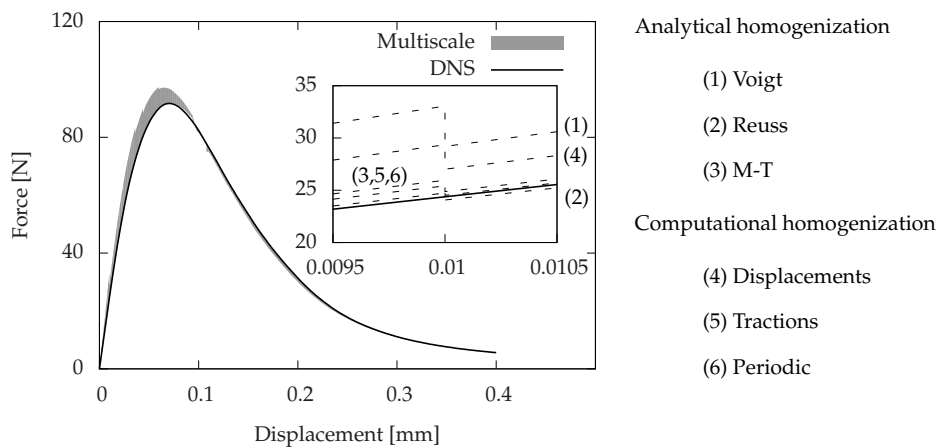


Figure 5.14 Load-displacement curves for the direct numerical simulation (DNS) and multiscale analysis based on mesostructure II. The inset shows the close-up of the load-displacement curve around a zoom-in event. Depending on the homogenization assumption for the bulk, different curves are obtained. The coarse-fine compatibility constraints are enforced by collocation.

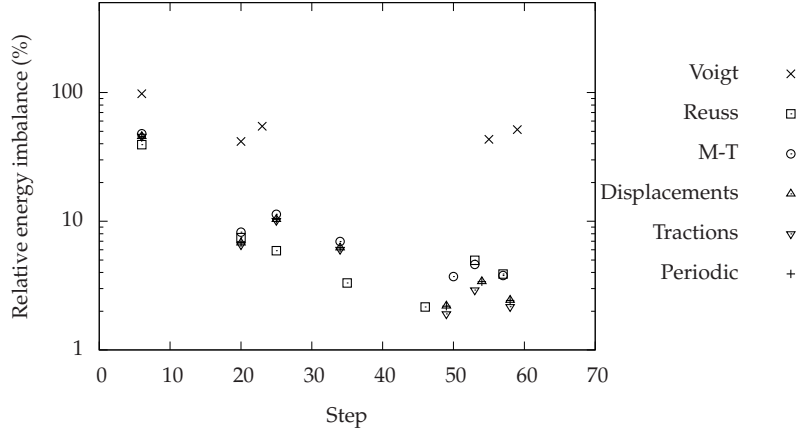


Figure 5.15 Evolution of relative energy imbalance $G_{r_{12}}^{(s)}$ after the zoom-in episodes for mesostructure I. One step is equivalent to a displacement increment of 2×10^{-3} mm.

der to monitor the evolution of energy jumps during the analysis. If more than one domain is affected by the zoom-in, the maximum of the relative energies $G_{r_{12}}^{(s)}$ is taken into account (see Figure 4.5).

Figures 5.15 and 5.16 evidence a gain in performance when computational homogenization schemes are used instead of analytical bounds. As argued in [65], high values of $\Delta G_{r_{12}}^{(s)}$ at the first zoom-in event can be explained by the fact that the initial coarse mesh is slightly too coarse to capture the linear solution field with a high accuracy. This effect vanishes after the zoom-in events that take place near the re-entrant corner. The energy jumps and the load-displacement curves obtained for mesostructure II show a larger spread in results.

The deviation between the multiscale response and the one obtained with a DNS is investigated by monitoring the error in the displacement and damage fields. The absolute, E_u , and relative, e_u , errors in the magnitude of the displacement field $\|\mathbf{u}\|_2$ between DNS and multiscale (Mult) analysis read

$$E_u = \|\mathbf{u}_{\text{DNS}}\|_2 - \|\mathbf{u}_{\text{Mult}}\|_2, \quad (5.47)$$

$$e_u = \frac{\|\mathbf{u}_{\text{DNS}}\|_2 - \|\mathbf{u}_{\text{Mult}}\|_2}{\|\mathbf{u}_{\text{DNS}}\|_2}, \quad (5.48)$$

with $\|\square\|_2$ being the Euclidean norm. The absolute error in the damage field

5.5 Numerical examples

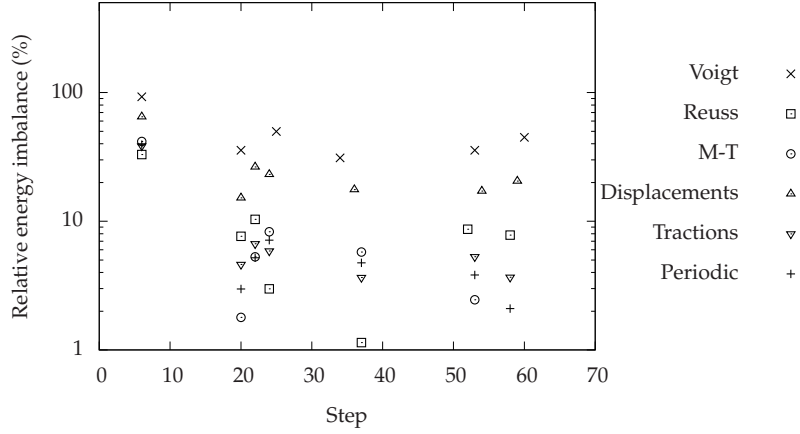


Figure 5.16 Evolution of relative energy imbalance $G_{r_{12}}^{(s)}$ after the zoom-in episodes for mesostructure II. One step is equivalent to a displacement increment of 2×10^{-3} mm.

can be computed as

$$E_\omega = |\omega_{\text{DNS}} - \omega_{\text{Mult}}|, \quad 0 \leq E_\omega \leq 1. \quad (5.49)$$

Both DNS and multiscale fields are compared at nodal points that correspond to each other. In those domains that are represented by a coarse resolution, the error is only computed at nodes which have a corresponding node in the fine scale resolution. Figure 5.17 clearly shows that both E_u and e_u decrease when the apparent properties are closer to the real effective properties [108]. Locally high values of the relative error e_u , which do not correspond to high values of the absolute error E_u , are observed —this is often encountered where the norm $\|\mathbf{u}_{\text{DNS}}\|_2$ of the displacement field is very low. The quality of the effective properties also influences the error in the damage evolution (Figure 5.18). The values of E_ω are lower and less spread when higher quality effective properties are adopted. However, a local error concentration is observed at the crack tip for mesostructure I. This is not due to the effective properties but can be caused by a certain delay in the activation of the fine scale domains. This poses a challenge for the strain predictors since they are based on the evolution of the strain at coarse domains and, in some cases, this is not enough to predict damage initiation at a finer resolution.

An important property of the presented multiscale approach is that the error accumulated is lowered and redistributed during the zoom-in events.

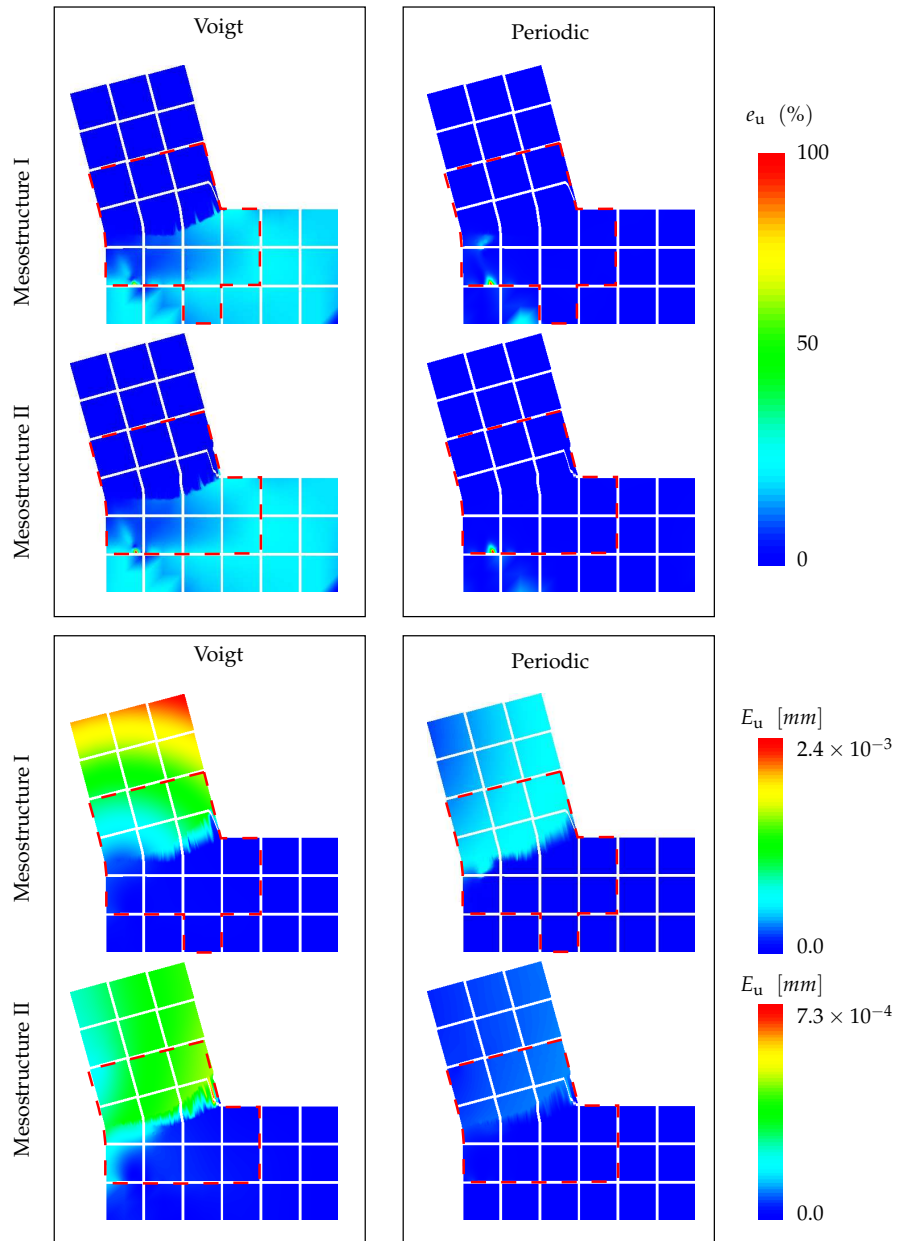


Figure 5.17 Solution field relative, e_u , and absolute, E_u , error between DNS and multiscale analyses with different effective properties for the elastic bulk. The dashed area contains fine scale domains. $10\times$ displacement magnification.

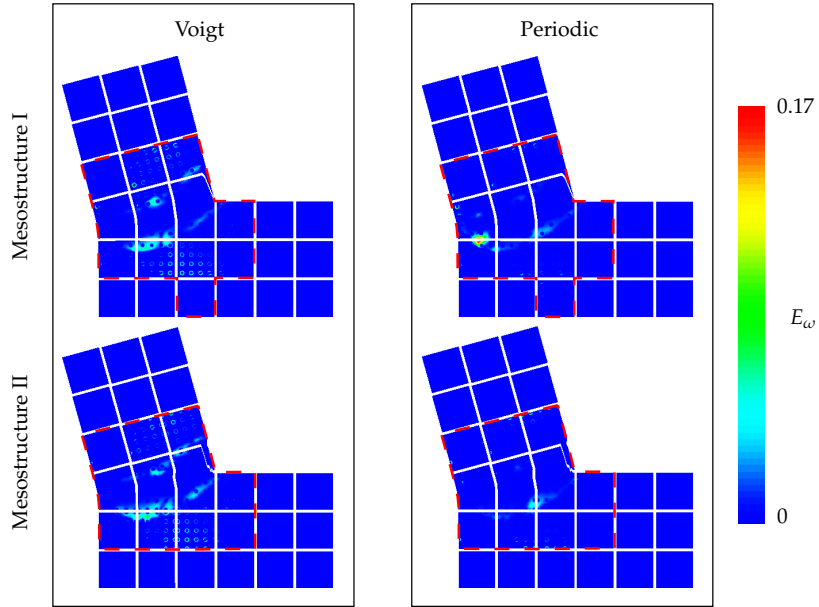


Figure 5.18 Damage field error E_ω between DNS and multiscale analyses with different effective properties for the elastic bulk. The dashed area contains fine scale domains. $10\times$ displacement magnification.

This effect is illustrated in Figure 5.19 where the distribution of e_u is plotted before and after the zoom-in of the three domains located at the re-entrant corner of the L-shape specimen. For this reason, once the fine resolutions are inserted, the multiscale response approaches the one of the DNS (Figures 5.13 and 5.14). This effect becomes obvious after the peak load where the difference between load-displacement curves diminishes.

5.5.2 Micro-macro connection and interface nature

In this section the previous L-shape specimen with steel reinforcement is reconsidered employing the most accurate choice of the effective properties (computational homogenization with periodic boundary conditions). The focus is now on the effectiveness of the micro-to-macro connection, i.e. collocation, average compatibility, normal collocation and average compatibility with stiffness weighting. The interscale constraint is selected for both concurrent multiscale analysis, i.e. the compatibility condition in (4.7), and zoom-in (see top part of Figure 4.5). As introduced in Sections 5.1 to 5.3, the

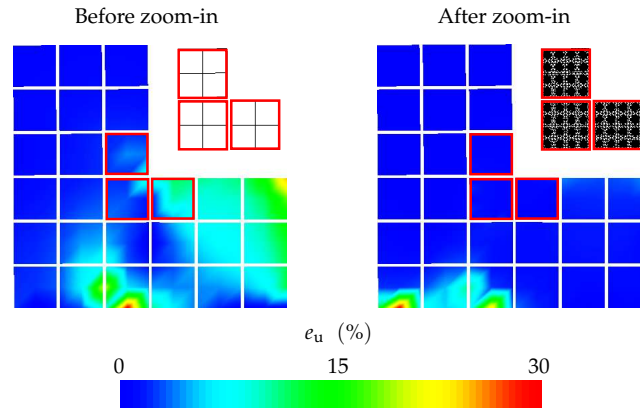


Figure 5.19 Solution field relative error e_u between DNS and multiscale analyses before and after a zoom-in event. The analysis is performed using mesostructure I. Collocation is used for the micro-macro link and effective properties based on computational homogenization (periodic boundary conditions) are utilized. $10\times$ displacement magnification.

different interscale relations adopted in this analysis are standard (or full) collocation, average compatibility, normal collocation and average compatibility with stiffness weighting.

The load-displacement curves depicted in Figures 5.20 and 5.21 show that all multiscale analyses are in very good agreement with the DNS. The magnitude of the jumps observed in the load-displacement curves is slightly smaller for the case of collocation methods. This is also evident in the energy imbalance plots which show, in general, lower energy values for the collocation interfaces (Figure 5.22). The difference between different locality constraints becomes more evident for mesostructure II where the heterogeneous boundary of the fine domains plays an important role during the zoom-in events and in the possible connection with an adjacent domain described with a different resolution. Note that the fine scale resolutions are not activated at the same time. In fact, the employed strain predictors are based on the strain development at the coarse domain. Since the collocation link is built using the coarse mesh shape functions the prediction of non-linearity is, in general, “more accurate”. When using weak constraints or modified collocated constraints, non-linearity is sometimes initiated during the zoom-in episodes.

The normal collocation constraint provides the biggest jumps in the load-displacement curves (Figures 5.20 and 5.21) and yields the softer mechanical interscale link. This behaviour is in agreement with the analyses presented

5.5 Numerical examples

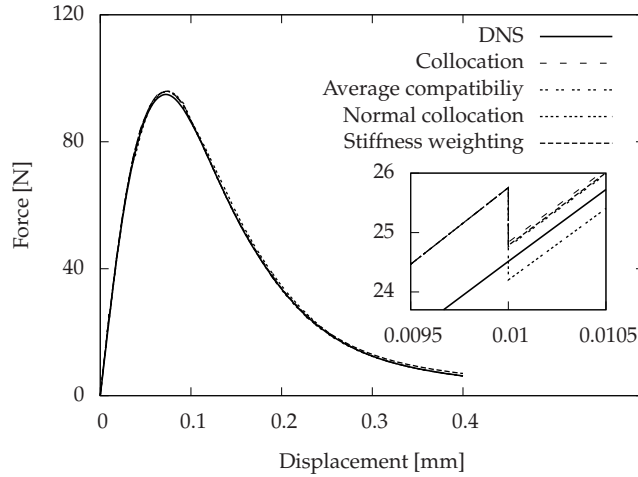


Figure 5.20 Load-displacement curves for the DNS and multiscale analysis for mesostructure I based on different micro-macro connections. The inset shows the close-up of the load-displacement curve around a zoom-in event.

in the following section. The magnitude of the jumps decreases with the average compatibility with stiffness weighting, average compatibility and collocation methods. Note that in Figure 5.21 the load-displacement curve corresponding to the average compatibility with stiffness weighting is almost indistinguishable from that of the DNS. Error distributions in displacement and damage are reported in Figures 5.23 and 5.24 for all investigated constraints. The error plots show that the multiscale analysis with collocation interface provides a better agreement with the DNS. The use of weak constraints results in a higher displacement error distribution (Figure 5.23), specially for the case of stiffness weighting. Hence, for mesostructures I and II containing stiff inclusions the field of Lagrange multipliers at non-conforming interfaces seems to be better approximated by the average compatibility interscale link.

Error distributions in the damage field (Figure 5.24) turn to be less sensitive to each of the investigated constraint although the same tendency as for e_u is observed. This indicates that the failure mechanism is well captured when using any of the proposed interscale links.

The computational cost of the interface problem is studied by monitoring the evolution of the number of degrees of freedom assembled in the interface system. This evolution is shown in Figure 5.25 in terms of the active

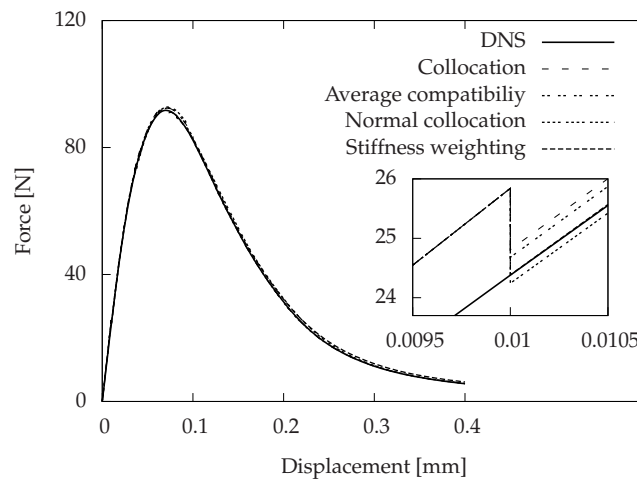


Figure 5.21 Load-displacement curves for the DNS and multiscale analysis for mesostructure II based on different micro-macro connections. The inset shows the close-up of the load-displacement curve around a zoom-in event.

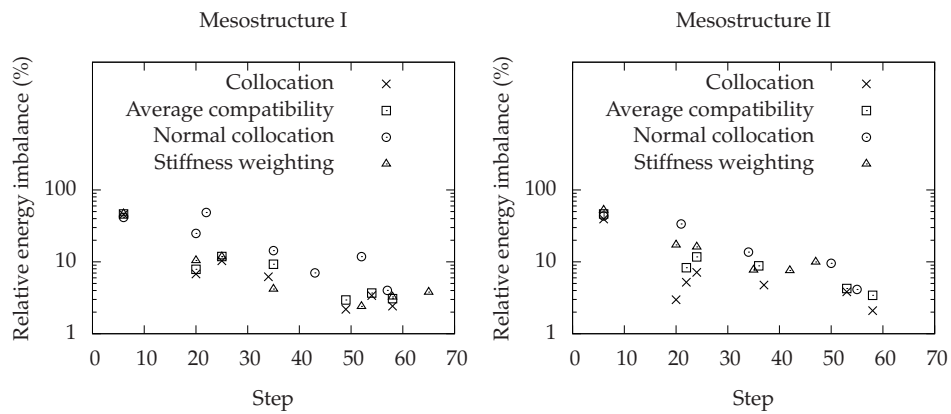


Figure 5.22 Evolution of relative energy imbalance $G_{r12}^{(s)}$ after the zoom-in episodes. One step is equivalent to a displacement increment of 2×10^{-3} mm.

5.5 Numerical examples

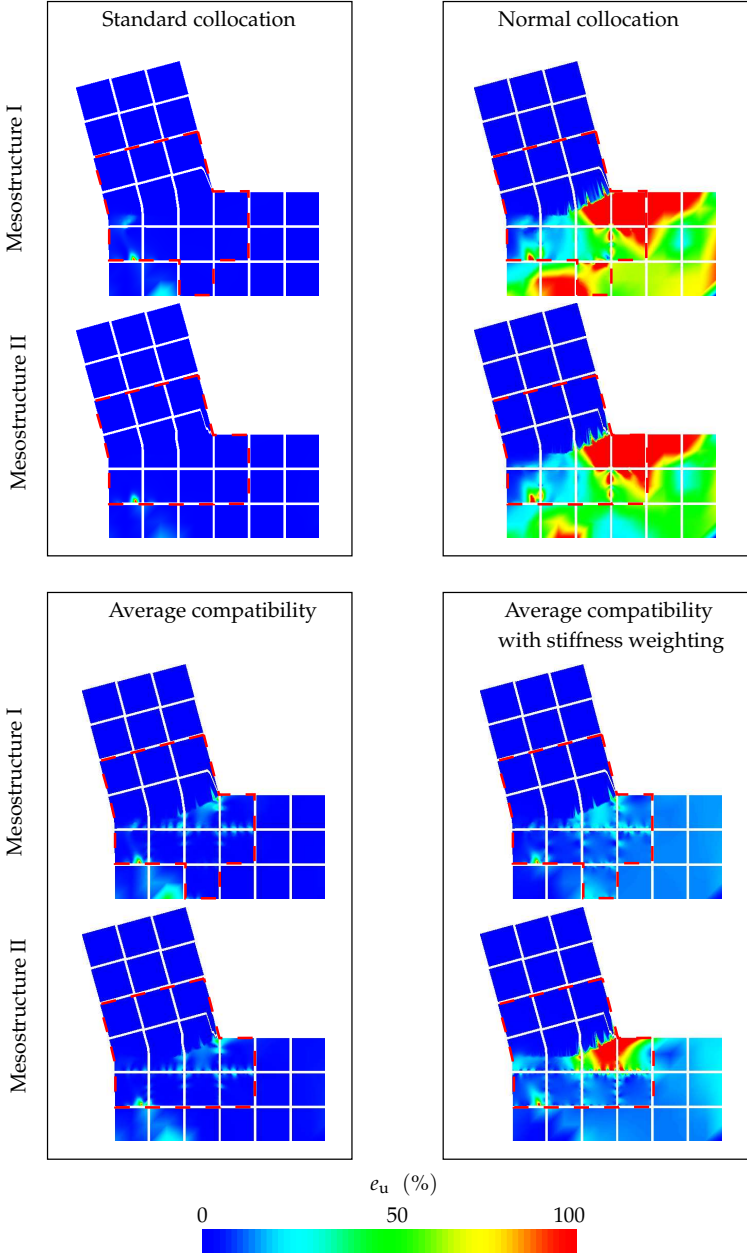


Figure 5.23 Solution field relative error e_u between DNS and multiscale analyses with different interscale relations. The dashed area contains fine scale domains. $10\times$ displacement magnification.

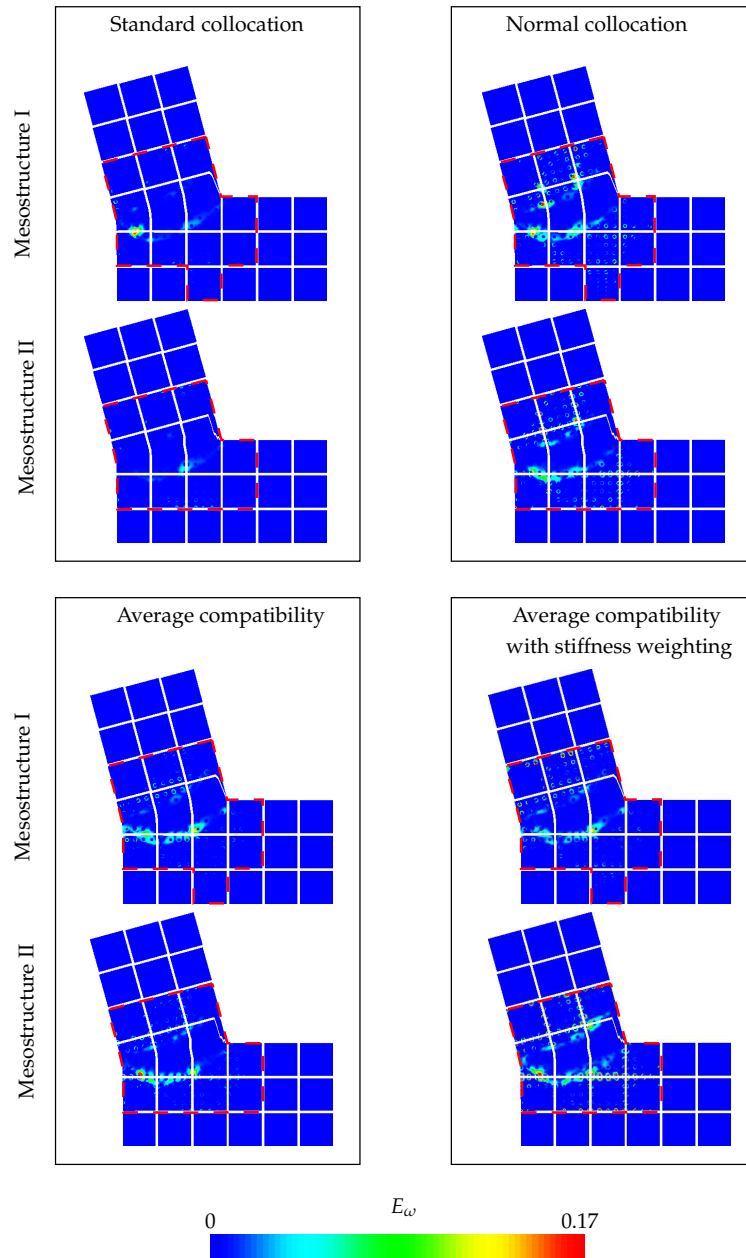


Figure 5.24 Damage field error E_ω between DNS and multiscale analyses with different interscale relations. The dashed area contains fine scale domains. $10\times$ displacement magnification.

5.5 Numerical examples

interface which reflects the ratio between the interface size of a multiscale analysis and a full fine resolution domain decomposition analysis. Obviously, the size of the interface increases monotonically during the propagation of non-linearity in the sample but the growth is more moderate if weak constraints are involved in the micro-to-macro connection. Hence, the tested weak constraints can be regarded as an attractive alternative to the collocation interface from a computational standpoint. Note that the use of normal collocation involves a lower number of DOFs when compared to collocation. As pointed out in Figure 5.5, this is due to the fact that only one displacement DOF per node is constrained. The results obtained with normal collocation constraints in this study involve a partial collocation link applied to the displacement DOFs and a full collocation link applied to the non-local equivalent strain DOF. For this reason, the size of the interface system cannot be significantly reduced. The number of Newton-Raphson iterations is expected to be slightly higher for the case of normal collocation when a large deformation setting is adopted. In such a case the implementation of non-linear multipoint constraints does not allow to employ the true Jacobian and this might influence the overall cost of the analysis.

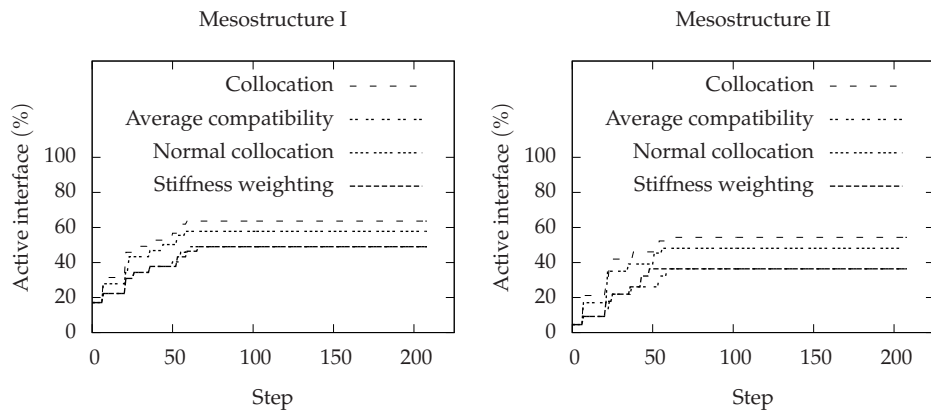


Figure 5.25 Evolution of the size of the interface problem. One step is equivalent to a displacement increment of 2×10^{-3} mm.

Material parameters	Soft inclusion	Matrix	Coarse bulk
E [N/mm ²]	20.0×10^2	40.0×10^3	Effective
ν [-]	0.2	0.2	Effective
$\tilde{\epsilon}_{nl}$ [-]	Mazars	Mazars	Mazars
κ_0 [-]	5.0×10^{-5}	8.5×10^{-5}	5.0×10^{-5}
c [mm ²]	1.5	1.5	1.5
$\omega(\kappa)$ [-]	Exponential	Exponential	[-]
α [-]	0.999	0.999	[-]
β [-]	400	400	[-]
Two-dimensional analysis type		Plane strain	

Table 5.3 Material parameters.

5.5.3 Influence of the heterogeneous interface with respect to the location of independent nodes

The goal of this section is to illustrate the behaviour of the proposed constraints in those cases where a highly heterogeneous interface may negatively influence the results of the multiscale analysis. This is the case when the position of the heterogeneous interface is such that all coarse grid nodes are linked to a material component which is too soft to carry and redistribute the stresses to the fine scale domain. In order to illustrate this issue, the previous example is reconsidered by taking into account weak inclusions instead of steel reinforcement. The two mesoscopic structures are redesigned by merging the ITZ with the matrix while the reinforcement inclusions are now given a lower value of the Young's modulus (more specifically, one order of magnitude difference in terms of the elastic properties is considered between the soft inclusion and the matrix as shown in the parameter list reported in Table 5.3).

The multiscale analyses are carried out for the two mesostructures considering the locality constraints previously described. As expected, the analyses with mesostructure I can be performed for all kind of constraints (Figure 5.26). However, when using mesostructure II, the analysis cannot be completed for the average compatibility and normal collocation constraint (Figure 5.27). The test concerning average collocation fails during the global relaxation iterations after zoom-in (point (1) in Figure 5.27). Divergence of the global relaxation iterative scheme indicates that the interface problem resulting after zoom-in in this particular mesostructure is not well conditioned. The fact that independent nodes are located along the weakest seg-

ment of the heterogeneous interface compromises the enforcement of the average compatibility condition.

With normal collocation, the test passes the first zoom-in but stops right after the second one (point (2) in Figure 5.27). In this case, the problem stems from damage development during the zoom-in at the soft inclusions. For this reason, global iterations fail at an attempt to re-equilibrate the whole structure. Using a more restrictive non-linear predictor the analysis can be continued. However, damage still develops during the following zoom-in events and the convergence of the global relaxation stage is compromised again. Both collocation and average compatibility with stiffness weighting prove to be sufficiently robust in this last test. In fact, the stiffness weighting constraint provides the closest results to the DNS (inset in Figures 5.26 and 5.27). Obviously, the worst case scenario that can be encountered is presented by considering a particular regular arrangement of the heterogeneities. Multiscale analysis performed on heterogeneous random media are not expected to follow the same pathological behaviour.

The evolution of energy imbalance for mesostructure I (Figure 5.28) is in agreement with that of the stiff inclusions (Figure 5.22). As evident from Figure 5.29, the two average compatibility techniques are the least expensive approaches in terms of the size of the interface problem. It can be concluded that the average compatibility constraint with stiffness weighting meets the best compromise between robustness, accuracy and computational cost in these analyses.

5.5.4 Effect of the interscale links in the linear elastic L-shape test

In order to filter the influence of weak non-linearities during zoom-in and the effect of the interscale link on the strain prediction, a linear elastic multiscale analysis is studied in this section for the L-shape test.

The L-shape specimen in Figure 5.10 is re-considered by discretizing the three domains corresponding to the re-entrant corner with a fine mesh while employing a coarse discretization for the remaining domains. Two different analyses are performed considering mesostructure II with stiff or soft inclusions as described in the previous section. The resulting global stiffness, shown in Table 5.4, is computed as the ratio between horizontal force and horizontal displacement at the uppermost edge of the specimen. In all analyses, the full collocation constraint results in a stiffer response than the average compatibility constraint. This is in agreement with the previously discussed constant strain and stress conditions. The responses provided by

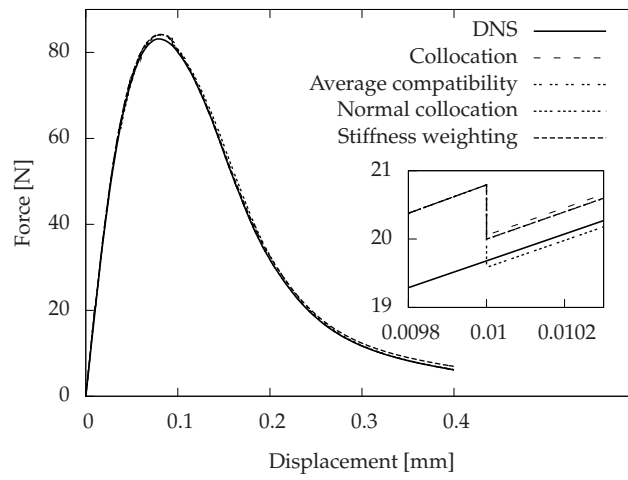


Figure 5.26 Load-displacement curves for the DNS and multiscale analysis for mesostructure I based on different micro-macro connections for problem with soft inclusions. The inset shows the close-up of the load-displacement curve around a zoom-in event.

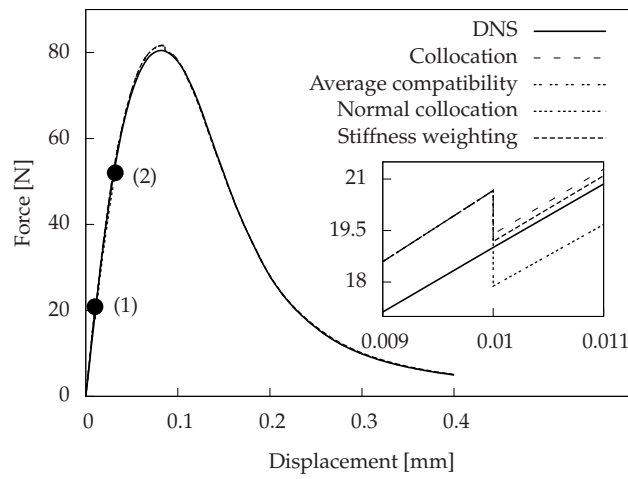


Figure 5.27 Load-displacement curves for the DNS and multiscale analysis for mesostructure II based on different micro-macro connections for problem with soft inclusions. The inset shows the close-up of the load-displacement curve around a zoom-in event.

5.5 Numerical examples

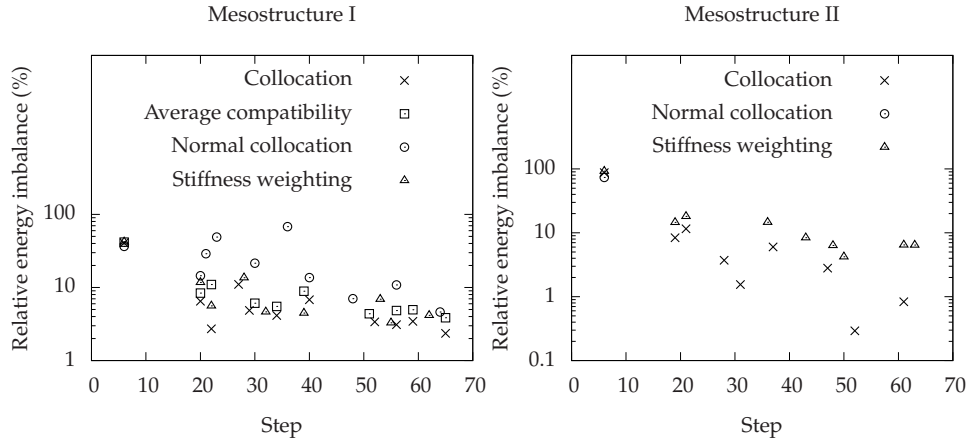


Figure 5.28 Evolution of relative energy imbalance $G_{r12}^{(s)}$ after the zoom-in episodes. One step is equivalent to a displacement increment of 2×10^{-3} mm.

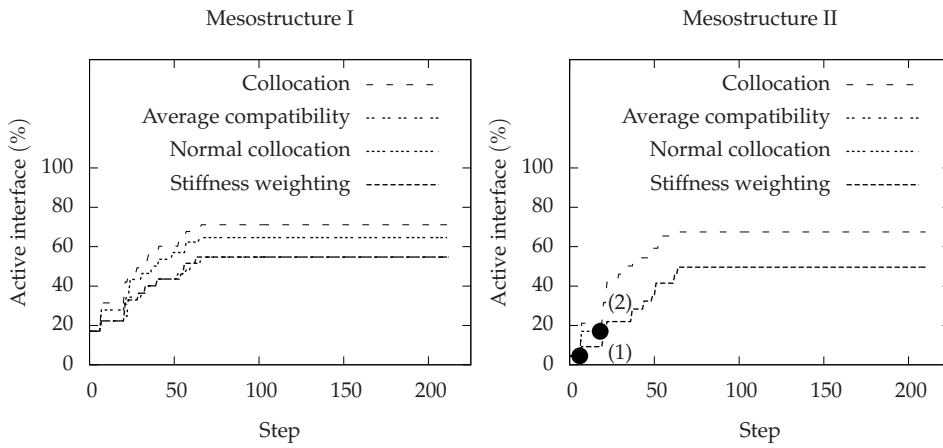


Figure 5.29 Evolution of the size of the interface problem. One step is equivalent to a displacement increment of 2×10^{-3} mm.

Analysis	Full coll.	Normal coll.	Av. comp.	Stiff. weight.
Stiff inclusions	2.495	2.470	2.492	2.486
Soft inclusions	1.951	1.850	1.917	1.948

Table 5.4 Global stiffness ($\times 10^3$) $[\text{N}/\text{mm}^2]$ at mesostructure II obtained with different inter-scale constraints.

the normal collocation link turn out to be the softest. This seems to be logical since stiffness vanished in the tangential direction of the interface thus reducing its bearing capacity. The response obtained with the stiffness weighting constraint is stiffer compared to that obtained with the average compatibility constraint for the case of soft inclusions. This tendency reverses when stiff inclusions are considered. This is due to the type of weighting and the ratio between stiff and soft interface segments.

5.6 Concluding remarks

The performance of an adaptive concurrent multiscale framework for brittle heterogeneous material is assessed. The objectivity of the solution with respect to a full fine scale analysis is measured in terms of the mechanical response, the energy imbalance after zoom-in events, and error distributions of displacement and damage fields. The quality of the multiscale result improves with an adequate choice of the effective elastic properties for the homogeneous coarse bulk. This holds for mesostructures with homogeneous and heterogeneous interfaces. However, a higher spread in results is observed for mesostructures with heterogeneous interfaces. This is because the boundary conditions used to compute effective elastic properties are sensitive to the heterogeneous RVE boundaries.

Compatibility constraints of strong and weak type are considered for both the micro-to-macro connection and the zoom-in process. Full collocation is found to be the stiffest link. This is in agreement with other methodologies based on the constant strain assumption. Average compatibility constraints, on the other hand, provide a softer link since they arise from a constant stress assumption. Average compatibility with stiffness weighting shows a mechanical behaviour which is close to the standard averaging. However, its overall behaviour, stiffer or softer than standard averaging, depends on the nature of the interface and the spatial distribution of the heterogeneities. Normal collocation is clearly the weakest link tested in this study due to the fact that the stiffness in the direction tangential to the interface is simply removed from all dependent DOFs.

From a computational point of view, weak interscale relations represent a cheap alternative to collocation techniques since the resulting interface problem involves a lower number of constraints. Although the analyses are performed considering regular heterogeneous media, conclusions can be regarded valid for a generic material since the arrangement of the inter-

5.6 Concluding remarks

face was designed to reproduce the most challenging scenarios. The computational cost is expected to be linked to the accuracy of the results. In this view, standard collocation techniques provide the most accurate analyses although they lead to the most expensive interface problem. The suggested average compatibility methods provide a solution whose quality is acceptable at a much lower computational cost. However, for a heterogeneous interface with soft inclusions, the arrangement of dependent and independent interface DOFs can seriously compromise the robustness of the average compatibility link. This issue is solved in the present study by using a stiffness weighting in order to build a more adequate set of interscale constraints. Finally, normal collocation leads to less accurate displacement and damage fields. In this approach the size of the interface problem is only slightly smaller than that obtained using full collocation and, for this reason, it does not seem to represent an adequate alternative.

To conclude, weak locality constraints show, in general, a good agreement between accuracy and computational cost. Only in the pathological cases studied in Section 5.5.3, i.e. weak inclusions placed at independent nodes, the weak interscale link does not seem to be stable. However, the proposed stiffness weighting technique proves to significantly improve the robustness of the non-weighted average compatibility for these particular heterogeneous interfaces.

Chapter 6

Multiscale analysis of failure in random granular heterogeneous materials*

The main objective of a general multiscale analysis is to capture the origin and evolution of the targeted physical processes at a fine scale and their impact at a coarse scale of observation. This can be achieved by accounting for a refined representation of the material which eventually requires a different simulation strategy. Examples of such techniques can be found in [19] where fracture in concrete is simulated with the use of a lattice-particle model whereas standard finite elements (FE) are employed for the linear elastic region. The study of localization phenomena in granular frictional materials presented in [114] considers a particle model at the areas affected by large deformations and standard FEs at the rest of the sample. Other multiscale strategies are based on local material refinement and scale resolution without varying the computational approach at different scales. For instance, FEs are employed at both macro and mesoscopic scales in [4, 37, 49].

The approach adopted in this manuscript can be classified in this second group and, as described in Chapter 4, processes both macro and mesoscopic scales in a concurrent manner. The focus is on the multiscale analysis of concrete-like (Figure 6.1) samples and the influence of interscale links between macro and mesoscopic material resolutions.

As seen in Chapter 4 the adaptive multiscale approach takes into account the mesoscopic geometry during nucleation and growth of damage processes. Consequently, the interactions between subscale material heterogeneities and the macroscopic stress and strain fields is taken into account in a realistic manner. This gives rise to solutions which are in very good agreement with DNS. In this chapter the multiscale technique is utilized in those cases where the mesoscopic geometry is not regular but random, i.e. aggregates in a material matrix.

* This chapter is based on reference [63].

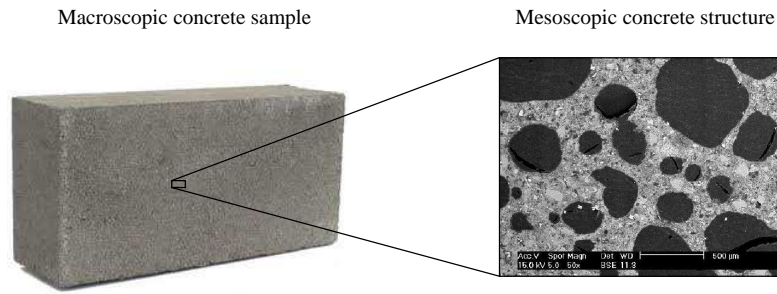


Figure 6.1 Macroscopic concrete sample and mesoscopic concrete structure (Roels et al. [99]).

6.1 General procedure for the concurrent multiscale analysis of random heterogeneous materials

A concurrent multiscale analysis based on non-overlapping domain decomposition techniques can be accomplished considering the steps listed below and illustrated in Figure 6.2.

1. Consider the material sample Ω in its full scale resolution together with the boundary conditions applied at Γ . The detail level chosen for the meso/microstructure defines the fine scale resolution of the analysis. The coarse scale resolution will be, in turn, given by the corresponding material sample with homogenized elastic properties $\langle \Omega \rangle^1$. The body is split according to a user defined criterion and leads to the definition of the interface surface Γ_1^2 . It is assumed here that the area of the RVE used to extract effective elastic properties is lower than, or equal to, the area of the smallest domain $\Omega^{(s)}$.
2. Perform a coarse FE discretization Ω^c of the body $\langle \Omega \rangle$. The coarse grid must be able to reproduce the geometry of the sample and the interface between domains, i.e. the boundary Γ and the interface Γ_1 can be exactly reproduced at Ω^c . Besides that, the coarse discretization is supposed to capture the spatial variation of the solution field gradient

¹The angle brackets $\langle \square \rangle$ are used to indicate that the body Ω is treated as homogeneous with effective mechanical properties.

²The surface Γ_1 can also be obtained using a graph partitioner on a predefined mesh. In this case, the FE discretization automatically accommodates to the geometry of Γ_1 . However, specifying the geometry of Γ_1 a priori can overcome problems related to domains with high aspect shape ratios.

during the linear elastic regime. If this is not the case, an appropriate refinement in terms of FE size or polynomial degree needs to be carried out at the corresponding domains. This process is eventually performed during the loading steps where such situation is encountered.

3. The coarse (c) discretization of the boundary Γ^c and coarse-to-coarse (cc) domain interface Γ_I^{cc} are obtained after the intersection between Ω^c and the geometrical surfaces Γ and Γ_I .
4. Obtain the fine scale FE mesh Ω^f considering the body Ω and the coarse surfaces Γ^c and Γ_I^{cc} ³. The boundary surface of the new mesh is obtained by subdivision of the discretized surfaces Γ^c and Γ_I^{cc} . All fine scale heterogeneities appearing in Ω need to be represented in Ω^f ⁴.
5. Perform the adaptive multiscale analysis on the decomposed body. Note that all interfaces between domains with equal FE resolution (coarse-to-coarse or fine-to-fine) are conforming. The non conforming interfaces Γ_I^{cf} between domains with different resolution (coarse-to-fine) contain a number of matching (independent) and non-matching (dependent) nodes.

It is highlighted that the multiscale strategy proposed in this manuscript is suitable for:

1. Arbitrary shape macroscopic specimens. The geometry of the macroscopic body does not have to be regular as depicted in most of the examples provided in this document.
2. Arbitrary domain decomposition. The user can provide an arbitrary decomposition which will be taken into account in the coarse and fine FE discretizations.

³The fine scale discretization $\Omega^{f,(s)}$ can be defined a priori or when zoom-in takes place. In the later option, a randomized meso-scale generator needs to be accounted for in which the coarse surfaces Γ^c and Γ_I^{cc} are considered and a conforming interface between the new mesh and neighbouring fine scale discretizations is guaranteed. The adaptive mesh generation can improve the efficiency of the multiscale analysis in those cases where only a small part of the material is analyzed with a fine scale mesh.

⁴Normally, the interior nodes of the coarse discretization of $\Omega^{(s)}$ do not need to be at the same location as some interior nodes in the fine discretization of the same domain. However, if the solution field is constrained in the interior of $\Omega^{(s)}$ (e.g., fixed displacement, temperature or concentration) the fine discretization needs to be obtained by mesh refinement (subdivision) of the coarse one keeping the nodes of Ω^c which are constrained.

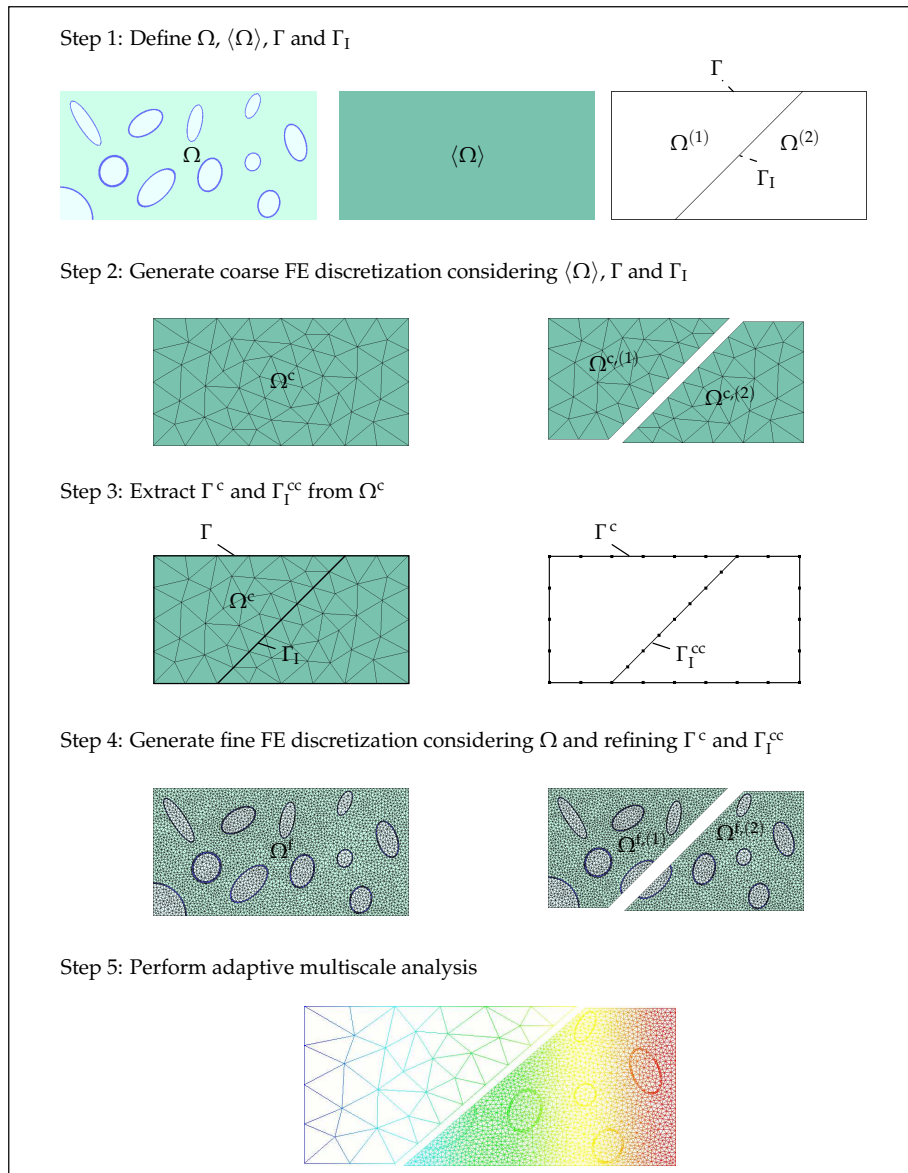


Figure 6.2 General procedure for the concurrent multiscale analysis

6.2 Numerical examples

3. Two and three-dimensional problems. All features of the multiscale framework reside in an algebraic level and, therefore, are directly compatible with a three-dimensional analysis.
4. Multiphysics problems. Coupled systems arising from multiphysics can also be addressed without further modifications. Obviously, the linear/non-linear predictors need to be based on the internal quantities that drive the constitutive relation.

In the following analysis, however, a regular domain decomposition is adopted. This is done for convenience since a sensitivity analysis is performed on the chosen domain decomposition. To this end, a periodic cell containing the microstructure is used and its translation into the two dimensional space defines the complete material sample. In this case, it is trivial to define different decompositions that provide domains of equal shape and dimensions. In addition, no fine mesh model needs to be setup at forehand.

A representative volume element (RVE) of the heterogeneous random material is considered. The RVE is set to be periodic with a repetition period l equal to the RVE dimensions. Therefore, a general material sample of length $L > l$ can be represented by a vector translation of the RVE (see Figure 6.3 (top)). Note that the mesh needs to be periodic as well in order to match with the adjacent mesh as shown in Figure 6.3 (bottom). The resulting interface is, therefore, conforming.

6.2 Numerical examples

Several multiscale analyses of a concrete-like material are summarized in this section. They are designed to test the basic features of the multiscale approach introduced in Chapter 4.

6.2.1 Tensile test

A concrete sample is subjected to tensile loading as depicted in the top part of Figure 6.4. The body is decomposed into three non-overlapping domains. As shown in Figure 6.4 (bottom), homogeneous coarse scale domains are represented by a single bilinear quadrilateral element whereas fine scale domains contain the mesoscale constituents and are meshed using linear triangular elements. Note that the mesoscopic structure is obtained by a two-dimensional translation of a material unit cell with periodic boundaries.

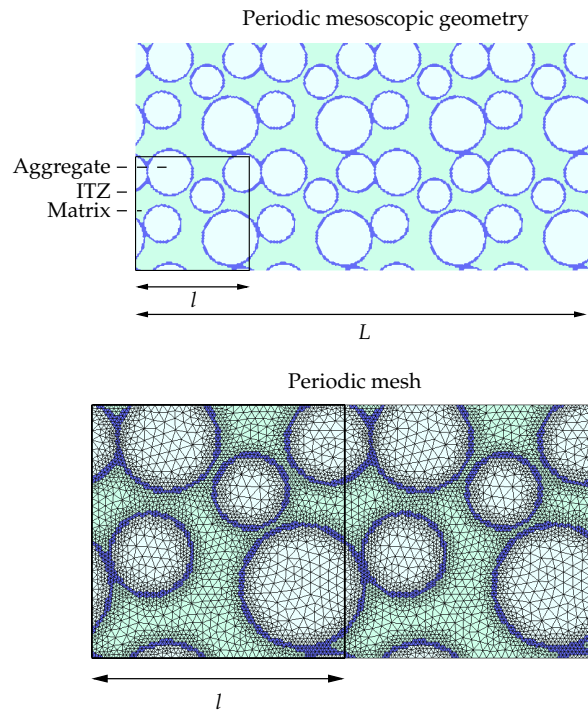


Figure 6.3 Periodic mesoscopic geometry (top) and conforming interface between periodic meshes (bottom).

6.2 Numerical examples

Material parameters			Aggregates	Matrix	ITZ
E	Young's mod.	[GPa]	35.0	30.0	20.0
ν	Poisson's ratio	[-]	0.2	0.2	0.2
$\tilde{\epsilon}_{nl}$	Non-loc. equiv. strain	[-]	Mazars	Mazars	Mazars
κ_0	Dam. init. thres.	[-]	dummy	0.124×10^{-4}	0.1×10^{-4}
c	Grad. param.	[mm ²]	0.75	0.75	0.75
$\omega(\kappa)$	Dam. evol. law	[-]	Exp.	Exp.	Exp.
α	Resid. stress param.	[-]	0.999	0.999	0.999
β	Soft. rate param.	[-]	500	500	500
Two-dimensional analysis type				Plane strain	

Table 6.1 Material data for the concrete specimen.

A Gradient-Enhanced Damage model (cf. Appendix A) is used in this study to model crack growth and coalescence in the material. A list of material parameters for each phase is given in Table 6.1. Initially, a set of coarse scale domains is considered with effective elastic properties considering periodic boundary conditions for a representative volume element (RVE). A representative quantity of the non-local equivalent strain $\tilde{\epsilon}_{nl}$ is computed for each domain and serves as an indicator for the appearance of non-linearity (see Chapter 3). The damage initiation threshold κ_0 of the homogeneous bulk is taken as the minimum damage initiation threshold of the three concrete phases. The plane strain assumption is far from realistic in this case since all heterogeneities have a finite size in the out-of-plane direction. However, a plane stress assumption is also not fully correct since the out-of-plane direction plays a relevant role in the analysis. Both are expected to provide different results compared to a three-dimensional analysis which would account for all possible damage percolation paths. Due to the initial constant strain and stress distribution in the homogeneous bulk, a zoom-in is performed simultaneously for all domains. Damage nucleates at the ITZ and propagates through the matrix giving rise to a series of damage bands perpendicular to the loading direction (Figure 6.5). Due to the non-symmetry of the mesoscale geometry and the applied boundary conditions strains localize at the leftmost section of the sample with the appearance of a dominant damage band.

The applied load against the displacement registered at the right edge of the sample is compared to the one obtained with a DNS (Figure 6.6). The differences between both simulations are hardly visible except from the stage

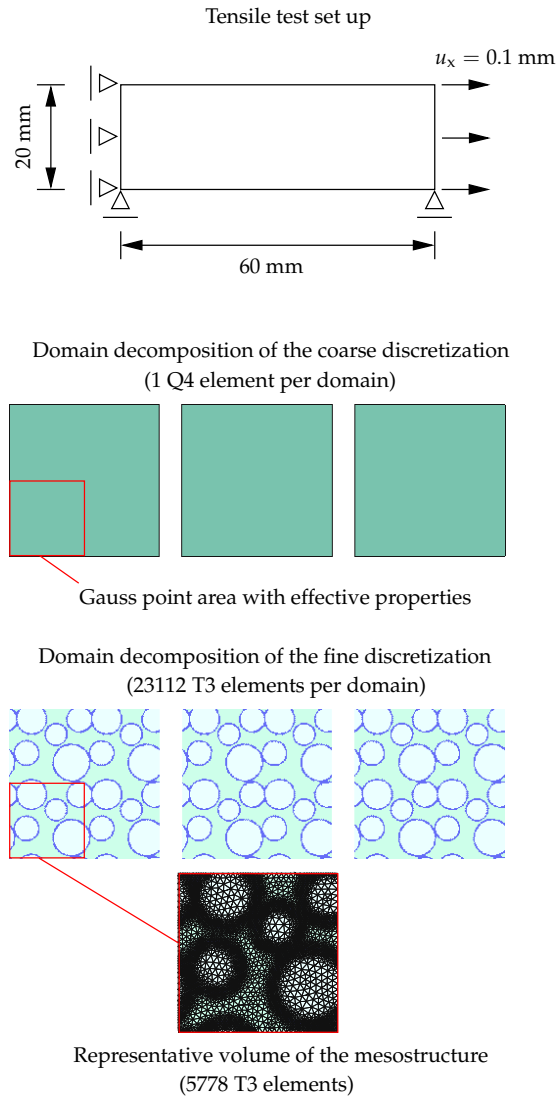


Figure 6.4 Description of the tensile test for the concrete specimen (top) and domain decomposition of the coarse and fine FE discretizations (bottom).

6.2 Numerical examples

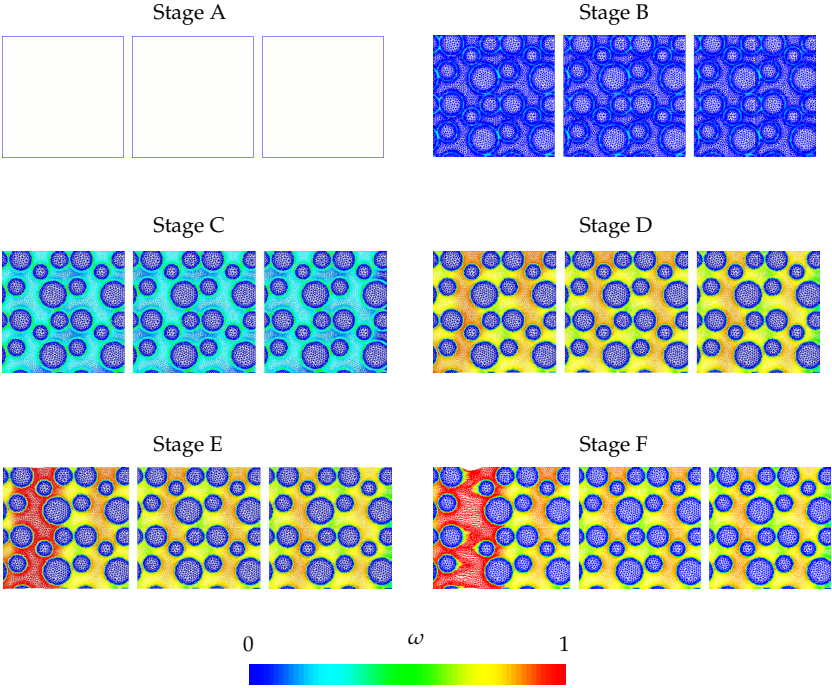


Figure 6.5 Damage evolution during the adaptive multiscale analysis of the tensile test. $25\times$ displacement magnification.

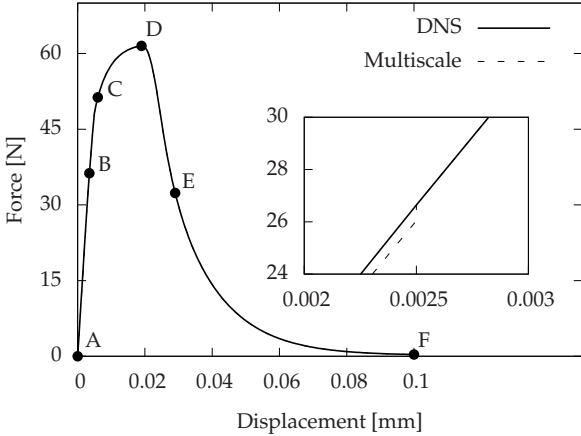


Figure 6.6 Load-displacement curves for the tensile test DNS and multiscale analysis. The inset shows the close-up of the load-displacement curve around a zoom-in event.

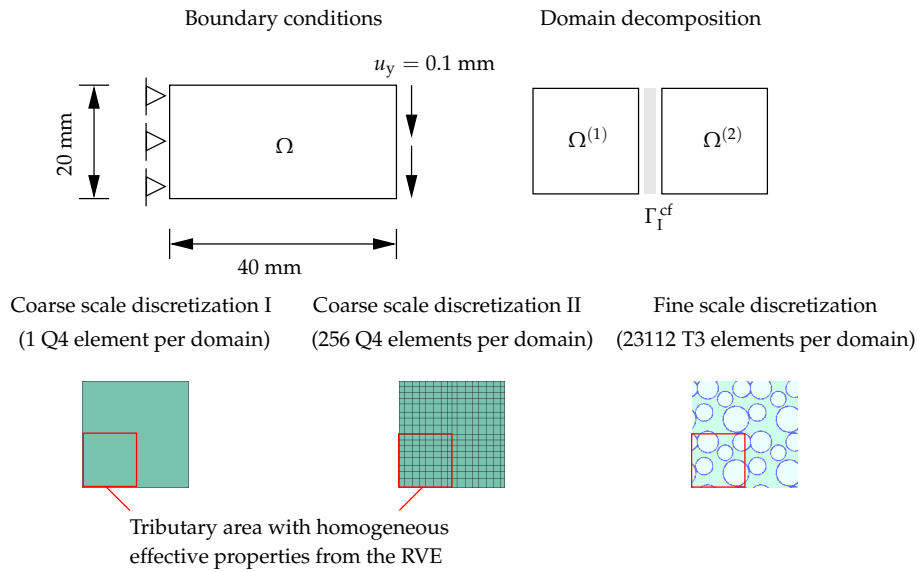


Figure 6.7 Boundary conditions for the bending test and domain decomposition (top). FE discretizations for the coarse and fine domains (bottom).

in which zoom-in is applied and a load variation is registered.

6.2.2 Influence of the interscale link in bending test

In this example a bending test is performed on a concrete beam (Figure 6.7 (top)). The sample is decomposed into two non-overlapping domains with the same geometry. The idea is to test different micro-to-macro connections that glue the different scale resolutions shown at the top of Figure 6.8. In this case the multiscale analysis is “static” and the resolutions do not change during the test. A linear elastic model is used for the homogeneous bulk and the three concrete phases considering the same moduli as in the previous section (Table 6.1). Two different coarse resolutions (discretizations I and II) are considered (Figure 6.7 (bottom)). Effective elastic properties are retrieved from the same RVE used in Section 6.2.1. Note that in the second discretization the area of the RVE is larger than the area that can be attributed to a coarse element integration point. However, the total area in which homogenization takes place is determined by the number of sub-areas with homogeneous properties. In this case the refinement is only employed to provide a higher flexibility to the coarse mesh and to avoid shear locking.

6.2 Numerical examples

Coarse mesh	Full col.	Normal col.	Av. comp.	Stiff. weight
I	0.906	0.832	0.697	0.697
II	0.846	0.845	0.846	0.847

Table 6.2 Global stiffness [$\times 10^3 \text{N/mm}$] for the static multiscale test with different interscale constraints. The reference stiffness of the DNS is $0.845 \times 10^3 \text{ N/mm}$.

The bending stiffness of the system is calculated as the relation between the vertical components of the force and displacement at the right edge of the sample. Table 6.2 contains the bending stiffness for each interscale constraint when using any of the two coarse discretizations for domain $\Omega^{(2)}$. In general, the use of discretization II provides the closest values to the reference stiffness $0.845 \times 10^3 \text{ N/mm}$ obtained with a fine discretization of both domains. The full collocation constraint (5.19) turns out to perform better than the normal collocation constraint (5.23) when analyzing the deformation of the sample. In fact, the deformed configuration of the interface corresponding to the reference solution is a linear segment due to the small deformations assumption. In this view, the collocation constraints naturally provide an accurate deformation at the interface (Figure 6.8). Coincidentally, normal collocation is able to provide a closer value to the reference one due to two counteracting effects: the too coarse domain (stiffening) and the loose compatibility (softening).

The average compatibility constraint (5.7) and average compatibility with stiffness weighting (5.37) provide very similar results in this example. Only when using the second coarse discretization, the stiffness weighting constraint turns out to be slightly stiffer than the standard average compatibility.

A mechanical characterization of the proposed interscale links for simpler heterogeneous interfaces is discussed in more detail in Chapter 5.

6.2.3 Wedge split test

A multiscale simulation of the wedge split test, sketched in Figure 6.9, is carried out. The concrete sample is decomposed into 34 non-overlapping domains and the notch Γ^n is modelled by means of the traction free interface Γ_1^n . The fine scale discretization used for the different domains and the RVE sample are identical to the ones presented in the previous examples.

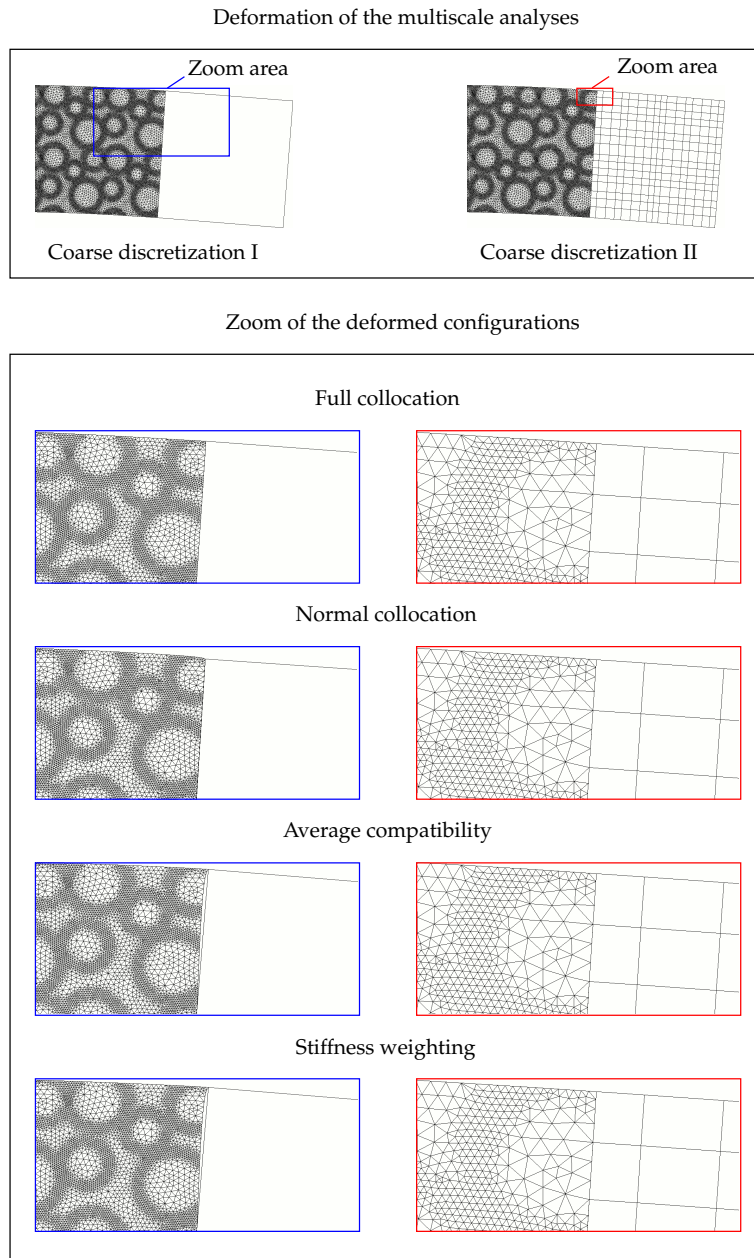


Figure 6.8 Deformed configurations using different interscale constraints. $25\times$ displacement magnification.

6.2 Numerical examples

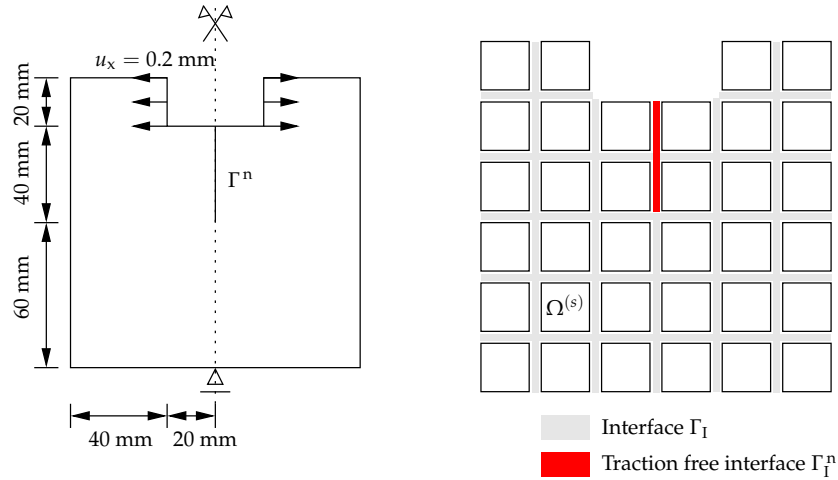


Figure 6.9 Boundary conditions (left) and domain decomposition (right) for the wedge split test.

The coarse discretization II employed in Section 6.2.2 is adopted here for the coarse scale domains. A Gradient-Enhanced Damage model is adopted again and the material parameters for each phase are listed in Table 6.1. The adaptive multiscale strategy considered in Section 6.2.1 with a full collocation interscale link is adopted in this example.

The damage evolution after zoom-in at domains affected by non-linearity is shown in Figures 6.10 and 6.11. Despite the symmetry in the boundary conditions and geometry of the sample the final crack path is not aligned with the notch. This is due to the heterogeneous mesostructure and its interaction with the stress and strain fields at the fine resolution. It is observed in Figure 6.11 (bottom) that damage concentrates in an elongated region between the stiff aggregates. The tortuousness of the damage percolation path is conditioned by the spatial arrangement of the heterogeneities. This is also illustrated in Figure 6.12 (right) where the distribution of the non-local equivalent strain reflects the area in which strain localization (cracking) occurs.

As observed in Figure 6.10 (bottom), the load-displacement curve is in agreement with the one of the DNS and differences are not visible after zooming at all domains involved in the non-linear processes. The overall cost of the multiscale analysis is clearly lower than the one of the DNS since during the computation domains remain coarse and linear unless refine-

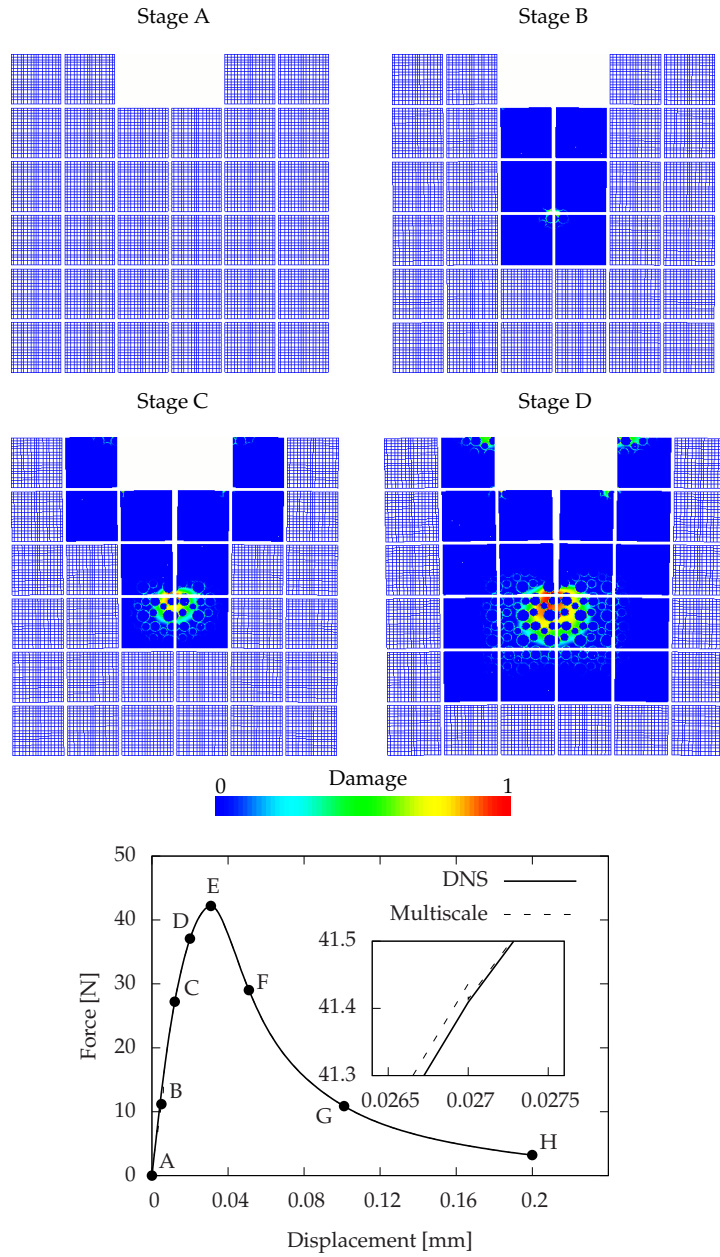


Figure 6.10 Top: Damage evolution during the adaptive multiscale analysis of the wedge split test. $50\times$ displacement magnification. Bottom: force-displacement plots of the multiscale and DNS analyses.

6.2 Numerical examples

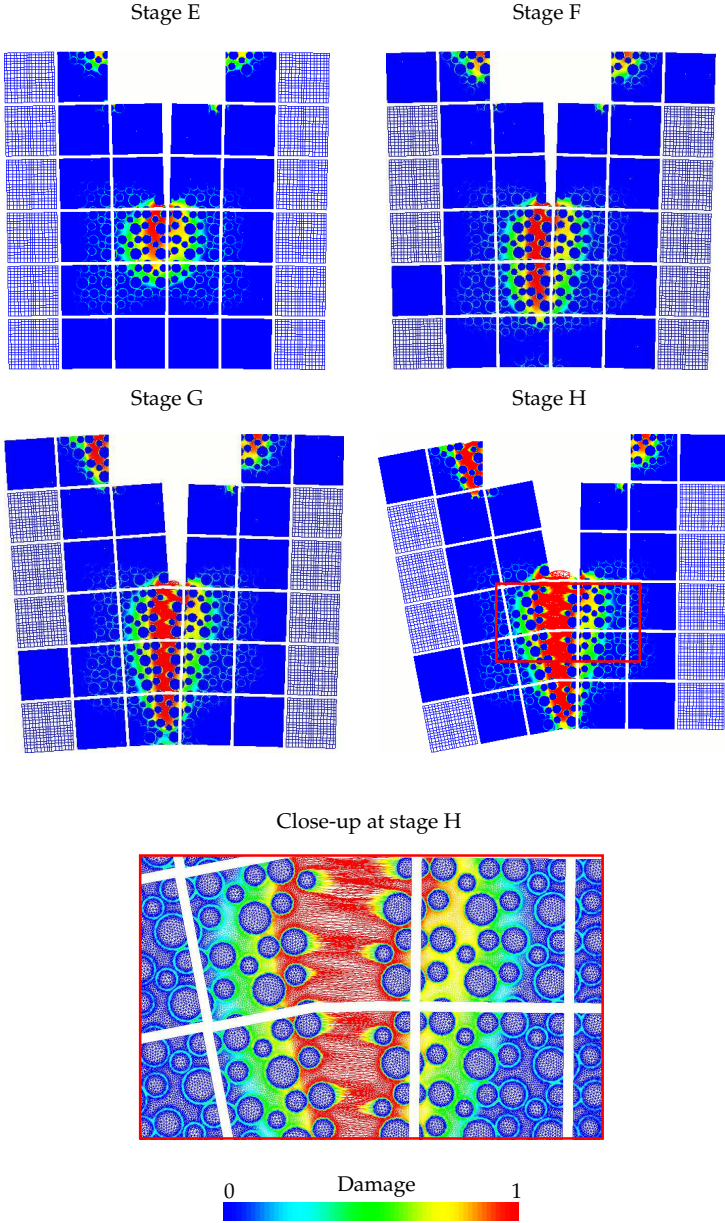


Figure 6.11 Top: Damage evolution during the adaptive multiscale analysis of the wedge split test. Bottom: Zoom-in at stage H. $50\times$ displacement magnification.

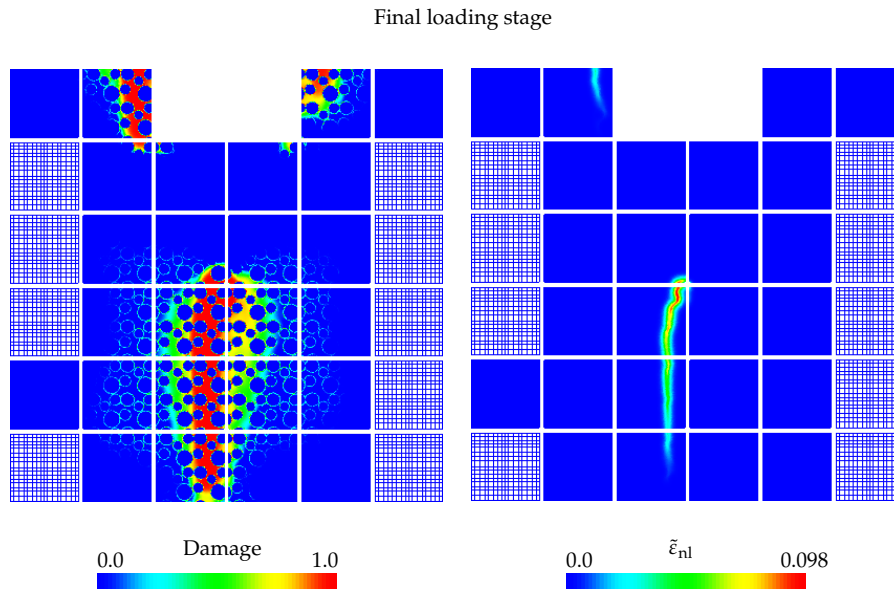


Figure 6.12 Damage (left) and non-local equivalent strain (right) contours at ultimate loading stages in the undeformed meshes.

ment is needed.

6.2.4 Objectivity of the proposed multiscale approach

The proposed multiscale approach requires the input of three main variables or parameters that are crucial for a complete set up of the analysis. These parameters need to be defined by the user and are identified as:

- the fine scale discretization used to describe all mesoscopic heterogeneities,
- the coarse scale discretization used at the homogeneous linear elastic bulk, and
- the domain decomposition (size and geometry of the mesh partitions).

Consequently, the result of the adaptive multiscale analysis needs to be completely independent or objective with respect to the three user defined parameters.

Objectivity with respect to the fine scale discretization is trivial to justify provided that a regularized model is utilized to simulate the envisaged material non-linearity. In the present study, damage nucleation and propagation are modelled with the use of a Gradient-Enhanced Damage model [87] (see Appendix A). Mesh independent results are automatically guaranteed by the model given a minimum size of the FEs which is connected to the length scale parameter c .

The size of the coarse scale FEs need to be sufficiently small in order to correctly reproduce the spatial variation of the solution field gradients during the linear elastic regime. To this end, error estimators should be utilized to ensure that the coarse scale discretization is fine enough throughout the elastic regime. This feature is not accounted for in the present document since it is assumed that the coarse scale discretization provided at the initial stage is already appropriate. Nevertheless, a sensitivity analysis is performed on the previous wedge split example (Section 6.2.3) in which three different coarse meshes are selected. The wedge split test, considering a decomposition into 34 domains, is reproduced for an initial coarse discretization of 2176, 8704 and 34816 bilinear Q4 elements at the whole sample, i.e. including all domains. As shown in Figure 6.13 (left) the damage contours are plotted for the last loading stage. No significant differences can be observed between damage plots. By inspecting the resulting force-displacement response in Figure 6.14 the maximum relative error between multiscale analyses and DNS at the peak is around 0.02%. This value corresponds to the coarsest discretization (2176 Q4) and the error diminishes upon mesh refinement. Consequently, the response of the multiscale framework is objective with respect to the coarse scale mesh.

The wedge split test is again reproduced considering the intermediate coarse discretization (8704 Q4) and three domain decompositions with 34, 68 and 136 partitions. No remarkable differences can be noticed by visual inspection of the damage distribution plots in Figure 6.13 (right). This indicates that the decomposition does not influence material non-linearity in the sample and, therefore, the overall mechanical response is not changed. By inspecting the resulting force-displacement response in Figure 6.15 the maximum relative error between multiscale analyses and DNS at the peak is around 0.06%. The highest overestimation of the peak load corresponds to the partition into 136 domains. This can be explained considering that a lower fine scale area is accounted for in this analysis and, therefore, the solution is slightly stiffer due to the larger amount of coarse scale domains.

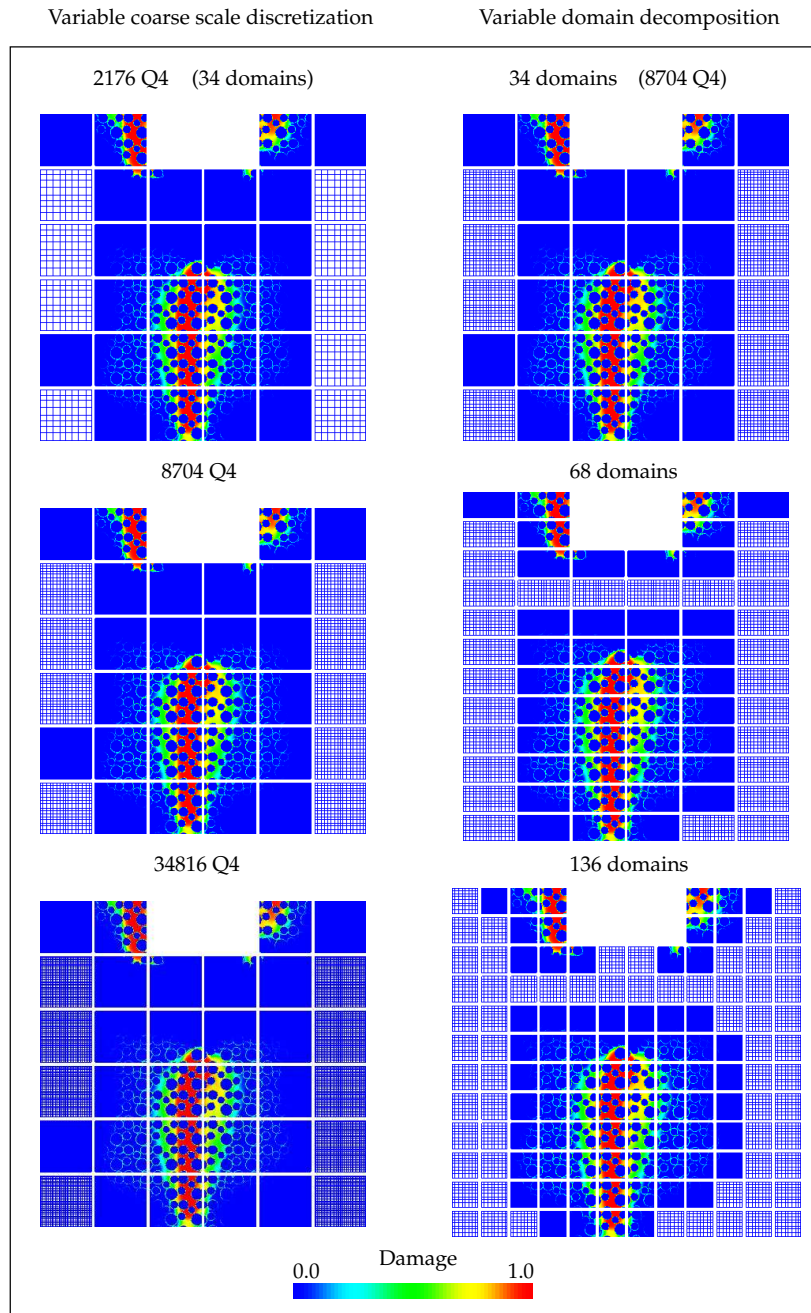


Figure 6.13 Damage distribution at ultimate loading stage with different coarse discretizations (left) and domain decompositions (right). Results are shown in the undeformed meshes.

6.2 Numerical examples

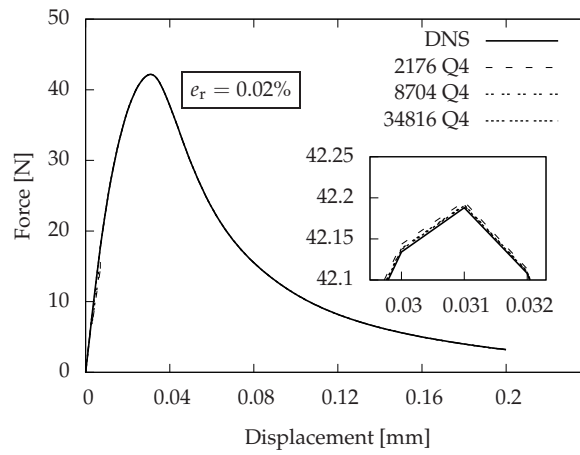


Figure 6.14 Force-displacement plots for different coarse discretizations and a decomposition in 34 domains.

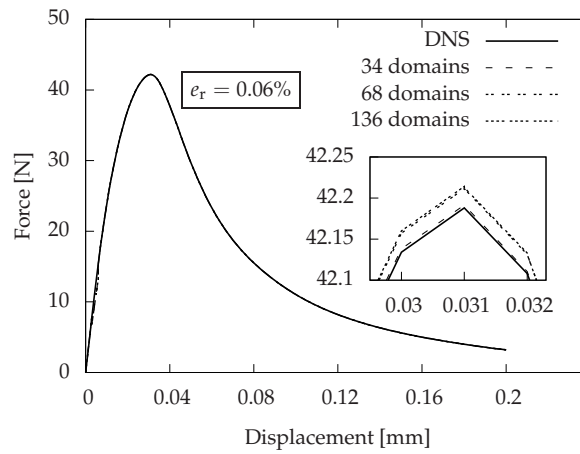


Figure 6.15 Force-displacement plots for different domain decompositions and a coarse discretization of 8704 Q4 elements.

Essentially, it can be concluded that the response of the multiscale framework is objective with respect to the domain decomposition.

6.3 Future opportunities: 3D analysis

Failure mechanisms in random granular materials are inherently three-dimensional. Although such an analysis is out of the scope of the present work, the algorithm of the adaptive multiscale framework is ready for it without further modifications. All multiscale ingredients reside at an algebraic level and, therefore, the analysis of a three-dimensional material sample does not affect the proposed algorithm. The different multiscale constraints introduced in this manuscript can be used in a 3D analysis as mentioned in Chapter 5. In order to properly handle the required interpolation processes during the zoom-in and construction of the interscale constraints, a numerical inverse mapping algorithm is recommended (cf. [103]).

In order to illustrate the performance of the adaptive multiscale framework, a tension test is performed on a homogeneous bar with variable height (Figure 6.16). The sample is decomposed into seven domains according to the planes $x = 20$, $x = 40$, $x = 60$, $x = 80$, $x = 100$ and $x = 120$ mm, respectively. The coarse domains are discretized with one 8-noded hexahedron while the fine domains contain 375 8-noded hexahedra. The constitutive model is linear elastic with Young's modulus $E = 35$ GPa and Poisson's ratio $\nu = 0.2$ and zoom-in is performed when the strain component $\varepsilon_{xx} > 8.0 \times 10^{-4}$ at any integration point within the domain. Horizontal displacement contours on the deformed configuration at different loading stages are depicted in Figure 6.17.

6.4 Concluding remarks

The concurrent framework presented in this manuscript proves to be adequate for the multiscale analysis of failure phenomena in quasi-brittle materials such as concrete. The nucleation and evolution of fracture processes is well captured and the overall response turns out to be in agreement with the DNS. The computational cost of the analysis is essentially linked to the extension of the fracture process zone. In this scenario, the domain decomposition plays an important role since larger domains will trigger a larger refined area when zoom-in takes place.

6.4 Concluding remarks

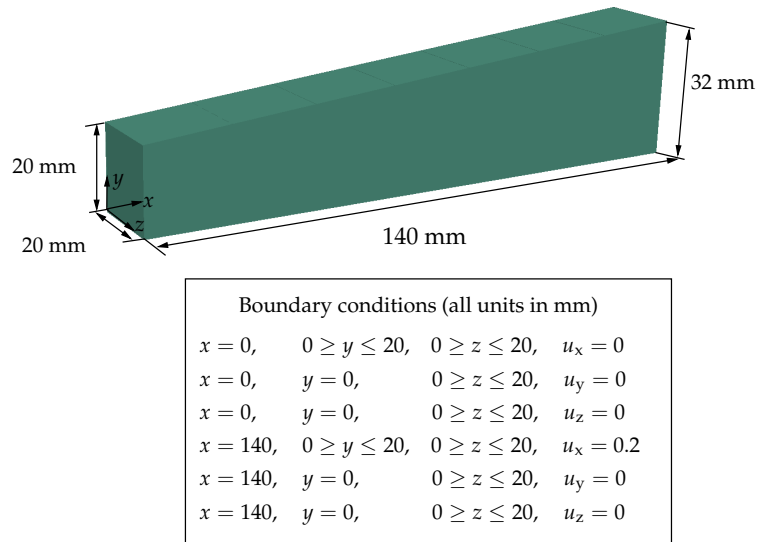


Figure 6.16 Geometry and boundary conditions for the three-dimensional test

Different interscale relations can be supported by the current framework. It is observed that collocation techniques generally provide a stiffer link than average compatibility constraints.

The results given by the adaptive multiscale framework shown to be objective with respect to the size of the coarse and fine scale discretizations and the adopted domain decomposition.

Three-dimensional structures can be analyzed as well without extra modifications to the multiscale algorithm. Although it is not addressed in this study, the multiscale algorithm is also ready to be used for multiphysics problems with coupling of the governing equations.

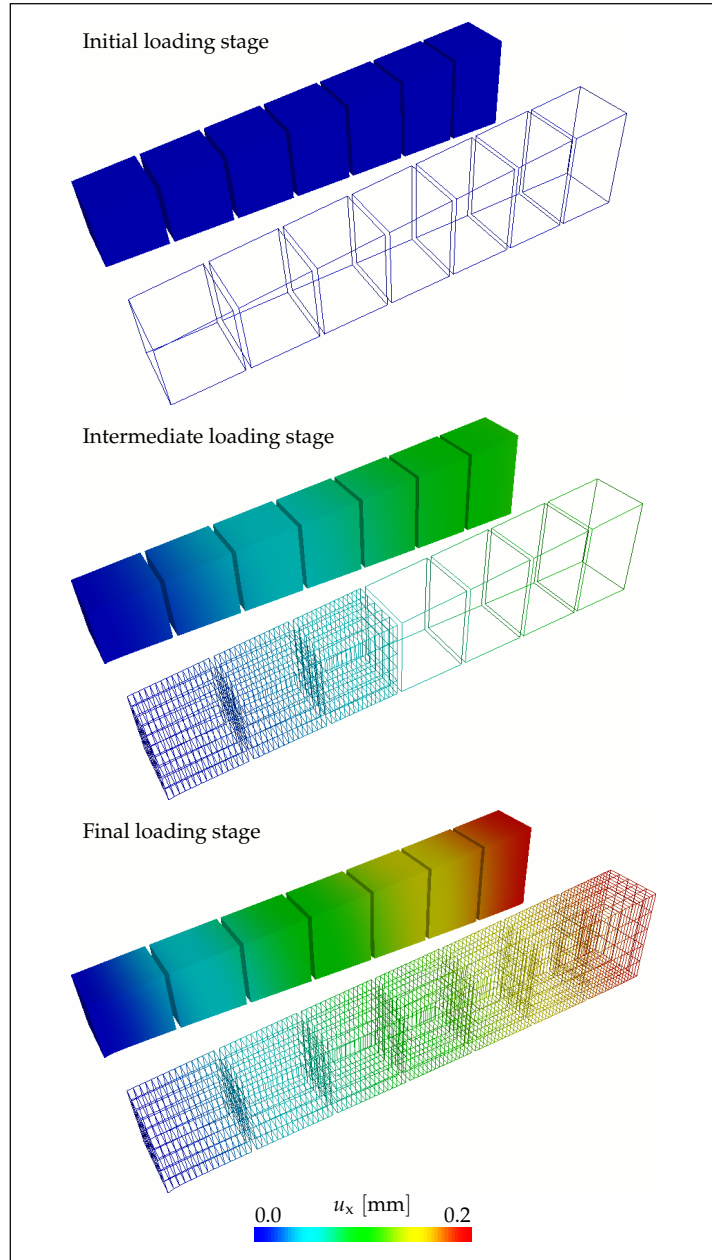


Figure 6.17 Horizontal displacement contours and deformed grids at different loading stages. $100\times$ displacement magnification.

Chapter 7

Conclusions and recommendations

An adequate simulation tool for the analysis of complex heterogeneous materials is essential in both engineering and material design applications. To this end, multiscale analysis is regarded as an effective methodology to properly understand the role of lower scale constituents and their interactions with complex phenomena such as crack nucleation and growth. The main novelty presented in this thesis consists on a new concurrent multiscale approach adequate for the study of failure phenomena in quasi-brittle materials. The algorithm has been obtained by performing a number of extensions to the non-linear FETI framework (cf. Chapter 2). A list of these extensions is given below.

- In Chapter 3, a number of simplifications to the FETI solver are performed at linear domains. These simplifications constitute a by-pass to the assembly and factorization stages by storing the corresponding linear quantities. Consequently, the computational cost is linked to the extension of the non-linear domains. For this reason, the strategy results adequate for the simulation of quasi-brittle and brittle materials where the non-linearity is localized at failure zones. The presence of non-linearity in each domain is predicted using a heuristic expression, based on internal variables, which depends on the constitutive model.
- In Chapter 4 the efficient non-linear FETI framework introduced in Chapter 3 is extended for the multiscale analysis of quasi-brittle heterogeneous materials. These extensions constitute a key contribution in the present thesis. The main ingredients for the multiscale domain decomposition analysis consist in a strategy to glue incompatible meshes, a zoom-in technique to export the coarse scale deformation to the fine scale and a relaxation stage to guarantee global equilibrium. An adaptive multiscale analysis is performed by modifying the domain scale resolution at those domains that enter the non-linear regime. To this end, the non-linear predictors developed in Chapter 3 are utilized. The adaptive multiscale framework is compatible with the

solver simplifications proposed in Chapter 3. For this reason, the final framework is particularly adequate for the modelling of quasi-brittle materials that show localized failure patterns.

- Chapter 5 focuses on different micro-to-macro connections employed in the context of a non-overlapping multiscale domain decomposition technique. Different connections of strong and weak type are investigated and two new constraints are introduced. Normal collocation is proposed as a variation of the standard collocation technique and average compatibility with stiffness weighting constitutes a competitive alternative to weak compatibility techniques. The performance of the proposed interscale constraints is investigated for the case of highly heterogeneous interfaces both in “static” and adaptive multiscale analyses.
- A general procedure for the multiscale analysis of random heterogeneous materials is outlined in Chapter 6. The proposed framework is assessed for granular heterogeneous materials such as concrete and results are compared to DNS.

7.1 Summary of conclusions

In view of the performance of the presented framework, the following conclusions are listed below.

- As presented in Chapter 3, the simplifications to the FETI solver yield an efficient framework for the study of failure in brittle and quasi-brittle materials. Results turn out to be in good agreement with DNS and the cost of the analyses is related to the non-linear areas of interest. Different predictors for the non-linear regime are studied. The cost of the computations increase when more “conservative” predictors are utilized since non-linear behaviour is expected in a larger area of the material. The decomposition type and number of subdomains highly influences the efficiency of the framework. When the decomposition is based on material phases, the separation between linear and non-linear domains becomes more accurate and the efficiency of the framework is improved. A decomposition into a high number of subdomains naturally minimizes the number of FEs that are fully processed by the solver. However, the benefits of such decomposition may be mitigated by an increasing size of the interface problem.

7.1 Summary of conclusions

- The multiscale analyses presented in Chapter 4 are remarkably close to those obtained with DNS. Results prove to correctly capture the initiation and growth of non-linearity at a reduced computational cost when compared to full scale computations. The agreement with DNS is obviously subjected to an adequate choice of the effective elastic properties for the homogeneous bulk and a sufficiently refined coarse scale discretization. The domain decomposition type, i.e. number and shape of domains, hardly affects the multiscale analysis and, for this reason, the presented framework proves to be objective with respect to a user defined decomposition.
- Analyses shown in Chapter 5 indicate that the use of interscale links of a strong type generally result in globally stiffer mechanical responses while weak or average constraints tend to provide a softer mechanical behaviour. It is noticed that weak interscale connections involve a lower number of constraints and, therefore, the resulting interface problem becomes computationally cheaper. Standard collocation techniques generally lead to the most accurate results. However, the use of average compatibility with stiffness weighting seems to be an adequate choice in those cases where the stiffness contrasts at the interface are remarkably high. Normal collocation and standard average compatibility constraints are found to be less robust when tested in certain pathological cases.
- As demonstrated in Chapter 6 the proposed framework proves to be a valuable tool for the multiscale analysis of random heterogeneous quasi-brittle materials such as concrete. Results are in very good agreement with full scale analyses and the objectivity of the proposed framework is thoroughly assessed with respect to the coarse and fine scale discretizations and the domain decomposition. It is proven that the FETI multiscale framework can be used in 3D analysis without further modifications.
- Softening behaviour is simulated throughout this study with the use of a Gradient-Enhanced Damage model (cf. Appendix A). However, all extensions performed to the FETI framework are compatible with other constitutive models or numerical strategies to simulate cracking and strain localization provided that an appropriate indicator for switching the refinements is devised.

7.2 Recommendations and future research

Although the presented framework is capable of accomplishing the goals proposed for this thesis (cf. Section 1.2), there is room for a number of significant improvements and further research which are detailed below.

- The academical implementation used in this study is based on an interpreter and not on a standard compiled code. This implies that CPU times can not be measured and the quantification of the solver efficiency is given as a function of the size of the system to be processed and not as the speed up factor compared to DNS. For this reason, a full parallel implementation in a programming language suitable to be compiled can significantly improve the performance of the framework and quantify its efficiency.
- A full parallel implementation of the FETI code is obtained through the use of iterative solvers for the interface flexibility problem which is never explicitly assembled in practice. Although iterative solvers for symmetric and non-symmetric systems (cf. Appendix C) are available, they still perform poorly for highly heterogeneous problems (Appendix E). In this view, more research needs to be carried out in order to improve the efficiency of the preconditioners (cf. Appendix D) in these type of solvers. In addition, preconditioning the coarse grid and recycling previously computed directions of descent should also be applied.
- Implementing the above mentioned FETI extensions in a parallel computing environment raises another challenge: the work load at linear and non-linear domains is clearly unbalanced if each processor handles one domain. This is caused by the difference in scale resolution and/or the solver simplifications performed at linear domains. Hence, techniques such as automatic load-balancing and multi-threading should be considered to handle this issue.
- The use of error estimators for the coarse FE discretizations is recommended in the adaptive multiscale analysis. In this manner, an adequate coarse mesh is guaranteed during the linear elastic analysis and high energy imbalances are prevented during the zoom-in and relaxation stages.

7.2 Recommendations and future research

- The efficiency of the non-linear predictors developed in Chapter 3 can be improved by complementing their formulation with other criteria, e.g. the distance between the boundary of the domain and the damage or non-linear front.
- All multiscale extensions to FETI have been designed in the context of a quasi-static analyses. Extensions for dynamic analysis may entail modifications to the zoom-in and relaxation processes in order to avoid possible spurious wave reflections at the interface.
- Considering that all ingredients of the multiscale analysis reside at an algebraic level, it is recommended to evaluate the complete methodology on 3D and multiphysics engineering-relevant problems without further modifications to the multiscale algorithms.

Appendix A

Selected model for quasi-brittle failure*

Failure phenomena start with the nucleation of microcracks at those regions where the integrity of the material is lost. The growth and coalescence of microcracks tend to concentrate large strains in a process zone that eventually leads to complete loss of load-carrying capacity of the material.

In order to simulate such phenomena, two main numerical strategies can be outlined. Fracture mechanics has given rise to computational approaches based on a discontinuous description of the failure phenomena via the use of cohesive zones [44]. Traditional FE formulations allow cracks to propagate along predefined FE boundaries but its obvious dependence on the spatial discretization is solved by the use of re-meshing, embedding cohesive surfaces and more recently, with the introduction of discontinuous kinematics [74, 115]. On the other hand, damage mechanics techniques [62] can account for diffuse stiffness degradation but upon strain localization they suffer from spatial FE discretization. Objectivity of the numerical response can be reached via the introduction of nonlocality both in the integral [89] or differential form [87]. However, spurious damage growth can be detected at ultimate localization stages since the deformations at the process zone enter the nonlocal averaging of FEs surrounding the crack [29].

A.1 Gradient enhanced damage model and its FE implementation

Failure mechanisms are simulated in this study considering the continuous degradation of the elastic material moduli via the introduction of a damage variable as described in [62]. The total stress σ and strain ε tensors are related through the isotropic elasticity-based damage constitutive law

$$\sigma = (1 - \omega) \mathbf{D}^e : \varepsilon, \quad \text{with } \omega \in [0, 1]. \quad (\text{A.1})$$

The range of the scalar variable ω represents the transition from a virgin material ($\omega = 0$) with intact elastic moduli \mathbf{D}^e into a fully damaged one

* This appendix is based on the work of Simone in [104].

($\omega = 1$). Damage growth is controlled by the damage loading function

$$f(\tilde{\varepsilon}, \kappa) = \tilde{\varepsilon} - \kappa, \quad (\text{A.2})$$

where κ is a history dependent parameter which represent the highest equivalent strain reached at a particular point. The evolution of the deformation history parameter κ is governed by the Kuhn-Tucker relations

$$f \leq 0, \dot{\kappa} \geq 0, f\dot{\kappa} = 0. \quad (\text{A.3})$$

Two expressions of the equivalent strain are considered in this study. The equivalent strain $\tilde{\varepsilon}$, according to the modified Von Mises definition [14], can be expressed as

$$\tilde{\varepsilon} = \frac{\gamma - 1}{2\gamma(1 - 2\nu)} + \frac{1}{2\gamma} \sqrt{\frac{(\gamma - 1)^2}{(1 - 2\nu)^2} I_1^2 - \frac{12\gamma}{(1 + \nu)^2} J_2}, \quad (\text{A.4})$$

where I_1 and J_2 are the first invariants of the strain tensor and the second invariant of the deviatoric tensor, respectively, the ratio between compressive and tensile strength is denoted by γ , and ν represents the Poisson's ratio. Following the proposal by Mazars et al. in [70], the equivalent strain can be defined in terms of positive principal strain components $\langle \varepsilon_j \rangle$ as

$$\tilde{\varepsilon} = \sqrt{\sum_{j=1}^{N_{\text{dim}}} \langle \varepsilon_j \rangle^2}, \quad (\text{A.5})$$

where N_{dim} refers to the number of dimensions. In local damage models, damage growth is made a function of the history parameter κ . Here, we consider the exponential damage evolution law

$$\omega(\kappa) = 1 - \frac{\kappa_0}{\kappa} \left[1 - \alpha + \alpha e^{-\beta(\kappa - \kappa_0)} \right], \quad (\text{A.6})$$

where κ_0 represents the threshold value of the history parameter for damage initiation, and α and β denote two model parameters influencing residual stress and initial slope of the stress-strain curve, respectively.

Without a regularization strategy, strains would localize into a narrow band of infinitesimal width while its value would approach infinity. This would cause the problem to become ill-posed. A way to circumvent this drawback is the introduction of a nonlocal strain quantity as proposed

in [89]. In this study a differential version of the nonlocal damage model known as the gradient-enhanced damage model [87] is considered. The equilibrium equation is coupled to a modified Helmholtz equation which regulates the evolution of the nonlocal equivalent strain. In the absence of body forces, the governing equations read

$$\nabla \cdot \boldsymbol{\sigma} = \mathbf{0}, \quad (\text{A.7a})$$

$$\tilde{\boldsymbol{\varepsilon}} = \tilde{\boldsymbol{\varepsilon}}_{\text{nl}} - c \nabla^2 \tilde{\boldsymbol{\varepsilon}}_{\text{nl}}, \quad (\text{A.7b})$$

with $\tilde{\boldsymbol{\varepsilon}}_{\text{nl}}$ the nonlocal equivalent strain, $\tilde{\boldsymbol{\varepsilon}}$ the local equivalent strain, and $c = l^2/2$ where l is the internal length scale. The modified Helmholtz equation in (A.7b) is combined with the boundary condition

$$\nabla \tilde{\boldsymbol{\varepsilon}}_{\text{nl}} \cdot \mathbf{n} \quad \text{on } \Gamma, \quad (\text{A.8})$$

\mathbf{n} being the outward unit normal at the boundary Γ of the body Ω . The gradient parameter c represents the internal length scale needed to regularize the problem and is related to the width of the localization band. In this model, both the history parameter κ and the loading function f are functions of the nonlocal equivalent strain $\tilde{\boldsymbol{\varepsilon}}_{\text{nl}}$.

Considering the linearization at iteration i with respect to $i - 1$, the discretized weak form of the field equations is expressed in matrix form as

$$\begin{bmatrix} \mathbf{K}_{i-1}^{\text{uu}} & \mathbf{K}_{i-1}^{\text{ue}} \\ \mathbf{K}_{i-1}^{\text{eu}} & \mathbf{K}_{i-1}^{\text{ee}} \end{bmatrix} \begin{bmatrix} \delta \mathbf{u}_i \\ \delta \tilde{\boldsymbol{\varepsilon}}_{\text{nl},i} \end{bmatrix} = \begin{bmatrix} \delta \mathbf{f}_i^{\text{u}} \\ \delta \mathbf{f}_i^{\text{e}} \end{bmatrix} = \begin{bmatrix} \mathbf{f}_{\text{ext}}^{\text{u}} \\ \mathbf{0} \end{bmatrix} - \begin{bmatrix} \mathbf{f}_{\text{int},i-1}^{\text{u}} \\ \mathbf{f}_{\text{int},i-1}^{\text{e}} \end{bmatrix}, \quad (\text{A.9})$$

where

$$\mathbf{K}_{i-1}^{\text{uu}} = \int_{\Omega} \mathbf{B}_{\text{u}}^{\text{T}} \mathbf{D}_{i-1}^{\text{dam}} \mathbf{B}_{\text{u}} d\Omega, \quad (\text{A.10})$$

$$\mathbf{K}_{i-1}^{\text{ue}} = - \int_{\Omega} \mathbf{B}_{\text{u}}^{\text{T}} \mathbf{s}_{i-1}^{\text{ue}} \mathbf{N}_{\varepsilon} d\Omega, \quad (\text{A.11})$$

$$\mathbf{K}_{i-1}^{\text{eu}} = - \int_{\Omega} \mathbf{N}_{\varepsilon}^{\text{T}} \mathbf{s}_{i-1}^{\text{eu}} \mathbf{B}_{\text{u}} d\Omega, \quad (\text{A.12})$$

and

$$\mathbf{K}_{i-1}^{\text{ee}} = \int_{\Omega} \left(\mathbf{N}_{\varepsilon}^{\text{T}} \mathbf{N}_{\varepsilon} + \mathbf{B}_{\varepsilon}^{\text{T}} c \mathbf{B}_{\varepsilon} \right) d\Omega, \quad (\text{A.13})$$

with

$$\mathbf{D}^{\text{dam}} = (1 - \omega_{i-1}) \mathbf{D}^{\text{el}}, \quad (\text{A.14})$$

$$\mathbf{s}_{i-1}^{\text{ue}} = \mathbf{D}^{\text{el}} \varepsilon_{i-1} \begin{bmatrix} \frac{\partial \omega}{\partial \kappa} \end{bmatrix}_{i-1} \begin{bmatrix} \frac{\partial \kappa}{\partial \tilde{\varepsilon}_{\text{nl}}} \end{bmatrix}_{i-1}, \quad (\text{A.15})$$

and

$$\mathbf{s}_{i-1}^{\text{eu}} = \begin{bmatrix} \frac{\partial \tilde{\varepsilon}}{\partial \varepsilon} \end{bmatrix}_{i-1}. \quad (\text{A.16})$$

The force vectors read

$$\mathbf{f}_{\text{ext}}^{\text{u}} = \int_{\Gamma_t} \mathbf{N}_{\text{u}}^{\text{T}} \hat{\mathbf{t}} d\Gamma, \quad (\text{A.17})$$

$$\mathbf{f}_{\text{int},i-1}^{\text{u}} = \int_{\Omega} \mathbf{B}_{\text{u}}^{\text{T}} \sigma_{i-1} d\Omega \quad (\text{A.18})$$

and

$$\mathbf{f}_{\text{int},i-1}^{\varepsilon} = \int_{\Omega} \left(\mathbf{N}_{\varepsilon}^{\text{T}} \mathbf{N}_{\varepsilon} \tilde{\varepsilon}_{\text{nl},i-1} + \mathbf{B}_{\varepsilon}^{\text{T}} c \mathbf{B}_{\varepsilon} \tilde{\varepsilon}_{\text{nl},i-1} - \mathbf{N}_{\varepsilon}^{\text{T}} \tilde{\varepsilon}_{i-1} \right) d\Omega. \quad (\text{A.19})$$

In the above expressions, the matrices \mathbf{N} and \mathbf{B} contain the shape functions and their derivatives, and the elastic \mathbf{D}^{el} and damaged \mathbf{D}^{dam} constitutive tensors, together with the stress and strain tensors, are written in matrix form.

A.2 Numerical aspects in a FETI framework

In the FETI method, the variational form of the governing equations results in a hybrid variational statement in which the inter-domain continuity condition is accounted for. When considering a gradient-enhanced damage model, the field of Lagrange multipliers for a given interface node reads

$$\boldsymbol{\lambda} = \begin{bmatrix} \lambda_{\text{u}} \\ \lambda_{\tilde{\varepsilon}_{\text{nl}}} \end{bmatrix}. \quad (\text{A.20})$$

The Lagrange multipliers λ_{u} account for the displacement degrees of freedom and $\lambda_{\tilde{\varepsilon}_{\text{nl}}}$ refer to the nonlocal equivalent strain degree of freedom arising from the modified Helmholtz equation. In case of an explicit calculation

of the nonlocal equivalent strain, as it is normally done in integral nonlocal formulations [89], it might be necessary to access information from an adjacent domain if the average is performed close to the interface. In this case, it is convenient to facilitate the access to data at neighboring domains via auxiliary global arrays.

Another aspect that requires special treatment is related to the non-symmetry of the interface problem (cf. Chapter 2 and appendix C) when using the gradient-enhanced damage model. The stiffness matrix that results from the discrete set of equations is non-symmetric and not necessarily positive-definite but its null space (cf. Appendix B) originates from the space derivative of the shape functions and, therefore, both left and right kernels coincide. The origin of the non-symmetry is linked to the damage model and not to the gradient formulation. Obviously, the resulting flexibility operator F_I of the interface problem becomes non-symmetric too. In this scenario, if an iterative solver is chosen for the solution of the interface problem, the Bi-Conjugate Stabilized Gradient (Bi-CGSTAB) or Generalized Minimal Residual (GMRES) can be used as explained in [5]. Results of the FETI analysis with a gradient-enhanced damage model using adequate preconditioners for the iterative solver are presented in Appendices C and D.

Appendix B

A family of generalized inverses*

When the stiffness matrix of the discrete system of governing equations for $\Omega^{(s)}$ is non-singular, the displacement field $\mathbf{u}^{(s)}$ is expressed as

$$\mathbf{u}^{(s)} = \mathbf{K}^{(s)-1} \left(\mathbf{f}^{(s)} - \mathbf{B}^{(s)\text{T}} \boldsymbol{\lambda} \right). \quad (\text{B.1})$$

However, when a domain is disconnected from its neighbors and its local fixations or constraints are not sufficient to render the system statically determined, the local stiffness $\mathbf{K}^{(s)}$ is singular, and the solution in (B.1) does not hold. This problem can be elegantly solved by introducing the concept of generalized inverse. To this end, let us rewrite the local system of discrete governing equations for domain $\Omega^{(s)}$ arising from (2.4) in a matrix form as

$$\begin{bmatrix} \mathbf{K}_{11}^{(s)} & \mathbf{K}_{12}^{(s)} \\ \mathbf{K}_{21}^{(s)} & \mathbf{K}_{22}^{(s)} \end{bmatrix} \begin{bmatrix} \mathbf{u}_1^{(s)} \\ \mathbf{u}_2^{(s)} \end{bmatrix} = \begin{bmatrix} \mathbf{b}_1^{(s)} \\ \mathbf{b}_2^{(s)} \end{bmatrix}, \quad (\text{B.2})$$

where $\mathbf{b}^{(s)}$ is the difference between external forces $\mathbf{f}^{(s)}$ and the forces $\mathbf{B}^{(s)\text{T}} \boldsymbol{\lambda}$ arising from the interdomain links. The system in (B.2) is partitioned assuming that $\mathbf{K}_{11}^{(s)}$ is a nonsingular square matrix of dimension equal to the rank of $\mathbf{K}^{(s)}$. If $\mathbf{K}^{(s)}$ is a square matrix of dimension n , the p columns corresponding to $\mathbf{K}_{12}^{(s)}$ and $\mathbf{K}_{22}^{(s)}$ in (B.2) are linearly dependent on the first $n - p$ columns. Consequently, there exists a matrix \mathbf{W} of dimension $(n - p) \times p$ such that

$$\begin{bmatrix} \mathbf{K}_{12}^{(s)} \\ \mathbf{K}_{22}^{(s)} \end{bmatrix} = \begin{bmatrix} \mathbf{K}_{11}^{(s)} \\ \mathbf{K}_{21}^{(s)} \end{bmatrix} \mathbf{W}. \quad (\text{B.3})$$

The first set of equations in (B.3) yields

$$\mathbf{W} = \mathbf{K}_{11}^{(s)-1} \mathbf{K}_{12}^{(s)} \quad (\text{B.4})$$

* This appendix is based on the work of Farhat and Rixen in [24].

which can be substituted in the second set of equations to give

$$\mathbf{K}_{22}^{(s)} - \mathbf{K}_{21}^{(s)} \mathbf{K}_{11}^{(s)-1} \mathbf{K}_{12}^{(s)} = \mathbf{0}. \quad (\text{B.5})$$

The left hand side of (B.5) is identified as the condensed stiffness matrix when $\mathbf{u}_1^{(s)}$ has been eliminated from the system in (B.2). Therefore, $\mathbf{u}_2^{(s)}$ defines a set of fixations that renders the structure statically determined. The system in (B.3) can then be rewritten as

$$\begin{bmatrix} \mathbf{K}_{11}^{(s)} & \mathbf{K}_{12}^{(s)} \\ \mathbf{K}_{21}^{(s)} & \mathbf{K}_{22}^{(s)} \end{bmatrix} \begin{bmatrix} -\mathbf{W} \\ \mathbf{I}_{p \times p} \end{bmatrix} = \mathbf{0}_{n \times p}, \quad (\text{B.6})$$

where $\mathbf{I}_{p \times p}$ is the identity matrix of dimension p , and $\mathbf{0}_{n \times p}$ is a $n \times p$ zero matrix. The p column vectors obtained by concatenating row-wise \mathbf{W} and $\mathbf{I}_{p \times p}$ clearly define a null space for the stiffness $\mathbf{K}^{(s)}$ represented as

$$\mathbf{R}^{(s)} = \begin{bmatrix} \mathbf{r}_1^{(s)} & \dots & \mathbf{r}_p^{(s)} \end{bmatrix} = \begin{bmatrix} -\mathbf{K}_{11}^{(s)-1} \mathbf{K}_{12}^{(s)} \\ \mathbf{I}_{p \times p} \end{bmatrix}. \quad (\text{B.7})$$

Note that the vectors $\mathbf{r}_1^{(s)}$ to $\mathbf{r}_p^{(s)}$ define a set of displacement directions that do not contribute to the deformation energy. In other words, the null space of $\mathbf{K}^{(s)}$ satisfying

$$\mathbf{K}^{(s)} \mathbf{R}^{(s)} = \mathbf{0}_{n \times p} \quad (\text{B.8})$$

represent the rigid body modes for domain $\Omega^{(s)}$.

When dealing with the solution of singular systems it is necessary to work with the concept of a generalized inverse as indicated in [24]. The generalized inverse $\mathbf{K}^{(s)+}$ of a stiffness matrix $\mathbf{K}^{(s)}$ can be defined as an operator that fulfills

$$\mathbf{K}^{(s)} \mathbf{K}^{(s)+} \mathbf{K}^{(s)} = \mathbf{K}^{(s)}. \quad (\text{B.9})$$

Using the block notation introduced in (B.2), a simple generalized inverse for $\mathbf{K}^{(s)}$ is obtained as

$$\mathbf{K}^{(s)[11]+} = \begin{bmatrix} \mathbf{K}_{11}^{(s)-1} & \mathbf{0} \\ \mathbf{0} & \mathbf{0} \end{bmatrix}, \quad (\text{B.10})$$

where the fixations determined by $\mathbf{u}_2^{(s)}$ have been set to $\mathbf{0}$. The relation in (B.10) shows how the generalized inverse is computed when a factorisation technique is applied, the choice of temporary links $\mathbf{u}_2^{(s)}$ being found automatically during factorisation as the ones for which zero pivots appear. Nevertheless, it should be stressed that a generalized inverse satisfying (B.9) is not unique and, therefore, a family of generalized inverses can be defined using the nullspace $\mathbf{R}^{(s)}$ of $\mathbf{K}^{(s)}$ and the nullspace $\tilde{\mathbf{R}}^{(s)}$ of $\mathbf{K}^{(s)\text{T}}$ by

$$\mathbf{K}^{(s)+} = \mathbf{K}^{(s)[11]+} + \mathbf{R}^{(s)}\mathbf{C} + \mathbf{D}\tilde{\mathbf{R}}^{(s)\text{T}} \quad (\text{B.11})$$

for any matrices \mathbf{C} and \mathbf{D} .

Appendix C

Iterative Solvers for the FETI interface problem

Iterative solvers search for approximations of all unknowns simultaneously as opposed to sequential factorization schemes in direct solvers. For this reason, they are naturally parallel and require a small amount of memory since the arrays involved in the computations do not need to be explicitly assembled. Although direct methods are widely accepted due to their robustness, the need for large computations has favored the migration to iterative solvers.

Essentially, iterative solvers can be classified into stationary and non-stationary solvers. Stationary methods seek a solution of the linear system $\mathbf{Ku} = \mathbf{f}$ via successive approximations in the form

$$\mathbf{u}^{(k)} = \mathbf{A}\mathbf{u}^{(k-1)} + \mathbf{a}, \quad (\text{C.1})$$

where neither \mathbf{A} nor \mathbf{a} depend on the iteration count k . Despite the fact that its formulation is rather simple, they are regarded as less efficient methods compared to non-stationary solvers. In the latter, the computations involve quantities that do change at each iteration k . The purpose of this text is to provide the algorithms of a few well established methods which can cover a large number of applications when implemented in a FETI framework. In this view the algorithms for the non-stationary Preconditioned Conjugate Gradient (PCG) and the Bi-Conjugate Gradient Stabilized (Bi-CGSTAB) methods are introduced in the following text. For an exhaustive overview of iterative solvers the reader is referred to the work of Barret et al. in [5].

C.1 The Preconditioned Conjugate Gradient (PCG) method

The PCG method is suitable for the solution of symmetric positive definite systems. It basically looks for a solution of $\mathbf{Ku} = \mathbf{f}$ in a subspace spanning the columns $\mathbf{Y}_k = [\mathbf{y}_1, \dots, \mathbf{y}_k]$. Each successive approximation

$$\mathbf{u}_k = \mathbf{Y}_k \boldsymbol{\eta}_k. \quad (\text{C.2})$$

The direction of search at iteration $k + 1$ is related to the residual $\mathbf{r}_k = \mathbf{f} - \mathbf{K}\mathbf{u}_k$ and made orthogonal to all previous directions, i.e. $\mathbf{Y}_k^T \mathbf{y}_{k+1} = \mathbf{0}$. At iteration $k + 1$ the approximation

$$\mathbf{u}_{k+1} = \mathbf{Y}_k \boldsymbol{\eta}_k + \mathbf{y}_{k+1} \eta_{k+1} = \mathbf{u}_k + \mathbf{y}_{k+1} \eta_{k+1}. \quad (\text{C.3})$$

Substituting the expression $\mathbf{u}_{k+1} = \mathbf{Y}_{k+1} \boldsymbol{\eta}_{k+1}$ to the system $\mathbf{K}\mathbf{u} = \mathbf{f}$ and premultiplying by \mathbf{Y}_{k+1}^T yields

$$\left(\mathbf{Y}_{k+1}^T \mathbf{K} \mathbf{Y}_{k+1} \right) \boldsymbol{\eta}_{k+1} = \mathbf{Y}_{k+1}^T \mathbf{f}. \quad (\text{C.4})$$

Taking into account the orthogonality condition of \mathbf{y}_{k+1} with respect to the previous k search directions

$$\left(\mathbf{y}_{k+1}^T \mathbf{K} \mathbf{y}_{k+1} \right) \eta_{k+1} = \mathbf{y}_{k+1}^T \mathbf{f}. \quad (\text{C.5})$$

Considering that $\mathbf{f} = \mathbf{r}_k + \mathbf{K}\mathbf{u}_k$ and the orthogonality $\mathbf{y}_{k+1}^T \mathbf{K} \mathbf{Y}_k = \mathbf{0}$

$$\eta_{k+1} = \frac{\mathbf{y}_{k+1}^T \mathbf{r}_k}{\mathbf{y}_{k+1}^T \mathbf{K} \mathbf{y}_{k+1}}. \quad (\text{C.6})$$

The search directions

$$\mathbf{y}_{k+1} = \tilde{\mathbf{K}}^{-1} \mathbf{r}_k + \mathbf{Y}_k \boldsymbol{\beta} \quad (\text{C.7})$$

where $\tilde{\mathbf{K}}^{-1}$ is a preconditioner which approximates the inverse \mathbf{K}^{-1} and $\boldsymbol{\beta}$ are the coefficients of orthogonalization with respect to the k previous directions.

Because of the construction of the method, the preconditioner $\tilde{\mathbf{K}}^{-1}$ must be symmetric positive definite and the computational cost of calculating $\tilde{\mathbf{K}}^{-1} \mathbf{r}_k$ must be low. The convergence of the PCG is controlled by the condition number of $\tilde{\mathbf{K}}^{-1} \mathbf{K}$ which indicates that the algorithm converges faster with a good estimate of the inverse.

In the sequel the algorithm of the PCG is presented for the targeted positive-semi-definite interface problem introduced in (2.13a). Due to the splitting of Lagrange multipliers

$$\boldsymbol{\lambda} = \boldsymbol{\lambda}_0 + \mathbf{P} \bar{\boldsymbol{\lambda}} \quad (\text{C.8})$$

with the initial guess

$$\boldsymbol{\lambda}_0 = \mathbf{Q} \mathbf{G}_I \left(\mathbf{G}_I^T \mathbf{Q} \mathbf{G}_I \right)^{-1} \mathbf{e} \quad (\text{C.9})$$

and considering the projection

$$\mathbf{P} = \mathbf{I} - \mathbf{Q}\mathbf{G}_I \left(\mathbf{G}_I^T \mathbf{Q}\mathbf{G}_I \right)^{-1} \mathbf{G}_I^T \quad (\text{C.10})$$

a solution for the interface unknowns is found by successive approximations of λ in order to satisfy

$$\mathbf{P}^T \mathbf{F}_I \mathbf{P} \bar{\lambda} = \mathbf{P}^T (\mathbf{d} - \mathbf{F}_I \lambda_0). \quad (\text{C.11})$$

A PCG algorithm for (C.11) is sketched in Box 2. Note that the strategy boils down to the construction of orthogonal directions of search \mathbf{p}^k in order to update the solution field $\mathbf{P}\bar{\lambda}$ used in (C.8). Although recurrent orthogonality of directions is indicated in the algorithm, full orthogonalization is used in practice due to numerical errors. Different choices for the preconditioner $\tilde{\mathbf{F}}_I^{-1}$ are commented in Appendix D. The cost of the algorithm is linked to the number of inner products and matrix vector multiplications indicated in Box 2. However, the products by the preconditioner and \mathbf{F}_I are, in a real implementation, not performed as matrix-vector products but as domain wise operations corresponding to local solves.

C.2 Preconditioned Bi-Conjugate Gradient Stabilized (Bi-CGSTAB)

The Bi-CGSTAB [111] is one of the non-stationary iterative methods capable of solving non-symmetric linear systems. It can be used within a FETI framework for those cases in which the interface problem (cf. (2.8)) is non-symmetric due to the non-symmetry of the flexibility operator \mathbf{F}_I . These type of situations arise when the local stiffness matrices $\mathbf{K}^{(s)}$ are non-symmetric due to the adopted constitutive material relation. Achdou et al. [1] have developed other strategies based on the FETI method to tackle non-symmetric systems.

An algorithm of the Bi-CGSTAB used to solve the semi-definite problem in C.11 is given in Box 3. Note that the Bi-CGSTAB involves inner products and matrix-vector products which makes it computationally more expensive than the PCG. As mentioned in Section C.1 recurrent orthogonality is used to update the search directions while in practice full orthogonalization is recommended.

Box 2 Preconditioned Conjugate Gradient (PCG) algorithm

```

 $\mathbf{r}^0 = \mathbf{d} - \mathbf{F}_I \lambda^0$ 
Initialize  $\mathbf{w}^0 = \mathbf{P}^T \mathbf{r}^0$ 
Project for  $k = 1, 2, \dots$ 
  (*)  $\bar{\mathbf{p}}^{k-1} = \mathbf{P} \bar{\mathbf{F}}_I^{-1} \mathbf{w}^{k-1}$ 
Precondition + Re-project (*)  $\rho_{k-1} = (\mathbf{w}^{k-1})^T \bar{\mathbf{p}}^{k-1}$ 
  if  $k = 1$ 
     $\mathbf{p}^k = \bar{\mathbf{p}}^{k-1}$ 
  else
     $\beta_{k-1} = (\rho_{k-1}) / (\rho_{k-2})$ 
     $\mathbf{p}^k = \bar{\mathbf{p}}^{k-1} + \beta_{k-1} \mathbf{p}^{k-1}$ 
  endif
Project (*)  $\mathbf{v}^k = \mathbf{P}^T \mathbf{F}_I \mathbf{p}^k$ 
  (*)  $\alpha_k = (\rho_{k-1}) / ((\mathbf{p}^k)^T \mathbf{v}^k)$ 
Update
   $\lambda^k = \lambda^{k-1} + \alpha_k \mathbf{p}^k$ 
   $\mathbf{w}^k = \mathbf{w}^{k-1} - \alpha_k \mathbf{v}^k$ 
  if  $\|\mathbf{w}^k\| \leq \epsilon \|\mathbf{d}\| \rightarrow$  converged, stop
end

```

(*) Inner product

(*) Matrix-vector product

Box 3 Preconditioned Bi-Conjugate Gradient Stabilized (Bi-CGSTAB) algorithm

```

Initialize  $\mathbf{r}^0 = \mathbf{d} - \mathbf{F}_I \boldsymbol{\lambda}^0$ 
Project  $\mathbf{w}^0 = \mathbf{P}^T \mathbf{r}^0$ 
 $\bar{\mathbf{w}} = \mathbf{w}^0$ 
for  $k = 1, 2, \dots$ 
(*)  $\rho_{k-1} = \bar{\mathbf{w}}^T \mathbf{w}^{k-1}$ 
    if  $\rho_{k-1} = 0$  method fails
    if  $k = 1$ 
         $\mathbf{p}^k = \mathbf{w}^{k-1}$ 
    else
         $\beta_{k-1} = (\rho_{k-1} / \rho_{k-2}) (\alpha_{k-1} / \omega_{k-1})$ 
         $\mathbf{p}^k = \mathbf{w}^{k-1} + \beta_{k-1} (\mathbf{p}^{k-1} - \omega_{k-1} \mathbf{v}^{k-1})$ 
    endif
Precondition + Re-project (*)  $\bar{\mathbf{p}} = \mathbf{P} \bar{\mathbf{F}}_I^{-1} \mathbf{p}^{k-1}$ 
Project (*)  $\mathbf{v}^k = \mathbf{P}^T \mathbf{F}_I \bar{\mathbf{p}}$ 
(*)  $\alpha_k = \rho_{k-1} / (\bar{\mathbf{w}}^T \mathbf{v}^k)$ 
 $\mathbf{s} = \mathbf{w}^{k-1} - \alpha_k \mathbf{v}^k$ 
    if  $\|\mathbf{s}\| \leq 1.0e^{-15} \rightarrow$  set  $\boldsymbol{\lambda}^k = \boldsymbol{\lambda}^{k-1} + \alpha_k \bar{\mathbf{p}}$ , stop
Precondition + Re-project (*)  $\bar{\mathbf{s}} = \mathbf{P} \bar{\mathbf{F}}_I^{-1} \mathbf{s}$ 
Project (*)  $\mathbf{t} = \mathbf{P}^T \mathbf{F}_I \bar{\mathbf{s}}$ 
(**)  $\omega_k = \mathbf{t}^T \mathbf{s} / (\mathbf{t}^T \mathbf{t})$ 
Update  $\boldsymbol{\lambda}^k = \boldsymbol{\lambda}^{k-1} + \alpha_k \bar{\mathbf{p}} + \omega_k \bar{\mathbf{s}}$ 
 $\mathbf{w}^k = \mathbf{s} - \omega_k \mathbf{t}$ 
    if  $\|\mathbf{w}^k\| \leq \epsilon \|\mathbf{d}\| \rightarrow$  converged, stop
    if  $\omega_k = 0 \rightarrow$  cannot continue
end

```

(*) Inner product
(*) Matrix-vector product

Appendix D

Mechanically consistent preconditioners for the FETI interface problem*

Given a linear system of equations $\mathbf{K}\mathbf{u} = \mathbf{f}$, a preconditioner $\tilde{\mathbf{K}}^{-1}$ consists of an approximation of the inverse \mathbf{K}^{-1} used to improve the convergence of an iterative solver. Accurate, but computationally expensive preconditioners, tend to provide the best convergence ratios. Hence, an adequate preconditioner requires a certain compromise between the cost of its construction and the accuracy compared to the ideal use of the real inverse.

A preconditioner for the interface problem arising from the FETI method (cf. Appendix C) is denoted by $\tilde{\mathbf{F}}_I^{-1}$ and is seen as an approximation of the inverse of the flexibility operator \mathbf{F}_I^{-1} . Two types of preconditioners have been developed for the FETI method: the numerically scalable Dirichlet preconditioner $\tilde{\mathbf{F}}_I^{\text{D-1}}$ as introduced in [22] and the lumped preconditioner $\tilde{\mathbf{F}}_I^{\text{L-1}}$ that lumps the Dirichlet operator on the substructure interface (cf. [21, 25]). They can be written as

$$\tilde{\mathbf{F}}_I^{\text{D-1}} = \sum_{s=1}^{s=N_s} \mathbf{B}^{(s)} \begin{bmatrix} \mathbf{0} & \mathbf{0} \\ \mathbf{0} & \mathbf{S}_{\text{bb}}^{(s)} \end{bmatrix} \mathbf{B}^{(s)\text{T}}, \quad (\text{D.1a})$$

$$\tilde{\mathbf{F}}_I^{\text{L-1}} = \sum_{s=1}^{s=N_s} \mathbf{B}^{(s)} \begin{bmatrix} \mathbf{0} & \mathbf{0} \\ \mathbf{0} & \mathbf{K}_{\text{bb}}^{(s)} \end{bmatrix} \mathbf{B}^{(s)\text{T}}, \quad (\text{D.1b})$$

where the matrices $\mathbf{B}^{(s)}$ contain the boolean coefficients that enforce connectivity between substructures. For convenience, the coefficients of the stiffness matrix belonging to the interface are assembled last in $\mathbf{K}_{\text{bb}}^{(s)}$. The matrix partition $\mathbf{S}_{\text{bb}}^{(s)}$ is known as the Schur complement of a substructure $\Omega^{(s)}$ and reads

$$\mathbf{S}_{\text{bb}}^{(s)} = \mathbf{K}_{\text{bb}}^{(s)} - \mathbf{K}_{\text{bi}}^{(s)} \mathbf{K}_{\text{ii}}^{(s)-1} \mathbf{K}_{\text{ib}}^{(s)}, \quad (\text{D.2})$$

* This appendix is based on the work of Rixen and Farhat in [98].

where the subscripts i and b denote the internal and boundary DOFs respectively.

D.1 Extension to mechanically consistent preconditioners

Preconditioning the projected residual \mathbf{w} by the Dirichlet or the Lumped preconditioners (cf. equation (D.1)) yields

$$\bar{\lambda} = \tilde{\mathbf{F}}_I^{-1} \mathbf{w} = \sum_{s=1}^{s=N_s} \mathbf{b}^{(s)} \left(\mathbf{S}_{bb}^{(s)} \text{ or } \mathbf{K}_{bb}^{(s)} \right) \mathbf{b}^{(s)\top} \mathbf{w}, \quad (\text{D.3})$$

where $\mathbf{b}^{(s)}$ represents the restriction of $\mathbf{B}^{(s)}$ to the interface boundary of substructure $\Omega^{(s)}$. The correction of the Lagrange multiplier field $\bar{\lambda}$ as introduced in (D.3) can be understood as a three step procedure in which:

1. displacement corrections are imposed at the subdomain interfaces as

$$\Delta \mathbf{u}_b^{(s)} = \mathbf{b}^{(s)\top} \mathbf{w}, \quad (\text{D.4})$$

2. the corresponding interface nodal forces are computed as

$$\Delta \mathbf{f}_b^{(s)} = \left(\mathbf{S}_{bb}^{(s)} \text{ or } \mathbf{K}_{bb}^{(s)} \right) \Delta \mathbf{u}_b^{(s)}, \quad \text{and} \quad (\text{D.5})$$

3. the jump of interface nodal forces is computed to obtain the Lagrange multiplier corrections

$$\bar{\lambda} = \sum_{s=1}^{s=N_s} \mathbf{b}^{(s)} \Delta \mathbf{f}_b^{(s)}. \quad (\text{D.6})$$

The concept of mechanically consistent preconditioner, as introduced in [98], follows the three step procedure defined in (D.4) to (D.6) but, in addition, the displacement increments $\Delta \mathbf{u}_b^{(s)}$ and Lagrange multiplier corrections $\bar{\lambda}$ fulfill compatibility and near equilibrium concepts. As illustrated in Figure D.1, the initial projected residual \mathbf{w} denotes the displacement gap at both sides of the interface. Mechanically consistent displacement increments $\Delta \mathbf{u}_b^{(s)}$ are constructed such that the corrected interface displacements $\tilde{\mathbf{u}}_b^{(s)}$ satisfy the interface compatibility

$$\sum_{s=1}^{s=N_s} \mathbf{b}^{(s)} \tilde{\mathbf{u}}_b^{(s)} = \sum_{s=1}^{s=N_s} \mathbf{b}^{(s)} \left(\mathbf{u}_b^{(s)} + \Delta \mathbf{u}_b^{(s)}(\mathbf{w}) \right) = \mathbf{0}. \quad (\text{D.7})$$

D.2 Homogeneous problems (Multiplicity scaling)

This compatibility is indicated by the dotted line in Figure D.1 (step 2). After preconditioning (based on the boundary stiffness $\mathbf{K}_{\text{bb}}^{(s)}$ or the Schur complement \mathbf{S}_{bb}) the force distribution is found for the displacement compatibility condition. The nodal forces $\Delta \mathbf{f}_b^{(s)}$ can only satisfy force equilibrium if the corrected displacements $\tilde{\mathbf{u}}_b^{(s)}$ coincide with the exact solution.

The Lagrange multiplier corrections $\bar{\lambda}$ are defined based on the force increments $\Delta \mathbf{f}_b^{(s)}$. Mechanically consistent Lagrange multiplier corrections $\bar{\lambda}$ imply

$$\mathbf{b}^{(s)\text{T}} \bar{\lambda} = \Delta \mathbf{f}_b^{(s)}, \quad (\text{D.8a})$$

$$\text{if } \Delta \mathbf{f}_b^{(s)} - \sum_{r=1, r \neq s}^{s=N_s} \mathbf{b}^{(r)} \Delta \mathbf{f}_b^{(r)} = \mathbf{0}, \quad (\text{D.8b})$$

which reflects the equilibrium of all forces acting on an interface. In other words, the construction of $\bar{\lambda}$ is done in a way that, as the forces $\Delta \mathbf{f}_b^{(s)}$ approach equilibrium, the relation in (D.8a) is satisfied.

D.2 Homogeneous problems (Multiplicity scaling)

The mechanically consistent versions of the Dirichlet and lumped preconditioners for homogeneous problems can be written as

$$\tilde{\mathbf{F}}_I^{\text{D}^{-1}} = \sum_{s=1}^{s=N_s} \mathbf{A}^{(s)} \mathbf{B}^{(s)} \begin{bmatrix} \mathbf{0} & \mathbf{0} \\ \mathbf{0} & \mathbf{S}_{\text{bb}}^{(s)} \end{bmatrix} \mathbf{B}^{(s)\text{T}} \mathbf{A}^{(s)}, \quad (\text{D.9a})$$

$$\tilde{\mathbf{F}}_I^{\text{L}^{-1}} = \sum_{s=1}^{s=N_s} \mathbf{A}^{(s)} \mathbf{B}^{(s)} \begin{bmatrix} \mathbf{0} & \mathbf{0} \\ \mathbf{0} & \mathbf{K}_{\text{bb}}^{(s)} \end{bmatrix} \mathbf{B}^{(s)\text{T}} \mathbf{A}^{(s)}, \quad (\text{D.9b})$$

where $\mathbf{A}^{(s)}$ is a diagonal matrix storing the inverse of the multiplicity of the edges that intersect the substructure $\Omega^{(s)}$.

D.3 Heterogeneous problems (Smoothing procedures)

The multiplicity based averaging procedure is not mechanically sound when heterogeneous problems are taken into account. Hence, both Dirichlet and Lumped preconditioners cease to provide an optimal performance.

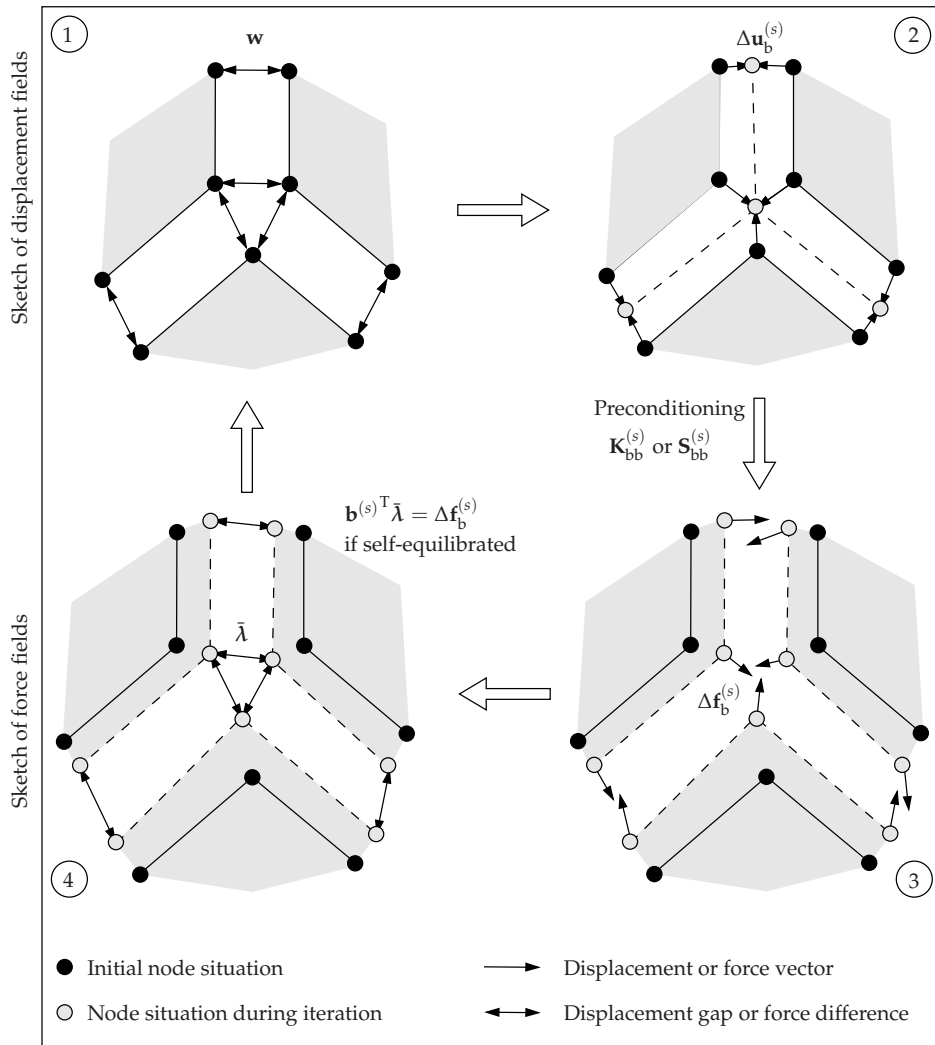


Figure D.1 Sketch of a FETI interface iteration with a mechanically consistent preconditioner.

The multiplicity based averaging procedure described in (D.9) can be seen as particular case of a more general averaging procedure in which the multiplicity scaling is complemented with a smoothing procedure where the underlying coefficients $\boldsymbol{\beta}^{(s)}$ can take different values in each substructure. The new form of the Dirichlet and Lumped preconditioners reads

$$\tilde{\mathbf{F}}_I^{\text{D}^{-1}} = \sum_{s=1}^{s=N_s} \boldsymbol{\beta}^{(s)} \mathbf{B}^{(s)} \begin{bmatrix} \mathbf{0} & \mathbf{0} \\ \mathbf{0} & \mathbf{S}_{\text{bb}}^{(s)} \end{bmatrix} \mathbf{B}^{(s)\text{T}} \boldsymbol{\beta}^{(s)}, \quad (\text{D.10a})$$

$$\tilde{\mathbf{F}}_I^{\text{L}^{-1}} = \sum_{s=1}^{s=N_s} \boldsymbol{\beta}^{(s)} \mathbf{B}^{(s)} \begin{bmatrix} \mathbf{0} & \mathbf{0} \\ \mathbf{0} & \mathbf{K}_{\text{bb}}^{(s)} \end{bmatrix} \mathbf{B}^{(s)\text{T}} \boldsymbol{\beta}^{(s)}, \quad (\text{D.10b})$$

In the superlumped smoothing procedure [98] the stiffness of each subdomain is lumped into its interface and the lumped stiffness matrix is diagonal and equal to $\text{diag}(\mathbf{K}_{\text{bb}})$. The smoothing coefficients in $\boldsymbol{\beta}^{(s)}$ are computed independently from each other as the ratio between the spring stiffness of a certain DOF and the sum of the spring stiffnesses of all reciprocal DOFs belonging to a different substructure. This procedure is referred to as k-scaling.

The coefficients $\boldsymbol{\beta}^{(s),i}$ of an interface edge $\Gamma_I^{(s),i} \subset \Gamma_I \cap \Gamma_I^{(s)}$ can be constructed as

$$\boldsymbol{\beta}^{(s),i} = \text{diag}(\mathbf{K}_{\text{bb}}^{(s),i}) \left(\sum_{r:\Gamma_I^{(s),i} \subset \Gamma_I \cap \Gamma_I^{(r)}} \text{diag}(\mathbf{K}_{\text{bb}}^{(r),j}) \right)^{-1}. \quad (\text{D.11})$$

The diagonal matrix $\boldsymbol{\beta}^{(s)}$ contains the smoothing coefficients associated with the interface DOFs belonging to the neighbors of $\Omega^{(s)}$.

The same idea can be used for the stiffness matrix on the interface instead of the lumped matrix and (D.11) can be re-written as

$$\boldsymbol{\beta}^{(s),i} = \text{diag}(\mathbf{S}_{\text{bb}}^{(s),i}) \left(\sum_{r:\Gamma_I^{(s),i} \subset \Gamma_I \cap \Gamma_I^{(r)}} \text{diag}(\mathbf{S}_{\text{bb}}^{(r),j}) \right)^{-1}. \quad (\text{D.12})$$

This procedure is referred to as s-scaling. Although the methodology is probably efficient, the Schur complement is normally never computed explicitly. For this reason, the s-scaling technique is never used in practice.

Appendix E

Assessment of the interface FETI solver for highly heterogeneous structures

The iterative solvers introduced in Appendix C in combination with the mechanically consistent preconditioners discussed in Appendix D are assessed for the solution of interface problems arising from the decomposition of an heterogeneous structure. The convergence of the iterative solver with different preconditioners is studied for linear elastic heterogeneous materials and non-linear analysis of damage growth and propagation (cf. Appendix A).

E.1 Convergence study in a linear elastic heterogeneous material

The benchmark test presented in [98] is adapted in this section in order to assess the behaviour of the introduced preconditioners. An elastic heterogeneous domain is loaded in tension as shown in Figure E.1 (top). The material sample consists of stiff and weak regions. The contrast between Young's moduli $E_{\text{Stiff}}/E_{\text{Weak}}$ is varied in the analyses while the Poisson's ratio $\nu = 0.2$. All computations are performed under plane stress conditions.

The structure is meshed using regular quadrilateral bi-linear elements and it is partitioned into nine regular subdomains. As shown in Figure E.1 (bottom), three different configurations are considered which account for different positions of the material interface with respect to the partitions.

The behaviour of various preconditioners is assessed according to the number of iterations needed at the interface problem. Both CG and Bi-CGSTAB are used and the convergence is monitored according to the norm of the projected residual $\|\mathbf{w}\|$. The interface problem is converged when $\|\mathbf{w}\| \leq \epsilon \|\mathbf{d}\|$, being $\|\mathbf{d}\|$ the norm of the interface gap created between substructures. The tolerance ϵ is set to 10^{-6} in all cases.

From the results summarized in Tables E.1 and E.2, a number of observations are listed below.

- All solvers perform similarly for the homogeneous case although a slight decrease of the iterations is observed for the Bi-CGSTAB solver.

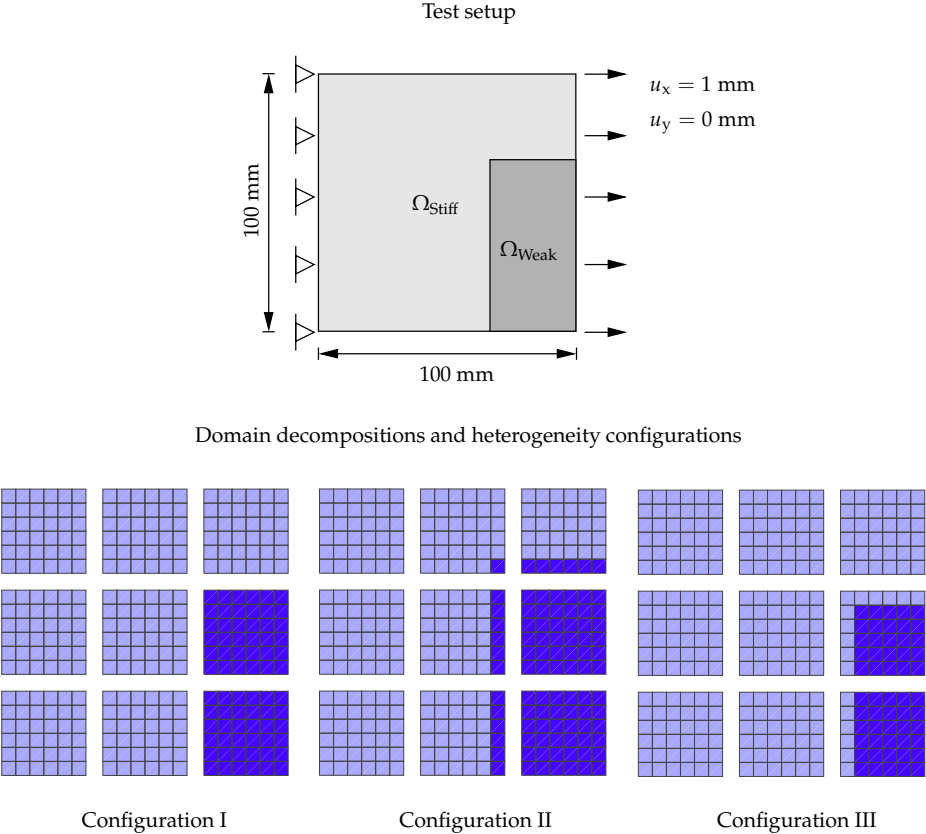


Figure E.1 Tension test on a linear elastic heterogeneous sample (top) and configuration of the material material interface with respect to the partition (bottom).

E.1 Convergence study in a linear elastic heterogeneous material

$E_{\text{Stiff}}/E_{\text{Weak}} = 1$				
CG	Multiplicity scaling		Smoothing procedures	
	Dirichlet	Lumped	Dirichlet	Lumped
Configuration I	10	14	10	14
Configuration II	10	14	10	14
Configuration III	10	14	10	14
Bi-CGSTAB	Multiplicity scaling		Smoothing procedures	
	Dirichlet	Lumped	Dirichlet	Lumped
Configuration I	7	11	7	11
Configuration II	7	11	7	11
Configuration III	7	11	7	11

$E_{\text{Stiff}}/E_{\text{Weak}} = 10^3$				
CG	Multiplicity scaling		Smoothing procedures	
	Dirichlet	Lumped	Dirichlet	Lumped
Configuration I	48	52	20	26
Configuration II	10	14	10	14
Configuration III	10	14	10	14
Bi-CGSTAB	Multiplicity scaling		Smoothing procedures	
	Dirichlet	Lumped	Dirichlet	Lumped
Configuration I	139	130	30	45
Configuration II	7	11	7	11
Configuration III	7	11	7	11

$E_{\text{Stiff}}/E_{\text{Weak}} = 10^4$				
CG	Multiplicity scaling		Smoothing procedures	
	Dirichlet	Lumped	Dirichlet	Lumped
Configuration I	48	53	21	27
Configuration II	22	26	21	26
Configuration III	20	25	20	25
Bi-CGSTAB	Multiplicity scaling		Smoothing procedures	
	Dirichlet	Lumped	Dirichlet	Lumped
Configuration I	635	1268	67	106
Configuration II	65	132	64	109
Configuration III	59	73	50	69

Table E.1 Effect of interface positioning and stiffness contrast. Results for $\mathbf{Q} = \mathbf{I}$.

$E_{\text{Stiff}}/E_{\text{Weak}} = 1$				
CG	Multiplicity scaling		Smoothing procedures	
	Dirichlet	Lumped	Dirichlet	Lumped
Configuration I	9	14	9	14
Configuration II	9	14	9	14
Configuration III	9	14	9	14
Bi-CGSTAB	Multiplicity scaling		Smoothing procedures	
	Dirichlet	Lumped	Dirichlet	Lumped
Configuration I	7	12	7	10
Configuration II	7	10	7	10
Configuration III	7	10	7	10

$E_{\text{Stiff}}/E_{\text{Weak}} = 10^3$				
CG	Multiplicity scaling		Smoothing procedures	
	Dirichlet	Lumped	Dirichlet	Lumped
Configuration I	47	52	15	21
Configuration II	15	20	14	20
Configuration III	19	24	19	24
Bi-CGSTAB	Multiplicity scaling		Smoothing procedures	
	Dirichlet	Lumped	Dirichlet	Lumped
Configuration I	88	133	9	15
Configuration II	10	14	10	14
Configuration III	35	49	28	46

$E_{\text{Stiff}}/E_{\text{Weak}} = 10^4$				
CG	Multiplicity scaling		Smoothing procedures	
	Dirichlet	Lumped	Dirichlet	Lumped
Configuration I	47	52	15	21
Configuration II	16	20	15	20
Configuration III	19	24	19	24
Bi-CGSTAB	Multiplicity scaling		Smoothing procedures	
	Dirichlet	Lumped	Dirichlet	Lumped
Configuration I	338	347	9	15
Configuration II	10	14	10	14
Configuration III	58	68	49	69

Table E.2 Effect of interface positioning and stiffness contrast. Results for $\mathbf{Q} = \tilde{\mathbf{F}}_1^{-1}$.

E.2 The role of damage

- The performance of both solvers diminishes when accounting for the heterogeneous cases. The number of interface iterations grow with the contrast between heterogeneities.
- The position of the heterogeneity interface with respect to the domain boundaries plays a also a crucial role. Configuration I is found to be the worst scenario when no special smoothing procedure is adopted.
- The introduced k-scaling and s-scaling smoothing procedures clearly improve the performance of both solvers specially for the first configuration. However, only a slight improvement in the convergence is observed when comparing s-scaling technique with the computationally cheaper k-scaling procedure.
- Preconditioning the coarse grid with $\mathbf{Q} = \tilde{\mathbf{F}}_I^{-1}$ generally improves the convergence as shown already in [9] and [95]. Its impact is more obvious for the Bi-CGSTAB solver when a high stiffness ratio is considered in Configuration I.
- It is observed that the Bi-CGSTAB performs slightly better than the CG solver for the homogeneous case. However, it shows a higher sensitivity to the arrangement of the heterogeneities. For this reason, a smoothing procedure like the k-scaling and the choice $\mathbf{Q} = \tilde{\mathbf{F}}_I^{-1}$ to form the projector \mathbf{P} is highly recommended.

E.2 The role of damage

Damage nucleation and propagation induces heterogeneity in the material due to degradation processes. Hence, an homogeneous or weakly heterogeneous material sample can progressively become highly heterogeneous when softening and failure phenomena take place. The next examples are dedicated to study and characterize the performance of the Bi-CGSTAB solver within FETI using the Gradient-Enhanced Damage model introduced in Appendix A. The choice of a Bi-CGSTAB solver is motivated from the fact that the flexibility operator \mathbf{F}_I is non-symmetric due to the non-symmetry of the associated stiffnesses $\mathbf{K}^{(s)}$ arising from the FE implementation of a GDAM model. Other options for the iterative solver (cf. Generalized Minimal Residual (GMRES) [5]) can be adopted too. However, the main focus is on the preconditioners and, for this reason, this study is restricted to one type of iterative solvers.

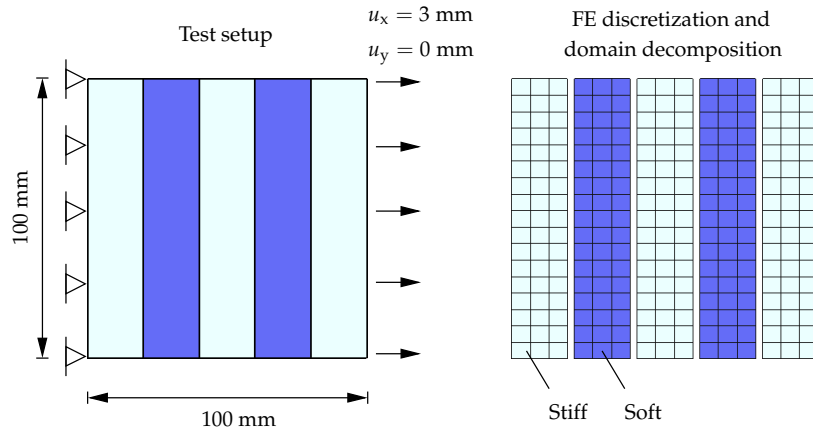


Figure E.2 Tension test setup (left), FE discretization and domain decomposition (right).

E.2.1 Damage-induced stiffness contrasts aligned with domain boundaries

A particular case of damage evolution within a FETI framework can be encountered when the extension of the damaged region is limited by the domain boundaries. This situation is reproduced in the test sketched in Figure E.2 where a composite material with stiff and soft layers is loaded in uniaxial tension. A regular domain decomposition is chosen according to the arrangement of material layers in the sample. Material model and iterative solver parameters are summarized in Table E.3. Note that the Dirichlet preconditioner is always utilized and the coarse grid is preconditioned using $\mathbf{Q} = \tilde{\mathbf{F}}_I^{-1}$. Only the type of scaling (multiplicity or smoothing) is varied in the analyses.

The distribution of damage in the material sample at ultimate loading stages is localized in the softer material regions (Figure E.3 top). The performance of the iterative solver is challenged with the progressive growth of damage and, consequently, the increasing contrast between soft and stiff layers. The number of interface iterations increases progressively for the analysis with a multiplicity scaling preconditioner (Figure E.3 bottom). The scaling with a smoothing technique turns to be, in this case, a more adequate choice since the increase in iterations is hardly noticed.

The stiffness contrast due to damage propagation (Figure E.3 top) shows some similarities with a transition from configurations I and II in the pre-

E.2 The role of damage

Material model data			Stiff component	Soft component
E	Young's modulus	[N/mm ²]	30.0×10^3	30.0×10^3
ν	Poisson's ratio	[-]	0.2	0.2
$\tilde{\epsilon}_{nl}$	Non-local equivalent strain	[-]	Mazars	Mazars
κ_0	Damage initiation threshold	[-]	5.0	2.5×10^{-3}
c	Gradient parameter	[mm ²]	72	72
$\omega(\kappa)$	Damage evolution law	[-]	Exponential	Exponential
α	Residual stress parameter	[-]	0.999	0.999
β	Softening rate parameter	[-]	100	100
Two-dimensional analysis type			Plane strain	
Iterative solver parameters				
Iterative solver type		BiConjugate Gradient Stabilized (Bi-CGSTAB)		
Preconditioner type		Dirichlet, $\tilde{\mathbf{F}}_I^{-1} = \tilde{\mathbf{F}}_I^{D^{-1}}$		
Coarse grid preconditioner		$\mathbf{Q} = \tilde{\mathbf{F}}_I^{-1}$		
Scaling type		Multiplicity or smoothing		

Table E.3 Material model (top) and iterative solver parameters (bottom) for the tension test on the composite material.

vious section (Figure E.2). It has been already observed that the scaling using smoothing procedures improves the convergence for this type of heterogeneity which is in agreement with the results obtained in this analysis.

E.2.2 Random growth of damage with respect to the domain boundaries

In practice, the situation reported in Section E.2.1 is not likely to happen. This is specially the case when dealing with random heterogeneous materials and mesh partitions. In order to study the behaviour of the iterative solver and preconditioners in such a scenario, a tensile test is performed on a granular material sample (top of Figure E.4). The beam contains two notches in its middle which are aligned vertically. Stresses are expected to concentrate between the notches due to the decrease of the cross section causing strain localization and failure. The specimen is decomposed in 10 domains using a graph partitioner (bottom of Figure E.4). Table E.4 contains all material data for the three phases (aggregates, matrix and ITZ) as well as the adopted parameters for the iterative interface solver. All computa-

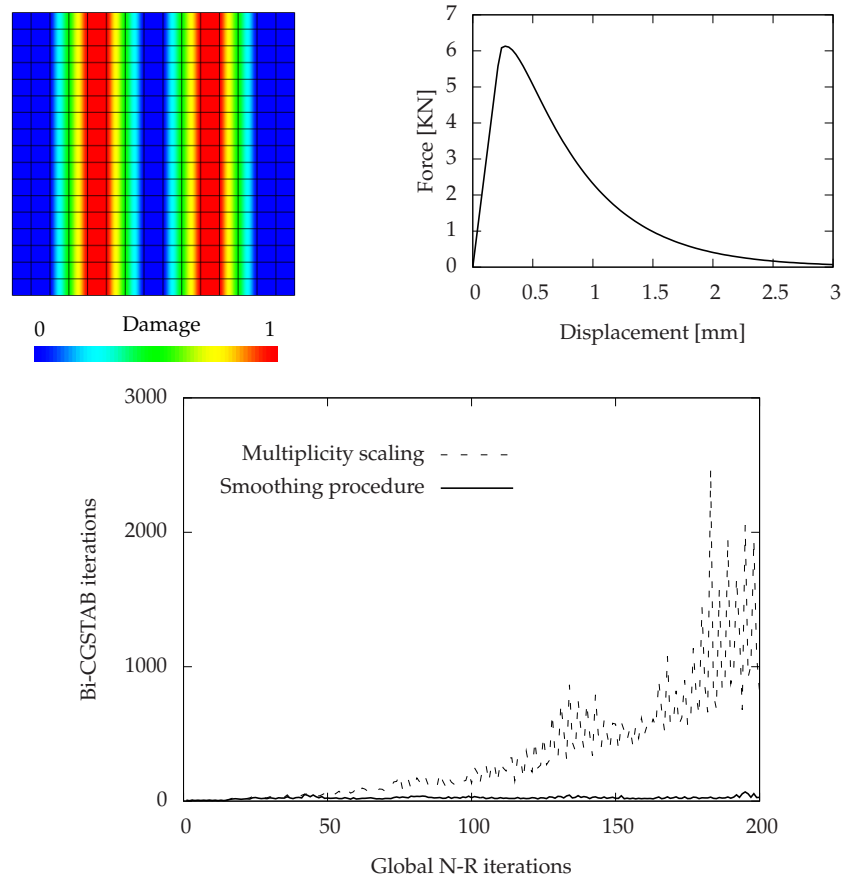


Figure E.3 Damage contours (top left), force-displacement plot (top right) and number of Bi-CGSTAB iterations (bottom).

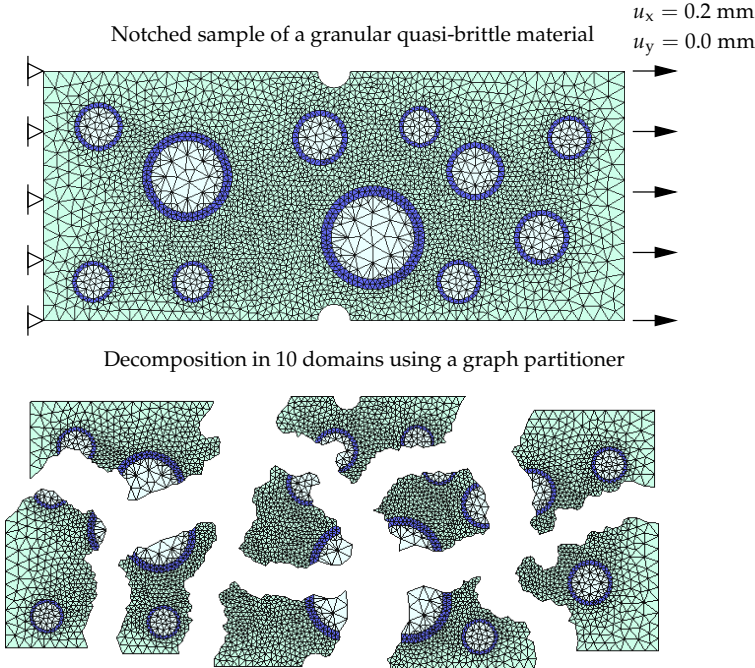


Figure E.4 Notched beam sample of a granular quasi-brittle material (top). Decomposition in 10 non-overlapping domains using a graph partitioner (bottom).

Material parameters			Aggregates	Matrix	ITZ
E	Young's modulus	[GPa]	30.0	25.0	20.0
ν	Poisson's ratio	[-]	0.2	0.2	0.2
$\tilde{\epsilon}_{nl}$	Equiv. strain (non-loc.)	[-]	Mazars	Mazars	Mazars
κ_o	Dam. init.	[-]	Dummy	3×10^{-4}	2.5×10^{-4}
c	Gradient param.	[mm ²]	1.0	1.0	1.0
$\omega(\kappa)$	Dam. evol. law	[-]	Exponential	Exponential	Exponential
α	Resid. stress param.	[-]	0.999	0.999	0.999
β	Soft. rate param.	[-]	100	100	100
Two-dimensional analysis type				Plane strain	
Iterative solver parameters					
Iterative solver type			BiConjugate Gradient Stabilized (Bi-CGSTAB)		
Preconditioner type			Dirichlet, $\tilde{\mathbf{F}}_I^{-1} = \tilde{\mathbf{F}}_I^{D^{-1}}$		
Coarse grid preconditioner			$\mathbf{Q} = \mathbf{I}$ or $\mathbf{Q} = \tilde{\mathbf{F}}_I^{-1}$		
Scaling type			Multiplicity or smoothing		

Table E.4 Material model (top) and iterative solver parameters (bottom) for the notched beam test.

tions are performed with the Bi-CGSTAB and the Dirichlet preconditioner. The coarse grid is preconditioned using $\mathbf{Q} = \tilde{\mathbf{F}}_I^{-1}$ and varying the type of scaling except for one case in which $\mathbf{Q} = \mathbf{I}$ and no scaling is applied.

As observed in Figure E.5, the differences between the three analyses are hardly visible in the linear elastic regime (stage A) but they increase progressively with damage growth and propagation (stages B to D). This is specially visible for the case $\mathbf{Q} = \mathbf{I}$ with no scaling. The analyses considering $\mathbf{Q} = \tilde{\mathbf{F}}_I^{-1}$ do not differ much from each other in terms of the efficiency of the solver. They both sense the presence of heterogeneity due to damage growth and in some stages the multiplicity scaling is found to perform better than the scaling with smoothing procedures.

E.3 General remarks

Although the Bi-CGSTAB presents the advantage of solving non-symmetric systems of equations it appears to be more sensitive to the presence of high stiffness contrasts than the CG. In general, preconditioning the coarse grid with $\mathbf{Q} = \tilde{\mathbf{F}}_I^{-1}$ improves the efficiency of both solvers remarkably. In the

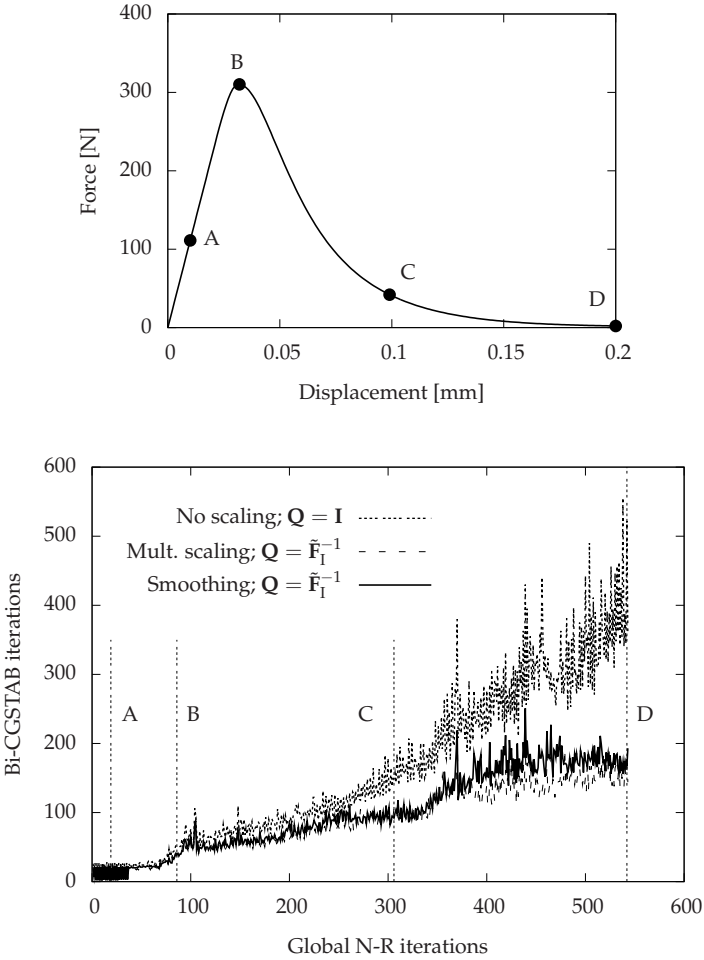


Figure E.5 Force-displacement plot (top) and number of Bi-CGSTAB iterations (bottom).

same spirit, the Dirichlet preconditioner $\tilde{\mathbf{F}}_1^{-1} = \tilde{\mathbf{F}}_1^{\text{D}^{-1}}$ is found to be a valuable tool to improve the performance of the iterative solver, however it renders the iterative solution scheme more expensive from a computational point of view. The scaling used to derive mechanically consistent preconditioners proves to enhance the efficiency of the solver but the benefit of using smoothing techniques instead of the multiplicity scaling diminish for arbitrarily distributed heterogeneities.

It is concluded that more research needs to be done in order to provide robust and efficient preconditioners that can deal with high stiffness contrasts due to evolving damage or non-linearity in a decomposed material. In this view, the work of Spillane and Rixen in [106] is seen as a clear contribution to improve the robustness of FETI. This challenging step is crucial for the development of a parallel implementation capable of exploring a wider range of interesting problems in computational mechanics.

References

The number printed in italics indicates the page where the publication is cited.

- [1] Y. Achdou, C. Japhet, P. Le Tallec, F. Nataf, F. Rogier, and M. Vidrascu. Domain decomposition methods for non-symmetric problems. In *Eleventh International Conference on Domain Decomposition Methods*, pages 3–17, 1999. {157}
- [2] O. Allix, P. Kerfriden, and P. Gosselet. On the control of the load increments for a proper description of multiple delamination in a domain decomposition framework. *International Journal for Numerical Methods in Engineering*, 83(11):1518–1540, 2010. {23}
- [3] G. M. Amdahl. Validity of the single processor approach to achieving large scale computing capabilities. In *Proceedings of the joint computer conference*, pages 483–485. ACM, 1967. {13}
- [4] A. Mobasher Amini, D. Dureisseix, and P. Cartraud. Multi-scale domain decomposition method for large-scale structural analysis with a zooming technique: Application to plate assembly. *International Journal for Numerical Methods in Engineering*, 79(4):417–443, 2009. {6, 50, 76, 80, 81, 117}
- [5] R. Barrett, M. Berry, T. F. Chan, J. Demmel, J. M. Donato, J. Dongarra, V. Eijkhout, R. Pozo, C. Romine, and H. Van Der Vorst. *Templates for the Solution of Linear Systems: Building Blocks for Iterative Methods*. SIAM Press, Philadelphia, PA, 1993. {13, 149, 155, 171}
- [6] F. B. Belgacem. The mortar finite element method with lagrange multipliers. *Numerische Mathematik*, 84(2):173–197, 1999. {76}
- [7] T. Belytschko and J. H. Song. Coarse-graining of multiscale crack propagation. *International Journal for Numerical Methods in Engineering*, 81(5):537–563, 2010. {2, 4}
- [8] C. Bernardi, Y. Maday, and A. Patera. A new nonconforming approach to domain decomposition: The mortar element method. In H. Brezis and J. L. Lions, editors, *Nonlinear Partial Differential Equations and their Application*, volume XI of *College de France Seminar*, pages 13–51. Pitman, London, 1994. {47, 76, 80}
- [9] M. Bhardwaj, D. Day, C. Farhat, M. Lesoinne, K. Pierson, and D. Rixen. Application of the FETI method to ASCI problems—scalability results on 1000 processors and discussion of highly heterogeneous problems. *International Journal for Numerical Methods in Engineering*, 47(1-3):513–535, 2000. {12, 14, 171}
- [10] J. H. Bramble, R. E. Ewing, R. R. Parashkevov, and J. E. Pasciak. Domain decomposition methods for problems with partial refinement. *SIAM Journal on Scientific and Statistical Computing*, 13(1):397, 1992. {76, 82}
- [11] E. W. C. Coenen, V. Kouznetsova, and M. G. D. Geers. Multi-scale continuous-discontinuous framework for computational-homogenization-localization. *Journal of the Mechanics and Physics of Solids*, 60(8):1486–1507, 2012. {5}
- [12] R. R. Craig and M. C. C. Bampton. Coupling of substructures for dynamic analysis. *American Institute of Aeronautics and Astronautics - Journal*, 6(7):1313–1319, 1968. {19}

- [13] P. Cresta, O. Allix, C. Rey, and S. Guinard. Nonlinear localization strategies for domain decomposition methods: Application to post-buckling analyses. *Computer Methods in Applied Mechanics and Engineering*, 196(8):1436–1446, 2007. {15}
- [14] J. H. P. de Vree, W. A. M. Brekelmans, and M. A. J. van Gils. Comparison of nonlocal approaches in continuum damage mechanics. *Computers & Structures*, 55:581–588, 1995. {146}
- [15] F. Desrumaux, F. Meraghni, and M. L. Benzeggagh. Generalised Mori-Tanaka scheme to model anisotropic damage using numerical eshelby tensor. *Journal of Composite Materials*, 35(7):603–624, 2001. {58}
- [16] H. B. Dhia and G. Rateau. The arlequin method as a flexible engineering design tool. *International Journal for Numerical Methods in Engineering*, 62(11):1442–1462, 2005. {76}
- [17] C. A. Duarte and D. J. Kim. Analysis and applications of a generalized finite element method with global-local enrichment functions. *Computer Methods in Applied Mechanics and Engineering*, 197(6-8):487–504, 2008. {4}
- [18] C. A. Duarte, T. J. Liszka, and W. W. Tworzydło. Clustered generalized finite element methods for mesh unrefinement, nonmatching and invalid meshes. *International Journal for Numerical Methods in Engineering*, 69(11):2409–2440, 2007. {76}
- [19] J. Eliáš and Z. P. Bažant. Fracturing in concrete via lattice-particle model. In E. Oñate and D. R. J. Owen, editors, *II International Conference on Particle-Based Methods — Fundamentals and Applications*, Barcelona, Spain, 2011. {117}
- [20] J. D. Eshelby. The determination of the elastic field of an ellipsoidal inclusion, and related problems. *Proceedings of the Royal Society of London. Series A, Mathematical and Physical Sciences*, 241(1226):376–396, 1957. {58}
- [21] C. Farhat. A Lagrange multiplier based divide and conquer finite element algorithm. *J. Comput. Sys. Engrg.*, 2:149–156, 1991. {161}
- [22] C. Farhat, J. Mandel, and F. X. Roux. Optimal convergence properties of the FETI domain decomposition method. *Comput. Meths. Appl. Mech. Engrg.*, 115:367–388, 1994. {161}
- [23] C. Farhat, K. Pierson, and M. Lesoinne. The second generation FETI methods and their application to the parallel solution of large-scale linear and geometrically non-linear structural analysis problems. *Computer Methods in Applied Mechanics and Engineering*, 184(2-4):333–374, 2000. {15}
- [24] C. Farhat and D. J. Rixen. Linear algebra. In S. G. Braun, editor, *Encyclopedia of Vibration*, pages 710–720. Elsevier, Oxford, 2001. {11, 151, 152}
- [25] C. Farhat and F. X. Roux. A method of finite element tearing and interconnecting and its parallel solution algorithm. *International Journal for Numerical Methods in Engineering*, 32(6):1205–1227, 1991. {9, 11, 46, 161}
- [26] C. Farhat and F. X. Roux. Implicit parallel processing in structural mechanics. *Computational Mechanics Advances*, 2:1–24, 1994. {12}
- [27] F. Feyel. A multilevel finite element method (FE²) to describe the response of highly non-linear structures using generalized continua. *Computer Methods in Applied Mechanics and Engineering*, 192(28-30):3233–3244, 2003. {1, 50}
- [28] F. Feyel and J. L. Chaboche. FE² multiscale approach for modelling the elastoviscoplastic behaviour of long fibre SiC/Ti composite materials. *Computer Methods in Applied Mechanics and Engineering*, 183(3-4):309–330, 2000. {4, 75}

References

- [29] M. G. D. Geers, R. de Borst, W. A. M. Brekelmans, and R. H. J. Peerlings. Strain-based transient-gradient damage model for failure analyses. *Computer Methods in Applied Mechanics and Engineering*, 160(1-2):133–153, 1998. {41, 145}
- [30] M. G. D. Geers, V. G. Kouznetsova, and W. A. M. Brekelmans. Multi-scale computational homogenization: Trends and challenges. *Journal of Computational and Applied Mathematics*, 234(7):2175–2182, 2010. {4}
- [31] N. Germain, J. Besson, F. Feyel, and P. Gosselet. High-performance parallel simulation of structure degradation using non-local damage models. *International Journal for Numerical Methods in Engineering*, 71(3):253–276, 2007. {20}
- [32] L. Giraud, S. Gratton, and E. Martin. Incremental spectral preconditioners for sequences of linear systems. *Applied Numerical Mathematics*, 57(11-12):1164–1180, 2007. {20}
- [33] I. M. Gitman, H. Askes, and L. J. Sluys. Coupled-volume multi-scale modelling of quasi-brittle material. *European Journal of Mechanics - A/Solids*, 27(3):302–327, 2008. {4, 76}
- [34] P. Gosselet and C. Rey. Non-overlapping domain decomposition methods in structural mechanics. *Archives of Computational Methods in Engineering*, 13(4):515–572, 2006. {9}
- [35] P. Gosselet, C. Rey, and J. Pebrel. Total and selective reuse of krylov subspaces for the resolution of sequences of nonlinear structural problems. *International Journal for Numerical Methods in Engineering*, 2012. doi: 10.1002/nme.4441. {15}
- [36] P. A. Guidault, O. Allix, L. Champaney, and C. Cornuault. A multiscale extended finite element method for crack propagation. *Computer Methods in Applied Mechanics and Engineering*, 197(5):381–399, 2008. {6}
- [37] P. A. Guidault, O. Allix, L. Champaney, and J. P. Navarro. A two-scale approach with homogenization for the computation of cracked structures. *Computers & Structures*, 85(17-18):1360–1371, 2007. {6, 117}
- [38] P. A. Guidault and T. Belytschko. On the l^2 and the h^1 couplings for an overlapping domain decomposition method using lagrange multipliers. *International Journal for Numerical Methods in Engineering*, 70(3):322–350, 2007. {76}
- [39] Z. Guo, M. Stroeven, W. Yang, and P. Stroeven. Hades, successor of space system; developments and new territories for exploration. In *12th International Congress for Stereology, ICS'XII*, Saint-Etienne, France, September 2007. 8 pages. {36}
- [40] J. L. Gustafson. Reevaluating Amdahl's law. *Communications of the ACM*, 31(5):532–533, 1988. {14}
- [41] Z. Hashin. Elasticity of random media. *Journal of Rheology*, 9(1):381–406, 1965. {59}
- [42] M. Hestenes and E. Stiefel. Methods of conjugate gradients for solving linear systems. *Journal of Research of the National Bureau of Standards*, 49:409–436, 1952. {13}
- [43] R. Hill. Elastic properties of reinforced solids: Some theoretical principles. *Journal of the Mechanics and Physics of Solids*, 11(5):357–372, 1963. {2, 58, 59, 75, 76}
- [44] A. Hillerborg, M. Modéer, and P. E. Petersson. Analysis of crack formation and crack growth in concrete by means of fracture mechanics and finite elements. *Cement and Concrete Research*, 6(6):773–782, 1976. {145}

- [45] J. Hinojosa. *Sur la robustesse d'une méthode de décomposition de domaine mixte avec relocalisation non linéaire pour le traitement des instabilités géométriques dans les grandes structures raidies*. PhD thesis, LMT-Cachan, 2012. {15}
- [46] J. D. Hoffman. *Numerical Methods for Engineers and Scientists*. Marcel Dekker, Inc., New York - Basel, second edition, 2001. {23}
- [47] D. A. Hordijk. *Local Approach to Fatigue of Concrete*. PhD thesis, Delft University of Technology, 1991. Also published as Tensile and tensile fatigue behaviour of concrete: Experiments, modelling and analyses. *HERON*, 37(1):3–79,1992. {27}
- [48] T. J. R. Hughes, G. R. Feijóo, L. Mazzei, and J. B. Quincy. The variational multiscale method—a paradigm for computational mechanics. *Computer Methods in Applied Mechanics and Engineering*, 166(1-2):3–24, 1998. {5, 76}
- [49] A. Hund and E. Ramm. Locality constraints within multiscale model for non-linear material behaviour. *International Journal for Numerical Methods in Engineering*, 70(13):1613–1632, 2007. {5, 76, 117}
- [50] A. Ibrahimbegović and D. Marković. Strong coupling methods in multi-phase and multi-scale modeling of inelastic behavior of heterogeneous structures. *Computer Methods in Applied Mechanics and Engineering*, 192(28-30):3089–3107, 2003. {5}
- [51] H. M. Inglis, P. H. Geubelle, and K. Matous. Boundary condition effects on multiscale analysis of damage localization. *Philosophical Magazine*, 88(16):2373, 2008. {76}
- [52] L. Kaczmarczyk, C. J. Pearce, and N. Bićanić. Scale transition and enforcement of RVE boundary conditions in second-order computational homogenization. *International Journal for Numerical Methods in Engineering*, 74(3):506–522, 2008. {4}
- [53] G. Karypis and V. Kumar. METIS - unstructured graph partitioning and sparse matrix ordering system, version 2.0, 1995. {37}
- [54] P. Kerfriden, O. Allix, and P. Gosselet. A three-scale domain decomposition method for the 3D analysis of debonding in laminates. *Computational Mechanics*, 44(3):343–362, 2009. {6}
- [55] H. G. Kim. Interface element method (IEM) for a partitioned system with non-matching interfaces. *Computer Methods in Applied Mechanics and Engineering*, 191(29-30):3165–3194, 2002. {76}
- [56] A. Klawonn and O. Rheinbach. Robust FETI-DP methods for heterogeneous three dimensional elasticity problems. *Computer Methods in Applied Mechanics and Engineering*, 196(8):1400–1414, 2007. {89}
- [57] A. Klawonn, O. Rheinbach, and O. B. Widlund. An analysis of a FETI-DP algorithm on irregular subdomains in the plane. *SIAM Journal on Numerical Analysis*, 46(5):2484–2504, 2008. {89}
- [58] V. Kouznetsova, W. A. M. Brekelmans, and F. P. T. Baaijens. An approach to micro-macro modeling of heterogeneous materials. *Computational Mechanics*, 27(1):37–48, 2001. {50, 56, 59, 75}
- [59] V. Kouznetsova, M. G. D. Geers, and W. A. M. Brekelmans. Multi-scale constitutive modelling of heterogeneous materials with a gradient-enhanced computational homogenization scheme. *International Journal for Numerical Methods in Engineering*, 54(8):1235–1260, 2002. {4}
- [60] P. Ladevèze, O. Loiseau, and D. Dureisseix. A micro-macro and parallel computational strategy for highly heterogeneous structures. *International Journal for Numerical Methods in Engineering*, 52(12):121–138, 2001. {6, 76}

References

- [61] P. Le Tallec, Y. H. De Roeck, and M. Vidrascu. Domain-decomposition methods for large linearly elliptic three dimensional problems. *Journal of Computational and Applied Mathematics*, 34:93–117, 1991. {9}
- [62] J. Lemaitre and J.-L. Chaboche. *Mechanics of Solid Materials*. Cambridge University Press, Cambridge, UK, 1994. {145}
- [63] O. Lloberas-Valls, F. P. X. Everdij, D. J. Rixen, A. Simone, and L. J. Sluys. Concurrent multiscale analysis of heterogeneous materials. In J. Eberhardsteiner, H. J. Böhm, and F. G. Rammerstorfer, editors, *CD-ROM Proceedings of the 6th European Congress on Computational Methods in Applied Sciences and Engineering (ECCOMAS 2012)*, Vienna, Austria, 2012. {117}
- [64] O. Lloberas-Valls, D. J. Rixen, A. Simone, and L. J. Sluys. Domain decomposition techniques for the efficient modeling of brittle heterogeneous materials. *Computer Methods in Applied Mechanics and Engineering*, 200(13–16):1577–1590, 2011. {19, 95}
- [65] O. Lloberas-Valls, D. J. Rixen, A. Simone, and L. J. Sluys. Multiscale domain decomposition analysis of quasi-brittle heterogeneous materials. *International Journal for Numerical Methods in Engineering*, 89(11):1337–1366, 2012. {45, 76, 95, 100}
- [66] O. Lloberas-Valls, D. J. Rixen, A. Simone, and L. J. Sluys. On micro-to-macro connections in domain decomposition multiscale methods. *Computer Methods in Applied Mechanics and Engineering*, 225–228(0):177–196, 2012. {75}
- [67] D. Marković and A. Ibrahimbegović. On micro-macro interface conditions for micro scale based FEM for inelastic behavior of heterogeneous materials. *Computer Methods in Applied Mechanics and Engineering*, 193(48-51):5503–5523, 2004. {50}
- [68] T. J. Massart, R. H. J. Peerlings, and M. G. D. Geers. An enhanced multi-scale approach for masonry wall computations with localization of damage. *International Journal for Numerical Methods in Engineering*, 69(5):1022–1059, 2007. {4, 76}
- [69] K. Matous, M. G. Kulkarni, and P. H. Geubelle. Multiscale cohesive failure modeling of heterogeneous adhesives. *Journal of the Mechanics and Physics of Solids*, 56(4):1511–1533, 2008. {4, 76}
- [70] J. Mazars and G. Pijaudier-Cabot. Continuum damage theory - Application to concrete. *Journal of Engineering Mechanics*, 115(2):345–365, 1989. {95, 146}
- [71] J. Mergheim. A variational multiscale method to model crack propagation at finite strains. *International Journal for Numerical Methods in Engineering*, 80(3):269–289, 2009. {5, 23}
- [72] S. Mesarovic and J. Padbidri. Minimal kinematic boundary conditions for simulations of disordered microstructures. *Philosophical Magazine*, 85(1):65, 2005. {76}
- [73] C. Miehe and A. Koch. Computational micro-to-macro transitions of discretized microstructures undergoing small strains. *Archive of Applied Mechanics*, 72(4):300–317, 2002. {4, 58, 59, 75, 76}
- [74] N. Moës, J. Dolbow, and T. Belytschko. A finite element method for crack growth without remeshing. *International Journal for Numerical Methods in Engineering*, 46(1):131–150, 1999. {145}
- [75] T. Mori and K. Tanaka. Average stress in matrix and average elastic energy of materials with misfitting inclusions. *Acta Metallurgica*, 21(5):571–574, 1973. {58}
- [76] H. Moulinec and P. Suquet. A numerical method for computing the overall response of nonlinear composites with complex microstructure. *Computer Methods in Applied Mechanics and Engineering*, 157(1-2):69–94, 1998. {1, 59, 75}

- [77] H. B. Mühlhaus and F. Oka. Dispersion and wave propagation in discrete and continuous models for granular materials. *International Journal of Solids and Structures*, 33(19):2841–2858, 1996. {2}
- [78] O. S. Narayanaswamy. Processing nonlinear multipoint constraints in the finite element method. *International Journal for Numerical Methods in Engineering*, 21(7):1283–1288, 1985. {86}
- [79] S. Nemat-Nasser and M. Hori. *Micromechanics: Overall properties of heterogeneous materials*. Elsevier, 1999. {1, 2, 56, 59, 75}
- [80] V. P. Nguyen, O. Lloberas-Valls, M. Stroeve, and L. J. Sluys. Homogenization-based multiscale crack modelling: from micro-diffusive damage to macro cracks. *Computer Methods in Applied Mechanics and Engineering*, 200(9-12):1220–1236, 2010. {4, 5, 76}
- [81] V. P. Nguyen, O. Lloberas-Valls, M. Stroeve, and L. J. Sluys. On the existence of representative volumes for softening quasi-brittle materials—a failure zone averaging scheme. *Computer Methods in Applied Mechanics and Engineering*, 199(45-48):3028–3038, 2010. {5}
- [82] V. P. Nguyen, O. Lloberas-Valls, M. Stroeve, and L. J. Sluys. Computational homogenization for multiscale crack modeling. implementational and computational aspects. *International Journal for Numerical Methods in Engineering*, 89(2):192–226, 2012. {5}
- [83] V. P. Nguyen, M. Stroeve, and L. J. Sluys. An enhanced continuous-discontinuous multiscale method for modeling mode-I cohesive failure in random heterogeneous quasi-brittle materials. *Engineering Fracture Mechanics*, 79:78–102, 2012. {5}
- [84] J. T. Oden, K. Vemaganti, and N. Moës. Hierarchical modeling of heterogeneous solids. *Computer Methods in Applied Mechanics and Engineering*, 172(1-4):3–25, 1999. {5}
- [85] J. Pamin and R. de Borst. Gradient-enhanced damage and plasticity models for plain and reinforced concrete. In W. Wunderlich, editor, *Proceedings of the European Conference on Computational Mechanics—ECCM’99*, pages 482–483, paper no. 636, Munich, 1999. Technical University of Munich. {27}
- [86] J. Pebre, C. Rey, and P. Gosselet. A nonlinear Dual-Domain decomposition method: Application to structural problems with damage. *international journal of multiscale computational engineering*, 6(3):251–262, 2008. {15}
- [87] R. H. J. Peerlings, R. de Borst, W. A. M. Brekelmans, and J. H. P. de Vree. Gradient enhanced damage for quasi-brittle materials. *International Journal for Numerical Methods in Engineering*, 39(19):3391–3403, 1996. {95, 133, 145, 147}
- [88] F. Perales, S. Bourgeois, A. Chrysochoos, and Y. Monerie. Two field multibody method for periodic homogenization in fracture mechanics of nonlinear heterogeneous materials. *Engineering Fracture Mechanics*, 75(11):3378–3398, 2008. {5}
- [89] G. Pijaudier-Cabot and Z. P. Bažant. Non-local damage theory. *Journal of Engineering Mechanics*, 113:1512–1533, 1987. {145, 147, 149}
- [90] A. Quarteroni and A. Valli. *Domain decomposition methods for partial differential equations*. Oxford University Press, 1999. {9}
- [91] L. Quiroz and P. Beckers. Non-conforming mesh gluing in the finite elements method. *International Journal for Numerical Methods in Engineering*, 38(13):2165–2184, 1995. {76, 82}
- [92] A. Reuss. Berechnung der fließgrenze von mischkristallen auf grund der plastizitätsbedingung für einkristalle. *ZAMM - Journal of Applied Mathematics and Mechanics*, 9:49–585, 1929. {56, 75}

References

- [93] F. Risler and C. Rey. On the reuse of Ritz vectors for the solution of nonlinear elasticity problems by domain decomposition methods. *Contemporary Mathematics*, 218:334–340, 1998. {15}
- [94] F. Risler and C. Rey. Iterative accelerating algorithms with krylov subspaces for the solution to large-scale nonlinear problems. *Numerical Algorithms*, 23(1):1–30, 2000. {19, 44}
- [95] D. J. Rixen. *Substructuring and dual methods in structural analysis*. PhD thesis, Publications de la Faculté des Sciences Appliquées, no. 175, Université de Liège, Belgium, 1997. {12, 47, 171}
- [96] D. J. Rixen. Dual schur complement method for semi-definite problems. In J. Mandel, C. Farhat, and X.-C. Cai, editors, *Contemporary Mathematics*, volume 218, pages 341–348. 1998. {50}
- [97] D. J. Rixen. Extended preconditioners for the FETI method applied to constrained problems. *International Journal for Numerical Methods in Engineering*, 54(1):1–26, 2002. {48, 49}
- [98] D. J. Rixen and C. Farhat. A simple and efficient extension of a class of substructure based preconditioners to heterogeneous structural mechanics problems. *International Journal for Numerical Methods in Engineering*, 44(4):489–516, 1999. {89, 161, 162, 165, 167}
- [99] S. Roels, J. Sermijn, and J. Carmeliet. Modelling unsaturated moisture transport in autoclaved aerated concrete: a microstructural approach. In *6th symposium on Building Physics in the Nordic countries*, pages 167–174, 2002. {118}
- [100] F. X. Roux. Parallel implementation of a domain decomposition method for non-linear elasticity problems. In D. Keyes, Y. Saad, and D. Truhlar, editors, *Domain-Based Parallelism and Problem Decomposition Methods in Computational Science and Engineering*, pages 161–175. SIAM, 1995. {15}
- [101] P. J. Sánchez, P. J. Blanco, A. E. Huespe, and R. A. Feijóo. Failure-oriented multi-scale variational formulation: Micro-structures with nucleation and evolution of softening bands. *Computer Methods in Applied Mechanics and Engineering*, 257:221–247, 2013. {5}
- [102] H. A. Schwarz. *Gesammelte Mathematische Abhandlungen*, volume 2. Verlag von Julius Springer, Berlin, 1890. {9}
- [103] G. H. C. Silva, R. Le Riche, J. Molimard, and A. Vautrin. Exact and efficient interpolation using finite elements shape functions. *European Journal of Computational Mechanics/Revue Européenne de Mécanique Numérique*, 18(3–4):307–331, 2009. {136}
- [104] A. Simone. Assessment of a gradient-enhanced continuum damage model and its implementation. Technical report, Delft University of Technology, 2000. {145}
- [105] A. Simone, G. N. Wells, and L. J. Sluys. From continuous to discontinuous failure in a gradient-enhanced continuum damage model. *Computer Methods in Applied Mechanics and Engineering*, 192(41-42):4581 – 4607, 2003. {27, 41}
- [106] N. Spillane and D. J. Rixen. Automatic spectral coarse spaces for robust FETI and BDD algorithms. *International Journal for Numerical Methods in Engineering*, 2012. submitted. {178}
- [107] P. Le Tallec and M. Vidrascu. Generalized Neumann-Neumann preconditioners for iterative substructuring. In P. E. Bjørstad, M. S. Espedal, and D. E. Keyes, editors, *Proceedings of the 9th International Conference on Domain Decomposition Methods*, pages 413–425, Bergen, Norway, 1996. {49}
- [108] K. Terada, M. Hori, T. Kyoya, and N. Kikuchi. Simulation of the multi-scale convergence in computational homogenization approaches. *International Journal of Solids and Structures*, 37(16):2285–2311, 2000. {101}

- [109] J. F. Unger. An $FE^2 - X^1$ approach for multiscale localization phenomena. *Journal of the Mechanics and Physics of Solids*, 61(4):928–948, 2013. {5}
- [110] O. van der Sluis, P. J. G. Schreurs, and H. E. H. Meijer. Effective properties of a viscoplastic constitutive model obtained by homogenisation. *Mechanics of Materials*, 31(11):743–759, 1999. {2, 59}
- [111] H. A. van der Vorst. Bi-CGSTAB: a fast and smoothly converging variant of Bi-CG for the solution of nonsymmetric linear systems. *SIAM Journal on Scientific and Statistical Computing*, 13(2):631–644, 1992. {157}
- [112] C. V. Verhoosel, J. J. C. Remmers, and M. A. Gutiérrez. A partition of unity-based multiscale approach for modelling fracture in piezoelectric ceramics. *International Journal for Numerical Methods in Engineering*, 82(8):966–994, 2010. {4, 5}
- [113] W. Voigt. Ueber die beziehung zwischen den beiden elasticitätsconstanten isotroper körper. *Annalen der Physik*, 274(12):573–587, 1889. {56, 75}
- [114] C. Wellmann and P. Wriggers. A two-scale model of granular materials. *Computer Methods in Applied Mechanics and Engineering*, 205–208(0):46–58, 2012. {117}
- [115] G. N. Wells and L. J. Sluys. A new method for modelling cohesive cracks using finite elements. *International Journal for Numerical Methods in Engineering*, 50(12), 2001. {145}
- [116] G. Wimmer, T. Steinmetz, and M. Clemens. Reuse, recycle, reduce (3R) - strategies for the calculation of transient magnetic fields. *Applied Numerical Mathematics*, 59(3-4):830–844, 2009. {19}
- [117] Z. Yuan and J. Fish. Multiple scale eigendeformation-based reduced order homogenization. *Computer Methods in Applied Mechanics and Engineering*, 198(21-26):2016–2038, 2009. {4}
- [118] J. Yvonnet and Q. C. He. The reduced model multiscale method (R3M) for the non-linear homogenization of hyperelastic media at finite strains. *Journal of Computational Physics*, 223(1):341–368, 2007. {19}
- [119] O. C. Zienkiewicz. *The Finite Element Method*. London: McGraw-Hill, 1967. {2, 9}
- [120] T. I. Zohdi and P. Wriggers. *An Introduction to Computational Micromechanics*. Springer, 2008. {75}

Summary

Computational material design is progressively gaining momentum in the engineering world. Recent breakthroughs in high performance computing and emerging multiscale algorithms have facilitated the simulation of materials at different scales of observation. In particular, the multiscale study of failure phenomena has attracted the attention of many scientists as it is crucial to assess the performance of engineering materials and structures under given loading conditions.

In this thesis, a concurrent multiscale method is proposed for the failure analysis of quasi-brittle materials. A main novelty resides in providing a different treatment, from a numerical standpoint, to linear elastic and non-linear regions. Considering that, upon strain localization, the non-linearity concentrates at particular failure zones, most of the computational effort, in terms of algorithmic complexity, is spent in these regions. Domain decomposition techniques, such as the Finite Element Tearing and Interconnecting (FETI) method, are used to partition the structure in a number of non-overlapping domains. Non-linearity is predicted employing heuristic indicators for each domain based on internal quantities linked to the selected constitutive model. A number of standard operations, such as matrix assembly and factorizations, are bypassed in linear elastic domains leading to a more efficient framework compared to a full finite element analysis.

Multiscale analysis is achieved by means of an adaptive refinement at those domains that are affected by damage processes. This refinement is done in terms of material scale and finite element size and different alternatives are explored to connect the non-matching meshes. It is verified that the framework is able to correctly capture the initiation and growth of non-linearity at a reduced computational cost when compared to full scale computations. The overall cost is obviously linked to the extension of the non-linear zone and, therefore, depends on the selected material and the type of problem. For this reason, the strategy is specially attractive for the study of failure in quasi-brittle materials.

Samenvatting

Het ontwerp van materialen met behulp van numerieke methoden wint stelselmatig aan belang binnen de ingenieurswereld. Recente ontwikkelingen op het gebied van supercomputers en de opkomst van multischaal algoritmes maken het mogelijk om materialen op verschillende schalen van waarneming te simuleren. Dit is van wezenlijk belang voor het onderzoek naar schadefenomenen, welke een doorslaggevende invloed hebben op de prestaties van materialen en constructies onder gegeven belastingscondities.

In dit proefschrift wordt een methode voorgesteld waarmee schadeanalyse van quasi-brosse materialen gelijktijdig op verschillende schalen van waarneming uitgevoerd wordt. De belangrijkste innovatie ligt in de verschillende behandeling, uit numeriek oogpunt, van de zones waar lineair en niet-lineair gedrag optreedt. De methode laat toe om het merendeel van de beschikbare reken capaciteit in te zetten voor de simulatie van die zones waar de rekken zich concentreren en waar niet-lineair gedrag zich voordoet.

Door middel van domein-decompositie technieken, zoals de "Finite Element Tearing and Interconnecting" (FETI) methode, wordt de constructie eerst in een aantal niet-overlappende domeinen gesplitst. Vervolgens wordt op basis van een heuristische indicator ingeschat of toekomstig niet-lineair gedrag waarschijnlijk is voor elk sub-domein. De heuristische indicator is gebaseerd op interne grootheden, gerelateerd aan het geselecteerde materiaalmodel. Omdat een aantal standaard operaties, zoals matrix opbouw en decompositie, vermeden kunnen worden in de lineaire sub-domeinen, is de voorgestelde methode efficiënter dan een volledige eindige elementen analyse.

De sub-domeinen die door het schadeproces beïnvloed worden, worden adaptief verfijnd, zowel wat de schaal betreft waarop het materiaal beschreven wordt, als op het vlak van de ruimtelijke discretisatie. Verschillende alternatieven werden onderzocht om de koppeling tussen sub-domeinen met een verschillende ruimtelijke discretisatie te realiseren. Tevens werd geverifieerd dat de voorgestelde methode de initiatie en groei van niet-lineariteiten correct voorspelt, en dat de simulaties minder rekenintensief zijn dan een berekening op een enkele schaal. In de voorgestelde

methode zijn de rekenkosten direct gerelateerd aan de omvang van de niet-lineaire zone, die op haar beurt samenhangt met het materiaal en het type probleem onder studie. De voorgestelde methodiek is daarom bij uitstek geschikt voor de studie van schadeprocessen in quasi-brosse materialen, waar schade zich concentreert in een zone met beperkte omvang.

Propositions

Appended to the dissertation

Multiscale domain decomposition analysis of quasi-brittle materials

by O. Lloberas-Valls

- 1 Computational multiscale analysis provides a solution where a full scale approach would turn out to be prohibitive. In such a scenario, the algorithm may never be verified.
- 2 Conducting independent scientific work will push you to your own limits. Collaboration will bring you beyond them.
- 3 I love simple ideas. If they work, they have a great chance to be easily disseminated and followed. If they don't, at least it is possible to understand why.
- 4 A good academic career is only achieved by great and disciplined researchers. A good idea can be devised by anyone.
- 5 One particular mystery which is not revealed by any religion is the human need for a religion itself.
- 6 Repetition of wars, crises and conflicts in history makes me think of a remake film. I wonder if they would appear with the same frequency if people would live longer; most experienced spectators prefer to watch something new rather than a known story.
- 7 ...And by the way, have you ever heard of Robert-Houdin? Speaking of magicians, I mean. Oh no, of course not... Houdin was the greatest magician who ever lived. And do you know what he said? "A magician", he said, "is just an actor. Just an actor playing the part of a magician."
Extracted from the film *F for fake*, Orson Welles, 1976.

However, it is simpler to transmit the solution to a problem (or revealing the "trick") rather than the engagement, curiosity and creativity to solve the mystery in new ones.

These propositions are regarded as opposable and defensible, and been approved as such by the supervisors Prof. dr. ir. L. J. Sluys, Prof. dr. ir. D. J. Rixen and Dr. A. Simone.

Stellingen

Behorende bij het proefschrift

Multischaal domein-decompositie analyse van quasi-brosse materialen

door O. Lloberas-Valls

- 1 Numerieke multischaal analyse biedt een antwoord in situaties waar berekeningen op een enkele schaal prohibitief zijn. Onder dergelijke omstandigheden is het niet altijd mogelijk de juistheid van het algoritme te verifiëren.
- 2 Zelfstandig onderzoek verrichten spoort je aan om je grenzen te verleggen. Samenwerking met andere onderzoekers laat je jezelf overstijgen.
- 3 Ik hou van eenvoudige ideeën. Indien ze sluitend zijn, dan is er een grote kans dat ze algemeen verspreid raken en navolging krijgen. Indien ze incorrect blijken, is het tenminste mogelijk om te begrijpen waarom.
- 4 Een succesvolle academische carrière is enkel weggelegd voor briljante en gedisciplineerde onderzoekers. Daarentegen kan iedereen een goed idee hebben.
- 5 Het is een mysterie dat de menselijke behoefte aan religie door geen enkele religie wordt verklaard.
- 6 De herhaling van oorlogen, crisissen en conflicten door de geschiedenis heen doet me denken aan het heruitbrengen van een bestaande film in een nieuw jasje. Ik vraag me af of dit met dezelfde frequentie zou gebeuren indien mensen langer zouden leven; de meeste film liefhebbers prefereren toch iets nieuws boven een oud verhaal.
- 7 Trouwens, heb je ooit van Robert-Houdin gehoord? De magiër, bedoel ik. Nee, waarschijnlijk niet... Houdin was de grootste magiër die ooit geleefd heeft. En weet je wat hij zei? "Een Magiër", zei hij, "is enkel een acteur. Een acteur die de rol van magiër speelt." Citaat uit de film *F for Fake* van Orson Welles, 1976.

Het is eenvoudiger om de oplossing (ofwel de truc achter de illusie) door te geven dan het engagement, de nieuwsgierigheid en de creativiteit om een nieuw raadsel te ontrafelen.

Deze stellingen worden opponeerbaar en verdedigbaar geacht en zijn als zodanig goedgekeurd door de promotoren, Prof. dr. ir. L. J. Sluys, Prof. dr. ir. D. J. Rixen and Dr. A. Simone.

Curriculum vitae

December 13 th , 1978	Born in Terrassa, Spain, as Oriol Lloberas-Valls
1996	Batxillerat científic, Escola Pia de Terrassa, Spain
2004	Enginyer Geòleg, Universitat de Barcelona i Universitat Politècnica de Catalunya, Spain
2004 – 2006	PhD student, Faculty of Civil Engineering and Geosciences, Delft University of Technology
2006 – 2007	Consulting engineer, Tec-cuatro S.A., Barcelona (Spain)
2007 – May 2013	PhD student, Faculty of Civil Engineering and Geosciences, Delft University of Technology

